DISSERTATION

Study of real space wave functions with electron energy loss spectrometry

ausgeführt zum Zwecke der Erlangung des akademischen Grades eines
Doktors der technischen Wissenschaften
unter der Leitung von

Univ. Prof. Peter Schattschneider

E138
Institut für Festkörperphysik

eingereicht an der
Technischen Universität Wien
Fakultät für Physik

von

Dipl.-Ing. Stefan Löffler

e0325258
Jägerstraße 69/1/12
A-1200 Wien

Wien, im November 2013

Kurzfassung

In der vorliegenden Arbeit werden neue Methoden vorgestellt, mit deren Hilfe Elektronenwellenfunktionen in Festkörpern mittels Transmissionselektronenmikroskopie (TEM) und Elektronenenergieverlustspektrometrie (EELS) direkt im Realraum vermessen werden können. Zu diesem Zweck wird sowohl die Theorie der elastischen Elektronenbeugung als auch die der inelastischen Elektronenstreuung im Dichtematrixformalismus dargestellt. Dabei werden die zentralen Größen der inelastischen Elektronenstreuung — der gemischte dynamische Formfaktor (MDFF) und der doppelt-differentielle Streuwirkungsquerschnitt (DDSCS) — verwendet. Zusätzlich zur formalen Theorie werden verschiedene Näherungen diskutiert und ihre jeweiligen Gültigkeitsbereiche erläutert. Darüber hinaus wird eine Methode zur Diagonalisierung des MDFFs beschrieben, welche die Simulation von energiegefilterten TEM Bildern mit bisher unerreichter Genauigkeit ermöglicht.

Nach der Darlegung der Theorie wird diese an Hand realer Beispiele praktisch erläutert. Einerseits wird anhand des Modellsystems Silizium gezeigt, wie Radialwellenfunktionen im Festkörper vermessen werden können. Die Übereinstimmung zwischen den theoretischen Vorhersagen und den experimentellen Daten erweist sich dabei als hervorragend. Andererseits wird abgeleitet, wie die Winkelabhängigkeit der Wellenfunktionen bestimmt werden kann. Es stellt sich heraus, dass die Symmetrie des untersuchten Systems ausschlaggebend für den Erfolg derartiger Untersuchungen ist. Mit den hier präsentierten neuen Techniken wird es in Zukunft möglich sein, elektronische Eigenschaften mit atomarer Auflösung zu vermessen, was technologisch bedeutend ist — besonders in den Materialwissenschaften.

Summary

In this work, new methods to study the real space wave functions of electrons in a solid using transmission electron microscopy (TEM) and electron energy loss spectrometry (EELS) are presented. To this end, the theory of both elastic and inelastic electron scattering is treated in a density-matrix formalism. In the process, the central quantities of inelastic electron scattering — the mixed dynamic form factor (MDFF) and the double differential scattering cross section (DDSCS) — are introduced. In addition to the formal theory, several approximations and simplifications, as well as their respective validities, are discussed. Furthermore, a method for diagonalizing the mixed dynamic form factor is described, which allows calculating high resolution energy filtered TEM images with unprecedented accuracy.

Subsequently, several applications of the aforementioned theory to real-world examples are presented. On the one hand, the example of Silicon serves to demonstrate how the radial wave functions in the bulk can be measured; the agreement with the theoretical predictions proves to be very good. On the other hand, the determination of the wave functions' azimuthal dependence is derived. It turns out that the symmetry of the system under investigation is crucial to the success of this endeavor. With the new techniques presented here, it will be possible to measure electronic properties with atomic resolution, which can be of great importance, particularly in material science.

Acknowledgements

First of all, I want to thank my supervisor Prof. Peter Schattschneider, Prof. Johannes Bernardi, and the whole USTEM team at the Vienna University of Technology. Peter gave me the opportunity to work on the interesting topics presented in this thesis. In addition, his ability to pose unexpected questions and to come up with new mathematical theorems was extraordinarily helpful. Johannes and the whole USTEM team not only provided the TEM and EELS facilities, but also a great work environment and support.

In particular, I am very grateful for the help Dr. Michael Stöger-Pollach and Dipl.-Ing. Walid Hetaba provided. From Michael, I learned many practical aspects of TEM and EELS. He also helped with the measurements of the Ångström-sized electron vortices presented in sec. 2.2. From Walid, I learned many aspects of WIEN2κ and DFT. Moreover, I very much appreciate the work of Prof. Christoph Eisenmenger-Sittner and his group, as well as Dipl.-Ing. Andreas Steiger-Thirsfeld, our FIB operator, who fabricated the holographic mask described in sec. 2.2.4. Additionally, I want to mention Dipl.-Ing. Viktoria Motsch, who worked with me on the diagonalization of the MDFF (see sec. 3.6) as part of her master's thesis, and Prof. Johan Verbeeck from the University of Antwerp, with whom I published several papers on electron vortex beams.

Of course, I am also greatly indebted to the Austrian Science Fund (FWF), which funded the project "Orbital Mapping" (grant number I543-N20), and to the Austrian Society for Electron Microscopy (ASEM), which provided a great network of electron microscopists and also supported my participations in several scientific conferences.

Last but not least, I want to thank my family, my girlfriend Dipl.-Ing. Mag. Veronika Doblhoff-Dier (without whom the linguistic aspect of this thesis would be much worse), and my friends for their continuous love and support over the years.

Contents

List of Abbreviations and Notations

ALCHEMI   atom location by channeling enhanced microanalysis

AREELS   angle resolved electron energy loss spectrometry

CCD   charge-coupled device

CTF   contrast transfer function

DDSCS   double differential scattering cross-section

DFF   dynamic form factor

DFT   density functional theory

DOS   density of states

EDX   energy dispersive X-rays

EEL   electron energy loss

EELS   electron energy loss spectrometry

EFSAD   energy-filtered selected area diffraction

EFSTEM   energy-filtered scanning transmission electron microscopy

EFTEM   energy-filtered transmission electron microscopy

ELCE   energy losses by channeled electrons

ELNES   energy-loss near edge structure

EMCD   energy-loss magnetic chiral dichroism

FEG   field emission gun

FFT   fast Fourier transform

FIB   focused ion beam

HLO   Hydrogen-like orbital

HRTEM   high resolution transmission electron microscopy

HWHM   half-width at half-maximum

IAM   independent atom model

MDFF   mixed dynamic form factor

OAM   orbital angular momentum

pDOS   partial density of states

rMDFF   real space MDFF

SAD	selected area diffraction
SEA	spectrometer entrance aperture
SEM	scanning electron microscopy
SNR	signal to noise ratio
STEM	scanning transmission electron microscopy
STM	scanning tunneling microscopy
STO	Slater-type orbital
TDS	thermal diffuse scattering
TEM	transmission electron microscope, also: transmission electron microscopy
XDOS	cross density of states
XMCD	X-ray magnetic circular dichroism
ZOLZ	zero order Laue zone

$\Re(z)$, $\Im(z)$	are the real and imaginary parts of z, respectively
$\arg(z)$	is the argument of z, i.e., $\arg\left(a\mathrm{e}^{\mathrm{i}\phi}\right) = b$
i	is the imaginary unit
e	is Euler's number
$\boldsymbol{r}$	is a vector
$\boldsymbol{M}$	is a matrix
$\hat{A}$	is an operator
$\langle\hat{A}\rangle$	is the expectation value of $\hat{A}$
$x := y$	means "x is defined to be y"
$\hat{\mathcal{F}}[f]$	denotes the Fourier transform of f

List of Figures

List of Tables

Preface

Beneath many section and chapter headings throughout this thesis, the phrase "This section is based on..." can be found. The references cited were vital resources for writing the section in question, apply to the whole section, and are therefore put in the beginning to emphasize their role.[1] In addition, the cited manuscripts often contain additional information not presented here (mostly because it would be beyond the scope of this work).

The organization of this work is the following: chapter 1 gives an introduction and overview of the formalisms and instruments used. It is followed by a summary of the description of elastic propagation of electrons in chapter 2, which is essential for understanding how the probe beam is formed in the condenser system and how it behaves in the sample. Subsequently, the theoretical description of inelastic scattering of fast electrons is developed from first principles in chapter 3. This constitutes the theoretical core of this work. In chapter 4, the whole theoretical framework is applied to analyze experiments and predict new findings. Finally, chapter 5 completes the main part of this work with conclusions and an outlook. In the following appendix, the computer programs, formulas, and some (lengthy) derivations used throughout this thesis are collected.

---

[1] Of course, intentional verbatim citations are marked as such.

1. Introduction

Dass ich erkenne, was die Welt
Im Innersten zusammenhält.
[So that I may perceive whatever holds
The world together in its inmost folds.]

(Johann Wolfgang von Goethe)

1.1. Motivation

For millennia, people have been wondering and speculating about the nature of the matter that surrounds us. Many theories were formed and dropped again. Interestingly, what started as a rather abstract concept in ancient greek — ατομοσ, the indivisible, the smallest imaginable object, which cannot be cut into smaller pieces — has survived until (or rather: has been revived in) modern chemistry and physics, albeit only by name, as sub-atomic particles such as protons, neutrons, and electrons are well-established nowadays. Among the pioneers of our current quantum mechanical understanding of the atom were Niels Bohr and Erwin Schrödinger.

This understanding of atoms and, consequently, matter on the nanometer scale is the foundation for the understanding, interpretation, and prediction of many material properties, ranging from the stability of chemical compounds, electrical conductivity, and magnetism to nuclear fission and decay, to name just a few. This work, in particular, will focus on electron orbitals, i.e., the probability distribution of finding an electron at a given position in the material. They are the origin of effects such as bonding, electric conductivity, magnetism, and most optical properties.

In order to investigate orbitals, one needs to be able to design experiments that interact with the electrons of the material in very defined manner and in a very confined region (typically of the order of $< 1\,\text{Å}$). To the best of my knowledge, this has only been achieved by scanning tunneling microscopy (STM) [1, 2] so far. However, since STM is inherently a surface-sensitive technique, and the electronic states on the surface are usually quite different from those inside a bulk sample (owing to the different boundary conditions), this method is hardly useful for many aspects of material science.

Thus, it is the aim of this work to pave the way for studying the orbitals in a material using a transmission electron microscope (TEM) and electron energy loss spectrometry (EELS). The TEM is particularly suited for the task, as with it, atomic resolution can be achieved routinely [3]. EELS, in turn, is a versatile method to investigate the interaction of the probe electrons in the TEM with the electrons in the

target [4]. Thus, TEM and EELS are the perfect choice for this endeavor. Moreover, many other analytical techniques such as high resolution images, electron diffraction and energy dispersive X-rays (EDX) can be combined with TEM and EELS in-situ, offering a range of additional possibilities to study the specimen.

1.2. Transmission Electron Microscopy and Electron Energy Loss Spectrometry

This section is based on [3, 4]

In principle, the TEM, invented by Knoll and Ruska in 1932 [5], works in a very similar way as an optical transmission microscope. Instead of light, however, it uses electrons as a probe. These electrons are emitted in the so-called "gun" (for all experiments in this work, a field emission gun (FEG) was used to ensure that the beam is sufficiently coherent [3]). This electron beam is then transfered to the sample via the condenser lens system. After passing through (and interacting with) the sample, the beam is transfered to a viewing screen, a charge-coupled device (CCD), or other analytical tools, via the objective and projective lens systems. Since electrons can be described as waves, the principal properties of optical microscopy still hold (such as diffraction, propagation, interference, etc.). There are two major differences between photons and electrons, however: (i) electrons are charged, and (ii) electrons have mass.

The fact that electrons are charged makes them easy to accelerate to very high kinetic energies, corresponding to very short wave lengths and hence very high spatial resolution. The fact that they have mass, on the other hand, implies that they do not travel at the speed of light, and hence can be treated (semi-)classically in certain situations (see sec. 1.3). At the same time, these properties also have negative side effects. Because of the long-ranged nature and high strength of the Coulomb interaction, the probe electrons interact much more strongly with matter than photons (in a comparable energy range). Therefore, TEM samples must be thin (typically $\lesssim 100\,\text{nm}$), a high vacuum chamber must be used, and a profound understanding of the effect this interaction has on image formation is required. Additionally, not all achievements of optics (such as aspheric lenses [6]) can be used in a TEM directly. Nowadays, many of these difficulties have been overcome and a profound understanding of the image formation in a TEM is available. Thus, it is possible to achieve atomic resolution routinely. Moreover, it is possible to investigate the crystal structure of the sample accurately using electron diffraction, owing to the wave nature of the electrons.

Electron energy loss (EEL) spectrometers are analytical tools that can be attached to a TEM (or, in some cases, installed inside). They use magnetic fields to discriminate the electrons of the probe beam with respect to their energy. That way, it is possible to analyze how many electrons have transferred which amount of energy to the sample. In high-end devices, it is also possible to select electrons with a certain energy and subsequently record the image formed solely by these electrons.

Energy transfer from the probe beam to the target is usually only possible in a

quantized way, i.e., by initiating certain transitions of the particles in the target. Possible excitations include thermal diffuse scattering (TDS), collective excitations such as plasmons, or single excitations of (typically tightly bound) electrons. This work will focus on the last type. Since the energy levels in a solid depend crucially on the nuclei, these single excitations are characteristic of the atomic species present inside the sample. Consequently, this method can be used routinely to analyze (and quantize) the chemical composition. Bonding effects and charge transfer also give rise to changes in the energy levels, by which individual bond states and valence states can be determined [3].

1.3. Assumptions and simplifications

The description of combined TEM and EELS measurements in general (and of elastic and inelastic scattering in particular) is very complex. To break it down to a manageable problem, several assumptions and simplifications have to be made. A list of the general ones used throughout this work is provided in the following.

Paraxial trajectories In TEMs, the electrons typically have a large kinetic energy in the range of tens to hundreds of keV. Deflecting such a beam by large angles would require very strong forces which are technically demanding[1]. Thus, the electron velocity's component orthogonal to the optical axis is small and, consequently, the electron beam normally travels close to the optical axis (i.e., in the so-called "paraxial region"). Therefore, normal TEMs can be several meters high while the diameters of the sample and the inner column are typically of the order of a few millimeters.

In addition, the treatment of magnetic lenses within the framework of ray optics is only applicable in the paraxial region, i.e., when the distance of the "beam" from the optical axis is much smaller than the typical extent of and distance between successive "optical" elements.

Relativistic corrections As is commonly done in the field of EELS, the quantum mechanical description in this work will be based on the non-relativistic Schrödinger formalism. The reasons for this approach are manifold:

- For probe electrons accelerated by a potential difference of 200 kV, the kinetic energy is still smaller than the rest energy by more than a factor of 2.

- Antimatter, the creation or annihilation of matter, and similar relativistic effects are not the focus of this work.

- The probe beam has no spin-polarization. In addition, the spin–spin interaction between probe and target is typically negligible due to the very short time a probe electron needs to pass through the sample [7].

---

[1]One instance where strong forces are used is the electron energy loss (EEL) spectrometer, in which very strong magnetic fields are used to separate the electrons by their kinetic energy [3, 4].

- The dominant contribution to the interaction between probe and target is the electric interaction, which is typically orders of magnitude stronger than the magnetic interaction.

- The external magnetic field produced by the pole pieces can be treated similarly to optical lenses (except for an image rotation [8]): the lenses can be described in a contrast transfer function (CTF) approach [3] and beams passing through them obey the basic lens equations.

Due to the speed of the electron, it is, however, necessary to introduce some relativistic corrections (sometimes referred to as kinematic corrections [9]). Most notably, this manifests itself in a change of the electron's wave length, momentum, and mass. For example, it is necessary to calculate the wavelength of the electron from the relativistic momentum given by $p = \sqrt{(E_0 + m_0 c^2)^2 - m_0^2 c^4}/c$. This yields [3]

$$\lambda = \frac{h}{p} = \frac{h}{\sqrt{2 m_0 E_0 \left(1 + \frac{E_0}{2 m_0 c^2}\right)}}, \tag{1.1}$$

where h is the Planck constant, m_0 is the rest mass of the electron, c is the speed of light, and $E_0 = e \cdot V$ is the energy gained by an electron of charge e when accelerated in a homogeneous electrostatic field of potential difference V. Hence, the electron's wave vector has the length $k := 2\pi/\lambda$.

Similarly, the (characteristic) momentum transfer associated with an energy loss of E is (in first order Taylor approximation in E) given by [10, 11]

$$q_E := k|_{E_0} - k|_{E_0 - E} \approx k|_{E_0} \cdot \frac{E}{2 E_0} \cdot \frac{1 + \frac{E_0}{m_0 c^2}}{1 + \frac{E_0}{2 m_0 c^2}}. \tag{1.2}$$

Since the electron's mass only enters as a constant pre-factor throughout this work, it's relativistic correction will not be treated here explicitly.

Periodic single crystals   Only ideal, periodic single crystals are considered for the elastic propagation, unless noted otherwise. This excludes, e.g., amorphous samples or quasicrystals. In particular, boundary effects are ignored and the specimens are treated similarly to infinite crystals. This entails that the lattice can be described by discrete points in momentum space. In addition, defects are generally neglected (or assumed to not perturb the elastic propagation of the probe electron significantly, e.g., in the case of dopant atoms).[2]

---

[2]Note that many of the results found in this work can also be applied to non-ideal systems as well with reasonable accuracy (in fact, all experimental data presented is inherently measured with imperfect samples). However, in the theoretical treatment, only the ideal case will be considered for the sake of clarity and simplicity.

Single electron approximation   Each inelastic scattering event is modeled as an interaction between exactly two electrons. The fact that only one probe electron is considered can be justified by estimating the (classical) distance between probe electrons in the TEM. With a velocity of $v \approx 0.7c$, an emission current of $I \approx 1\,\mu\text{A}$ [3], and the assumption of equidistant electrons, the distance can be estimated to be[3]

$$d \approx \frac{ve}{I} > 30\,\mu\text{m}. \tag{1.3}$$

Hence, there is at most one probe electron in the sample. This fact can be transferred to a quantum mechanical description of the probe electron as wave packet.

The single electron approximation for the target electrons is a more severe simplification, of course. The number of electrons in the crystal is of the order of 10^{23}. However, it is a common approximation to describe them in a density functional theory (DFT) approach as one electron in an effective mean field potential. The fact that this works well for a wide variety of materials warrants the use of this approximation in itself.

In addition, the electronic transitions treated in this work are core losses. These depend inherently on the initial state that is located deep inside the potential well of a nucleus. Hence, the probability density of an electron in the initial state is large only in close proximity to the nucleus, and the influence of neighboring atoms is negligible. As will be shown in sec. 3.7, the fact that the initial state is so localized in real space results in the selection of those parts of the final states that are similarly close to the nucleus, where the influence of neighboring atoms is small, and in the fact that scattering events at different atoms are incoherent. As a consequence, many effects in core losses can even be (and often are) described in an independent atom model (IAM).

1$^{\text{st}}$ order Born approximation   All inelastic scattering is treated in the 1$^{\text{st}}$ order Born approximation. That is, instead of solving the Lippmann-Schwinger equation

$$|\psi\rangle = |\phi\rangle + \hat{G}\hat{V}|\psi\rangle, \tag{1.4}$$

with the incident state $|\phi\rangle$, the outgoing state $|\psi\rangle$, the scattering operator $\hat{V}$, and the (homogeneous) Green's function $\hat{G}$, the simplification

$$|\psi\rangle = |\phi\rangle + \hat{G}\hat{V}|\phi\rangle, \tag{1.5}$$

is used.

Single scattering distribution   In this work, multiple scattering effects are ignored. For pure core losses, multiple scattering is irrelevant because of the small scattering cross sections (corresponding to a large inelastic mean free path) and because of the large energy loss involved. Assuming the probe would undergo two inelastic core loss interactions with respective energy losses of $E \gtrsim 100\,\text{eV}$, the resulting peak in the spectrum at $2E$ is far from the single scattering peak at E.

---

[3] Note that the distance between the electrons is much larger than the extent of an electron's wave packet, which can be estimated as $\Delta z \sim v\hbar/\Delta E \approx 1\,\mu\text{m}$ for an energy width of $\Delta E \approx 0.8\,\text{eV}$.

The only relevant contributions to the energy-loss near edge structure (ELNES) can thus come from low losses such as TDS, intra-band transitions, Cherenkov losses, and plasmons, which are all in the range of approximately $0\,\mathrm{eV}$ to $50\,\mathrm{eV}$. The description of these (which requires many-body systems, imperfect lattices, etc.) is not necessary for understanding the fundamentals of core losses and will, thus, not be treated here.

Experimentally, low losses cannot be avoided completely, of course, but their influence on the core loss regime can be minimized by using very thin samples. In addition, the remaining contributions can be compensated for by deconvolution methods [4, 12]. Moreover, it is noteworthy that only the ELNES is affected by this. The edge onset of core losses is not affected by low loss features, as the convolution is given implicitly by

$$I_{\mathrm{CL}}(E) = \int_{-\infty}^{\infty} I_{\mathrm{CL}}(E - \epsilon) I_{\mathrm{LL}}(\epsilon) \mathrm{d}\epsilon, \tag{1.6}$$

where I_{CL} is the core loss (multiple) scattering distribution and I_{LL} is the low loss scattering distribution. Because of $I_{\mathrm{CL}}(E - \epsilon < 0) = 0$, $I_{\mathrm{LL}}(\epsilon < 0) = 0$, it follows that $E = 0$ implies $\epsilon = 0$.

1.4. The density matrix formalism

This section is based on [13–16].

In quantum mechanics, a system is typically described by a wave function. This wave function can be interpreted as a vector in a linear vector space. Consequently, all mathematical concepts known for such vector spaces can immediately be applied to quantum mechanical states as well. One often-used property is the ability to write a wave function as a sum (i.e. a coherent superposition) of other wave functions. In particular, if one chooses a basis of the vector space, any wave function in it can be described as a superposition of the chosen basis vectors.

Hereby, however, it is assumed that one knows precisely which state the system is in. If, on the other hand, this is not the case, one has to describe the system as a statistical mixture of all possible states the system can be in [13]. Such a mixture is *not* a coherent superposition, but rather an incoherent sum weighted by statistical probabilities.

As an example, consider the well known system of a particle in a one-dimensional box of width 1. The eigenbasis of the Hamiltonian (in real space representation) is given by

$$B = \left\{ \sqrt{2} \sin(n\pi x) : n \in \mathbb{Z}, n > 0 \right\}. \tag{1.7}$$

First, assume that the system is in the known state

$$\psi(x) = \sin(\pi x) + \sin(2\pi x). \tag{1.8}$$

The system is said to be in a "pure state". ψ is defined essentially by the phase and amplitude relations between the two basis vectors. The probability density of this

state is given by

$$\rho(x) = |\psi(x)|^2 = \sin(\pi x)^2 + 2\sin(\pi x)\sin(2\pi x) + \sin(2\pi x)^2. \qquad (1.9)$$

On the other hand, if the system were in an unknown state comprised of the two states $\sqrt{2}\sin(\pi x)$ and $\sqrt{2}\sin(2\pi x)$, it would have to be described by a statistical mixture of those two states — it is said to be in a "mixed state". In that case, it is no longer possible to assign a (single) wave function to the system as was done in eq. 1.8. The probability density can still be calculated, however, yielding

$$\rho(x) = w \left| \sqrt{2}\sin(\pi x) \right|^2 + (1-w) \left| \sqrt{2}\sin(2\pi x) \right|^2$$
$$= 2 \left[w\sin(\pi x)^2 + (1-w)\sin(2\pi x)^2 \right], \qquad (1.10)$$

where w and $(1-w)$ are the statistical weights. Assuming even weights, i.e., $w = 1 - w = 1/2$, gives

$$\rho(x) = \sin(\pi x)^2 + \sin(2\pi x)^2. \qquad (1.11)$$

This result is obviously very different from eq. 1.9. It is noteworthy, though, that the result does not depend on the particular choice of basis — which would be unphysical. If, in the previous derivations, one performs the substitutions $\sin(n\pi x) \to \frac{1}{2i}\left(e^{in\pi x} - e^{-in\pi x} \right)$ to describe the system in a $\left\{ e^{in\pi x} \right\}$ basis, the results are the same.

One elegant way to handle both coherent superpositions and incoherent statistical mixtures properly is the density operator $\hat{\rho}$ or its matrix elements which comprise the density matrix $\boldsymbol{\rho}$. If a system has to be described by a statistical mixture of N different wave functions $|\psi_i\rangle$ with statistical weights w_i, the density operator is given by

$$\hat{\rho} = \sum_{i=1}^{N} w_i \left| \psi_i \right\rangle \left\langle \psi_i \right|. \qquad (1.12)$$

Applied to the previous examples, this gives[4]

$$\hat{\rho} = \frac{1}{2} \left(|1\rangle + |2\rangle \right) \left(\langle 1| + \langle 2| \right)$$
$$= \frac{1}{2} \left(|1\rangle\langle 1| + |2\rangle\langle 2| + |1\rangle\langle 2| + |2\rangle\langle 1| \right) \qquad (1.13)$$

for the pure state and

$$\hat{\rho} = w |1\rangle\langle 1| + (1-w) |2\rangle\langle 2|$$
$$= \frac{1}{2} \left(|1\rangle\langle 1| + |2\rangle\langle 2| \right) \qquad (1.14)$$

for the mixed state of the previous example. Clearly, the density operators of the pure and the mixed state differ by the occurrence of "off-diagonal" elements, i.e., elements

---

[4]Note that $|n\rangle$ is used for the state with real space representation $\langle x|n \rangle = \sqrt{2}\sin(n\pi x)$.

of the form $|a\rangle \langle b|$ with $a \neq b$, in the pure state. These off-diagonal elements describe correlations between the basis vectors — the basis vectors never occur independently. Note that the off-diagonal elements depend crucially on the basis used — by choosing a suitable ("physical") basis, the off-diagonal elements can be eliminated (see sec. 3.6). If this is done, the distinction between pure states and mixed states is that the former consists of only one remaining term, whereas the latter consists of several terms.

From the density operator, all quantum mechanical properties can be calculated. For instance, the probability of finding the system in a state $|a\rangle$ is given by $\langle a|\hat{\rho}|a\rangle$.[5] Applied to the previous examples, the probability of finding a particle described by the systems at position x — corresponding exactly to the probabilities given in eqs. 1.9 and 1.11 — can be calculated as $\langle x|\hat{\rho}|x\rangle$. Using $\langle x|n\rangle = \sqrt{2}\sin(n\pi x)$, this yields

$$\langle x|\hat{\rho}|x\rangle = \frac{1}{2}\left(\langle x|1\rangle\langle 1|x\rangle + \langle x|2\rangle\langle 2|x\rangle + \langle x|1\rangle\langle 2|x\rangle + \langle x|2\rangle\langle 1|x\rangle\right)$$
$$= \sin(\pi x)^2 + \sin(2\pi x)^2 + 2\sin(\pi x)\sin(2\pi x) \tag{1.15}$$

for the pure state and

$$\langle x|\hat{\rho}|x\rangle = \left(w\langle x|1\rangle\langle 1|x\rangle + (1-w)\langle x|2\rangle\langle 2|x\rangle\right)$$
$$= 2w\sin(\pi x)^2 + 2(1-w)\sin(2\pi x)^2$$
$$= \sin(\pi x)^2 + \sin(2\pi x)^2 \tag{1.16}$$

for the mixed state. Obviously, these are the same results as before. Similarly, properties such as the expectation value of an operator $\hat{A}$ are obtained by computing the trace over the density operator after applying $\hat{A}$:

$$\langle \hat{A}\rangle = \mathrm{tr}\left(\hat{A}\hat{\rho}\right) = \sum_{\boldsymbol{b}\in B}\langle \boldsymbol{b}|\hat{A}\hat{\rho}|\boldsymbol{b}\rangle. \tag{1.17}$$

For more information about the density matrix, the interested reader is referred to the literature, e.g., [13].

---

[5]For continuum states, this may only be defined in a distributional sense. For a discussion of the details of normalization, see chap. B.

2. Elastic propagation of electrons

> The simplicities of natural laws arise through the complexities of the language we use for their expression.
>
> *(Eugene Paul Wigner)*

One crucial aspect about understanding EELS and image formation is the elastic propagation of the wave function of the probe electron. The reason for this is that the elastic propagation changes the wave function, and with it the probability for certain excitations. As an example, one can consider the electron beam emanating from an ideal, point-like source. This beam then propagates elastically through the TEM column to the specimen. Inside the specimen, the situation becomes even more complex as the wave function can undergo many elastic scattering processes (diffraction) in the periodic potential of the crystal. After an inelastic scattering event, the same situation occurs again: before it can be measured in a detector, the scattered wave again has to propagate through the rest of the sample, undergoing many elastic scattering processes on the way, and the rest of the TEM column until it reaches the detector.

In particular, inside a specimen, one has to deal with effects like channeling or the so-called pendellösung [3]. Channeling can be exploited to enhance (or dampen) the signal originating from some particular sites inside the specimen, as is used in atom location by channeling enhanced microanalysis (ALCHEMI) [17, 18] or energy losses by channeled electrons (ELCE) [19, 20]. In other contexts, however, it would be considered an artifact. For example, highly localized beams (as in scanning transmission electron microscopy (STEM), but also directly after a core loss excitation, as its region of influence is limited by the extent of the target's initial state, see sec. 3.7) tend to channel along atomic columns [21]. In the worst case, this can result in a signal from an inelastic scattering event on one kind of atom at the position of a column that does not contain any atoms of said kind at all. Moreover, the pendellösung results in a signal oscillating in a highly complex way with sample thickness [22, 23]. In addition, elastic scattering typically will lead to interference effects if the probe beam is sufficiently coherent [24].

Hence, understanding the influence of elastic scattering — both in the vacuum of the TEM column as well as in a periodic potential — is essential for interpreting any experiments. In addition, the effects of lens aberrations, defocus, and non-ideal sources — which can be considered to be boundary conditions for the description of the elastic propagation — will be treated in this chapter as well.

2.1. The evolution operator

2.1.1. Time evolution

Generally, the propagation of the electron wave function is governed by the time-dependent Schrödinger equation which is given by

$$\hat{H}\left|\psi\right\rangle = i\hbar\partial_t\left|\psi\right\rangle.\tag{2.1}$$

In the Schrödinger picture, this can be solved formally by setting

$$\left|\psi(t)\right\rangle = \hat{U}(t, t_0)\left|\psi(t_0)\right\rangle\tag{2.2}$$

with the time evolution operator

$$\hat{U}(t, t_0) := \hat{T}e^{-\frac{i}{\hbar}\int_{t_0}^{t}\hat{H}dt},\tag{2.3}$$

where $\hat{T}$ is the time ordering operator. This section will deal solely with elastic scattering, i.e., the energy of the electron remains unchanged (for the inelastic case, see sec. 3.1). Under this assumption, the Hamiltonian $\hat{H}$ is time-independent. Hence, the time evolution operator can be simplified to

$$\hat{U}(t, t_0) := e^{-\frac{i}{\hbar}(t-t_0)\hat{H}}.\tag{2.4}$$

It is important to note that, due to the conservation of the norm of the wave function, $\hat{U}$ must be unitary (which can be seen immediately from eq. 2.4 as $\hat{H}$ is hermitian). This implies that orthonormal states are transformed into orthonormal states and that the norm of a state is preserved. Additionally, the fact that elastic scattering can be described in a wave function approach implies that pure state density matrices remain in a pure state when subjected to elastic scattering. This will become important in the next chapters.

2.1.2. Depth evolution

For fast electrons in the paraxial approximation, the optical axis (taken to be the z axis) is distinguished from the axes in any perpendicular plane. This suggests a separation ansatz[1]

$$\left|\psi\right\rangle = e^{-\frac{iEt}{\hbar}}e^{ik_z\hat{z}}\left|\alpha\right\rangle,\tag{2.5}$$

where k_z is a constant (typically chosen as $k_z = 2\pi/\lambda$, where λ is the wavelength of the electron). Because $e^{ik_z\hat{z}}$ is time-independent, the Schrödinger equation becomes

$$\hat{H}e^{ik_z\hat{z}}\left|\alpha\right\rangle = Ee^{ik_z\hat{z}}\left|\alpha\right\rangle.\tag{2.6}$$

---

[1]Actually, this ansatz can be applied to any problem, not just the paraxial approximation. In the paraxial case discussed below, however, $\left|\alpha\right\rangle$ is assumed to vary only slowly with z, which will lead to significant simplifications.

Using the identity

$$\hat{H}e^{ik_z\hat{z}} = e^{ik_z\hat{z}}\left(\hat{H} + e^{-ik_z\hat{z}}[\hat{H}, e^{ik_z\hat{z}}]\right), \tag{2.7}$$

eq. 2.6 can be rearranged to take the form of an effective Schrödinger equation,

$$\hat{\mathcal{H}}\ket{\alpha} := \left(\hat{H} + e^{-ik_z\hat{z}}[\hat{H}, e^{ik_z\hat{z}}]\right)\ket{\alpha} = E\ket{\alpha}. \tag{2.8}$$

Assuming that the Hamiltonian can be written as[2]

$$\hat{H} = \frac{\hat{\boldsymbol{p}}^2}{2m_e} + \hat{H}' \quad \text{with} \quad [\hat{H}', e^{ik_z\hat{z}}] = 0, \tag{2.9}$$

where m_e is the mass of the electron and $\hat{\boldsymbol{p}} = \hat{\boldsymbol{p}}_\perp + \hat{p}_z\boldsymbol{e}_z$ is the momentum operator, the commutator relations

$$\begin{aligned}
[\hat{\boldsymbol{p}}_\perp, e^{ik_z\hat{z}}] &= 0 \\
[\hat{p}_z, e^{ik_z\hat{z}}] &= \hbar k_z e^{ik_z\hat{z}} \\
[\hat{p}_z^2, e^{ik_z\hat{z}}] &= \hat{p}_z[\hat{p}_z, e^{ik_z\hat{z}}] + [\hat{p}_z, e^{ik_z\hat{z}}]\hat{p}_z \\
&= \hbar k_z\left(\hat{p}_z e^{ik_z\hat{z}} + e^{ik_z\hat{z}}\hat{p}_z\right) \\
&= \hbar k_z\left(e^{ik_z\hat{z}}\hat{p}_z + [\hat{p}_z, e^{ik_z\hat{z}}] + e^{ik_z\hat{z}}\hat{p}_z\right) \\
&= \hbar^2 k_z^2 e^{ik_z\hat{z}} + 2\hbar k_z e^{ik_z\hat{z}}\hat{p}_z
\end{aligned} \tag{2.10}$$

yield

$$e^{-ik_z\hat{z}}[\hat{H}, e^{ik_z\hat{z}}] = \frac{\hbar^2 k_z^2 + 2\hbar k_z\hat{p}_z}{2m_e}. \tag{2.11}$$

Thus, the effective Schrödinger equation takes the form

$$\hat{\mathcal{H}}\ket{\alpha} = \left(\frac{\hat{\boldsymbol{p}}_\perp^2 + \hat{p}_z^2 + 2\hbar k_z\hat{p}_z + \hbar^2 k_z^2}{2m_e} + \hat{H}'\right)\ket{\alpha} = E\ket{\alpha}. \tag{2.12}$$

In the paraxial approximation, it is assumed that the $e^{ik_z\hat{z}}$ term accurately describes the fast oscillations of the wave function in z direction. Consequently, it is assumed that $\ket{\alpha}$ varies only very slowly with z, or (equivalently), that

$$\langle\hat{p}_z^2\rangle \ll \hbar k_z\langle\hat{p}_z\rangle \quad \text{and} \quad \langle\hat{p}_z^2\rangle \ll \hbar^2 k_z^2. \tag{2.13}$$

Therefore, $\hat{\mathcal{H}}$ can be approximated by

$$\hat{\mathcal{H}} \approx \frac{\hat{\boldsymbol{p}}_\perp^2 + 2\hbar k_z\hat{p}_z + \hbar^2 k_z^2}{2m_e} + \hat{H}' \tag{2.14}$$

for the states of interest.

---

[2] $[\hat{H}', e^{ik_z\hat{z}}] = 0$ is the usual case in absence of magnetic fields with components perpendicular to the optical axis, in which situation $A_z = 0$ holds.

By rearranging the terms, eq. 2.12 can be transformed to

$$-\hat{p}_z \ket{\alpha} = \left(\frac{\hat{\boldsymbol{p}}_\perp^2}{2\hbar k_z} + \frac{\hbar k_z}{2} + \frac{m_e(\hat{H}' - E)}{\hbar k_z} \right) \ket{\alpha}. \tag{2.15}$$

Observing that $\hat{p}_z = -\mathrm{i}\hbar\partial_z$, this can again be written in a way reminiscent of a time-dependent Schrödinger equation in which z plays the role of time:

$$\mathrm{i}\hbar\partial_z \ket{\alpha} = \left(\frac{\hat{\boldsymbol{p}}_\perp^2}{2\hbar k_z} + \frac{\hbar k_z}{2} + \frac{m_e(\hat{H}' - E)}{\hbar k_z} \right) \ket{\alpha} =: \hat{\mathcal{H}}_\perp \ket{\alpha}. \tag{2.16}$$

Hence, the formalism of sec. 2.1.1 can be applied analogously, with[3]

$$\ket{\alpha(z)} = \hat{U}(z, z_0) \ket{\alpha(z_0)}$$
$$\mathrm{i}\hbar\partial_z \hat{U}(z, z_0) = \hat{\mathcal{H}}_\perp \hat{U}(z, z_0)$$
$$\hat{U}(z, z_0) = \exp\left(-\frac{\mathrm{i}}{\hbar} \int_{z_0}^{z} \hat{\mathcal{H}}_\perp(z') \mathrm{d}z' \right). \tag{2.17}$$

2.2. Propagation of electrons in free space

2.2.1. Eigenfunctions of the Hamiltonian

The Hamiltonian of an electron in free space is given by [14, 27, 28]

$$\hat{H} = \frac{(\hat{\boldsymbol{p}} - e\hat{\boldsymbol{A}})^2}{2m_e} + e\hat{V}, \tag{2.18}$$

where e is the charge of the electron, $\hat{\boldsymbol{A}}$ is the vector potential operator of an external magnetic field, and $\hat{V}$ is the operator of an external (scalar) potential. In the absence of external fields[4], this simplifies to the well-known form

$$\hat{H} = \frac{\hat{\boldsymbol{p}}^2}{2m_e}. \tag{2.19}$$

In the notation of eq. 2.16, this corresponds to $\hat{H}' = 0$. Assuming $\ket{\alpha}$ is z-independent (i.e., $\partial_z \ket{\alpha} = 0$)[5] and with $E = \hbar^2(k_\perp^2 + k_z^2)/(2m_e)$, eq. 2.16 can be simplified to

$$\hat{\boldsymbol{p}}_\perp^2 \ket{\alpha} = \hbar^2 k_\perp^2 \ket{\alpha}. \tag{2.20}$$

In Cartesian coordinates, this can be solved easily by a separation ansatz for x and y, yielding $\mathrm{e}^{\mathrm{i}k_x x}\mathrm{e}^{\mathrm{i}k_y y}$. Together with eq. 2.5, this gives rise to the well-known plane waves[6]

---

[3]Note that it is implied here that $\hat{H}_\perp$ is z-independent or that $\hat{H}_\perp$ is diagonal in z and $[\hat{H}_\perp(z), \hat{H}_\perp(z')] = 0 \; \forall z, z'$ [25]. If that is not the case, z ordering is necessary.

[4]The fields of magnetic lenses can be treated in a CTF approach [3], similar to the an effective lens in optics [8]. See also sec. 2.2.5.

[5]The following results can be derived from the original Schrödinger equation (eq. 2.1) in the same way. Note that $\partial_z \ket{\alpha} = 0$ ensures that eq. 2.13 is always fulfilled.

[6]The normalization constant follows from the continuum normalization [14, 29]. See also chap. B and sec. C.1.

$\psi(\boldsymbol{r}) = \frac{1}{(2\pi)^{3/2}}e^{i\boldsymbol{k}\cdot\boldsymbol{r}}$. In momentum space — i.e., after Fourier transform — plane waves have the simple form

$$\tilde{\psi}(\boldsymbol{q}) = \delta(\boldsymbol{q} - \boldsymbol{k}). \tag{2.21}$$

In cylindrical coordinates, eq. 2.20 becomes [30]

$$-\hbar^2 \left(\partial^2_{r_\perp} + \frac{\partial_{r_\perp}}{r_\perp} + \frac{\partial^2_\varphi}{r^2_\perp} \right) \alpha(r_\perp, \varphi) = \hbar^2 k^2_\perp \alpha(r_\perp, \varphi). \tag{2.22}$$

With the separation ansatz $\alpha(r_\perp, \varphi) = R(r_\perp)\Phi(\varphi)$, this can be rearranged to read

$$\frac{R''(r_\perp)}{R(r_\perp)} + \frac{R'(r_\perp)}{r_\perp R(r_\perp)} + \frac{\Phi''(\varphi)}{r^2_\perp \Phi(\varphi)} + k^2_\perp = 0. \tag{2.23}$$

The solution for $\Phi(\varphi)$ takes the form $\Phi(\varphi) = e^{im\varphi}$. Due to the requirement of a single-valued wave function and the boundary conditions this enforces together with the coordinate system, m must be an integer. Physically, this form of $\Phi(\varphi)$ corresponds to an azimuthal phase gradient rather than a plane wave (see fig. 2.1). $R(r_\perp)$ is defined by the differential equation

$$r^2_\perp R''(r_\perp) + r_\perp R'(r_\perp) + \left[k^2_\perp r^2_\perp - m^2 \right] R(r_\perp) = 0. \tag{2.24}$$

Using the substitutions $x := k_\perp r$ and $y(x) := R\left(x/k_\perp \right)$, this can be transformed into Bessel's differential equation [31] of order m

$$x^2 y''(x) + x y'(x) + (x^2 - m^2) y(x) = 0, \tag{2.25}$$

provided that $k_\perp \neq 0$. The solutions of this differential equation are Bessel functions of first and second kind. Since only the Bessel functions of first kind are regular at the origin, the physical solutions are therefore $y(x) = J_m(x)$ and correspondingly $R(r_\perp) = J_m(k_\perp r_\perp)$ [28].

Hence, the complete basis set in cylindrical coordinates (after normalization) is

$$\psi(r_\perp, \varphi, z) = \frac{1}{2\pi} J_m(k_\perp r_\perp)e^{im\varphi}e^{ik_z z}. \tag{2.26}$$

These are the so-called Bessel waves or (hollow cone) vortex waves. For low m, they are shown in fig. 2.1.

It is noteworthy that for $m \neq 0$, there is a phase singularity at $r_\perp = 0$ because the whole phase range $[0, 2\pi)$ caused by the $e^{im\varphi}$ factor is present in this one point. This would make the wave function ambiguous. Due to a property of the Bessel functions, namely $J_m(0) = 0$ for $m \neq 0$, this phase singularity is "masked out", however, and an unambiguous wave function is recovered.

In addition, like plane waves, these states extend to infinitely large r. For large arguments $x \gg |m^2 - 1/4|$, the Bessel functions behave as [31]

$$J_m(x) \approx \sqrt{\frac{2}{\pi x}} \cos \left(x - \frac{m\pi}{2} - \frac{\pi}{4} \right), \tag{2.27}$$
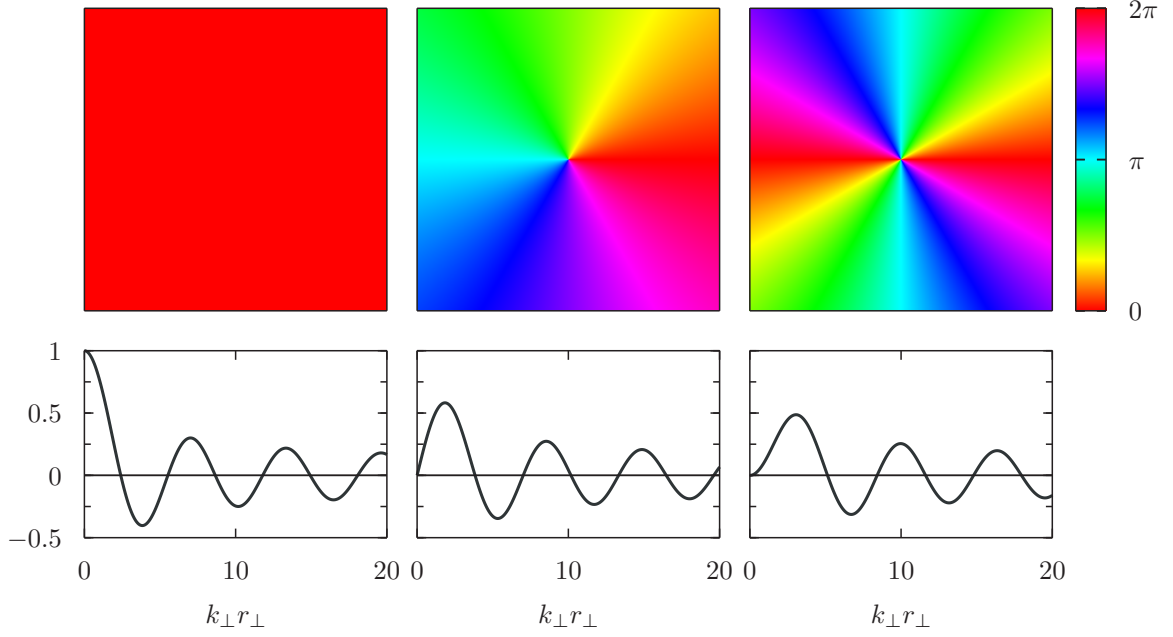
Figure 2.1.: Azimuthal phase ($\arg(e^{im\varphi})$, upper row) and radial part ($J_m(k_\perp r_\perp)$) of Bessel waves as given by eq. 2.26 and $m = 0$ (left), $m = 1$ (center), and $m = 2$ (right).

i.e., their squared radial norm — which is proportional to $x \cdot J_m(x)^2$ — oscillates with a constant amplitude. In momentum space, the Bessel waves become[7]

$$
\begin{aligned}
\tilde{\psi}(\boldsymbol{q}) &= \frac{1}{2\pi} \frac{1}{(2\pi)^{\frac{3}{2}}} \int J_m(k_\perp r_\perp) e^{im\varphi_r} e^{ik_z z} e^{-i\boldsymbol{q}\cdot\boldsymbol{r}} \mathrm{d}^3 r \\
&= \frac{\delta(q_z - k_z)}{(2\pi)^{\frac{3}{2}}} \int_0^{2\pi} \int_0^\infty J_m(k_\perp r_\perp) e^{im\varphi_r} e^{-iq_\perp r_\perp \cos(\varphi_r - \varphi_q)} r_\perp \mathrm{d}r_\perp \mathrm{d}\varphi_r \\
&= \frac{e^{im\varphi_q}\delta(q_z - k_z)}{(2\pi)^{\frac{3}{2}}} \int_0^{2\pi} \int_0^\infty J_m(k_\perp r_\perp) e^{i[m\varphi - q_\perp r_\perp \cos(\varphi)]} r_\perp \mathrm{d}r_\perp \mathrm{d}\varphi \\
&= \frac{(-i)^m e^{im\varphi_q}\delta(q_z - k_z)}{\sqrt{2\pi}} \int_0^\infty J_m(k_\perp r_\perp) J_m(q_\perp r_\perp) r_\perp \mathrm{d}r_\perp \\
&= \frac{(-i)^m}{k_\perp \sqrt{2\pi}} e^{im\varphi_q} \delta(q_z - k_z) \delta(q_\perp - k_\perp). \tag{2.28}
\end{aligned}
$$

From this, it is evident that the azimuthal phase $e^{im\varphi_q}$ is also present in momentum space. Additionally, the eigenfunctions in eq. 2.26 of the free space Hamiltonian describe a hollow cone illumination [3, 32] as can be seen from the $\delta(q_\perp - k_\perp)$ factor.

---

[7]The subscripts r and q are used to distinguish between real space and momentum space angles, respectively.

2.2.2. Probability current density and orbital angular momentum

The probability current density[8] associated with an electron wave function $\psi(\boldsymbol{r})$ is defined as[9]

$$\boldsymbol{j}(\boldsymbol{r}) := \frac{\hbar}{m_e} \Im\left(\psi(\boldsymbol{r})^* \nabla \psi(\boldsymbol{r})\right) \tag{2.29}$$

(see sec. 3.3 for more details). Thus, the probability current density associated with a plane wave is given by

$$\boldsymbol{j}(\boldsymbol{r}) = \frac{\hbar}{(2\pi)^3 m_e} \Im\left(\mathrm{e}^{-\mathrm{i}\boldsymbol{k}\cdot\boldsymbol{r}}\left(\boldsymbol{e}_x\partial_x + \boldsymbol{e}_y\partial_y + \boldsymbol{e}_z\partial_z\right)\mathrm{e}^{\mathrm{i}\boldsymbol{k}\cdot\boldsymbol{r}}\right) = \frac{\hbar\boldsymbol{k}}{(2\pi)^3 m_e}. \tag{2.30}$$

Using the probability density

$$\rho(\boldsymbol{r}) = \frac{1}{(2\pi)^3}\mathrm{e}^{-\mathrm{i}\boldsymbol{k}\cdot\boldsymbol{r}}\mathrm{e}^{\mathrm{i}\boldsymbol{k}\cdot\boldsymbol{r}} = \frac{1}{(2\pi)^3}, \tag{2.31}$$

this can be rewritten as

$$\boldsymbol{j}(\boldsymbol{r}) = \rho(\boldsymbol{r})\frac{\hbar\boldsymbol{k}}{m_e}. \tag{2.32}$$

It is no surprise that this resembles the classical picture of particle density times velocity, where the latter (classically) is given by $\boldsymbol{v} = \boldsymbol{p}/m_e \sim \hbar\boldsymbol{k}/m_e$.

The probability current density associated with a Bessel wave in cylindrical coordinates is given by

$$\begin{aligned}
\boldsymbol{j}(\boldsymbol{r}) &= \frac{\hbar}{(2\pi)^2 m_e} \Im\left(J_m(k_\perp r_\perp)\mathrm{e}^{-\mathrm{i}m\varphi}\mathrm{e}^{-\mathrm{i}k_z z}\left(\boldsymbol{e}_{r_\perp}\partial_{r_\perp} + \frac{\boldsymbol{e}_\varphi\partial_\varphi}{r_\perp} + \boldsymbol{e}_z\partial_z\right)J_m(k_\perp r_\perp)\mathrm{e}^{\mathrm{i}m\varphi}\mathrm{e}^{\mathrm{i}k_z z}\right) \\
&= \frac{\hbar}{(2\pi)^2 m_e} \Im\left(k_\perp J_m(k_\perp r_\perp)J_m'(k_\perp r_\perp)\boldsymbol{e}_{r_\perp} + \frac{\mathrm{i}m}{r_\perp}J_m^2(k_\perp r_\perp)\boldsymbol{e}_\varphi + \mathrm{i}k_z J_m^2(k_\perp r_\perp)\boldsymbol{e}_z\right) \\
&= \frac{\hbar}{(2\pi)^2 m_e}\left(\frac{m}{r_\perp}\boldsymbol{e}_\varphi + k_z\boldsymbol{e}_z\right)J_m^2(k_\perp r_\perp) \\
&= \rho(\boldsymbol{r})\frac{\hbar}{m_e}\left(\frac{m}{r_\perp}\boldsymbol{e}_\varphi + k_z\boldsymbol{e}_z\right). \tag{2.33}
\end{aligned}$$

Eq. 2.33 describes a probability current density flowing predominantly along the z axis, but with an additional angular velocity. This also explains the name "hollow cone

---

[8]In scattering theory, the formulas usually refer to a particle current density, not an electrical current density. The latter can be calculated simply by multiplying the particle current density with the electrical charge.

[9]An equivalent definition is $\boldsymbol{j}(\boldsymbol{r}) := \frac{\hbar}{m_e}|\psi(\boldsymbol{r})|^2\nabla\arg\psi(\boldsymbol{r})$. The equivalency can be seen by inserting $\psi(\boldsymbol{r}) = A(\boldsymbol{r})\mathrm{e}^{\mathrm{i}\varphi(\boldsymbol{r})}$ (where $A(\boldsymbol{r})$ and $\varphi(\boldsymbol{r})$ are real-valued functions) into eq. 2.29, yielding

$$\boldsymbol{j}(\boldsymbol{r}) = \frac{\hbar}{m_e}\Im\left(A(\boldsymbol{r})\mathrm{e}^{-\mathrm{i}\varphi(\boldsymbol{r})}\nabla A(\boldsymbol{r})\mathrm{e}^{\mathrm{i}\varphi(\boldsymbol{r})}\right) = \frac{\hbar}{m_e}\Im\left[A(\boldsymbol{r})\nabla A(\boldsymbol{r}) + \mathrm{i}A(\boldsymbol{r})^2\nabla\varphi(\boldsymbol{r})\right] = \frac{\hbar}{m_e}A(\boldsymbol{r})^2\nabla\varphi(\boldsymbol{r}).$$

As eq. 2.29 is closely related to the definitions of the probability current density in the density matrix formalism (eq. 3.25), it will be used throughout this section.

vortex wave" (sometimes simply referred to as "vortex wave") as its probability density propagates along spiral trajectories [33].

The orbital angular momentum (OAM) operator is defined as [27, 34]

$$\hat{\boldsymbol{L}} := \hat{\boldsymbol{r}} \times \hat{\boldsymbol{p}} \tag{2.34}$$

and its z component in real space is given by

$$\hat{L}_z = -\mathrm{i}\hbar \left(x\partial_y - y\partial_x \right) = -\mathrm{i}\hbar\partial_\varphi. \tag{2.35}$$

Applying $\hat{L}_z$ to plane waves yields

$$\hat{L}_z \frac{\mathrm{e}^{\mathrm{i}\boldsymbol{k}\cdot\boldsymbol{r}}}{(2\pi)^{3/2}} = -\mathrm{i}\hbar(xk_y - yk_x)\frac{\mathrm{e}^{\mathrm{i}\boldsymbol{k}\cdot\boldsymbol{r}}}{(2\pi)^{3/2}}. \tag{2.36}$$

Owing to the position dependence of the prefactor, it is clear that plane waves are no eigenfunctions of $\hat{L}_z$ which implies that their OAM is no good quantum number. The expectation value $\langle\hat{L}_z\rangle$ is

$$\langle\hat{L}_z\rangle = \frac{\int \mathrm{e}^{-\mathrm{i}\boldsymbol{k}\cdot\boldsymbol{r}}\hat{L}_z\mathrm{e}^{\mathrm{i}\boldsymbol{k}\cdot\boldsymbol{r}}\mathrm{d}^3\boldsymbol{r}}{\int \mathrm{e}^{-\mathrm{i}\boldsymbol{k}\cdot\boldsymbol{r}}\mathrm{e}^{\mathrm{i}\boldsymbol{k}\cdot\boldsymbol{r}}\mathrm{d}^3\boldsymbol{r}} \sim -\mathrm{i}\hbar \int (xk_y - yk_x)\mathrm{d}^2\boldsymbol{r}_\perp = 0 \tag{2.37}$$

because the integrand is an odd function with respect to both x and y.[10] Hence, plane waves carry no (net) OAM.

On the other hand, applying $\hat{L}_z$ to Bessel waves yields

$$\hat{L}_z \left[\frac{1}{2\pi} J_m(k_\perp r_\perp)\mathrm{e}^{\mathrm{i}m\varphi}\mathrm{e}^{\mathrm{i}k_z z} \right] = m\hbar \left[\frac{1}{2\pi} J_m(k_\perp r_\perp)\mathrm{e}^{\mathrm{i}m\varphi}\mathrm{e}^{\mathrm{i}k_z z} \right]. \tag{2.38}$$

Hence, Bessel beams are eigenfunctions of $\hat{L}_z$ and carry an OAM of $m\hbar$ [28].

2.2.3. Propagation

To understand the behavior and the probability density of an electron wave as it travels through a TEM, it is necessary to study its propagation behavior. According to Huygens' principle [35, 36], the propagation of any wave can be described by a coherent superposition of spherical waves distributed homogeneously over the phase front of the original wave. For practical purposes, this can be described as Fresnel diffraction (in the near-field, i.e., for short propagation distances) or the Fraunhofer diffraction (in the far-field, i.e., large propagation distances) [36].

Fraunhofer diffraction is simply given by the Fourier transform of the original wave. Its importance to electron microscopy comes from the fact that when using a focusing lens, the far-field (at infinite distance) is mapped to the focal plane of the lens. Therefore, the wave function in the focal plane of a lens can easily be computed by Fourier transforming the wave function that enters the lens.

---

[10]The details of the normalization were omitted for the sake of clarity.
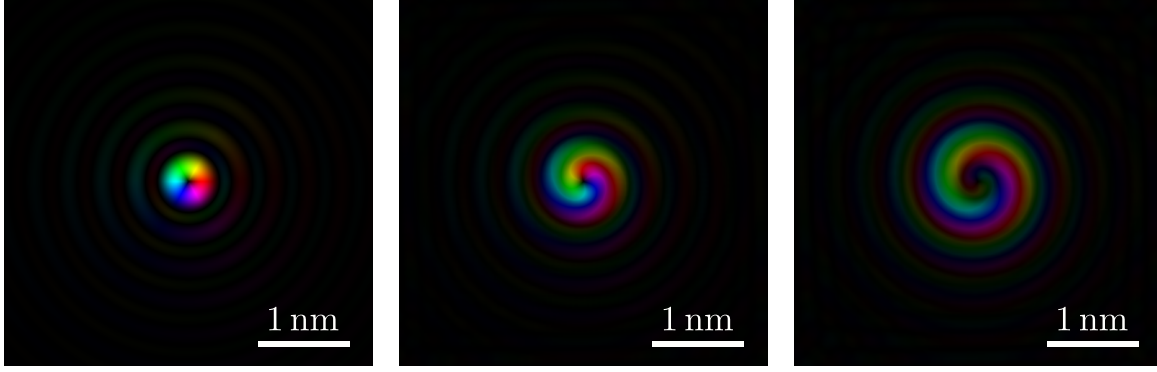
Figure 2.2.: Amplitude and phase of a vortex given by eq. 2.43 in focus (left), after a propagation of $50\,\mathrm{nm}$ (middle), and after a propagation of $100\,\mathrm{nm}$ through free space as calculated using the IXCHEL program. For the calculation, the parameters $m = 1$, $q_\perp = (2\pi\alpha r_\perp)/(\lambda R_{\mathrm{ap}})$, $R_{\mathrm{ap}} = 25\,\mu\mathrm{m}$, $\lambda = 2.507\,\mathrm{pm}$, and $\alpha = 6.9\,\mathrm{mrad}$ as well as a z step size of $1\,\mathrm{nm}$ were used. The phase is color-coded as in fig. 2.1, while the brightness reflects the wave function amplitude.

For the near-field propagation, on the other hand, the depth evolution operator from eq. 2.17 can be used. With eqs. 2.16 and 2.19, it takes the form

$$\hat{U}(z, z_0) = \exp\left(-\frac{\mathrm{i}}{\hbar}\int_{z_0}^{z}\left(\frac{\hat{\boldsymbol{p}}_\perp^2}{2\hbar k_z} + \frac{\hbar k_z}{2} - \frac{m_e E}{\hbar k_z}\right)\mathrm{d}z'\right). \tag{2.39}$$

In momentum space representation and assuming that the incident beam has the energy $E = (\hbar k_z)^2/(2m_e)$, this operator simplifies to

$$\hat{U}(z, z_0) = \exp\left(\mathrm{i}\int_{z_0}^{z}\frac{k_\perp^2}{2k_z}\mathrm{d}z'\right) = \mathrm{e}^{\frac{\mathrm{i}(z-z_0)}{2k_z}k_\perp^2}. \tag{2.40}$$

This is the well-known Fresnel propagator [37] used to describe Fresnel diffraction. It can simply be multiplied with a wave function given at z_0 (in momentum space representation) to obtain the wavefunction at z.

The Fresnel propagator plays a central role not only in the multislice approach for image simulations (see sec. 2.3.2), but also if one introduces a (small) defocus in the experiment. To calculate a defocused lens, one first has to obtain the wave distribution in the focal plane of the lens, which can then be transformed to the actual plane of investigation by the Fresnel propagator.

As expected, a plane wave with $k_\perp = 0$ is not changed by the propagator. For Bessel waves in momentum space representation, $k_\perp$ is constant, so the whole wave gets a constant phase factor. Thus, it changes (in fact, it rotates — see sec. 2.2.2), but its intensity distribution remains the same for all z. For vortex beams generated by a finite aperture, the situation is different, however: fig. 2.2 shows the propagation of a vortex as given by eq. 2.43 from the ideal focus onwards using the Fresnel propagator

approach. It is clearly evident that even after moderate propagation, the vortex appears curled. This is easy to understand: the wave functions given by eq. 2.26 rotate at a constant speed which is defined by $k_\perp$ (see above). The vortices given by eq. 2.43 are created by homogeneously illuminating a (circular) mask aperture. In momentum space, they can therefore easily be decomposed into hollow-cone states (eq. 2.26) similar to infinitesimally small onion rings. Each of these rings rotates at a different speed (owing to different values of $k_\perp$), resulting in a curling effect in momentum space. This also carries over to real space in the Fourier back-transform, as can be seen in fig. 2.2.

It must be emphasized, though, that L_z remains constant. This is an immediate consequence of the fact that the original vortex (eq. 2.43) is a superposition of eigenstates of $\hat{L}_z$ (eq. 2.26) to a single eigenvalue m.

2.2.4. Producing beams

This section is based on [28, 38].

In order to study the wave functions presented in sec. 2.2.1 in more detail, one has to actually produce them in a TEM. Plane waves are well-known and have been used for many years in electron microscopy [3]. They are typically produced by placing a (nearly) point-like emitter in the focal point of a lens which then transforms the electron wave coming from the emitter to a plane wave.

Vortex waves, on the other hand, have been created on purpose[11] in the TEM only recently [33, 38, 39]. All the experimental vortex beams used throughout this work were produced by the holographic mask technique [38] with the mask placed in the C_2 aperture plane [28, 33, 40, 41].

In holography, an arbitrary "object" wave function can be (re)constructed by sending a well-defined reference wave through a particularly shaped mask [42, 43]. The mask shape is given by the overlap of the reference wave and the object wave. In the case of vortex beams in a TEM, the reference wave is typically assumed to be a plane wave. Furthermore, a tilt is introduced between the reference wave and the object wave to ensure a proper separation of the (re)constructed vortex beam from the (unavoidable) transmitted plane wave. Thus, the mask transmission intensity I — which is naturally given in a plane perpendicular to the optical axis — can be calculated by

$$I(\boldsymbol{r}_\perp) \propto \left| e^{i\phi} + e^{i\boldsymbol{k}_\perp \cdot \boldsymbol{r}_\perp + im\varphi} \right|^2 = 2 + e^{i(\boldsymbol{k}_\perp \cdot \boldsymbol{r}_\perp + m\varphi - \phi)} + e^{-i(\boldsymbol{k}_\perp \cdot \boldsymbol{r}_\perp + m\varphi - \phi)}$$
$$= 2 + 2\cos\left(\boldsymbol{k}_\perp \cdot \boldsymbol{r}_\perp + m\varphi - \phi\right) = 4\cos^2\left[\frac{\boldsymbol{k}_\perp \cdot \boldsymbol{r}_\perp + m\varphi - \phi}{2}\right], \qquad (2.41)$$

where $\boldsymbol{k}_\perp$ is the in-plane component of the deflection vector (which gives rise to the tilt) and ϕ is a phase offset between the reference and object waves that can be used to tune the mask shape. Fig. 2.3 shows two such simulated masks.

---

[11]For example, vortex waves can also arise from inelastic scattering — see chap. 3.
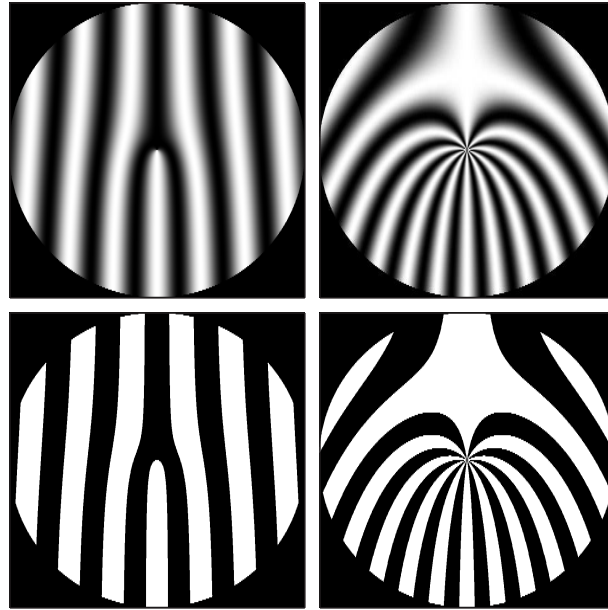
Figure 2.3.: Simulated vortex mask images with $k_\perp = 20/R_{\mathrm{ap}}$. The upper row shows continuously varying patterns as given by eq. 2.41 while the lower row shows the corresponding patterns after binarization with a threshold of 50 %. The left column shows masks for $m = 1$, the right column shows masks for $m = 10$. The axes are in arbitrary units. White signals full transmission, black corresponds to full absorption.

Eq. 2.41 describes a continuously varying transmission intensity which is achievable in optics, but not in electron microscopy.[12] Hence, the mask has to be binarized, i.e., each point is assigned either full or no transmission, depending on whether the formula produces a value above or below a chosen threshold. Such a binarized mask produces higher order vortex beams in addition to the desired ones [33, 40, 41], similar to high frequencies appearing in the Fourier transform of a sharp edge.

For the production of the holographic mask aperture, a circular condenser aperture with a hole diameter of 50 μm was used. This hole was closed with synthetic resin and subsequently sputter-coated with several hundred nanometers of Cr. Then, the glue was removed in Acetone and the binarized, calculated pattern was milled into the Cr layer by a focused ion beam (FIB). The resulting mask is shown in fig. 2.4. Both the bars and the spaces between them were approximately 1.3 μm wide.

Fig. 2.5 shows the Fourier transform (which corresponds to the image in the focal plane of the condenser lens) of the experimental mask under homogeneous illumination

---

[12]Partial transmission implies partial absorption, which is usually achieved by sending the beam through matter. Due to the strong elastic interaction between electrons and matter (see sec. 2.3), this would significantly alter the beam shape and direction instead of only attenuating it. In order to avoid such an unwanted effect, only full transmission or complete absorption (which can be achieved by fabricating the mask from a heavy material with a thickness of several hundred nanometers or more) should be used.
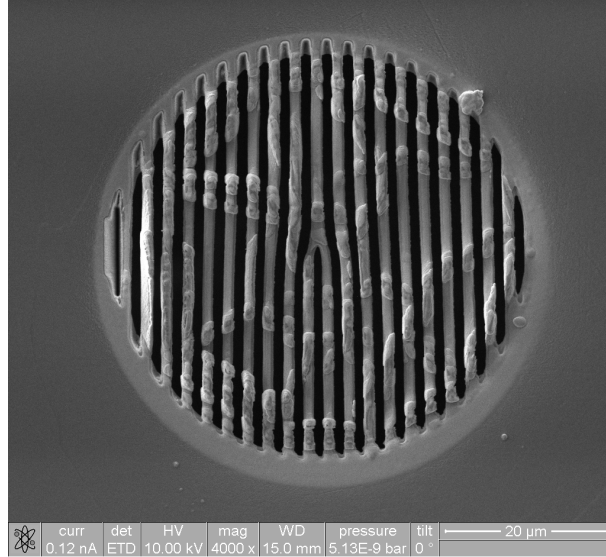
Figure 2.4.: In-situ SEM image of the vortex mask aperture after FIB milling. The diameter of the aperture is $50\,\mu m$.
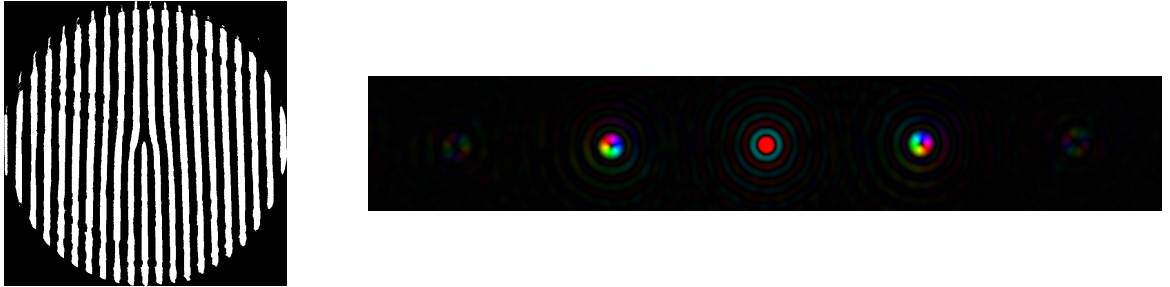
Figure 2.5.: Binarized mask (left) and its Fourier transform (right). In both cases, only the region of interest is shown. The mask diameter is $50\,\mu m$, the distance between adjacent vortices is $\approx 10\,nm$ for a convergence semi-angle of $2.43\,mrad$. The phase color code is the same as in fig. 2.1.

with a plane wave. As will be shown in sec. 2.2.3, this corresponds exactly to the wave function in the sample plane. It must be emphasized that this setup does not correspond to the hollow cone illumination that is an eigenfunction of the free space Hamiltonian. Such a beam could only be produced approximately by a ring-like holographic mask and would be extremely weak. Instead, the beams produced here are coherent superpositions of many such eigenfunctions to fulfill the boundary condition of homogeneous illumination in the aperture plane [28].

As mentioned before, higher order vortices, which correspond to higher orders of diffraction of the mask grating, are visible in fig. 2.5. Standard diffraction theory gives the spacing between the centers of subsequent vortices as

$$x = L \tan \theta \approx L \frac{\lambda |\boldsymbol{k}_\perp|}{2\pi} \approx \frac{R_{\mathrm{ap}}}{\delta} \cdot \frac{\lambda}{\alpha} = N_{\mathrm{ap}} \cdot \frac{\lambda}{\alpha}. \tag{2.42}$$

Pos.	$|m| = 0$	$|m| = 1$	$|m| = 2$	$|m| = 3$	$|m| = 4$	$|m| = 5$
max	0.00	1.23	1.96	2.63	3.27	3.88
min	1.92	2.94	3.89	4.89	5.57	6.22

Table 2.1.: List of the f factors in eq. 2.44 for the first maximum and the first minimum of the intensities of vortex beams.

Here, L is the (effective) focal length of the C_2 lens, θ is the diffraction angle, R_{ap} is the radius of the mask aperture, α is the convergence semi-angle, λ is the wave length of the electrons, δ is the period length of the grating, and N_{ap} is the number of bars[13] in the aperture. In the experiments presented here, $R_{ap} = 25\,\mu m$, $\lambda = 2.507\,pm$ and $\delta = 2.6\,\mu m$ were used [41]. The convergence semi-angle α varied between modes from 2.43 mrad in "micro-probe" mode to 6.9 mrad in "nano-probe" mode. This gives a separation of vortices of about 10 nm and 2.5 nm, respectively.

For comparison, the sizes of the vortices in the focal plane of the condenser system can be estimated from the Fourier transform of the vortex wave in eq. 2.41, truncated by the mask of radius R_{ap}:

$$\hat{\mathcal{F}}\left[\Theta(r_\perp - R_{ap})e^{im\varphi}\right] = \frac{1}{2\pi} \int_0^{R_{ap}} \int_0^{2\pi} e^{im\varphi_r - r_\perp q_\perp \cos(\varphi_r - \varphi_q)} r_\perp \mathrm{d}r_\perp \mathrm{d}\varphi_r$$

$$= (-i)^{|m|} e^{im\varphi_q} \int_0^{R_{ap}} J_{|m|}(r_\perp q_\perp) r_\perp \mathrm{d}r_\perp$$

$$= \frac{(-i)^{|m|} R_{ap}^2}{(|m| + 2)|m|!} e^{im\varphi_q} \left(\frac{q_\perp R_{ap}}{2}\right)^{|m|}$$

$$\,_1F_2\left(1 + \frac{|m|}{2}; 2 + \frac{|m|}{2}, 1 + |m|; -\left(\frac{q_\perp R_{ap}}{2}\right)^2\right). \quad (2.43)$$

Here, Θ is the Heaviside step function and $\,_pF_q(\cdot;\cdot;\cdot)$ is the generalized hypergeometric function. The prefactor $(q_\perp R_{ap}/2)^{|m|}$ ensures that the singularity at $q_\perp = 0$ is masked out for $m \neq 0$. In fig. 2.6, the radial parts of eq. 2.43 are compared to those of the hollow cone states in eq. 2.26. Note that — owing to the $e^{im\varphi_q}$ azimuthal dependence — the OAM of these vortex beams is $m\hbar$, as for Bessel beams.

With eq. 2.43, the extent of the vortex can be characterized, e.g., by the first maximum or the first minimum of the intensity.[14] This gives

$$q_\perp = \frac{2f}{R_{ap}} \Leftrightarrow x \approx \frac{R_{ap}}{\alpha} \cdot \frac{\lambda}{2\pi} \cdot \frac{2f}{R_{ap}} = \frac{\lambda f}{\pi \alpha}, \quad (2.44)$$

where f is a constant that can be derived numerically from eq. 2.43, possible values of which are collected in tab. 2.1. For $m = 1$ and the abovementioned parameter values,

---

[13]Branching bars should be counted once.
[14]The intensity is given by the absolute value squared as usual.
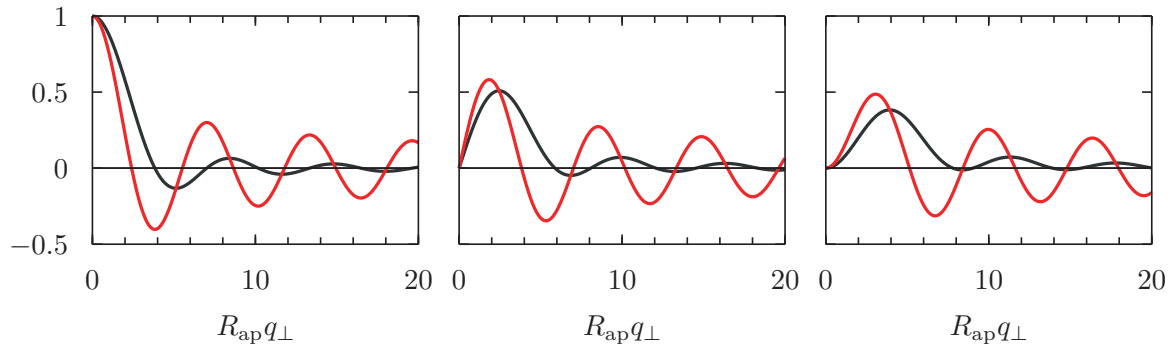
Figure 2.6.: Radial parts of finite aperture vortex beams (black) as given by eq. 2.43 compared with hollow cone vortex beams (red) as given by eq. 2.26 for $m = 0$ (left), $|m| = 1$ (middle), and $|m| = 2$ (right).

this gives a vortex radius (distance between the center and the first maximum of the vortex) of approximately $0.4\,\text{nm}$ in micro-probe mode and of approximately $0.14\,\text{nm}$ in nano-probe mode. Similarly, the distance between the center and the first minimum of the vortex is approximately $1\,\text{nm}$ in micro-probe mode or $0.34\,\text{nm}$ in nano-probe mode. This is about an order of magnitude smaller than the distance between adjacent vortices calculated above, so it is justified to speak of well-separated (independent) vortices.

2.2.5. The effect of lenses and partial coherence

This section is based on [41].

In order to get radial profiles comparable to those shown in fig. 2.6, azimuthal averages were taken for several radii[15] around the vortices in the recorded images. As can be seen in fig. 2.7, the theoretical framework presented in the previous sections does not describe the measurements well: evidently, the width of the $m = 0$ beam is underestimated and, contrary to the calculations, the dip in the center of the experimental $m = 1$ vortex is far from pronounced. In addition, the side-bands seem smeared out compared to the theoretical predictions. As will be shown in this section, this can be attributed primarily to two facts: (i) the real magnetic lenses differ from the ideal imaging system assumed above and (ii) the electron gun is not an ideal, coherent point-source.

The primary issue with real lenses (and instruments in general) is that they have a non-uniform CTF. This means that not all spatial frequencies are transmitted in the same way — a problem that is common, e.g., in high resolution transmission electron microscopy (HRTEM) [3]. An additional problem arises from lens aberrations — in particular from the spherical aberration — which typically dampen the CTF at increasing momentum transfers.

---

[15]Care was taken that the maximal radius used for averaging was less than half the distance between adjacent vortices to avoid artifacts from neighboring vortices.
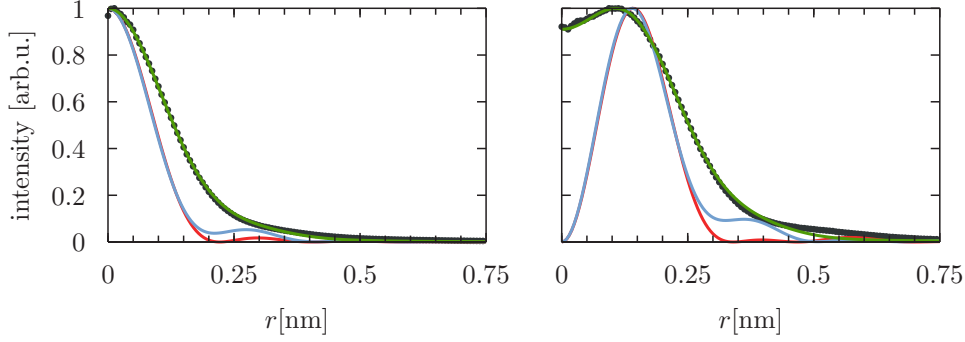
Figure 2.7.: Comparison of the experimental vortex profiles (dots) with that of calculated vortex beams for $m = 0$ (left) and $m = 1$ (right). The red curve was calculated for an ideal lens as predicted by eq. 2.43. The blue curve was calculated taking into account the spherical aberration as predicted by eq. 2.45. The green curve was calculated taking into account the spherical aberration and the source size as predicted by eq. 2.48. The experiment was performed with $200\,\mathrm{kV}$ acceleration voltage in nano-probe mode. For the calculation, the parameters $q_\perp = (2\pi\alpha r)/(\lambda R_{\mathrm{ap}})$, $R_{\mathrm{ap}} = 25\,\mu\mathrm{m}$, $\lambda = 2.507\,\mathrm{pm}$, $\alpha = 6.9\,\mathrm{mrad}$, and $\alpha_{\mathrm{incoh}} = 21.4\,\mathrm{nrad}$ were used. All profiles are normalized to their maxima.

The transfer of a wave function $\tilde{\psi}$ by a real lens into the focal point is typically modeled as [3, 41]

$$\psi(\boldsymbol{r}) = \hat{\mathcal{F}}^{-1}\left[\mathrm{e}^{\mathrm{i}\chi(\boldsymbol{q})}\tilde{\psi}(\boldsymbol{q})\right] \tag{2.45}$$

with

$$\chi(\boldsymbol{q}) = \pi\Delta f\lambda q^2 + \frac{\pi}{2}C_s\lambda^3 q^4. \tag{2.46}$$

Here, λ is the wavelength of the incident wave, Δf denotes the defocus of the lens, and C_s is the spherical aberration coefficient (with a unit of length). It should be noted that this simplified model (i) assumes that astigmatism has been corrected, (ii) ignores higher-order aberrations[16], and (iii) omits the envelope functions, the effect of which will be dominated by the aperture cut-off here. The partial coherence of the electron gun also decreases the influence of the envelope function, which will be treated separately below.

In fig. 2.7, the result of applying the imaging equation 2.45 to the vortices given by eq. 2.43 is shown. Due to the spherical aberration, the sharp minima are smeared out to the point where they are rather shoulders than minima. However, the central dip is still present, which contradicts the experimental evidence.

What has not been taken into account so far, though, is the finite extent of the electron gun. Different points of the gun emit incoherent electron waves [3]. In the condenser plane (which is conjugate, i.e., reciprocal, to the plane the gun is in), this

---

[16]In microscopes without C_s correction, higher-order aberrations are typically much smaller than the spherical aberration.

corresponds to different incoherent waves arriving at slightly different angles. This tilt, in turn, leads to slight displacements in the sample plane, corresponding to the different emissions points in the gun. In a phenomenological model, this can be described by the convolution of the "ideal" intensity function with a Gaussian broadening function $e^{-r^2/(2\sigma^2)}$ [3, 41], where σ is the size of the gun projected onto the observation plane.

For a description that is independent of the choice of micro- or nano-probe mode, it is convenient to use

$$\sigma = R_{\mathrm{ap}}\frac{\alpha_{\mathrm{incoh}}}{\alpha}, \tag{2.47}$$

where α_{incoh} describes the angular range of the incoherent plane waves impinging on the condenser plane, which is independent of the probe mode. In the TEM used for this work, α_{incoh} was determined to be $21.4\,\mathrm{nrad}$ [41].

Assuming a radially symmetric intensity profile $|\psi(r)|^2$, the intensity after convolution is given by[17]

$$\Psi(\boldsymbol{r}) = \int |\psi(r')|^2 e^{-\frac{|\boldsymbol{r}-\boldsymbol{r}'|^2}{2\sigma^2}} \mathrm{d}^2 r'$$
$$= \int_0^\infty \int_0^{2\pi} |\psi(r')|^2 e^{-\frac{r^2+r'^2-2rr'\cos\varphi'}{2\sigma^2}} \mathrm{d}\varphi' r' \mathrm{d}r'$$
$$= 2\pi e^{-\frac{r^2}{2\sigma^2}} \int_0^\infty \int_0^{2\pi} |\psi(r')|^2 e^{-\frac{r'^2}{2\sigma^2}} I_0\left(\frac{rr'}{\sigma^2}\right) r' \mathrm{d}r', \tag{2.48}$$

where $I_0(x)$ is the modified Bessel function of first kind. This intensity is, once again, radially symmetric, as one would expect.[18] Fig. 2.7 shows that using the CTF approach together with the source size broadening gives excellent agreement between the theoretical and the experimental curves.

The value of α_{incoh} was obtained by fitting the theoretical curves to the experimental ones. Hence, it is unclear to this point if the models presented here indeed describe the complete wave functions or just their behavior in the plane used for fitting. In particular, since only the waves' intensities are experimentally accessible, it is still unclear if the measured waves indeed show the characteristic vortex phase. To confirm this, a method similar to the wave form reconstruction through a defocus series [44–46] can be used.

To this end, the defocus series shown in fig. 2.8 was recorded by changing the excitation of the objective lens.[19] In order to improve the spatial resolution and to

---

[17]To simplify the integral, the x' axis is aligned with the direction of $\boldsymbol{r}$.

[18]Note that applying this to a constant intensity profile (such as those of a plane wave) does not alter the image.

[19]A curious fact is that for the TECNAI TF20 microscope with a SuperTWIN lens used in this work, the real defocus was about 2.2 times the value indicated by the software. This is attributed to the fact that the system uses a combined condenser-objective lens system and the defocus value indicated by the software is (presumably) intended for HRTEM imaging only. In HRTEM imaging, one typically uses a plane wave incident on the sample. A defocus in the pre-specimen region has no influence on this plane wave. For a focused beam, on the other hand, a change in the pre-specimen region changes the plane in which the wave is focused *in addition* to the changes
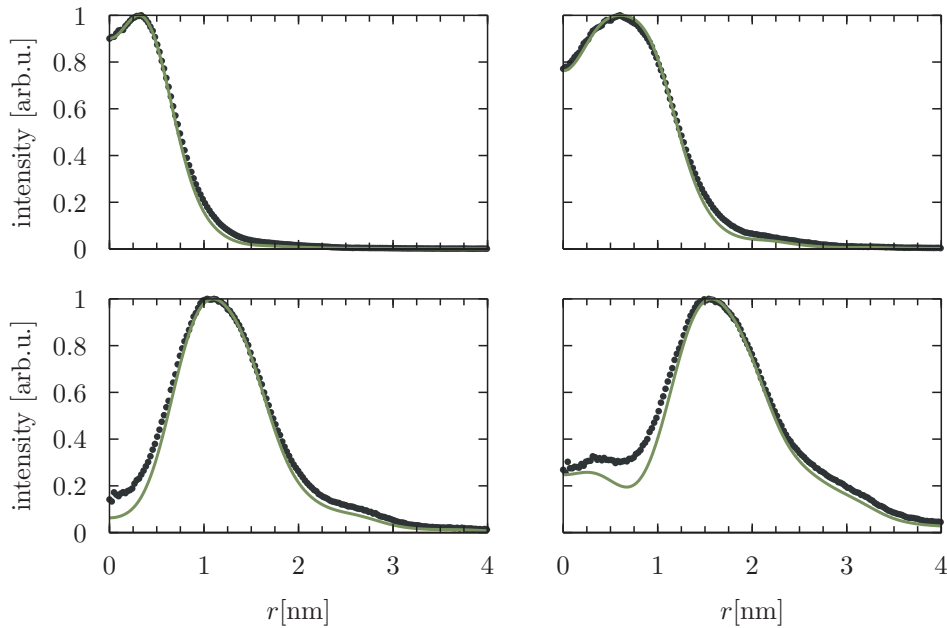
Figure 2.8.: Defocus series of the experimental vortex profiles (dots) and the calculated vortex beams taking into account the spherical aberration and source size as predicted by eq. 2.48 for $m = 1$ (red line). The indicated defocus values of $175\,\mathrm{nm}$ (top left), $350\,\mathrm{nm}$ (top right), $525\,\mathrm{nm}$ (bottom left), and $700\,\mathrm{nm}$ (bottom right) correspond to real defoci of $200\,\mathrm{nm}$, $545\,\mathrm{nm}$, $890\,\mathrm{nm}$, and $1250\,\mathrm{nm}$, respectively. The experiments were performed with $200\,\mathrm{kV}$ acceleration voltage in micro-probe mode. For the calculation, the parameters $q_\perp = (2\pi\alpha r)/(\lambda R_{\mathrm{ap}})$, $R_{\mathrm{ap}} = 25\,\mu\mathrm{m}$, $\lambda = 2.507\,\mathrm{pm}$, $\alpha = 2.43\,\mathrm{mrad}$, and $\alpha_{\mathrm{incoh}} = 21.4\,\mathrm{nrad}$ were used. All profiles are normalized to their maxima.

decrease the influence of the spherical aberration, the micro-probe mode was used for these experiments. The excellent agreement between theory and experiments proves that the electron waves produced in the TEM using the holographic mask technique are indeed real vortex beams.

---

in the post-specimen region which shift the plane that is imaged. This behavior was verified by the following procedure. First, a normal (i.e., non-vortex) beam was focused on a distinct, small feature on a specimen with zero (objective) defocus. Then, a defocus was applied to the objective lens. Contrary to the ideal case, in which the illuminated sample area would not change, the illuminated area was enlarged, indicating a shift of the pre-specimen focal length. Finally, the additional shift was determined by shifting the specimen in z direction until the illuminated area was approximately as large as before the procedure. The correction that needed to be applied was approximately as large as the defocus value indicated by the software.

2.3. Propagation of electrons in a periodic potential

As soon as the electron enters a crystal (or gets close to it), it interacts with the partially screened, positively charged nuclei via the Coulomb interaction. Experiments show that in this electromagnetic interaction, the elastic component dominates over the inelastic contributions. In an elastic scattering event, the direction of the electron's momentum is changed but its energy remains constant. This can be understood from the fact that the nuclei are much heavier than the electron. In the limit of infinitely heavy nuclei, energy and momentum conservation result in the fact that momentum can be transferred between the electron and the nucleus, but energy cannot.[20]

For plane waves, this can be understood in terms of Bragg's law: for certain directions, all partial waves interfere constructively, and hence an intensity maximum is found there. However, such a diffracted beam can be diffracted again, e.g., back to the original beam direction. Therefore, the intensity distribution is a complicated function of the position inside the sample. For two beams, this leads to the Howie-Whelan equations [3].

For a more rigorous description, one has to solve the Schrödinger equation with the periodic potential of the crystal. This can be achieved most easily by solving the effective Schrödinger equation 2.12 with $\hat{H}' = e\hat{V}$, where $\hat{V}$ is the Coulomb operator.

2.3.1. Bloch wave formalism

This section is based on [3, 24, 26, 47].

Due to its periodicity, the potential can be expanded into a discrete Fourier series as

$$\hat{V} = -\frac{\hbar^2}{2em_e} \sum_{\boldsymbol{g}} U_{\boldsymbol{g}} \mathrm{e}^{\mathrm{i}\boldsymbol{g}\cdot\hat{\boldsymbol{r}}}. \tag{2.49}$$

If one is only interested in small-angle scattering, i.e., scattering into the zero order Laue zone (ZOLZ), all (relevant) vectors $\boldsymbol{g}$ are perpendicular to the optical axis. Then, the potential becomes independent of the z coordinate. Using the separation ansatz $|\alpha\rangle = |XY\rangle \otimes |Z\rangle$ and

$$E = \frac{\hbar^2 k^2}{2m_e} = \frac{\hbar^2(k_\perp^2 + k_z^2)}{2m_e} \tag{2.50}$$

yields

$$\frac{\hbar^2}{2m_e} \left(\frac{\hat{\boldsymbol{p}}_\perp^2}{\hbar^2} + \frac{2k_z\hat{p}_z}{\hbar} + k_z^2 - \sum_{\boldsymbol{g}} U_{\boldsymbol{g}}\mathrm{e}^{\mathrm{i}\boldsymbol{g}\cdot\hat{\boldsymbol{r}}} \right) |XY\rangle \, |Z\rangle = \frac{\hbar^2(k_\perp^2 + k_z^2)}{2m_e} |XY\rangle \, |Z\rangle$$

$$\left(\frac{\hat{\boldsymbol{p}}_\perp^2}{\hbar^2} + \frac{2k_z\hat{p}_z}{\hbar} - \sum_{\boldsymbol{g}} U_{\boldsymbol{g}}\mathrm{e}^{\mathrm{i}\boldsymbol{g}\cdot\hat{\boldsymbol{r}}} \right) |XY\rangle \, |Z\rangle = k_\perp^2 |XY\rangle \, |Z\rangle$$

---

[20]For nuclei with finite mass, phonons can be excited in a TDS process. Due to the large mass difference between the electrons and the nuclei, the energy transferred in such excitations is very low, however.

$$\frac{1}{2k_z}\left(\frac{\hat{\boldsymbol{p}}_\perp^2}{\hbar^2} - k_\perp^2 - \sum_{\boldsymbol{g}} U_{\boldsymbol{g}} \mathrm{e}^{\mathrm{i}\boldsymbol{g}\cdot\hat{\boldsymbol{r}}}\right)|XY\rangle\,|Z\rangle = -\frac{\hat{p}_z}{\hbar}\,|XY\rangle\,|Z\rangle\,. \tag{2.51}$$

Obviously, $|Z\rangle$ must be an eigenstate of the $\hat{p}_z$ operator, namely a plane wave with wavevector $\gamma\boldsymbol{e}_z$.[21] Hence, the equation for $|XY\rangle$ becomes

$$\frac{1}{2k_z}\left(\frac{\hat{\boldsymbol{p}}_\perp^2}{\hbar^2} - k_\perp^2 - \sum_{\boldsymbol{g}} U_{\boldsymbol{g}} \mathrm{e}^{\mathrm{i}\boldsymbol{g}\cdot\hat{\boldsymbol{r}}}\right)|XY\rangle = -\gamma\,|XY\rangle\,. \tag{2.52}$$

This is again an eigenstate problem. In $\{|\boldsymbol{\chi}\rangle\}$ momentum space representation, it takes the form

$$\frac{(\chi^2 - k_\perp^2)}{2k_z}\langle\boldsymbol{\chi}|XY\rangle - \sum_{\boldsymbol{g},\boldsymbol{\chi}'}\frac{U_{\boldsymbol{g}}}{2k_z}\langle\boldsymbol{\chi}|\mathrm{e}^{\mathrm{i}\boldsymbol{g}\cdot\hat{\boldsymbol{r}}}|\boldsymbol{\chi}'\rangle\langle\boldsymbol{\chi}'|XY\rangle = -\gamma\langle\boldsymbol{\chi}|XY\rangle$$

$$\frac{(\chi^2 - k_\perp^2)}{2k_z}\langle\boldsymbol{\chi}|XY\rangle - \sum_{\boldsymbol{g},\boldsymbol{\chi}'}\frac{U_{\boldsymbol{g}}}{2k_z}\delta(\boldsymbol{\chi}-\boldsymbol{g}-\boldsymbol{\chi}')\langle\boldsymbol{\chi}'|XY\rangle = -\gamma\langle\boldsymbol{\chi}|XY\rangle$$

$$\frac{(k_\perp^2 - \chi^2)}{2k_z}\langle\boldsymbol{\chi}|XY\rangle + \sum_{\boldsymbol{g}}\frac{U_{\boldsymbol{g}}}{2k_z}\langle\boldsymbol{\chi}-\boldsymbol{g}|XY\rangle = \gamma\langle\boldsymbol{\chi}|XY\rangle\,. \tag{2.53}$$

This equation is also known as the secular equation.[22] It is obvious that only those plane wave components couple whose wave vectors differ by a reciprocal lattice vector $\boldsymbol{g}$.

In electron microscopy literature [3, 23, 26], $\langle\boldsymbol{\chi}-\boldsymbol{g}|XY\rangle$ is often denoted by $C^j_{-\boldsymbol{g}}$ and the state is written as

$$|XY\rangle = \sum_{\boldsymbol{g}} C^j_{\boldsymbol{g}}\,|\boldsymbol{\chi}_j + \boldsymbol{g}\rangle\,, \tag{2.54}$$

where j is an index for distinguishing different eigenvalues γ_j, and thus

$$\langle\boldsymbol{r}|\psi_j\rangle = \mathrm{e}^{\mathrm{i}(k_z + \gamma_j)z}\sum_{\boldsymbol{g}} C^j_{\boldsymbol{g}}\mathrm{e}^{\mathrm{i}(\boldsymbol{\chi}_j + \boldsymbol{g})\cdot\boldsymbol{r}}\,. \tag{2.55}$$

In practice, one typically fixes $\boldsymbol{\chi}_j$ (which is usually implied by the boundary conditions, e.g., an incident plane wave) and solves the eigenvalue problem for a limited set of $\boldsymbol{g}$. For the coefficients $U_{\boldsymbol{g}}$ of the potential, one can use parameterized potentials [48], calculated potentials (e.g., using WIEN2K [49]), or experimental data. Finally, the boundary conditions at the entrance surface must be met by expanding the incident wave function in the eigenstate basis $\{|\psi_{\boldsymbol{\chi},j}\rangle\}$.

---

[21] $\gamma\boldsymbol{e}_z$ must not be confused with $k_z\boldsymbol{e}_z$ used in eq. 2.5. The latter describes the fast oscillation of the electron's wave function due to its large energy which is independent of the crystal. The former describes the *additional* oscillation in z caused by the crystal. The total oscillation of the electron's wave function is given by the sum of both terms, as is apparent from eq. 2.55.

[22] Sometimes, the $U_{\boldsymbol{0}}$ term is taken out of the sum and combined with the $k_\perp^2$ term to form an effective wave vector.

	space group	a [nm]	Si positions
Si	227	0.54309	$x = y = z = 0$

Table 2.2.: Crystal structure parameters for Silicon [50].
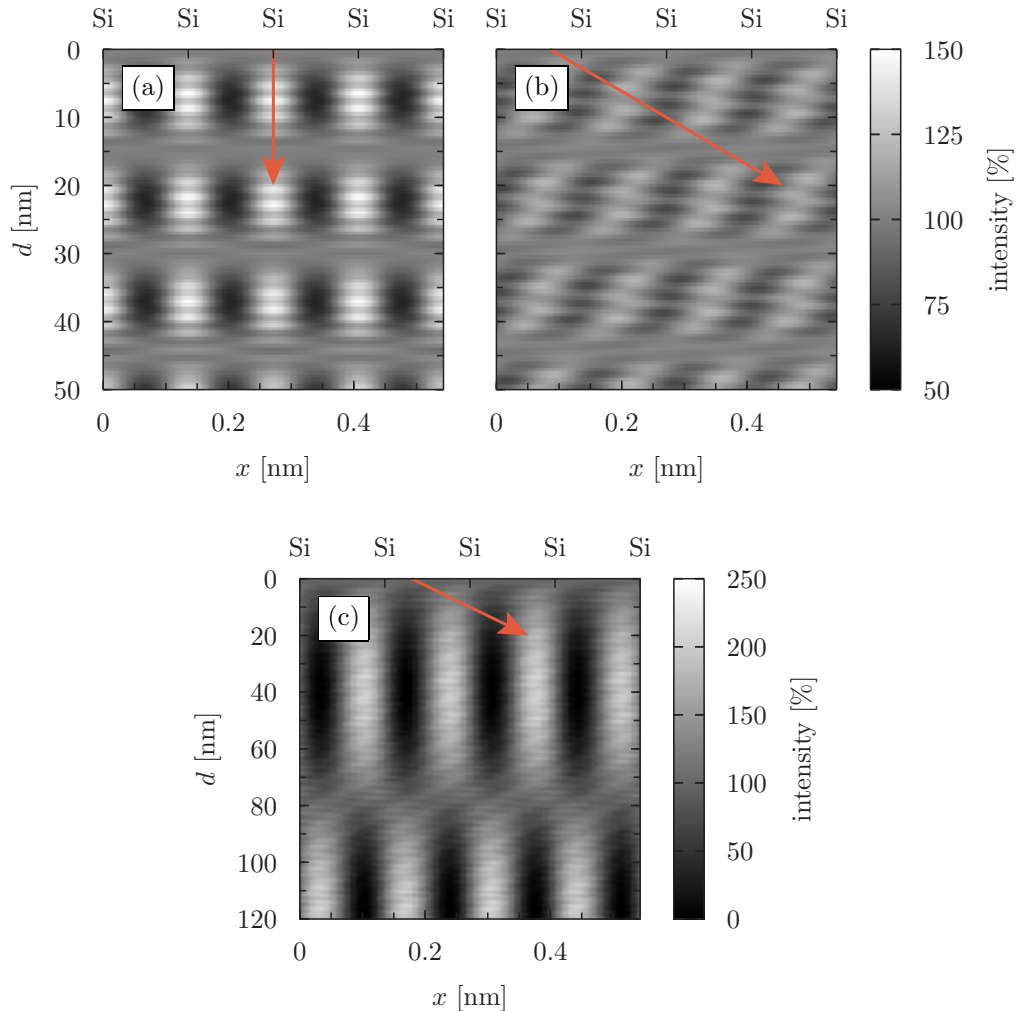
Figure 2.9.: Bloch wave intensity maps in Si for different thicknesses and angles of the incident wave using a systematic row including the $\boldsymbol{G} = (4\,0\,0)$ diffraction spot. (a) untilted incident beam, (b) incident beam tilted by $\boldsymbol{G}$, (c) incident beam tilted by $\boldsymbol{G}/2$. The Si atomic columns are marked (see tab. 2.2 for crystallographic details). The red arrows represent the incident beam directions. All intensities are relative to the incident beam intensity. In (c), the famous two-beam case [3] gives rise to very strong variations composed of mostly two plane wave components.

It is clear that for different γ_j, the $|\psi_{\boldsymbol{\chi},j}\rangle$ have different z dependences. For non-trivial combinations of two or more such $|\psi_{\boldsymbol{\chi},j}\rangle$, one therefore needs to take into account interference effects between different plane wave components. This manifests itself in different intensities in the diffraction pattern and can be interpreted as multiple elastic scattering between different plane waves. It also leads to complicated wave excitations as a function of thickness and of the angle of the incident wave [23, 26]. Some examples are given in fig. 2.9.

The Bloch wave method works well for ideal periodic potentials and incident plane waves. While this is often the case — mostly when performing diffraction experiments —, strictly speaking, it does not apply to situations where one wants to study samples with a potential that is distorted, e.g., by defects or dopant atoms. In addition, it does not apply to any kind of STEM technique.[23] In those situations, other methods such as the multislice approach are beneficial.

2.3.2. Multislice

In the multislice approach, the whole crystal is split into slices. In each slice, the potential is assumed to vary only weakly in z direction and thus $[\hat{\mathcal{H}}_\perp(z), \hat{\mathcal{H}}_\perp(z')] \approx 0$ holds in good approximation for all z, z' inside the same slice.[24] Assuming $k_\perp \ll k_z$, the total energy can be approximated by

$$E = \frac{\hbar^2 k_z^2}{2m_e}. \tag{2.56}$$

Thus, the effective hamiltonian (eq. 2.16) takes the form

$$\hat{\mathcal{H}}_\perp = \frac{\hat{\boldsymbol{p}}_\perp^2}{2\hbar k_z} + \frac{m_e e}{\hbar k_z}\hat{V} \tag{2.57}$$

and the evolution operator in eq. 2.17 in real space representation can be written as[25]

$$\begin{aligned}
\hat{U}(z, z_0) &= \exp\left[-\frac{\mathrm{i}}{\hbar}\int_{z_0}^z \langle z'|\hat{\mathcal{H}}_\perp|z'\rangle\,\mathrm{d}z'\right] \\
&= \exp\left[-\frac{\mathrm{i}}{\hbar}\int_{z_0}^z \left(-\frac{\hbar\Delta_\perp}{2k_z} + \frac{m_e e}{\hbar k_z}V(z')\right)\mathrm{d}z'\right] \\
&= \exp\left[\frac{\mathrm{i}(z-z_0)}{2k_z}\Delta_\perp - \frac{\mathrm{i}}{2k_z}v_{z,z_0}\right],
\end{aligned} \tag{2.58}$$

---

[23]In principle those can be treated with the Bloch wave approach as well [51], but the number of different $\boldsymbol{\chi}$ vectors to consider and hence the total number of Bloch waves to calculate gets very large.

[24]Provided that the potential is smooth and the slice is thin, this is a reasonable approximation. Alternatively, one could picture the potential as being replaced by an average potential that is constant along the z direction. In that case, the commutator would be exactly zero.

[25]As above, it is assumed that $\hat{H}'$ and thus $\hat{\mathcal{H}}_\perp$ are diagonal in z.

with the projected potential

$$v_{z,z_0} := \frac{2m_e e}{\hbar^2} \int_{z_0}^{z} V(z')) \mathrm{d}z'. \tag{2.59}$$

Iteratively solving this in real space is possible [54, 55] but time consuming. Alternatively, using the relation [37]

$$\exp(\hat{A}\varepsilon + \hat{B}\varepsilon) = \exp(\hat{A}\varepsilon)\exp(\hat{B}\varepsilon) + \frac{1}{2}[\hat{B}, \hat{A}]\varepsilon^2 + \mathcal{O}(\varepsilon^3), \tag{2.60}$$

one obtains, in first order approximation (i.e., for thin slices),

$$\hat{U}(z, z_0) \approx \exp\left(\frac{\mathrm{i}(z - z_0)}{2k_z}\Delta_\perp\right)\exp\left(-\frac{\mathrm{i}}{2k_z}v_{z,z_0}\right), \tag{2.61}$$

for the propagation through a single slice. The first factor is identical to the Fresnel propagator in free space (eq. 2.40), whereas the second one describes "instantaneous" (i.e., z-independent) scattering. Hence, in the multislice approach, the crystal can be pictured as split into a set of slices of vacuum, at the boundaries of which the electron "experiences" the effect of the potential in the form of "instantaneous" scattering in the projected potential.

In simulations, the propagator in eq. 2.61 has to be applied separately slice after slice to propagate a given wave function through the crystal. Similar to the free space case, the propagation through the slice of vacuum can be sped up considerably by transforming the wave function into momentum space via a fast Fourier transform (FFT) (see sec. 2.2.3). Still, the propagation remains a rather time- and memory-consuming process, but it has the advantage that non-uniform potentials as well as non-periodic wave functions can be used directly.

As an example, fig. 2.10 shows the propagation of focused vortex beams through a 10 nm thick Si specimen in [0 0 1] zone axis. Evidently, the exit wave function depends crucially on the position of the vortex beam. In particular, the exit wave typically does not exhibit the characteristic azimuthal phase gradient of a vortex beam, but rather a corrugated phase structure. This implies that the state is no longer an OAM eigenstate. The fact that OAM is not conserved in the crystal can easily be understood by noting that the $\hat{L}_z$ operator does not commute with the Hamiltonian in the presence of a potential that is not cylindrically symmetric around the vortex axis. Thus, $\langle \hat{L}_z \rangle$ is not a constant of motion and the electron wave does not remain in an OAM eigenstate [53, 56].

As a side-note, it should be mentioned that the wave function retains some of its vortex structure as long as the influence of the neighboring atomic columns (which are the cause for the breaking of symmetry) remains weak. In particular, this can be seen quite clearly if the vortex is positioned directly on an atomic column. In this situation, the gradient of the atomic potential leads to channeling, i.e., the electron beam remains close to the atomic column and thus retains its vortex structure to a large degree [56, 57].
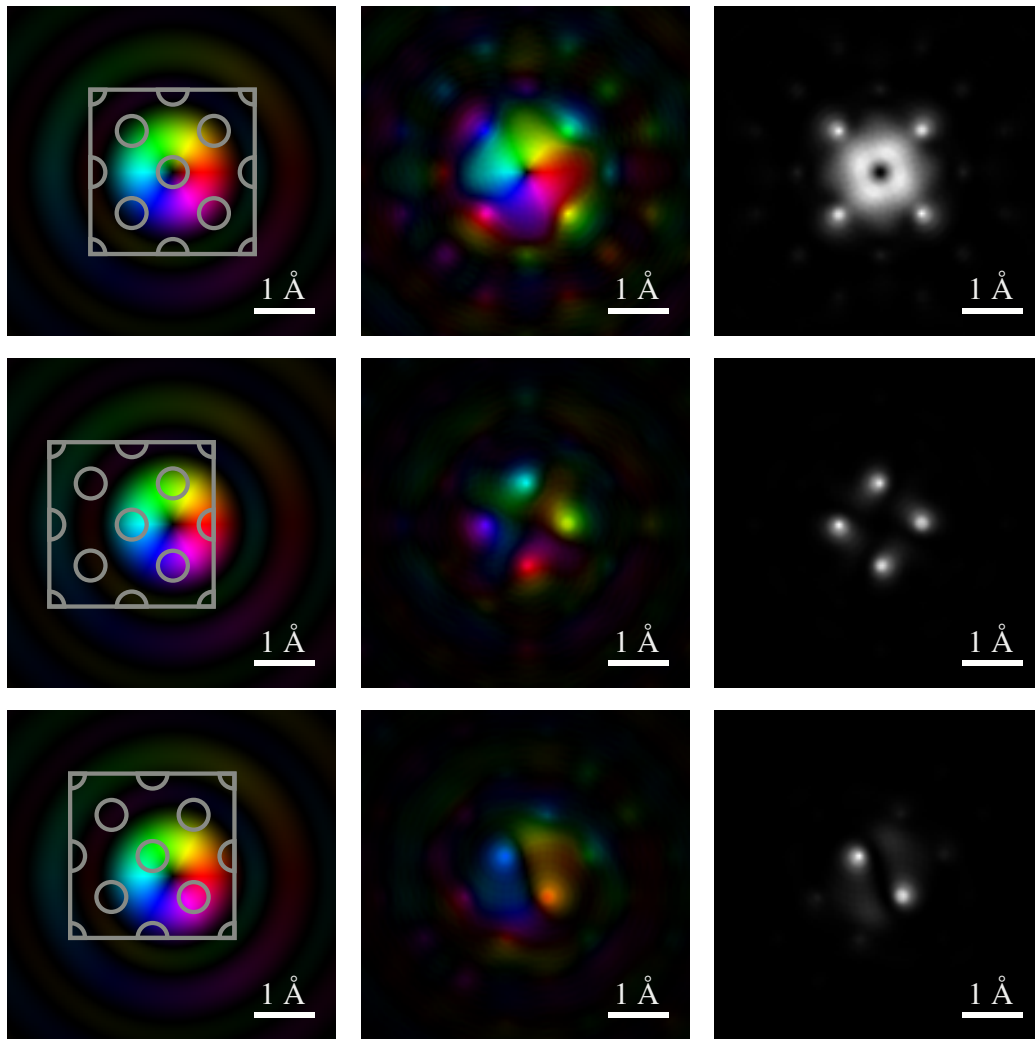
Figure 2.10.: Exit wave after propagating a vortex beam through a 10 nm thick Si crystal in [0 0 1] zone axis. Each row shows the simulation for a different position of the incident vortex with respect to the crystal. The left column shows the position of the incident vortex (a projected unit cell is superimposed). The middle column shows the amplitude and phase of the exit wave. The right column shows the intensity of the exit wave. For the calculations, the parameters $m = 1$, $\lambda = 2.507$ pm, and $\alpha = 6.9$ mrad were used. In the left and the middle column, the phase is color-coded as in fig. 2.1, while the brightness reflects the wave function amplitude. In the right column, the brightness reflects the intensity of the exit wave.

3. Inelastic scattering

> Essentially, all models are wrong, but some are useful.
>
> *(George E. P. Box)*

3.1. General description

> This section is based on the derivations of time-dependent perturbation theory found, e.g., in [14, 25].

Inelastic scattering (in the context of EELS) is the interaction between the quantum system of a probe electron and another quantum system (typically the sample or rather a subsystem thereof) in which energy is transferred from the probe to the target.[1] Thus, one needs to model the target system in addition to the probe electron system. Moreover, since the target system is not observed separately after the interaction — if that were possible easily, it would not be necessary to use a TEM — one has to apply the density matrix formalism (see sec. 1.4). To obtain the reduced density matrix of the probe beam after the inelastic interaction, the target system must be "traced out". That is, by the inelastic interaction, the (initially pure) probe state will generally be scattered into a mixed state.

Throughout this section, it is assumed that the inelastic scattering happens on much shorter time and length scales than the elastic propagation through the sample. This holds for core losses, where the extinction length of dynamical diffraction is much larger than the extension in z direction of the inelastic scattering kernel introduced below [51]. Thus, limits like $\lim_{t\to-\infty}$ and $\lim_{t\to\infty}$ have to be understood as "before the inelastic interaction" and "after the inelastic interaction", respectively, and not as "at the gun" and "at the detector". Consequently, elastic scattering (already discussed in chap. 2) and inelastic scattering can be treated separately and this section will deal with the inelastic effects only. For the combination of both effects, see sec. 3.8.

For fast electrons, typical excitation energies ($\lesssim 1\,\mathrm{keV}$) are much smaller than the kinetic energy ($\gtrsim 100\,\mathrm{keV}$). Thus, the inelastic interaction can be treated in a perturbation approach:

$$(\hat{H}_0 + \hat{V})\,|\psi\rangle = \mathrm{i}\hbar\partial_t\,|\psi\rangle, \tag{3.1}$$

---

[1]In principle, the reverse, i.e., transfer of energy from the target to the electron, would be possible from an energetic point of view, but entropically this is unfavorable.

where $\hat{H}_0 = \hat{1}_t \otimes \hat{H}_{0,p} + \hat{H}_{0,t} \otimes \hat{1}_p$ is the (exactly solvable) Hamiltonian that can be written as a sum of the Hamiltonians of the probe ($\hat{H}_{0,p}$) and of the target ($\hat{H}_{0,t}$), and $\hat{V}$ is the perturbation operator that couples the two systems.[2] Both $\hat{H}_0$ and $\hat{V}$ are assumed not to be explicitly time-dependent.

In the interaction picture, the state $|\psi(t)\rangle$ at a time t can be described as the time evolution of the corresponding state $|\psi(t_0)\rangle$ in the "distant past" t_0:

$$|\psi(t)\rangle_I = \hat{U}_I(t, t_0) |\psi(t_0)\rangle_I. \tag{3.2}$$

This time evolution operator is defined as [14, 25]

$$i\hbar \partial_t \hat{U}_I(t, t_0) = \hat{V}_I \hat{U}_I(t, t_0) \qquad \hat{U}_I(t_0, t_0) = \hat{1} \tag{3.3}$$

with

$$\hat{V}_I := e^{\frac{i}{\hbar}\hat{H}_0 t} \hat{V} e^{-\frac{i}{\hbar}\hat{H}_0 t}. \tag{3.4}$$

Formal integration of eq. 3.3 yields the equivalent formulation

$$\hat{U}_I(t, t_0) = \hat{1} - \frac{i}{\hbar} \int_{t_0}^t \hat{V}_I \hat{U}_I(\tau, t_0) d\tau. \tag{3.5}$$

In first order Born approximation, the term $\hat{U}_I(\tau, t_0)$ in the integral can be replaced by $\hat{1}$, yielding

$$\hat{U}_I(t, t_0) \approx \hat{1} - \frac{i}{\hbar} \int_{t_0}^t e^{\frac{i}{\hbar}\hat{H}_0 \tau} \hat{V} e^{-\frac{i}{\hbar}\hat{H}_0 \tau} d\tau. \tag{3.6}$$

Applied to an incident density operator[3]

$$\hat{\rho}_i = \sum_{\psi_i}\!\!\!\!\!\!\!\int p_{\psi_i} |\psi_i\rangle \langle\psi_i|, \tag{3.7}$$

the time evolution of the density operator is described by[4]

$$\hat{\rho} = \sum_{\psi_i}\!\!\!\!\!\!\!\int p_{\psi_i} \hat{U}_I(t, t_0) |\psi_i\rangle \langle\psi_i| \hat{U}_I^\dagger(t', t_0'). \tag{3.8}$$

---

[2] Note that, contrary to the notation in chap. 2, $\hat{V}$ does not denote the periodic crystal potential but rather the interaction operator between the probe electron and the sample electron. The crystal potential can be included in $\hat{H}_0$, as can the Hamiltonian of the atomic wave function. The reason for this relabeling is to facilitate comparison with existing literature on perturbation theory. Moreover, it can be justified by the fact that typically, $\hat{V}$ is the Coulomb operator in both cases — describing the interaction between the probe and the nucleus in one case and the interaction between the probe and a target electron in the other.

[3] The $\sum\!\!\!\!\int$ sign is used because in the cases discussed here, ψ_i will typically be a continuum state. It should also be emphasized that the index i used here is not a summation index, but rather a label for "initial" or "incident" states.

[4] Note that, in principle, there can be correlations between the states at different times t, t' (assuming $t - t'$ is smaller than the coherence time). In the following, however, this will not play an important role as only the asymptotic limit will be of interest.

Assuming that the $\{|\psi_i\rangle\}$ as well as the states $|\phi\rangle$ and $|\varphi\rangle$ are all eigenstates of $\hat{H}_0$ and that $\langle\psi_i|\phi\rangle = \langle\psi_i|\varphi\rangle = 0 \ \forall\,|\psi_i\rangle$,[5] the density matrix element with respect to $|\phi\rangle$ and $|\varphi\rangle$ reads

$$\langle\phi|\hat{\rho}|\varphi\rangle = \sum_{\psi_i} p_{\psi_i}\,\langle\phi|\hat{V}|\psi_i\rangle\,\langle\psi_i|\hat{V}^\dagger|\varphi\rangle \cdot$$

$$\int_{t_0}^{t}\left(e^{\frac{i}{\hbar}(E_\phi - E_{\psi_i})\tau}\frac{d\tau}{\hbar}\right)\int_{t_0'}^{t'}\left(e^{-\frac{i}{\hbar}(E_\varphi - E_{\psi_i})\tau}\frac{d\tau}{\hbar}\right). \tag{3.9}$$

In the asymptotic limit $(t, t' \to \infty, t_0, t_0' \to -\infty)$, this yields

$$\langle\phi|\hat{\rho}|\varphi\rangle = \sum_{\psi_i} p_{\psi_i}\,\langle\phi|\hat{V}|\psi_i\rangle\,\langle\psi_i|\hat{V}^\dagger|\varphi\rangle \cdot$$

$$\int_{-\infty}^{\infty}\left(e^{\frac{i}{\hbar}(E_\phi - E_{\psi_i})\tau}\frac{d\tau}{\hbar}\right)\int_{-\infty}^{\infty}\left(e^{-\frac{i}{\hbar}(E_\varphi - E_{\psi_i})\tau}\frac{d\tau}{\hbar}\right). \tag{3.10}$$

Using

$$\delta(E) = \frac{1}{2\pi}\int_{-\infty}^{\infty}e^{iEt}dt \quad \text{and} \quad \delta(-E) = \delta(E), \tag{3.11}$$

this gives

$$\langle\phi|\hat{\rho}|\varphi\rangle = 4\pi^2\sum_{\psi_i} p_{\psi_i}\,\langle\phi|\hat{V}|\psi_i\rangle\,\langle\psi_i|\hat{V}^\dagger|\varphi\rangle\,\delta(E_\phi - E_{\psi_i})\delta(E_\varphi - E_{\psi_i})$$

$$= 4\pi^2\sum_{\psi_i} p_{\psi_i}\,\langle\phi|\hat{V}|\psi_i\rangle\,\langle\psi_i|\hat{V}^\dagger|\varphi\rangle\,\delta(E_\phi - E_{\psi_i})\delta(E_\phi - E_\varphi), \tag{3.12}$$

a result that can be derived in a similar way by employing the S matrix formalism [14].

In the particular case of core-loss EELS, one can assume that the asymptotic states factorize into probe states (hereafter denoted by lower case letters) and target states (hereafter denoted by upper case letters), i.e., $|\psi_i\rangle = |I\rangle\,|i\rangle$, $|\phi\rangle = |F\rangle\,|f\rangle$, $|\varphi\rangle = |F'\rangle\,|f'\rangle$. In addition, it is reasonable to assume that the initial state of the probe beam is a pure state $|i\rangle\,\langle i|$ because elastic scattering does not create mixed states (see sec. 2.1.1). Thus, the incident density operator (eq. 3.7) takes the form

$$\hat{\rho}_i = \sum_{\psi_i} p_{\psi_i}\,|\psi_i\rangle\,\langle\psi_i| = \sum_I p_I\,|I\rangle\,|i\rangle\,\langle i|\,\langle I|, \tag{3.13}$$

where the $\sum$ reduces to a simple sum as the initial states of the target are bound states. It is noteworthy that this density operator is diagonal in $|I\rangle$.

---

[5]The assumption that all states $|\psi_i\rangle$, $|\phi\rangle$, and $|\varphi\rangle$ are eigenstates of $\hat{H}_0$ is reasonable since only the asymptotic states far away of the perturbation are of interest here. The assumption that the states before and after the interaction are orthogonal is justified because one works with energy eigenstates in core-loss EELS and is only interested in processes that actually change the energy.

Because the target system is not observed directly, one has to calculate the reduced density operator of the probe, $\hat{\rho}_p$, by "tracing out" the target's final states, yielding

$$\langle f|\hat{\rho}_p|f'\rangle = 4\pi^2 \sum_F \sum_I p_I(1-p_F)\,\langle f|\,\langle F|\hat{V}|I\rangle\,|i\rangle\,\langle i|\,\langle I|\hat{V}^\dagger|F\rangle\,|f'\rangle\,\cdot$$

$$\delta(E_F - E_I - E)\delta(E_f - E_{f'}), \tag{3.14}$$

for the reduced density matrix. Here, p_F denotes the occupation probability of the final state $|F\rangle$ and the measurable "energy loss" of the probe,

$$E := E_f - E_i, \tag{3.15}$$

was introduced.

One important result of this is that the reduced density matrix is block diagonal in the final state energy of the probe. No correlations occur between final states with different energies. Under these circumstances, $\delta(E_f - E_{f'})$ represents the continuum orthonormalization [14, 29] that vanishes in the end when one integrates over energy in the detector.[6]

At this point, it should also be noted that the reduced density matrix formed by the elements $\langle f|\hat{\rho}_p|f'\rangle$ — where $|f\rangle$, $|f'\rangle$ are the states of interest for core-loss EELS — is *not* normalized anymore. While the complete reduced density matrix is normalized, of course, it also contains many scattering channels that are not considered here (e.g., TDS, plasmon excitations, etc.). Thus, the fact that the reduced density matrix used here is not normalized simply reflects the fact that the portion of the outgoing intensity considered here (i.e., the signal in the detector) is (much) weaker than the incident intensity.

By using a particular basis $\{|b\rangle\}$ for the final states of the probe, inserting unit operators, and rearranging, one arrives at the equation

$$\iint \mathrm{d}b\,\mathrm{d}b'\,\langle b|f\rangle^*\,\langle b'|f'\rangle\,\rho_p(b,b') = 4\pi^2 \sum_F \sum_I p_I(1-p_F)\,\cdot$$

$$\iint \mathrm{d}b\,\mathrm{d}\tilde{b}\,\langle b|f\rangle^*\,\langle \tilde{b}|i\rangle\,\langle b|\,\langle F|\hat{V}|I\rangle\,|\tilde{b}\rangle\,\cdot$$

$$\iint \mathrm{d}b'\,\mathrm{d}\tilde{b}'\,\langle b'|f'\rangle\,\langle \tilde{b}'|i\rangle^*\,\langle \tilde{b}'|\,\langle I|\hat{V}^\dagger|F\rangle\,|b'\rangle\,\cdot$$

$$\delta(E_F - E_I - E)\delta(E_f - E_{f'}), \tag{3.16}$$

where $\rho_p(b,b') := \langle b|\hat{\rho}_p|b'\rangle$ is the reduced density matrix in $\{|b\rangle\}$ representation. Since eq. 3.16 must hold for all final states $|f\rangle$, $|f'\rangle$ (which are eigenstates of $\hat{H}_0$), it is

---

[6]Every detector has a finite energy resolution. Thus, one ultimately has to integrate, e.g., over all energies that are mapped onto a single pixel.

straight-forward to deduce the expression[7]

$$
\begin{aligned}
\rho_p(b, b') = \iint \mathrm{d}\tilde{b}\mathrm{d}\tilde{b}' \, \langle\tilde{b}|i\rangle \, \langle\tilde{b}'|i\rangle^* \cdot \\
\left(4\pi^2 \sum_F \sum_I p_I(1 - p_F) \, \langle b| \, \langle F|\hat{V}|I\rangle \, |\tilde{b}\rangle \, \langle\tilde{b}'| \, \langle I|\hat{V}^\dagger|F\rangle \, |b'\rangle \, \delta(E_F - E_I - E) \right) \\
=: \iint \mathrm{d}\tilde{b}\mathrm{d}\tilde{b}' \, \langle\tilde{b}|i\rangle \, \langle i|\tilde{b}'\rangle \, \mathbb{S}(b, b', \tilde{b}, \tilde{b}', E) \\
= \iint \mathrm{d}\tilde{b}\mathrm{d}\tilde{b}' \rho_i(\tilde{b}, \tilde{b}')\mathbb{S}(b, b', \tilde{b}, \tilde{b}', E). \quad\quad (3.17)
\end{aligned}
$$

Here, $\rho_i(\tilde{b}, \tilde{b}')$ is the density matrix of the initial state of the probe (in $\{|b\rangle\}$ representation) and the scattering kernel $\mathbb{S}(b, b', \tilde{b}, \tilde{b}', E)$ (in $\{|b\rangle\}$ representation) was introduced. It is noteworthy that the scattering kernel depends explicitly on the energy transfer E as the $\{|b\rangle\}$ states (unlike the $\{|f\rangle\}$ states) are not necessarily eigenfunctions of $\hat{H}_0$. Henceforth, the subscript p will be dropped as the remainder of this work deals solely with the (reduced) density matrix of the probe beam.

3.2. Inelastic scattering in the Coulomb potential and the mixed dynamic form factor

Of particular practical importance for EELS are the real space and the momentum space representations of the reduced density matrix in eq. 3.17 for Coulomb scattering. With

$$
\langle\boldsymbol{r}|\hat{V}|\tilde{\boldsymbol{r}}\rangle = \frac{e^2}{4\pi\epsilon_0} \frac{\delta(\boldsymbol{r} - \tilde{\boldsymbol{r}})}{|\boldsymbol{r} - \hat{\boldsymbol{R}}|} =: \hat{V}(\boldsymbol{r})\delta(\boldsymbol{r} - \tilde{\boldsymbol{r}}) \quad\quad (3.18)
$$

and, after a Fourier transform (see sec. C.3),

$$
\langle\boldsymbol{k}|\hat{V}|\tilde{\boldsymbol{k}}\rangle = \frac{e^2}{(2\pi)^3\epsilon_0} \frac{\mathrm{e}^{\mathrm{i}(\tilde{\boldsymbol{k}} - \boldsymbol{k})\cdot\hat{\boldsymbol{R}}}}{|\tilde{\boldsymbol{k}} - \boldsymbol{k}|^2} =: \hat{V}(\tilde{\boldsymbol{k}} - \boldsymbol{k}) =: \hat{V}(\boldsymbol{q}), \quad\quad (3.19)
$$

the scattering kernels become

$$
\begin{aligned}
\mathbb{S}(\boldsymbol{r}, \boldsymbol{r}', \tilde{\boldsymbol{r}}, \tilde{\boldsymbol{r}}', E) = 4\pi^2 \sum_F \sum_I p_I(1 - p_F) \, \langle F|\hat{V}(\boldsymbol{r})|I\rangle \, \langle I|\hat{V}^\dagger(\boldsymbol{r}')|F\rangle \cdot \\
\delta(E_F - E_I - E)\delta(\boldsymbol{r} - \tilde{\boldsymbol{r}})\delta(\boldsymbol{r}' - \tilde{\boldsymbol{r}}') \\
=: \mathbb{S}(\boldsymbol{r}, \boldsymbol{r}', E)\delta(\boldsymbol{r} - \tilde{\boldsymbol{r}})\delta(\boldsymbol{r}' - \tilde{\boldsymbol{r}}') \quad\quad (3.20)
\end{aligned}
$$

---

[7]The factor $\delta(E_f - E_{f'})$ is implied by the proper choice of the final states of the probe on the same energy shell and is not given explicitly here.

and

$$\mathbb{S}(\boldsymbol{k}, \boldsymbol{k}', \tilde{\boldsymbol{k}}, \tilde{\boldsymbol{k}}', E) = 4\pi^2 \sum_F \sum_I p_I (1 - p_F) \langle F|\hat{V}(\tilde{\boldsymbol{k}} - \boldsymbol{k})|I\rangle \langle I|\hat{V}^\dagger(\tilde{\boldsymbol{k}}' - \boldsymbol{k}')|F\rangle \cdot$$

$$\delta(E_F - E_I - E)$$

$$=: \mathbb{S}(\tilde{\boldsymbol{k}} - \boldsymbol{k}, \tilde{\boldsymbol{k}}' - \boldsymbol{k}', E)$$

$$=: \mathbb{S}(\boldsymbol{q}, \boldsymbol{q}', E). \tag{3.21}$$

Note that $\mathbb{S}(\boldsymbol{r}, \boldsymbol{r}', \tilde{\boldsymbol{r}}, \tilde{\boldsymbol{r}}', E)$ and $\mathbb{S}(\boldsymbol{k}, \boldsymbol{k}', \tilde{\boldsymbol{k}}, \tilde{\boldsymbol{k}}', E)$ are two representations (one in real space, the other in momentum space) derived from the same operator. As such, they are related to each other by a (quadruple) Fourier transform. Due to the properties of $\mathbb{S}$ and of the Fourier transform, it similarly holds that

$$\mathbb{S}(\boldsymbol{q}, \boldsymbol{q}', E) = \hat{\mathcal{F}}_{\boldsymbol{q}, -\boldsymbol{q}'}[\mathbb{S}(\boldsymbol{r}, \boldsymbol{r}', E)] \quad \text{and} \quad \mathbb{S}(\boldsymbol{r}, \boldsymbol{r}', E) = \hat{\mathcal{F}}_{\boldsymbol{r}, -\boldsymbol{r}'}[\mathbb{S}(\boldsymbol{q}, \boldsymbol{q}', E)]. \tag{3.22}$$

Consequently, the reduced density matrices read [58]

$$\rho(\boldsymbol{r}, \boldsymbol{r}') = \mathbb{S}(\boldsymbol{r}, \boldsymbol{r}', E)\rho_i(\boldsymbol{r}, \boldsymbol{r}')$$

$$\rho(\boldsymbol{k}, \boldsymbol{k}') = \iint \mathrm{d}\tilde{\boldsymbol{k}}\mathrm{d}\tilde{\boldsymbol{k}}' \mathbb{S}(\tilde{\boldsymbol{k}} - \boldsymbol{k}, \tilde{\boldsymbol{k}}' - \boldsymbol{k}', E)\rho_i(\tilde{\boldsymbol{k}}, \tilde{\boldsymbol{k}}')$$

$$= \iint \mathrm{d}\boldsymbol{q}\mathrm{d}\boldsymbol{q}' \mathbb{S}(\boldsymbol{q}, \boldsymbol{q}', E)\rho_i(\boldsymbol{k} + \boldsymbol{q}, \boldsymbol{k}' + \boldsymbol{q}'). \tag{3.23}$$

The scattering kernels are related to the mixed dynamic form factor (MDFF) $S(\boldsymbol{q}, \boldsymbol{q}', E)$ [59–61] and to the real space MDFF (rMDFF) $S(\boldsymbol{r}, \boldsymbol{r}', E)$ [62, 63] via (see sec. C.4)

$$\mathbb{S}(\boldsymbol{q}, \boldsymbol{q}', E) = \left(\frac{e^2}{4\pi^2\epsilon_0}\right)^2 \frac{S(\boldsymbol{q}, \boldsymbol{q}', E)}{q^2 q'^2}$$

$$\mathbb{S}(\boldsymbol{r}, \boldsymbol{r}', E) = \left(\frac{e^2}{4\pi^2\epsilon_0}\right)^2 \frac{\mathrm{e}^{\mathrm{i}q_E(z-z')}}{(2\pi)^3} \cdot$$

$$[K_0(q_E r_\perp)K_0(q_E r'_\perp)] \circledast_\perp \iint \mathrm{d}z\mathrm{d}z' \mathrm{e}^{-\mathrm{i}q_E(z-z')} S(\boldsymbol{r}, \boldsymbol{r}', E), \tag{3.24}$$

where K_0 is the modified Bessel function of second kind and $\circledast_\perp$ denotes a 2D convolution.

The MDFF is one of the most important concepts for the simulation of inelastic scattering and subsequent image formation [61]. Some of its most interesting and important properties are:

- it is hermitian in the sense that $S(\boldsymbol{q}, \boldsymbol{q}', E)^* = S(\boldsymbol{q}', \boldsymbol{q}, E)$ (this can be derived directly from eq. 3.21);

- it is related to the conventional dynamic form factor (DFF), which is given by $S(\boldsymbol{q}, \boldsymbol{q}, E)$ [16, 61, 64];

- it is closely related to the density–density correlation function of the target, i.e., $S(\boldsymbol{q}, \boldsymbol{q}', E) = \frac{1}{2\pi} \int_{-\infty}^{\infty} \langle \rho_{t,\boldsymbol{q}}(t) \rho_{t,-\boldsymbol{q}'}(0) \rangle_T \, \mathrm{e}^{\mathrm{i}\omega t} \mathrm{d}t$, where $\omega = E/\hbar$, E is the energy transfer in the inelastic interaction (which is implicitly given by the momentum transfer), $\rho_{t,\boldsymbol{q}}(t)$ is the Fourier transformed density operator of the target in the Heisenberg representation, and $\langle \ \rangle_T$ denotes the thermal average [61, 62];

- for targets with an inversion symmetry at the origin, the MDFF obeys the rule $S(\boldsymbol{q}, \boldsymbol{q}', E) = S(-\boldsymbol{q}, -\boldsymbol{q}', E)$ [61];

- for targets that are invariant under time-reversal, the relation $S(\boldsymbol{q}, \boldsymbol{q}', E) = S(-\boldsymbol{q}', -\boldsymbol{q}, E)$ holds [61];

- for crystalline samples, the MDFF must be zero unless $\boldsymbol{q} - \boldsymbol{q}' = \boldsymbol{g}$, where $\boldsymbol{g}$ is a reciprocal lattice vector [61, 62].

3.3. Probability current and the double differential scattering cross-section

The probability current density operator is defined as [65, 66][8]

$$\hat{\boldsymbol{j}}(\boldsymbol{r}) := \frac{1}{2m_e} \left(|\boldsymbol{r}\rangle \langle \boldsymbol{r}| \, \hat{\boldsymbol{p}} + \hat{\boldsymbol{p}}^\dagger \, |\boldsymbol{r}\rangle \langle \boldsymbol{r}| \right). \tag{3.25}$$

Therefore, the probability current associated with a density operator can easily be calculated as

$$\boldsymbol{j}(\boldsymbol{r}) = \mathrm{tr}\,[\hat{\boldsymbol{j}}(\boldsymbol{r})\hat{\rho}] = \sum_\psi \langle \psi | \hat{\boldsymbol{j}}(\boldsymbol{r}) \hat{\rho} | \psi \rangle. \tag{3.26}$$

In momentum space (i.e., $\{|\psi\rangle\} = \{|\boldsymbol{k}'\rangle\}$), this can be expanded as

$$\begin{aligned}
\boldsymbol{j}(\boldsymbol{r}) &= \frac{1}{2m_e} \int \mathrm{d}\boldsymbol{k}' \left[\langle \boldsymbol{k}'|\boldsymbol{r}\rangle \langle \boldsymbol{r}|\hat{\boldsymbol{p}}\hat{\rho}|\boldsymbol{k}'\rangle + \langle \boldsymbol{k}'|\hat{\boldsymbol{p}}^\dagger|\boldsymbol{r}\rangle \langle \boldsymbol{r}|\hat{\rho}|\boldsymbol{k}'\rangle \right] \\
&= \frac{1}{2m_e} \iint \mathrm{d}\boldsymbol{k}\mathrm{d}\boldsymbol{k}' \left[\langle \boldsymbol{k}'|\boldsymbol{r}\rangle \langle \boldsymbol{r}|\hat{\boldsymbol{p}}|\boldsymbol{k}\rangle \langle \boldsymbol{k}|\hat{\rho}|\boldsymbol{k}'\rangle + \langle \boldsymbol{k}'|\hat{\boldsymbol{p}}^\dagger|\boldsymbol{r}\rangle \langle \boldsymbol{r}|\boldsymbol{k}\rangle \langle \boldsymbol{k}|\hat{\rho}|\boldsymbol{k}'\rangle \right] \\
&= \frac{1}{2m_e} \iint \mathrm{d}\boldsymbol{k}\mathrm{d}\boldsymbol{k}' \, \langle \boldsymbol{k}'|\boldsymbol{r}\rangle \langle \boldsymbol{r}|\boldsymbol{k}\rangle \langle \boldsymbol{k}|\hat{\rho}|\boldsymbol{k}'\rangle \, \hbar(\boldsymbol{k} + \boldsymbol{k}') \\
&= \frac{1}{16\pi^3 m_e} \iint \mathrm{d}\boldsymbol{k}\mathrm{d}\boldsymbol{k}' \mathrm{e}^{\mathrm{i}(\boldsymbol{k}-\boldsymbol{k}')\cdot\boldsymbol{r}} \rho(\boldsymbol{k}, \boldsymbol{k}') \hbar(\boldsymbol{k} + \boldsymbol{k}').
\end{aligned} \tag{3.27}$$

For the recurring case that the density operator is a pure plane wave, i.e.,

$$\hat{\rho} = |\boldsymbol{k}_i\rangle \langle \boldsymbol{k}_i| \quad \text{and} \quad \rho(\boldsymbol{k}, \boldsymbol{k}') = \delta(\boldsymbol{k} - \boldsymbol{k}_i)\delta(\boldsymbol{k}' - \boldsymbol{k}_i), \tag{3.28}$$

---

[8]As before, this describes a particle current, not an electrical current. The electrical current can be calculated simply by multiplying the particle current by the charge.

this can be evaluated to yield

$$\boldsymbol{j}(\boldsymbol{r}) = \frac{\hbar \boldsymbol{k}_i}{(2\pi)^3 m_e} = \frac{\hbar \boldsymbol{k}_i}{m_e} \left| \langle \boldsymbol{r} | \boldsymbol{k}_i \rangle \right|^2. \tag{3.29}$$

This is the well-known probability current density of plane waves that can also be derived without the density matrix formalism (see sec. 2.2.2 and, e.g., [64]).

A useful concept in scattering theory related to the probability current density (or the "particle flux") is the scattering cross section. It is defined as the total probability current (i.e., number of particles per unit time) in a particular outgoing channel, divided by the incident probability current density [67]. In inelastic electron scattering, the outgoing channels are typically described by the energy (interval) and the direction (solid angle). This leads to the concept of the double differential scattering cross-section (DDSCS) by means of the ansatz [64]

$$\mathrm{d}j = \mathrm{d}\sigma(E, \Omega) \cdot j_i, \tag{3.30}$$

where $\mathrm{d}j$ is the total probability current in an infinitesimal energy range $\mathrm{d}E$ and an infinitesimal solid angle $\mathrm{d}\Omega$, $\mathrm{d}\sigma$ is the scattering cross section, and j_i is the incident probability current density.

Assuming the incident wave to be a plane wave, the incident probability current density is given by the absolute value of eq. 3.29. To calculate the differential total probability current in the outgoing channel, two steps have to be taken. On the one hand, the integral over all final states $\{|\boldsymbol{k}'\rangle\}$ has to be replaced by that over an infinitesimal range $\mathrm{d}\boldsymbol{k}_f$ — which effectively amounts to replacing the integral by a "multiplication" with $\mathrm{d}\boldsymbol{k}_f$ — to obtain the differential probability current density. On the other hand, this differential probability current density has to be integrated over the whole plane (perpendicular to $\boldsymbol{k}_f$) to get the differential probability current. This gives

$$\mathrm{d}\sigma = \frac{\mathrm{d}j}{j_i} = \frac{\mathrm{d}\boldsymbol{k}_f}{2k_i} \iint \mathrm{d}\boldsymbol{k} \mathrm{d}\boldsymbol{A} \cdot (\boldsymbol{k} + \boldsymbol{k}_f) \mathrm{e}^{\mathrm{i}(\boldsymbol{k} - \boldsymbol{k}_f) \cdot \boldsymbol{r}} \rho(\boldsymbol{k}, \boldsymbol{k}_f), \tag{3.31}$$

where $\mathrm{d}\boldsymbol{A}$ describes the vector-valued differential plane element with a direction perpendicular to the plane (i.e., parallel to $\boldsymbol{k}_f$).

With $E = \hbar^2(k_f^2 - k_i^2)/(2m_e)$, the infinitesimal range $\mathrm{d}\boldsymbol{k}_f$ can be rewritten in terms of the differentials $\mathrm{d}E$ and $\mathrm{d}\Omega$ using the identity

$$\mathrm{d}\boldsymbol{k}_f = k_f^2 \mathrm{d}k_f \mathrm{d}\Omega = \frac{m_e k_f}{\hbar^2} \mathrm{d}E \mathrm{d}\Omega. \tag{3.32}$$

Thus, the DDSCS can be calculated generally as

$$
\begin{aligned}
\frac{\partial^2 \sigma}{\partial E \partial \Omega} &= \frac{m_e k_f}{2\hbar^2 k_i} \iint \mathrm{d}\boldsymbol{k} \mathrm{d}\boldsymbol{A} \cdot (\boldsymbol{k} + \boldsymbol{k}_f) \mathrm{e}^{\mathrm{i}(\boldsymbol{k} - \boldsymbol{k}_f) \cdot \boldsymbol{r}} \rho(\boldsymbol{k}, \boldsymbol{k}_f) \\
&= \frac{m_e k_f}{2\hbar^2 k_i} \iint \mathrm{d}\boldsymbol{k} \mathrm{d}\boldsymbol{r}_\perp (k_\parallel + k_f) \mathrm{e}^{\mathrm{i}\boldsymbol{k}_\perp \cdot \boldsymbol{r}_\perp} \mathrm{e}^{\mathrm{i}(\boldsymbol{k}_\parallel - k_f) \cdot \boldsymbol{r}_\parallel} \rho(\boldsymbol{k}, \boldsymbol{k}_f) \\
&= \frac{2\pi^2 m_e k_f}{\hbar^2 k_i} \int \mathrm{d}\boldsymbol{k} \delta(\boldsymbol{k}_\perp)(k_\parallel + k_f) \mathrm{e}^{\mathrm{i}(\boldsymbol{k}_\parallel - k_f) \cdot \boldsymbol{r}_\parallel} \rho(\boldsymbol{k}, \boldsymbol{k}_f),
\end{aligned}
\tag{3.33}
$$

where the subscripts $\parallel$ and $\perp$ are used to label components parallel and perpendicular to $\boldsymbol{k}_f$, respectively.

In the absence of elastic scattering (e.g., for a single scattering atom), the density matrix is given by eq. 3.23. Together with an incident density matrix as the one given in eq. 3.28, the DDSCS takes the form[9]

$$\frac{\partial^2 \sigma}{\partial E \partial \Omega} = \frac{2\pi^2 m_e k_f}{\hbar^2 k_i} \int \mathrm{d}\boldsymbol{k} \delta(\boldsymbol{k}_\perp) \delta(E_{\boldsymbol{k}} - E_{\boldsymbol{k}_f})(k_\parallel + k_f) \mathrm{e}^{\mathrm{i}(\boldsymbol{k}_\parallel - k_f) \cdot \boldsymbol{r}_\parallel} \,\cdot$$

$$\iint \mathrm{d}\boldsymbol{q} \mathrm{d}\boldsymbol{q}' \mathbb{S}(\boldsymbol{q}, \boldsymbol{q}', E) \delta(\boldsymbol{k} + \boldsymbol{q} - \boldsymbol{k}_i) \delta(\boldsymbol{k}_f + \boldsymbol{q}' - \boldsymbol{k}_i)$$

$$= \frac{2\pi^2 m_e k_f}{\hbar^2 k_i} \int \mathrm{d}\boldsymbol{k} \delta(\boldsymbol{k}_\perp) \delta(E_{\boldsymbol{k}} - E_{\boldsymbol{k}_f})(k_\parallel + k_f) \mathrm{e}^{\mathrm{i}(\boldsymbol{k}_\parallel - k_f) \cdot \boldsymbol{r}_\parallel} \,\cdot$$

$$\mathbb{S}(\boldsymbol{k}_i - \boldsymbol{k}, \boldsymbol{k}_i - \boldsymbol{k}_f, E). \tag{3.34}$$

Using

$$\delta(E_{\boldsymbol{k}} - E_{\boldsymbol{k}_f}) = \delta\left(\frac{\hbar^2(k_\perp^2 + k_\parallel^2)}{2m_e} - \frac{\hbar^2 k_f^2}{2m}\right) = \frac{m_e}{\hbar^2 k_f} \delta\left(\sqrt{k_\perp^2 + k_\parallel^2} - k_f\right), \tag{3.35}$$

the DDSCS can be simplified further, yielding

$$\frac{\partial^2 \sigma}{\partial E \partial \Omega} = \frac{2\pi^2 m_e^2}{\hbar^4 k_i} \int \mathrm{d}\boldsymbol{k} \delta(\boldsymbol{k}_\perp) \delta\left(\sqrt{k_\perp^2 + k_\parallel^2} - k_f\right) \cdot$$

$$(k_\parallel + k_f) \mathrm{e}^{\mathrm{i}(\boldsymbol{k}_\parallel - k_f) \cdot \boldsymbol{r}_\parallel} \mathbb{S}(\boldsymbol{k}_i - \boldsymbol{k}, \boldsymbol{k}_i - \boldsymbol{k}_f, E)$$

$$= \frac{2\pi^2 m_e^2}{\hbar^4 k_i} \int \mathrm{d}\boldsymbol{k} \delta(\boldsymbol{k} - \boldsymbol{k}_f)(k_\parallel + k_f) \mathrm{e}^{\mathrm{i}(\boldsymbol{k}_\parallel - k_f) \cdot \boldsymbol{r}_\parallel} \mathbb{S}(\boldsymbol{k}_i - \boldsymbol{k}, \boldsymbol{k}_i - \boldsymbol{k}_f, E)$$

$$= \left(\frac{2\pi m_e}{\hbar^2}\right)^2 \cdot \frac{k_f}{k_i} \cdot \mathbb{S}(\boldsymbol{k}_i - \boldsymbol{k}_f, \boldsymbol{k}_i - \boldsymbol{k}_f, E), \tag{3.36}$$

the well-known equation for the single inelastic scattering of plane waves [62, 64, 68].

3.4. Calculating the mixed dynamic form factor

This section is based on [24, 68].

Up to now, the fundamental concepts of quantum mechanical inelastic scattering have been introduced. To apply this theoretical framework to simulations and experiments, the particular properties of the target need to be taken into account. As was outlined

---

[9]Note that the factor $\delta(E_{\boldsymbol{k}} - E_{\boldsymbol{k}_f})$ derived in sec. 3.1 is included here explicitly. It ensures the proper orthonormalization of the final states of the probe beam.

above, the central quantity in inelastic scattering is the MDFF, so this section and the following ones will concentrate on it. From eqs. 3.24, 3.21, and 3.19, the MDFF reads

$$S(\boldsymbol{q}, \boldsymbol{q}', E) := \sum_F \sum_I p_I(1 - p_F) \langle F|e^{i\boldsymbol{q}\cdot\hat{\boldsymbol{R}}}|I\rangle \langle I|e^{-i\boldsymbol{q}'\cdot\hat{\boldsymbol{R}}}|F\rangle \, \delta(E_F - E_I - E). \quad (3.37)$$

In principle, the sum over all initial and final states $\{|I\rangle, |F\rangle\}$ includes all states of *all* atoms. However, the periodicity of the crystal carries over to the MDFF, which is also periodic. In addition, the tight binding of the target's electrons contributing to core-loss EELS causes the initial states $\{|I\rangle\}$ to be highly localized in real space. As a result, the MDFF of a crystal can be written as an (incoherent) sum over individual MDFFs, each positioned at a different scattering center [62]. Thus, it is sufficient to concentrate on a single scattering center, as will be done in the following.

To actually use the MDFF, one needs to specify the initial and final states $\{|I\rangle, |F\rangle\}$ of the target. Because, in core-loss EELS, the initial state is typically very localized in the vicinity of the atomic nucleus, it is advantageous to place the origin in the center of the atom and to work with spherical harmonics. To that end, the MDFF can be rewritten using the plane wave expansion (also known as Rayleigh expansion) [65, 67],

$$e^{i\boldsymbol{q}\cdot\boldsymbol{R}} = 4\pi \sum_{\lambda=0}^{\infty} \sum_{\mu=-\lambda}^{\lambda} i^\lambda Y_\lambda^\mu(\boldsymbol{q}/q)^* Y_\lambda^\mu(\boldsymbol{R}/R) j_\lambda(qR), \quad (3.38)$$

where the Y_λ^μ are the spherical harmonics and j_λ is the spherical Bessel function of first kind, to read

$$S(\boldsymbol{q}, \boldsymbol{q}', E) = 16\pi^2 \sum_{\lambda\lambda'} i^{\lambda-\lambda'} \sum_{\mu\mu'} \sum_F \sum_I p_I(1-p_F) Y_\lambda^\mu(\boldsymbol{q}/q)^* Y_{\lambda'}^{\mu'}(\boldsymbol{q}'/q') \cdot$$
$$\langle F|Y_\lambda^\mu(\hat{\boldsymbol{R}}/\hat{R}) j_\lambda(q\hat{R})|I\rangle \langle F|Y_{\lambda'}^{\mu'}(\hat{\boldsymbol{R}}/\hat{R}) j_{\lambda'}(q'\hat{R})|I\rangle^* \delta(E_F - E_I - E). \quad (3.39)$$

This expression has the advantage that — in spherical coordinates — the individual matrix elements decompose into separate integrals for the angular and the radial part.

3.4.1. The mixed dynamic form factor for isolated atoms

The simplest case imaginable to actually calculate the MDFF is that of isolated atoms. Of course, this is somewhat unrealistic, since one usually does not deal with single, isolated atoms in experiments. As will be discussed in sec. 3.5, however, the MDFF in crystals often reduces to formulas identical to the ones derived here. Hence, it is definitely worthwhile to study this simple case before treating the more general and more complex case of crystals.

For isolated atoms without spin-polarization[10], both the initial and the final states can be considered to be eigenstates of the OAM operators $\hat{L}^2$ and $\hat{L}_z$. Furthermore, it

---

[10]This means that there is no preferred spin orientation — spin up and spin down states are degenerate (in any coordinate system). Therefore, the spin-dependency of the wave functions and, thus, the spin–orbit coupling are neglected. For the more general case, see the following sections.

is assumed that (i) only initial states with angular momentum quantum number l and only final states with angular momentum quantum number L contribute, (ii) states with the same angular momentum quantum number are independent, and (iii) all initial states are fully occupied ($p_I = 1$), while all final states are fully unoccupied ($p_F = 0$). In this case, the initial and final states are statistical mixtures of the wave functions

$$\langle \boldsymbol{R}|I\rangle = u_l(R)Y_l^m(\boldsymbol{R}/R)$$
$$\langle \boldsymbol{R}|F\rangle = u_L(R)Y_L^M(\boldsymbol{R}/R) \tag{3.40}$$

with the weights $1/(2l+1)$ and $1/(2L+1)$, respectively. Thus, the matrix elements in real space read

$$\langle F|Y_\lambda^\mu(\hat{\boldsymbol{R}}/\hat{R})j_\lambda(q\hat{R})|I\rangle = \left(\int_0^\infty u_L(R)^* j_\lambda(qR) u_l(R) R^2 \mathrm{d}R\right) \cdot$$
$$\int_{4\pi} Y_L^M(\Omega)^* Y_\lambda^\mu(\Omega) Y_l^m(\Omega) \mathrm{d}\Omega$$
$$=: (-1)^M \langle j_\lambda(q)\rangle \int_{4\pi} Y_L^{-M}(\Omega) Y_\lambda^\mu(\Omega) Y_l^m(\Omega) \mathrm{d}\Omega. \tag{3.41}$$

By virtue of the Wigner 3j symbols (eq. C.29), the matrix elements become

$$\langle F|Y_\lambda^\mu(\hat{\boldsymbol{R}}/\hat{R})j_\lambda(q\hat{R})|I\rangle =$$
$$(-1)^M \sqrt{\frac{(2L+1)(2\lambda+1)(2l+1)}{4\pi}} \begin{pmatrix} L & \lambda & l \\ 0 & 0 & 0 \end{pmatrix} \begin{pmatrix} L & \lambda & l \\ -M & \mu & m \end{pmatrix} \langle j_\lambda(q)\rangle. \tag{3.42}$$

Consequently, the MDFF takes the form[11]

$$S(\boldsymbol{q}, \boldsymbol{q}', E) = 16\pi^2 \sum_{\lambda\lambda'} \mathrm{i}^{\lambda-\lambda'} \sum_{\mu\mu'} \sum_{LM} \sum_{lm} Y_\lambda^\mu(\boldsymbol{q}/q)^* Y_{\lambda'}^{\mu'}(\boldsymbol{q}'/q')\cdot$$
$$\langle F|Y_\lambda^\mu(\hat{\boldsymbol{R}}/\hat{R})j_\lambda(q\hat{R})|I\rangle \langle F|Y_{\lambda'}^{\mu'}(\hat{\boldsymbol{R}}/\hat{R})j_{\lambda'}(q'\hat{R})|I\rangle^*$$
$$= 4\pi(2L+1)(2l+1) \sum_{\lambda\lambda'} \mathrm{i}^{\lambda-\lambda'} \sum_{\mu\mu'} \sum_{LM} \sum_{lm} Y_\lambda^\mu(\boldsymbol{q}/q)^* Y_{\lambda'}^{\mu'}(\boldsymbol{q}'/q')$$
$$\sqrt{(2\lambda+1)} \begin{pmatrix} L & \lambda & l \\ 0 & 0 & 0 \end{pmatrix} \begin{pmatrix} L & \lambda & l \\ -M & \mu & m \end{pmatrix} \langle j_\lambda(q)\rangle$$
$$\sqrt{(2\lambda'+1)} \begin{pmatrix} L & \lambda' & l \\ 0 & 0 & 0 \end{pmatrix} \begin{pmatrix} L & \lambda' & l \\ -M & \mu' & m \end{pmatrix} \langle j_{\lambda'}(q')\rangle^*. \tag{3.43}$$

By virtue of the permutation relations (eq. C.32) and the orthogonality relation (eq. C.31), this simplifies to

$$S(\boldsymbol{q}, \boldsymbol{q}', E) = 4\pi(2L+1)(2l+1) \cdot$$
$$\sum_{\lambda\mu} \sum_{Ll} Y_\lambda^\mu(\boldsymbol{q}/q)^* Y_\lambda^\mu(\boldsymbol{q}'/q') \begin{pmatrix} L & \lambda & l \\ 0 & 0 & 0 \end{pmatrix}^2 \langle j_\lambda(q)\rangle \langle j_\lambda(q')\rangle^* \tag{3.44}$$

---

[11]The final states are assumed to correspond to the correct energy and the integral over energy is performed such that the Dirac delta yields 1.

and by the addition theorem (eq. C.34) to

$$S(\boldsymbol{q}, \boldsymbol{q}', E) = (2L + 1)(2l + 1)(2\lambda + 1) \cdot$$

$$\sum_\lambda P_\lambda \left(\frac{\boldsymbol{q} \cdot \boldsymbol{q}'}{qq'} \right) \sum_{Ll} \begin{pmatrix} L & \lambda & l \\ 0 & 0 & 0 \end{pmatrix}^2 \langle j_\lambda(q) \rangle \langle j_\lambda(q') \rangle^* . \tag{3.45}$$

In this case, the magnetic quantum numbers do not influence the MDFF and all cross-terms $\lambda \neq \lambda'$ vanish.

As the Wigner 3j symbols fulfill similar conditions as those which are well-known from atomic scattering theory (in fact, they are closely related to Clebsch-Gordan coefficients; in particular, the triangle inequality $|L - l| \leq \lambda \leq L + l$ applies), λ is usually referred to as the transition order. As was investigated by Auerhammer and Rez [69], dipole-allowed transitions ($\lambda = 1$) are by far dominant for core-loss EELS under typical conditions (in particular, momentum transfers $q \ll 6\,\text{Å}^{-1}$). Therefore, many actual calculations are limited to the case $\lambda = \lambda' = 1$.

3.4.2. The mixed dynamic form factor for crystal wave functions

In experiments, one never has the luxury of dealing with isolated atoms. Instead, the best one can hope for are crystals. The MDFF for scattering centers inside (periodic) crystals will be developed in this subsection.

In core-loss EELS, the target's initial states $\{|I\rangle\}$ are tightly bound core states. They are typically well-localized around the atomic nucleus and thus the overlap between core states of neighboring atoms is negligibly small. Hence, core states of different atoms can be considered independent and uncorrelated. Furthermore, due to the close proximity to the nucleus, the electrostatic potential they experience is dominated by the atomic potential. In consequence, the influence of the potential of neighboring atoms is also negligible for these states. What is not negligible, however, — particularly for heavy atoms — is the spin–orbit coupling. Therefore, the initial states can be described in very good approximation by eigenstates of the total angular momentum operators $\hat{J}^2$ and $\hat{J}_z$ [68]:

$$\begin{aligned} |I\rangle &= |n, l, 1/2, j, j_z\rangle \\ &= \sum_{ms} |n, l, m, 1/2, s\rangle \langle l, m, 1/2, s | j, j_z \rangle \\ &= \sum_{ms} (-1)^{-l + \frac{1}{2} - j_z} \sqrt{2j + 1} \begin{pmatrix} l & \frac{1}{2} & j \\ m & s & -j_z \end{pmatrix} |n, l, m, 1/2, s\rangle . \end{aligned} \tag{3.46}$$

The spin quantum number $1/2$ will be omitted from the kets henceforth. The energy of $|I\rangle$ is dominated by the quantum numbers n, l, j.[12] This energy is directly observable

---

[12] j_z may give rise to a Zeeman splitting in the magnetic field of the objective lens of a TEM. For typical fields around 2 T, the Zeeman splitting is of the order of less than 1 meV and therefore well below the energy resolution of conventional energy loss spectrometers.

in EELS by selecting a particular edge. Therefore, the initial states are well-defined except for j_z, which may vary between $-j$ and j. States which differ only in j_z can be considered independent and therefore must be summed over incoherently.

For the final states $|F\rangle$, matters are a little more complicated. Since these states must be unoccupied, they are typically found in the conduction band and are strongly influenced by the crystal potential. Obviously, they can be uniquely identified by a set of quantum numbers, hereafter denoted collectively by ν where the set of all $|\nu\rangle$ forms an orthonormal basis set. For example, in a band structure formalism, ν would contain the wave vector and the band index.

For the matrix element $\langle F|\hat{V}|I\rangle = \langle \nu|\hat{V}|I\rangle$, only the part of the final states that has significant overlap with (at least one of) the initial states is of importance. Thus, one typically considers only the contribution inside a sphere around the scattering atom (e.g., a muffin-tin sphere in DFT calculations [49]). In this sphere, it is convenient to expand the final state into angular momentum eigenstates [24, 68]:

$$|\nu\rangle = \sum_{LMS} D^{\nu}_{LMS} |\nu, L, M, 1/2, S\rangle, \tag{3.47}$$

As the $\{|\nu\rangle\}$ are an orthonormal basis set, states with different ν are independent and have to be summed over incoherently. As for the initial states, the spin quantum number $1/2$ will be omitted henceforth.

For the sake of simplicity, $p_I = 1$ and $p_F = 0$ are assumed. The former expression specifies that all initial states are fully occupied, which is a reasonable assumption given their low energy. The latter expresses that all final states considered here are fully unoccupied.[13]

Inserting these assumptions into eq. 3.39 gives the MDFF in the form

$$S(\boldsymbol{q}, \boldsymbol{q}', E) = 16\pi^2(2j+1)\sum_{\lambda\lambda'}\mathrm{i}^{\lambda-\lambda'}\sum_{\mu\mu'}\sum_{j_z}\oint_{\nu}Y^{\mu}_{\lambda}(\boldsymbol{q}/q)^*Y^{\mu'}_{\lambda'}(\boldsymbol{q}'/q')\delta(E_F - E_I - E)\cdot$$

$$\sum_{ms}(-1)^{\frac{1}{2}-j_z}\begin{pmatrix} l & \frac{1}{2} & j \\ m & s & -j_z \end{pmatrix}\sum_{m's'}(-1)^{\frac{1}{2}-j_z}\begin{pmatrix} l & \frac{1}{2} & j \\ m' & s' & -j_z \end{pmatrix}\cdot$$

$$\sum_{LMS}(D^{\nu}_{LMS})^*\langle \nu, L, M, S\,|\,Y^{\mu}_{\lambda}(\hat{\boldsymbol{R}}/\hat{R})j_{\lambda}(q\hat{R})\,|\,n, l, m, s\rangle\cdot$$

$$\sum_{L'M'S'}D^{\nu}_{L'M'S'}\left\langle n, l, m', s'\,\middle|\,Y^{\mu'}_{\lambda'}(\hat{\boldsymbol{R}}/\hat{R})j_{\lambda'}(q'\hat{R})\,\middle|\,\nu, L', M', S'\right\rangle. \tag{3.48}$$

Note that the sums over s and s' reduce to δ_{sS} and $\delta_{s'S'}$, respectively, as the transition operator is spin-independent.

In order to evaluate the matrix elements, one can write the initial and final states in a real space representation. The resulting integrals have already been evaluated

---

[13]At a finite temperature, this is not strictly the case, of course. However, measurements are typically performed at or close to room temperature, which corresponds to thermal energies well below $0.1\,\mathrm{eV}$ which are thus below the energy resolution of most instruments.

when deriving eq. 3.42. Consequently, the MDFF takes the form

$$
S(\boldsymbol{q}, \boldsymbol{q}', E) = 4\pi \sum_{mm'} \sum_{\lambda\lambda'} \sum_{\mu\mu'} \sum_{LMS} \sum_{L'M'S'} \sum_{j_z} \oint_\nu \mathrm{i}^{\lambda-\lambda'} (-1)^{M+M'+1-2j_z} \cdot
$$

$$
(2l+1)(2j+1)\sqrt{(2L+1)(2L'+1)(2\lambda+1)(2\lambda'+1)} \cdot
$$

$$
\begin{pmatrix} l & \frac{1}{2} & j \\ m & S & -j_z \end{pmatrix} \begin{pmatrix} L & \lambda & l \\ 0 & 0 & 0 \end{pmatrix} \begin{pmatrix} L & \lambda & l \\ -M & \mu & m \end{pmatrix} Y_\lambda^\mu(\boldsymbol{q}/q)^* \langle j_\lambda(q) \rangle_{\nu n j LS} \cdot
$$

$$
\begin{pmatrix} l & \frac{1}{2} & j \\ m' & S' & -j_z \end{pmatrix} \begin{pmatrix} L' & \lambda' & l \\ 0 & 0 & 0 \end{pmatrix} \begin{pmatrix} L' & \lambda' & l \\ -M' & \mu' & m' \end{pmatrix} Y_{\lambda'}^{\mu'}(\boldsymbol{q}'/q') \langle j_{\lambda'}(q') \rangle_{\nu n j L'S'} \cdot
$$

$$
(D_{LMS}^\nu)^* D_{L'M'S'}^\nu \delta(E_F - E_I - E) \tag{3.49}
$$

with

$$
\langle j_\lambda(q) \rangle_{\nu n j LS} := \int_0^\infty u_{\nu LS}(R)^* j_\lambda(qR) u_{njS}(R) R^2 \mathrm{d}R. \tag{3.50}
$$

Due to the fact that $2j_z = 2m + 2s$ is always an odd integer as $2m$ is always an even integer and $2s = \pm 1$ is always odd, one see that $(-1)^{1-2j_z} = 1$ always holds. Thus, the MDFF can also be written as

$$
S(\boldsymbol{q}, \boldsymbol{q}', E) = \oint_\nu \sum_{mm'} \sum_{\lambda\lambda'} \sum_{\mu\mu'} \sum_{LMS} \sum_{L'M'S'} \mathrm{i}^{\lambda-\lambda'} 4\pi(2l+1) \cdot
$$

$$
\sqrt{(2L+1)(2L'+1)(2\lambda+1)(2\lambda'+1)} \cdot
$$

$$
Y_\lambda^\mu(\boldsymbol{q}/q)^* \langle j_\lambda(q) \rangle_{\nu n j LS} Y_{\lambda'}^{\mu'}(\boldsymbol{q}'/q') \langle j_{\lambda'}(q') \rangle_{\nu n j L'S'} \cdot
$$

$$
\begin{pmatrix} L & \lambda & l \\ 0 & 0 & 0 \end{pmatrix} \begin{pmatrix} L' & \lambda' & l \\ 0 & 0 & 0 \end{pmatrix} \begin{pmatrix} L & \lambda & l \\ -M & \mu & m \end{pmatrix} \begin{pmatrix} L' & \lambda' & l \\ -M' & \mu' & m' \end{pmatrix} \cdot
$$

$$
\sum_{j_z} (-1)^{M+M'} (2j+1) \begin{pmatrix} l & \frac{1}{2} & j \\ m & S & -j_z \end{pmatrix} \begin{pmatrix} l & \frac{1}{2} & j \\ m' & S' & -j_z \end{pmatrix} \cdot
$$

$$
(D_{LMS}^\nu)^* D_{L'M'S'}^\nu \delta(E_F - E_I - E) \tag{3.51}
$$

This is the same as the well-known formula for the MDFF published by Schattschneider et al. [68] except for an exchange of $\boldsymbol{q}$ and $\boldsymbol{q}'$ owing to the definition of the complex conjugate of the MDFF used here.[14]

In actual applications, it is usually assumed that the radial wave functions do not depend explicitly on ν, but only on the final state energy E_F (which implicitly depends on ν, of course). In this case, the integral over all states on an energy shell,

$$
X_{LMS,L'M'S'}(E_F) := \oint_{\substack{\nu \\ \text{energy shell}}} (D_{LMS}^\nu)^* D_{L'M'S'}^\nu \tag{3.52}
$$

is called the cross density of states (XDOS).

---

[14]In [68], terms of the form $\langle I | \mathrm{e}^{\mathrm{i}\boldsymbol{q}\cdot\hat{\boldsymbol{R}}} | F \rangle \langle F | \mathrm{e}^{-\mathrm{i}\boldsymbol{q}'\cdot\hat{\boldsymbol{R}}} | I \rangle$ appear in the definition of the MDFF instead of the terms $\langle F | \mathrm{e}^{\mathrm{i}\boldsymbol{q}\cdot\hat{\boldsymbol{R}}} | I \rangle \langle I | \mathrm{e}^{-\mathrm{i}\boldsymbol{q}'\cdot\hat{\boldsymbol{R}}} | F \rangle$ used here.

3.5. Dependence of the mixed dynamic form factor on the cross density of states

In the following, two special cases will be discussed that are of paramount importance as limiting cases in experiments. In both cases, the MDFF will be simplified under the assumption of certain properties of the XDOS.

3.5.1. The spin-unpolarized case

In the absence of spin-polarization, the two spin species $S = \uparrow$ and $S = \downarrow$ behave in exactly the same manner. Consequently, the radial wave functions (and with them $\langle j_\lambda(\boldsymbol{q}) \rangle$) are independent of the spin quantum number S. In addition, states with different spins are incoherent to one another. This can be modeled by including the spin direction $\bar{S}$ in the quantum numbers ν that identify the final states uniquely and set

$$D^\nu_{LMS} = D^{\bar\nu \bar S}_{LMS} = D^{\bar\nu}_{LM}\delta_{S\bar S}. \tag{3.53}$$

With this, the sums over S, S' can be carried out, yielding

$$
\begin{aligned}
S(\boldsymbol{q}, \boldsymbol{q}', E) = {\sum_{\bar\nu}}^f \sum_{mm'} \sum_{\lambda\lambda'} \sum_{\mu\mu'} \sum_{LM} \sum_{L'M'} \mathrm{i}^{\lambda-\lambda'} 4\pi(2j+1) \cdot \\
(-1)^{M+M'}\sqrt{(2L+1)(2L'+1)(2\lambda+1)(2\lambda'+1)} \cdot \\
Y^\mu_\lambda(\boldsymbol{q}/q)^* \langle j_\lambda(q) \rangle_{\bar\nu njL} Y^{\mu'}_{\lambda'}(\boldsymbol{q}'/q') \langle j_{\lambda'}(q') \rangle_{\bar\nu njL'} \cdot \\
\begin{pmatrix} L & \lambda & l \\ 0 & 0 & 0 \end{pmatrix}
\begin{pmatrix} L' & \lambda' & l \\ 0 & 0 & 0 \end{pmatrix}
\begin{pmatrix} L & \lambda & l \\ -M & \mu & m \end{pmatrix}
\begin{pmatrix} L' & \lambda' & l \\ -M' & \mu' & m' \end{pmatrix} \cdot \\
\sum_{j_z\bar S}(2l+1)\begin{pmatrix} l & \tfrac{1}{2} & j \\ m & \bar S & -j_z \end{pmatrix}\begin{pmatrix} l & \tfrac{1}{2} & j \\ m' & \bar S & -j_z \end{pmatrix} \cdot \\
(D^{\bar\nu}_{LM})^* D^{\bar\nu}_{L'M'}\delta(E_F - E_I - E).
\end{aligned}
\tag{3.54}
$$

Now, the sums over $\bar S$ and j_z can be carried out as well, giving

$$
\begin{aligned}
S(\boldsymbol{q}, \boldsymbol{q}', E) = {\sum_{\bar\nu}}^f \sum_{m} \sum_{\lambda\lambda'} \sum_{\mu\mu'} \sum_{LM} \sum_{L'M'} \mathrm{i}^{\lambda-\lambda'} 4\pi(2j+1) \cdot \\
(-1)^{M+M'}\sqrt{(2L+1)(2L'+1)(2\lambda+1)(2\lambda'+1)} \cdot \\
Y^\mu_\lambda(\boldsymbol{q}/q)^* \langle j_\lambda(q) \rangle_{\bar\nu njL} Y^{\mu'}_{\lambda'}(\boldsymbol{q}'/q') \langle j_{\lambda'}(q') \rangle_{\bar\nu njL'} \cdot \\
\begin{pmatrix} L & \lambda & l \\ 0 & 0 & 0 \end{pmatrix}
\begin{pmatrix} L' & \lambda' & l \\ 0 & 0 & 0 \end{pmatrix}
\begin{pmatrix} L & \lambda & l \\ -M & \mu & m \end{pmatrix}
\begin{pmatrix} L' & \lambda' & l \\ -M' & \mu' & m \end{pmatrix} \cdot \\
(D^{\bar\nu}_{LM})^* D^{\bar\nu}_{L'M'}\delta(E_F - E_I - E).
\end{aligned}
\tag{3.55}
$$

In systems for which one can additionally assume that states with different L, M are independent (e.g., if the potential is isotropic around the scattering center or if all

off-diagonal terms of the XDOS with $M \neq M'$ or $L \neq L'$ contributing to the transition orders λ and λ' in question vanish [24, 70]), this can be simplified further (using the same method as for the spin) to read

$$
S(\boldsymbol{q}, \boldsymbol{q}', E) = \sum_{\bar{\nu}}^{f} \sum_{m} \sum_{\lambda\lambda'} \sum_{\mu\mu'} \sum_{LM} i^{\lambda-\lambda'} 4\pi (2j+1)(2L+1) \sqrt{(2\lambda+1)(2\lambda'+1)} \cdot
$$
$$
Y_{\lambda}^{\mu}(\boldsymbol{q}/q)^* \langle j_{\lambda}(q) \rangle_{\bar{\nu}njL} \, Y_{\lambda'}^{\mu'}(\boldsymbol{q}'/q') \langle j_{\lambda'}(q') \rangle_{\bar{\nu}njL} \cdot
$$
$$
\begin{pmatrix} L & \lambda & l \\ 0 & 0 & 0 \end{pmatrix} \begin{pmatrix} L & \lambda' & l \\ 0 & 0 & 0 \end{pmatrix} \begin{pmatrix} L & \lambda & l \\ -M & \mu & m \end{pmatrix} \begin{pmatrix} L & \lambda' & l \\ -M & \mu' & m \end{pmatrix} \cdot
$$
$$
|D_{LM}^{\bar{\nu}}|^2 \delta(E_F - E_I - E). \tag{3.56}
$$

If, in addition, the final states with the same L are degenerate with respect to M[15] (i.e., the XDOS and the density of states (DOS) are independent of M), the sums over m, M and subsequently those over λ', μ' can be carried out, too, resulting in

$$
S(\boldsymbol{q}, \boldsymbol{q}', E) = \sum_{\bar{\nu}}^{f} \sum_{L\lambda} 4\pi (2j+1)(2L+1) \begin{pmatrix} L & \lambda & l \\ 0 & 0 & 0 \end{pmatrix}^2 |D_L^{\bar{\nu}}|^2 \delta(E_F - E_I - E) \cdot
$$
$$
\sum_{\mu} Y_{\lambda}^{\mu}(\boldsymbol{q}/q)^* \langle j_{\lambda}(q) \rangle_{\bar{\nu}njL} \, Y_{\lambda}^{\mu}(\boldsymbol{q}'/q') \langle j_{\lambda}(q') \rangle_{\bar{\nu}njL}. \tag{3.57}
$$

Since μ only appears in the spherical harmonics, this sum can also be carried out, giving

$$
S(\boldsymbol{q}, \boldsymbol{q}', E) = \sum_{L} \sum_{\lambda} (2j+1)(2L+1)(2\lambda+1) \begin{pmatrix} L & \lambda & l \\ 0 & 0 & 0 \end{pmatrix}^2 P_{\lambda}\left(\frac{\boldsymbol{q} \cdot \boldsymbol{q}'}{qq'} \right) \cdot
$$
$$
\sum_{\bar{\nu}}^{f} \langle j_{\lambda}(q) \rangle_{\bar{\nu}njL} \langle j_{\lambda}(q') \rangle_{\bar{\nu}njL} |D_L^{\bar{\nu}}|^2 \delta(E_F - E_I - E), \tag{3.58}
$$

which is the equivalent to eq. 3.45 for the isolated atom.

For the practically important case of dipole-allowed transitions ($\lambda = 1$), this expression for the MDFF simplifies further to

$$
S(\boldsymbol{q}, \boldsymbol{q}', E) = \sum_{L} 3(2j+1)(2L+1) \begin{pmatrix} L & 1 & l \\ 0 & 0 & 0 \end{pmatrix}^2 P_1\left(\frac{\boldsymbol{q} \cdot \boldsymbol{q}'}{qq'} \right) \cdot
$$
$$
\sum_{\bar{\nu}}^{f} \langle j_1(q) \rangle_{\bar{\nu}njL} \langle j_1(q') \rangle_{\bar{\nu}njL} |D_L^{\bar{\nu}}|^2 \delta(E_F - E_I - E)
$$
$$
=: \left(\sum_{\bar{\nu}}^{f} \sum_{L} A_{njL}^{\bar{\nu}}(E) \cdot \langle j_1(q) \rangle_{\bar{\nu}njL} \langle j_1(q') \rangle_{\bar{\nu}njL} \right) \frac{\boldsymbol{q} \cdot \boldsymbol{q}'}{qq'}. \tag{3.59}
$$

---

[15] In fact, it is sufficient if they are degenerate with respect to all M reachable from any m with transitions of order λ. For example, in cubic systems, the quantum numbers obey the condition that $(M - M')/4$ is integer [70]. Since $-1 \leq \mu, \mu' \leq 1$ for dipole-allowed transitions and $M = m + \mu, M' = m + \mu'$, all accessible states must obey $-2 \leq M - M' = \mu - \mu' \leq 2$ and hence only $M = M'$ contributes in this case (although there could be, e.g., cross-terms for $M, M' \in \{-2, 2\}$ as in the d-state e_g/t_{2g} splitting).

In conclusion, spin-unpolarized systems with sufficiently high symmetry (such that the XDOS is diagonal and states with the same L are degenerate with respect to M) behave in the same way as isolated atoms when it comes to inelastic scattering.

3.5.2. Fully spin-polarized case

In the fully spin-polarized case, one assumes that all final states corresponding to one spin species (without loss of generality assumed to be the spin down states here) are occupied.[16] Consequently, only transitions to target states with the other spin quantum number ($S = S' = \uparrow$ here) are possible. In this case, the MDFF takes the form

$$
S(\boldsymbol{q}, \boldsymbol{q}', E) = \sideset{}{'}\sum_{\nu} \sum_{mm'} \sum_{\lambda\lambda'} \sum_{\mu\mu'} \sum_{LM} \sum_{L'M'} \mathrm{i}^{\lambda-\lambda'} 4\pi(2l+1) \cdot
$$

$$
\sqrt{(2L+1)(2L'+1)(2\lambda+1)(2\lambda'+1)} \cdot
$$

$$
Y_\lambda^\mu(\boldsymbol{q}/q)^* \langle j_\lambda(q)\rangle_{\nu njL\uparrow} Y_{\lambda'}^{\mu'}(\boldsymbol{q}'/q') \langle j_{\lambda'}(q')\rangle_{\nu njL'\uparrow} \cdot
$$

$$
\begin{pmatrix} L & \lambda & l \\ 0 & 0 & 0 \end{pmatrix} \begin{pmatrix} L' & \lambda' & l \\ 0 & 0 & 0 \end{pmatrix} \begin{pmatrix} L & \lambda & l \\ -M & \mu & m \end{pmatrix} \begin{pmatrix} L' & \lambda' & l \\ -M' & \mu' & m' \end{pmatrix} \cdot
$$

$$
\sum_{j_z} (-1)^{M+M'} (2j+1) \begin{pmatrix} l & \frac{1}{2} & j \\ m & \frac{1}{2} & -j_z \end{pmatrix} \begin{pmatrix} l & \frac{1}{2} & j \\ m' & \frac{1}{2} & -j_z \end{pmatrix} \cdot
$$

$$
(D_{LM\uparrow}^\nu)^* D_{L'M'\uparrow}^\nu \delta(E_F - E_I - E). \tag{3.60}
$$

Due to the unique properties of the Wigner 3j symbols, $m + \frac{1}{2} = j_z = m' + \frac{1}{2}$ and hence $m = m'$ must hold. This leads to

$$
S(\boldsymbol{q}, \boldsymbol{q}', E) = \sideset{}{'}\sum_{\nu} \sum_{m} \sum_{\lambda\lambda'} \sum_{\mu\mu'} \sum_{LM} \sum_{L'M'} \mathrm{i}^{\lambda-\lambda'} 4\pi(2l+1) \cdot
$$

$$
\sqrt{(2L+1)(2L'+1)(2\lambda+1)(2\lambda'+1)} \cdot
$$

$$
Y_\lambda^\mu(\boldsymbol{q}/q)^* \langle j_\lambda(q)\rangle_{\nu njL\uparrow} Y_{\lambda'}^{\mu'}(\boldsymbol{q}'/q') \langle j_{\lambda'}(q')\rangle_{\nu njL'\uparrow} \cdot
$$

$$
\begin{pmatrix} L & \lambda & l \\ 0 & 0 & 0 \end{pmatrix} \begin{pmatrix} L' & \lambda' & l \\ 0 & 0 & 0 \end{pmatrix} \begin{pmatrix} L & \lambda & l \\ -M & \mu & m \end{pmatrix} \begin{pmatrix} L' & \lambda' & l \\ -M' & \mu' & m \end{pmatrix} \cdot
$$

$$
(-1)^{M+M'} (2j+1) \begin{pmatrix} l & \frac{1}{2} & j \\ m & \frac{1}{2} & -m-\frac{1}{2} \end{pmatrix}^2 \cdot
$$

$$
(D_{LM\uparrow}^\nu)^* D_{L'M'\uparrow}^\nu \delta(E_F - E_I - E). \tag{3.61}
$$

Assuming, as above, that the XDOS is (essentially) diagonal with respect to L and M (e.g., due to symmetry constraints or low transition order), and after dropping the $\uparrow$

---

[16] An example would be a ferromagnetic target with large band splitting whose magnetization is saturated in the field of the objective lens of the TEM. For the most common magnetic materials Fe, Co, and Ni, this is a reasonable assumption for the typical objective lens fields [71]. Then, the spin is quantized along the direction of the external magnetic field, which is taken as the z direction.

index, this simplifies to

$$S(\boldsymbol{q}, \boldsymbol{q}', E) = \sum_{\nu} \sum_{m} \sum_{\lambda\lambda'} \sum_{\mu\mu'} \sum_{LM} \mathrm{i}^{\lambda-\lambda'} 4\pi(2l+1)(2L+1)\sqrt{(2\lambda+1)(2\lambda'+1)} \cdot$$

$$Y_\lambda^\mu(\boldsymbol{q}/q)^* \langle j_\lambda(q)\rangle_{\nu n j L} \, Y_{\lambda'}^{\mu'}(\boldsymbol{q}'/q') \, \langle j_{\lambda'}(q')\rangle_{\nu n j L} \cdot$$

$$\begin{pmatrix} L & \lambda & l \\ 0 & 0 & 0 \end{pmatrix} \begin{pmatrix} L & \lambda' & l \\ 0 & 0 & 0 \end{pmatrix} \begin{pmatrix} L & \lambda & l \\ -M & \mu & m \end{pmatrix} \begin{pmatrix} L & \lambda' & l \\ -M & \mu' & m \end{pmatrix} \cdot$$

$$(2j+1) \begin{pmatrix} l & \frac{1}{2} & j \\ m & \frac{1}{2} & -m-\frac{1}{2} \end{pmatrix}^2 |D_{LM}^\nu|^2 \delta(E_F - E_I - E), \qquad (3.62)$$

which, in turn, enforces $\mu = \mu'$ and $M = m + \mu$:

$$S(\boldsymbol{q}, \boldsymbol{q}', E) = \sum_{\nu} \sum_{m} \sum_{\lambda\lambda'} \sum_{\mu} \sum_{L} \mathrm{i}^{\lambda-\lambda'} 4\pi(2l+1)(2L+1)\sqrt{(2\lambda+1)(2\lambda'+1)} \cdot$$

$$Y_\lambda^\mu(\boldsymbol{q}/q)^* \langle j_\lambda(q)\rangle_{\nu n j L} \, Y_{\lambda'}^\mu(\boldsymbol{q}'/q') \, \langle j_{\lambda'}(q')\rangle_{\nu n j L} \cdot$$

$$\begin{pmatrix} L & \lambda & l \\ 0 & 0 & 0 \end{pmatrix} \begin{pmatrix} L & \lambda' & l \\ 0 & 0 & 0 \end{pmatrix} \begin{pmatrix} L & \lambda & l \\ -m-\mu & \mu & m \end{pmatrix} \begin{pmatrix} L & \lambda' & l \\ -m-\mu & \mu & m \end{pmatrix} \cdot$$

$$(2j+1) \begin{pmatrix} l & \frac{1}{2} & j \\ m & \frac{1}{2} & -m-\frac{1}{2} \end{pmatrix}^2 |D_{L(m+\mu)}^\nu|^2 \delta(E_F - E_I - E). \qquad (3.63)$$

For the practically important case of dipole-allowed transitions ($\lambda = \lambda' = 1$), this expression for the MDFF simplifies to

$$S(\boldsymbol{q}, \boldsymbol{q}', E) = \sum_{\nu} \sum_{m} \sum_{\mu=-1}^{1} \sum_{L} 12\pi(2l+1)(2L+1)(2j+1) \begin{pmatrix} L & 1 & l \\ 0 & 0 & 0 \end{pmatrix}^2 \cdot$$

$$Y_1^\mu(\boldsymbol{q}/q)^* \langle j_1(q)\rangle_{\nu n j L} \, Y_1^\mu(\boldsymbol{q}'/q') \, \langle j_1(q')\rangle_{\nu n j L} \cdot$$

$$\begin{pmatrix} L & 1 & l \\ -m-\mu & \mu & m \end{pmatrix}^2 \begin{pmatrix} l & \frac{1}{2} & j \\ m & \frac{1}{2} & -m-\frac{1}{2} \end{pmatrix}^2 |D_{L(m+\mu)}^\nu|^2 \delta(E_F - E_I - E). $$

$$(3.64)$$

For systems where states with the same L can be considered degenerate with respect to M,[17] this can be written as [72]

$$S(\boldsymbol{q}, \boldsymbol{q}', E) = \sum_{\nu} \sum_{\mu=-1}^{1} \sum_{L} 12\pi(2l+1)(2L+1)(2j+1) \begin{pmatrix} L & 1 & l \\ 0 & 0 & 0 \end{pmatrix}^2 C_{\mu j l L} \cdot$$

$$Y_1^\mu(\boldsymbol{q}/q)^* \langle j_1(q)\rangle_{\nu n j L} \, Y_1^\mu(\boldsymbol{q}'/q') \, \langle j_1(q')\rangle_{\nu n j L} \, |D_L^\nu|^2 \delta(E_F - E_I - E) $$

$$(3.65)$$

---

[17]Strictly speaking, this degeneracy is lifted by the magnetic field. However, for typical fields, this energy splitting is well below $1\,\mathrm{meV}$, which, in turn, is well below the energy resolution of current instruments.

	$l \to L = l+1$			
	$j = l + \frac{1}{2}$		$j = l - \frac{1}{2}$	
$\mu = 1$	$\frac{1}{6(2l+1)} + \frac{l}{12(2l+1)(l+1)}$		$\frac{1}{6(2l+1)} - \frac{1}{12(2l+1)}$	
$\mu = 0$	$\frac{1}{6(2l+1)}$		$\frac{1}{6(2l+1)}$	
$\mu = -1$	$\frac{1}{6(2l+1)} - \frac{l}{12(2l+1)(l+1)}$		$\frac{1}{6(2l+1)} + \frac{1}{12(2l+1)}$	

	$l \to L = l-1$			
	$j = l + \frac{1}{2}$		$j = l - \frac{1}{2}$	
$\mu = 1$	$\frac{1}{6(2l+1)} - \frac{1}{12(2l+1)}$		$\frac{1}{6(2l+1)} + \frac{l+1}{12l(2l+1)}$	
$\mu = 0$	$\frac{1}{6(2l+1)}$		$\frac{1}{6(2l+1)}$	
$\mu = -1$	$\frac{1}{6(2l+1)} + \frac{1}{12(2l+1)}$		$\frac{1}{6(2l+1)} - \frac{l+1}{12l(2l+1)}$	

Table 3.1.: Tables of the coefficients $C_{\mu jlL}$ (eq. 3.67) for dipole-allowed transitions as calculated using *Mathematica* by Wolfram Research. Note that not all transitions are necessarily possible (e.g., for $l = 0$, only transitions with $j = l + \frac{1}{2}$ and $L = l + 1$ are possible).

with

$$C_{\mu jlL} := \sum_m \begin{pmatrix} L & 1 & l \\ -m-\mu & \mu & m \end{pmatrix}^2 \begin{pmatrix} l & \frac{1}{2} & j \\ m & \frac{1}{2} & -m-\frac{1}{2} \end{pmatrix}^2. \tag{3.66}$$

These coefficients can be calculated for all possible combinations of indices (see tab. 3.1). Interestingly, the values are all linear in μ:

$$C_{\mu jlL} = \begin{cases} \frac{1}{6(2l+1)} \cdot \left(1 + \frac{\mu}{2} \cdot C_{jlL}\right) & j,l,L \geq 0, |\mu| \leq 1, L = l \pm 1, j = l \pm \frac{1}{2} \\ 0 & \text{otherwise} \end{cases} \tag{3.67}$$

with

$$C_{jlL} = \begin{cases} -\left(-\frac{l}{l+1}\right)^{(L-1)\left(\frac{3}{2}-|L-j|\right)} & j,l,L \geq 0, L = l \pm 1, j = l \pm \frac{1}{2} \\ 0 & \text{otherwise.} \end{cases} \tag{3.68}$$

Thus, the expression for the MDFF can be rearranged to read

$$S(\boldsymbol{q}, \boldsymbol{q}', E) = \sum_\nu^f \sum_L 2\pi(2L+1)(2j+1) \begin{pmatrix} L & 1 & l \\ 0 & 0 & 0 \end{pmatrix}^2 |D_L^\nu|^2 \delta(E_F - E_I - E) \cdot$$

$$\langle j_1(q) \rangle_{\nu njL} \langle j_1(q') \rangle_{\nu njL} \left[\left(\sum_{\mu=-1}^1 Y_1^\mu(\boldsymbol{q}/q)^* Y_1^\mu(\boldsymbol{q}'/q') \right) + \right.$$

$$\left. \frac{C_{jlL}}{2} \left(Y_1^1(\boldsymbol{q}/q)^* Y_1^1(\boldsymbol{q}'/q') - Y_1^{-1}(\boldsymbol{q}/q)^* Y_1^{-1}(\boldsymbol{q}'/q') \right) \right]$$

$$
= \sum_{\nu} \hspace{-1.2em}\int \sum_{L} 2\pi(2L+1)(2j+1)\begin{pmatrix} L & 1 & l \\ 0 & 0 & 0 \end{pmatrix}^2 |D_L^\nu|^2 \delta(E_F - E_I - E) \cdot
$$

$$
\langle j_1(q)\rangle_{\nu njL} \langle j_1(q')\rangle_{\nu njL} \left(\frac{3}{4\pi} \cdot \frac{\boldsymbol{q}\cdot\boldsymbol{q}'}{qq'} + \mathrm{i}C_{jlL}\Im\left(Y_1^1(\boldsymbol{q}/q)^* Y_1^1(\boldsymbol{q}'/q')\right)\right).
$$

$$\tag{3.69}$$

With

$$
Y_1^1(\boldsymbol{q}/q) = -\sqrt{\frac{3}{8\pi}} \cdot \frac{q_x + \mathrm{i}q_y}{q}, \tag{3.70}
$$

the last term can be evaluated to

$$
\Im\left(Y_1^1(\boldsymbol{q}/q)^* Y_1^1(\boldsymbol{q}'/q')\right) = \frac{3}{8\pi} \cdot \frac{q_x q_y' - q_y q_x'}{qq'} = \frac{3}{8\pi} \cdot \frac{(\boldsymbol{q}\times\boldsymbol{q}')_z}{qq'}, \tag{3.71}
$$

giving

$$
S(\boldsymbol{q},\boldsymbol{q}',E) = \sum_{\nu}\hspace{-1.2em}\int \sum_{L} \frac{3}{2}(2L+1)(2j+1)\begin{pmatrix} L & 1 & l \\ 0 & 0 & 0 \end{pmatrix}^2 |D_L^\nu|^2 \delta(E_F - E_I - E) \cdot
$$

$$
\langle j_1(q)\rangle_{\nu njL} \langle j_1(q')\rangle_{\nu njL} \left(\frac{\boldsymbol{q}\cdot\boldsymbol{q}'}{qq'} + \mathrm{i}\frac{C_{jlL}}{2}\frac{(\boldsymbol{q}\times\boldsymbol{q}')_z}{qq'}\right) \cdot
$$

$$
=: \sum_{\nu}\hspace{-1.2em}\int \sum_{L} A_{\nu njL}(E) \cdot \langle j_1(q)\rangle_{\nu njL} \langle j_1(q')\rangle_{\nu njL} \left(\frac{\boldsymbol{q}\cdot\boldsymbol{q}'}{qq'} + \mathrm{i}\frac{C_{jlL}}{2}\frac{(\boldsymbol{q}\times\boldsymbol{q}')_z}{qq'}\right),
$$

$$\tag{3.72}$$

which is the generalization of eq. 3.59 to the spin-polarized case.

3.6. Diagonalization of the mixed dynamic form factor

This section is based on [58, 73]

The MDFF (eq. 3.51) not only looks very complicated, it is generally also quite time-consuming to calculate and effectively hides the underlying physics of the transitions. The numerical inefficiency comes from the fact that there are $(2\lambda + 1)(2\lambda' + 1)$ combinations (μ, μ') for each combination (λ, λ'), which all need to be taken into account in the calculation. However, this number of terms can be reduced as will be shown in this section.

The key observation is that the MDFF can be written in the form

$$
S(\boldsymbol{q},\boldsymbol{q}',E) = \sum_{\lambda\lambda'\mu\mu'} \sum_{LL'SS'} \left(Y_\lambda^\mu(\boldsymbol{q}/q)\langle j_\lambda(q)\rangle_{LS}\right)^* \Xi_{\lambda\mu LS,\lambda'\mu'L'S'} \left(Y_{\lambda'}^{\mu'}(\boldsymbol{q}'/q')\langle j_{\lambda'}(q')\rangle_{L'S'}\right)
$$

$$
= \sum_{\alpha\alpha'} g_\alpha(\boldsymbol{q})^* \,\Xi_{\alpha,\alpha'}\, g_{\alpha'}(\boldsymbol{q}')
$$

$$
= \boldsymbol{g}(\boldsymbol{q})^\dagger \cdot \boldsymbol{\Xi} \cdot \boldsymbol{g}(\boldsymbol{q}'). \tag{3.73}
$$

Here, it was assumed that the radial wave functions do not depend on ν, but only on the energies (and hence are identical for all ν considered, which lie on an energy shell). Moreover, the constant indices n, j, E were omitted for the sake of clarity. The formulation above makes clear that the MDFF is in fact a hermitian sesquilinear form[18]; hereby,

$$\alpha := (\lambda, \mu, L, S) \tag{3.74}$$

is a shorthand notation for all appearing indices,

$$g_\alpha(\boldsymbol{q}) := Y_\lambda^\mu(\boldsymbol{q}/q) \langle j_\lambda(q) \rangle_{LS} \tag{3.75}$$

are the components of the vector-valued function of $\boldsymbol{g}(\boldsymbol{q})$ which includes the complete $\boldsymbol{q}$ dependence of the MDFF, and

$$
\begin{aligned}
\Xi_{\alpha,\alpha'} = \oint_\nu \sum_{mm'} \sum_{MM'} & i^{\lambda-\lambda'} 4\pi(2l+1) \cdot \\
& \sqrt{(2L+1)(2L'+1)(2\lambda+1)(2\lambda'+1)} \cdot \\
& \begin{pmatrix} L & \lambda & l \\ 0 & 0 & 0 \end{pmatrix} \begin{pmatrix} L' & \lambda' & l \\ 0 & 0 & 0 \end{pmatrix} \begin{pmatrix} L & \lambda & l \\ -M & \mu & m \end{pmatrix} \begin{pmatrix} L' & \lambda' & l \\ -M' & \mu' & m' \end{pmatrix} \cdot \\
& \sum_{j_z} (-1)^{M+M'}(2j+1) \begin{pmatrix} l & \frac{1}{2} & j \\ m & S & -j_z \end{pmatrix} \begin{pmatrix} l & \frac{1}{2} & j \\ m' & S' & -j_z \end{pmatrix} \cdot \\
& (D_{LMS}^\nu)^* D_{L'M'S'}^\nu \delta(E_F - E_I - E)
\end{aligned}
\tag{3.76}
$$

are the components of a matrix. In the following, it is assumed that there are only finitely many α (which is equivalent to including only transitions and states up to certain maximum values of λ and L).

It is straight-forward to show that

$$\Xi_{\alpha,\alpha'}^* = \Xi_{\alpha',\alpha} \quad \Rightarrow \quad \boldsymbol{\Xi}^\dagger = \boldsymbol{\Xi}, \tag{3.77}$$

so $\boldsymbol{\Xi}$ is hermitian. Since all hermitian matrices are normal matrices and all normal matrices are diagonalizable by a unitary transformation, a unitary matrix $\boldsymbol{U}$ must exist for which

$$\boldsymbol{D} = \boldsymbol{U}\boldsymbol{\Xi}\boldsymbol{U}^\dagger \tag{3.78}$$

is diagonal. Therefore, the MDFF can be written as

$$
\begin{aligned}
S(\boldsymbol{q}, \boldsymbol{q}', E) &= \boldsymbol{g}(\boldsymbol{q})^\dagger \cdot \boldsymbol{\Xi} \cdot \boldsymbol{g}(\boldsymbol{q}') \\
&= \boldsymbol{g}(\boldsymbol{q})^\dagger \cdot \boldsymbol{U}^\dagger \boldsymbol{U} \cdot \boldsymbol{\Xi} \cdot \boldsymbol{U}^\dagger \boldsymbol{U} \boldsymbol{g}(\boldsymbol{q}') \\
&= (\boldsymbol{U}\boldsymbol{g}(\boldsymbol{q}))^\dagger \cdot \boldsymbol{D} \cdot (\boldsymbol{U}\boldsymbol{g}(\boldsymbol{q}')) \\
&=: \tilde{\boldsymbol{g}}(\boldsymbol{q})^\dagger \cdot \boldsymbol{D} \cdot \tilde{\boldsymbol{g}}(\boldsymbol{q}').
\end{aligned}
\tag{3.79}
$$

---

[18]For $\boldsymbol{q} = \boldsymbol{q}'$, this gives rise to a (real-valued) hermitian form. Hermitian forms are the generalization of quadratic forms over the real numbers to the complex field. Hence, in literature, the term "quadratic form" is sometimes used synonymously (albeit somewhat incorrectly).

This corresponds to a transformation from a spherical harmonics basis to a symmetry-adapted basis for the transitions. The former is the natural basis for the general description of the XDOS, while the latter is adapted to the calculation of a specific system. Numerically, the diagonalization has the advantage that the number of terms to consider is reduced from at most n^2 to at most n, assuming $\boldsymbol{\Xi}$ is an $n \times n$ matrix. Moreover, in practice, most diagonal elements of $\boldsymbol{D}$ will be negligibly small.

Even more, $\boldsymbol{\Xi}$ is not only hermitian, it is also positive-semidefinite. This is most easy to see by writing $\boldsymbol{\Xi}$ as[19]

$$\boldsymbol{\Xi} = \boldsymbol{\xi}^\dagger \cdot \boldsymbol{\xi} \quad \Leftrightarrow \quad \Xi_{\alpha,\alpha'} = \sum_\beta \xi^*_{\alpha,\beta} \xi_{\beta,\alpha'} \tag{3.80}$$

with $\beta = (\nu, j_z)$ and

$$\xi_{\beta,\alpha'} = \sum_{m'} \sum_{M'} (-1)^{M'} i^{-\lambda'} \sqrt{4\pi(2l+1)(2L'+1)(2\lambda'+1)(2j+1)} \cdot$$
$$\begin{pmatrix} L' & \lambda' & l \\ 0 & 0 & 0 \end{pmatrix} \begin{pmatrix} L' & \lambda' & l \\ -M' & \mu' & m' \end{pmatrix} \begin{pmatrix} l & \frac{1}{2} & j \\ m' & S' & -j_z \end{pmatrix} D^\nu_{L'M'S'}. \tag{3.81}$$

Since all matrices of the form $\boldsymbol{\xi}^\dagger \cdot \boldsymbol{\xi}$ are positive-semidefinite[20], $\boldsymbol{\Xi}$ is positive-semidefinite. Hence, all its eigenvalues (these are the diagonal elements of $\boldsymbol{D}$) are non-negative.

Physically, this can be understood from the relation of the MDFF to the density matrix of the probe electron and to the DDSCS. Since λ, μ, L, S are good quantum numbers, channels with different α can in principle be separated in experiments. The corresponding partial DDSCS would then be (c.f. eqs. 3.36 and 3.24)

$$\left.\frac{\partial^2 \sigma}{\partial E \partial \Omega}\right|_\alpha \propto g_\alpha(\boldsymbol{q}) \cdot \boldsymbol{\Xi} \cdot g_\alpha(\boldsymbol{q}) \geq 0, \tag{3.82}$$

because the DDSCS and the resulting probability current cannot be negative. Hence, one finds

$$\boldsymbol{x} \cdot \boldsymbol{\Xi} \cdot \boldsymbol{x} \geq 0 \quad \forall \boldsymbol{x}, \tag{3.83}$$

which is exactly the definition of a positive semi-definite matrix. Alternatively, it can be argued that the MDFF behaves as a density matrix (in fact, for an incident plane wave, the reduced density matrix directly after the interaction is $\rho(\boldsymbol{q}, \boldsymbol{q'}) \propto S(\boldsymbol{q}, \boldsymbol{q'}, E)$ (eqs. 3.23 and 3.24)). Thus, the diagonal elements of $\boldsymbol{D}$ correspond to probabilities, which must be non-negative.

As the diagonal elements of $\boldsymbol{D}$ are non-negative, the MDFF can also be written as a direct product

$$S(\boldsymbol{q}, \boldsymbol{q'}, E) = \bar{\boldsymbol{g}}(\boldsymbol{q})^\dagger \cdot \bar{\boldsymbol{g}}(\boldsymbol{q'}), \tag{3.84}$$

---

[19]Here, it is assumed that there are only finitely many values for ν which all lie on the "correct" energy shell.

[20]For a positive-semidefinite matrix $\boldsymbol{\Xi}$, it must hold that $\boldsymbol{x}^\dagger \cdot \boldsymbol{\Xi} \cdot \boldsymbol{x} \geq 0 \; \forall \boldsymbol{x}$. For $\boldsymbol{\Xi} = \boldsymbol{\xi}^\dagger \cdot \boldsymbol{\xi}$, this is equivalent to $\boldsymbol{x}^\dagger \cdot \boldsymbol{\xi}^\dagger \cdot \boldsymbol{\xi} \cdot \boldsymbol{x} = (\boldsymbol{\xi}\boldsymbol{x})^\dagger \cdot (\boldsymbol{\xi}\boldsymbol{x}) \geq 0 \; \forall \boldsymbol{x}$. Since a scalar product always obeys $\|\boldsymbol{y}\|^2 = \boldsymbol{y}^\dagger \cdot \boldsymbol{y} \geq 0 \; \forall \boldsymbol{y}$, setting $\boldsymbol{y} := \boldsymbol{\xi}\boldsymbol{x}$ proves that $\boldsymbol{\Xi}$ is positive-semidefinite.

where

$$\bar{g}_\alpha(\boldsymbol{q}) := \sqrt{D_{\alpha,\alpha}}\, \tilde{g}_\alpha(\boldsymbol{q}) \tag{3.85}$$

is a (not necessarily normalized) vector. This has the practical advantage that all information is contained in the vector $\bar{\boldsymbol{q}}(\boldsymbol{q})$ and one does not have to drag the matrix $\boldsymbol{D}$ through all calculations.

The rMDFF can be computed by a simple Fourier transform of the vector $\bar{\boldsymbol{g}}(\boldsymbol{q})$. Thus, the rMDFF reads

$$S(\boldsymbol{r}, \boldsymbol{r}', E) = \bar{\boldsymbol{g}}(\boldsymbol{r})^\dagger \cdot \bar{\boldsymbol{g}}(\boldsymbol{r}'). \tag{3.86}$$

Since the XDOS is a property of the target alone, $\boldsymbol{\Xi}$ is known in advance, and the transformation $\boldsymbol{U}$ only has to be computed once, which can be done in a pre-processing step before the rest of the simulation of the probe beam. In practice, this procedure is helpful if the time required to calculate the inelastic scattering (i.e., the time required to apply the MDFF to a given density matrix) is small compared to the total simulation time. This is the case, e.g., in multi-slice calculations, where the elastic propagation dominates the calculation time. In that case, diagonalizing the MDFF reduces the number of waves which have to be propagated through the crystal, thereby significantly reducing the computation time. If, on the other hand, the inelastic scattering is the dominant factor for the calculation (e.g., because the eigenfunctions of the elastic Hamiltonian and the decomposition of the probe beam into those functions are known), the diagonalization method may not be beneficial due to the additional matrix multiplications necessary to get $\bar{\boldsymbol{g}}(\boldsymbol{q})$.

3.6.1. Simple examples

In this section, the diagonalization technique will be applied to two simple toy-models. For more realistic simulations, see sec. 4.2.2.

3.6.1.1. The spin-unpolarized isolated atom

In the isolated atom model, L, M, and S are good quantum numbers. Hence, states with different L, M, or S are independent and, by definition, no cross-terms occur. Following the derivation in sec. 3.5.1, one arrives at a diagonal matrix

$$\Xi_{\alpha\alpha'} = \left[4\pi(2j+1)(2L+1) \begin{pmatrix} L & \lambda & l \\ 0 & 0 & 0 \end{pmatrix}^2 \sum_{\bar{\nu}} |D_L^{\bar{\nu}}|^2 \delta(E_F - E_I - E) \right] \delta_{\lambda\lambda'} \delta_{\mu\mu'} \delta_{LL'} \delta_{SS'}. \tag{3.87}$$

This is already in the required form, so no additional transformation is necessary. What makes this case interesting is the fact that many transformations are possible without altering the matrix $\boldsymbol{\Xi}$. Any unitary matrix $\boldsymbol{U}$ that is block-diagonal with respect to λ and L (i.e., it may mix terms with different M or S *within* a block, but never mixes blocks) leaves $\boldsymbol{\Xi}$ unchanged. This can be understood immediately

by writing the diagonal submatrix which has the diagonal element d as $d\mathbf{1}$ with a suitably-sized unit matrix and calculating the transformation

$$\mathbf{U} \cdot (d\mathbf{1}) \cdot \mathbf{U}^\dagger = d\mathbf{U}^{-1}\mathbf{U} = d\mathbf{1}. \tag{3.88}$$

Prominent examples of such behavior are most transitions commonly occurring in EELS experiments for systems which can be modeled well using the isolated atom model. In those systems, dipole-allowed transitions are dominant and only transitions with a particular L are considered,[21] as, for instance, in the case of K edges ($l = 0 \to L = 1$) or L$_{2,3}$ edges ($l = 1 \to L = 2$). Under these circumstances, only one block occurs, and $\mathbf{U}$ is trivially block-diagonal for all possible matrices. This implies that any basis is suitable for describing the EELS experiment. It also means that any basis inevitably leads to a rotationally invariant MDFF whose $\mathbf{q}$ and $\mathbf{q}'$ dependence is given by (see sec. 3.5.1)

$$P_\lambda \left(\frac{\mathbf{q} \cdot \mathbf{q}'}{qq'} \right) \langle j_\lambda(q) \rangle \langle j_\lambda(q') \rangle . \tag{3.89}$$

3.6.1.2. The fully spin-polarized case

In the fully spin-polarized case, it is evident from eq. 3.72 that even for dipole-allowed transitions, the MDFF is not diagonal in a Cartesian basis (q_x, q_y, q_z) as terms of the form $q_x q_y'$ etc. occur in the cross-product $\mathbf{q} \times \mathbf{q}'$. Assuming that the system under investigation has sufficiently high symmetry and the transition order is low enough, eq. 3.63 shows that the MDFF is in fact diagonal in a μ basis. Therefore, the diagonalization routine will not alter $\mathbf{\Xi}$. However, a lot can be learned from $\mathbf{\Xi}$, as will be shown in the following.

For simplicity, only the practically most relevant case of dipole-allowed transitions ($\lambda = 1$) of an L$_{2,3}$ edge ($l = 1 \to L = 2$) will be considered here. Inserting these values into eq. 3.65 gives[22]

$$\mathbf{\Xi}_{j=3/2} = \chi \begin{pmatrix} 3 & & \\ & 4 & \\ & & 5 \end{pmatrix} = \chi \left[\begin{pmatrix} 4 & & \\ & 4 & \\ & & 4 \end{pmatrix} + \begin{pmatrix} -1 & & \\ & 0 & \\ & & 1 \end{pmatrix} \right]$$

$$\mathbf{\Xi}_{j=1/2} = \chi \begin{pmatrix} 3 & & \\ & 2 & \\ & & 1 \end{pmatrix} = \chi \left[\begin{pmatrix} 2 & & \\ & 2 & \\ & & 2 \end{pmatrix} + \begin{pmatrix} 1 & & \\ & 0 & \\ & & -1 \end{pmatrix} \right] \tag{3.90}$$

with the abbreviation $\chi = \frac{4\pi}{3} \oint_\nu |D_2^\nu|^2 \delta(E_F - E_I - E)$.

This directly shows several interesting aspects. Both $\mathbf{\Xi}$ matrices are composed of two terms each: a "direct term" that is proportional to the unit matrix and an "OAM term"

---

[21] Of course final states with different L exist. However, these are separated in energy by crystal fields which — in the simple isolated atom model — are not included. What remains from a practical perspective is the fact that only transitions to one particular L are measurable at a given energy loss.

[22] The matrix elements which are zero are suppressed for clarity.

that is μ-dependent. The direct term exhibits the familiar $L_2 : L_3$ branching ratio of $1 : 2$. This has its origin in the number of available initial states $|I\rangle$ (2 for $j = 1/2$ vs. 4 for $j = 3/2$). Additionally, the μ-dependency of the OAM term indicates that the transfer of certain quanta of OAM is more likely than the transfer of others. This gives rise to vortex beams and describes the energy-loss magnetic chiral dichroism (EMCD) effect [38, 47, 68]. Moreover, the EMCD effect of the two edges is equal in magnitude, but with opposite signs, as is well-known from simulations and experiments (see, e.g., [47, 68]).

In summary, the theoretical approach presented here implicitly produces an accurate description of many effects, ranging from common isotropic EEL spectra over the branching ratio to more complex phenomena such as the EMCD effect.

3.7. Modeling the radial wave function overlap

In the last section, only the properties of the XDOS were considered (e.g., symmetries, degeneracies, etc.). This section will deal with the weighted radial wave function overlap and methods to calculate (or approximate) it.

3.7.1. Small angle approximation

The small angle approximation[23] is by far the most severe approximation discussed here, but also yields the simplest formula. Using the Taylor expansion of the spherical Bessel function (eq. C.19) up to first order,[24]

$$j_\lambda(qR) \approx \frac{(qR)^\lambda}{(2\lambda + 1)!!}, \tag{3.91}$$

the weighted radial wave function overlap can be written as

$$\langle j_\lambda(q) \rangle \approx \frac{q^\lambda}{(2\lambda + 1)!!} \int_0^\infty u_F(R)^* R^{\lambda+2} u_I(R) \mathrm{d}R =: \frac{q^\lambda}{(2\lambda + 1)!!} \cdot M_{L\lambda l}, \tag{3.92}$$

where M is a q-independent matrix element.

With this formula, the MDFF for spin-unpolarized isolated atoms, eq. 3.45, (or, similarly, eq. 3.58 for sufficiently symmetric crystals) takes the particularly simple form

$$S(\boldsymbol{q}, \boldsymbol{q}', E) = (2L + 1)(2l + 1)(2\lambda + 1) \cdot$$

$$\sum_\lambda P_\lambda \left(\frac{\boldsymbol{q} \cdot \boldsymbol{q}'}{qq'} \right) \frac{(qq')^\lambda}{((2\lambda + 1)!!)^2} \sum_{Ll} \begin{pmatrix} L & \lambda & l \\ 0 & 0 & 0 \end{pmatrix}^2 |M_{L\lambda l}|^2. \tag{3.93}$$

---

[23]This approximation is often (but in an unfortunate way) referred to as dipole approximation, although it does not directly have anything to do with the transition order directly.

[24]The "double factorial" is defined as $n!! = n \cdot (n-2) \cdot \ldots \cdot 3$ for odd integers n and as $n!! = n \cdot (n-2) \cdot \ldots \cdot 2$ for even integers.

If one considers only dipole-allowed transitions ($\lambda = 1$), this can be simplified further to read

$$S(\boldsymbol{q}, \boldsymbol{q}', E) = \frac{(2L+1)(2l+1)}{3} (\boldsymbol{q} \cdot \boldsymbol{q}') \sum_{Ll} \begin{pmatrix} L & 1 & l \\ 0 & 0 & 0 \end{pmatrix}^2 |M_{L1l}|^2 =: c\, \boldsymbol{q} \cdot \boldsymbol{q}', \qquad (3.94)$$

similar to eq. 3.89. This is a well-known, often used form of the MDFF [23, 51, 61, 62, 72, 74, 75]. However, by construction, it is only valid for small scattering angles; for large momentum transfers, it would diverge. This is unphysical, as it would give rise to a diverging total scattering cross section which would violate the conservation of intensity. As a "remedy", a cut-off momentum transfer is sometimes introduced [51, 62, 76, 77]. This is only reasonable if the imaging process is limited by a (sufficiently small) objective aperture that limits the scattering angles to the range where the small angle approximation holds. In particular, this is of no use for high-resolution imaging, where large scattering angles are required.

3.7.2. Atomic radial wave functions

This section is based on [78].

To alleviate the problems of the small angle approximation, one can calculate the weighted radial wave function overlap integral analytically for atomic wave functions. As will become apparent below, this results in formulas that are only slightly more complex (in a computational sense), but are applicable also to large momentum transfers. This has the advantage of enabling more accurate predictions and interpretations of experiments without the need for numerical integration of wave function data obtained from other programs such as DFT-based packages (which often requires a lot of effort). Moreover, the formulas derived in this section are easily implemented in any simulation program that already uses the dipole approximation, as it only requires the replacement of the $\boldsymbol{q} \cdot \boldsymbol{q}'$ term by a different term composed only of elementary functions and operations found in all programming languages.

3.7.2.1. Slater-type orbitals

Slater-type orbitals (STOs) are defined as [79, 80]

$$u_{I,F}(R) := N R^{n_{I,F}-1} e^{-\zeta_{I,F} R/a_\mu}, \qquad (3.95)$$

where $n_{I,F}$ is the effective principal quantum number of the initial or final state (which is not necessarily integer) and a_μ is the Bohr radius. $\zeta_{I,F} := (Z - s_{I,F})/n_{I,F}$ is the effective nuclear charge, with the physical nuclear charge Z and a screening factor s. The subscripts I and F serve to distinguish between initial and final states. The normalization constant is given by

$$N_{I,F} = \sqrt{\frac{(2\zeta_{I,F})^{2n_{I,F}+1}}{a_\mu^{2n_{I,F}+1} \Gamma(2n_{I,F}+1)}}. \qquad (3.96)$$

It is important to note that the STOs have the simplest form imaginable for solutions of the Schrödinger equation in a Coulomb potential[25]. In particular, they are nodeless and strictly positive, i.e., $U(R) > 0 \ \forall R > 0$. As a consequence, STOs of the same angular momentum quantum number L, but different principal quantum numbers n_I, n_F are not orthogonal.[26] Hence, STOs naturally give wrong predictions for transitions that do not change L (e.g., monopole transitions, some quadrupole transitions, etc.). Nevertheless, for the practically important dipole case (where only transitions $l \to l \pm 1$ are allowed due to the selection rules), STOs are a good approximation.

In the following, both the initial and the final state radial wave functions will be modeled using STOs. With this approach, the weighted radial wave function overlap reads

$$\langle j_\lambda(q) \rangle = N_I N_F \int_0^\infty R^{n_I + n_F} e^{-(\zeta_I + \zeta_F)R/a_\mu} j_\lambda(qR) \mathrm{d}R$$

$$=: N_I N_F \int_0^\infty R^n e^{-\zeta R} j_\lambda(qR) \mathrm{d}R, \tag{3.97}$$

where the abbreviations $n := n_I + n_F$ and $\zeta := (\zeta_I + \zeta_F)/a_\mu$ were introduced. With eq. C.23, this can also be written as

$$\langle j_\lambda(q) \rangle = N_I N_F \sum_{k=0}^{\lfloor \frac{\lambda+1}{2} \rfloor} \int_0^\infty \left[\frac{A_\lambda^k \sin(qR)}{q^{\lambda-2k+1}} R^{n-\lambda+2k-1} e^{-\zeta R} + \right.$$

$$\left. \frac{B_\lambda^k \cos(qR)}{q^{\lambda-2k+2}} R^{n_I+n_F-\lambda+2k-2} e^{-\zeta R} \right] \mathrm{d}R. \tag{3.98}$$

To evaluate the integrals, one can use eq. C.25 to find

$$\int_0^\infty R^a e^{(-\zeta+\mathrm{i}q)R} \mathrm{d}R = \frac{\Gamma(a+1)}{(\zeta - \mathrm{i}q)^{a+1}} = \Gamma(a+1) \left(\frac{\zeta + \mathrm{i}q}{\zeta^2 + q^2} \right)^{a+1} \quad \forall a > -1, \tag{3.99}$$

as well as Euler's formula [31],

$$\sin(qR) = \Im\left(e^{\mathrm{i}qR}\right) \qquad \cos(qR) = \Re\left(e^{\mathrm{i}qR}\right). \tag{3.100}$$

Observing that

$$\frac{\zeta + \mathrm{i}q}{\zeta^2 + q^2} = \frac{1}{\sqrt{\zeta^2 + q^2}} e^{\mathrm{i}\arctan\left(\frac{q}{\zeta}\right)}, \tag{3.101}$$

---

[25] The exponential term is the (square-integrable) solution of the asymptotic Schrödinger equation. The polynomial prefactor can be interpreted as the leading term close to the origin in the Hydrogen-like orbitals (see sec. 3.7.2.2).

[26] The orthogonality for states with different L is ensured by the properties of the spherical harmonics which model the angular part of the wave functions and which are not included here.

it follows that

$$\int_0^\infty R^a \mathrm{e}^{-\zeta R} \sin(qR) \mathrm{d}R = \Gamma(a+1)\frac{\Im\left((\zeta+iq)^{a+1}\right)}{(\zeta^2+q^2)^{a+1}}$$

$$= \Gamma(a+1)\frac{\sin\left((a+1)\arctan\left(\frac{q}{\zeta}\right)\right)}{(\zeta^2+q^2)^{\frac{a+1}{2}}}$$

$$\int_0^\infty R^a \mathrm{e}^{-\zeta R} \cos(qR) \mathrm{d}R = \Gamma(a+1)\frac{\Re\left((\zeta+iq)^{a+1}\right)}{(\zeta^2+q^2)^{a+1}}$$

$$= \Gamma(a+1)\frac{\cos\left((a+1)\arctan\left(\frac{q}{\zeta}\right)\right)}{(\zeta^2+q^2)^{\frac{a+1}{2}}}. \tag{3.102}$$

In addition, the identities

$$\cos(\arctan(x)) = \frac{1}{\sqrt{\frac{\sin(\arctan(x))^2+\cos(\arctan(x))^2}{\cos(\arctan(x))^2}}} = \frac{1}{\sqrt{1+x^2}}$$

$$\sin(\arctan(x)) = \sqrt{1-\cos(\arctan(x))^2} = \frac{x}{\sqrt{1+x^2}}$$

$$\cos(x-\arctan(y)) = \cos(x)\cos(\arctan(y)) + \sin(x)\sin(\arctan(y))$$

$$= \frac{1}{\sqrt{1+y^2}}\left(\cos(x)+y\sin(x)\right)$$

$$\sin(x-\arctan(y)) = \sin(x)\cos(\arctan(y)) - \cos(x)\sin(\arctan(y))$$

$$= \frac{1}{\sqrt{1+y^2}}\left(-y\cos(x)+\sin(x)\right) \tag{3.103}$$

hold for all $x, y \geq 0$.

Thus, the weighted radial wave function overlap takes the form

$$\langle j_\lambda(q)\rangle = N_I N_F \sum_{k=0}^{\lfloor\frac{\lambda+1}{2}\rfloor}\left[\frac{A_\lambda^k \Gamma(n-\lambda+2k)\sin\left((n-\lambda+2k)\arctan\left(\frac{q}{\zeta}\right)\right)}{q^{\lambda-2k+1}(\zeta^2+q^2)^{\frac{n-\lambda+2k}{2}}} + \right.$$

$$\left. \frac{B_\lambda^k \Gamma(n-\lambda+2k-1)\cos\left((n-\lambda+2k-1)\arctan\left(\frac{q}{\zeta}\right)\right)}{q^{\lambda-2k+2}(\zeta^2+q^2)^{\frac{n-\lambda+2k-1}{2}}}\right]$$

$$= \frac{N_I N_F}{q(\zeta^2+q^2)^{\frac{n}{2}}}\sum_{k=0}^{\lfloor\frac{\lambda+1}{2}\rfloor}\left(\frac{\zeta^2+q^2}{q^2}\right)^{\frac{\lambda}{2}-k}.$$

$$\left[A_\lambda^k \Gamma(n-\lambda+2k)\sin\left((n-\lambda+2k)\arctan\left(\frac{q}{\zeta}\right)\right) + \right.$$

$$\left. \sqrt{\frac{\zeta^2+q^2}{q^2}}B_\lambda^k \Gamma(n-\lambda+2k-1)\cos\left((n-\lambda+2k-1)\arctan\left(\frac{q}{\zeta}\right)\right)\right]$$

$$
= \frac{N_I N_F}{q^2 (\zeta^2 + q^2)^{\frac{n}{2}}} \sum_{k=0}^{\lfloor \frac{\lambda+1}{2} \rfloor} \left(\frac{\zeta^2 + q^2}{q^2} \right)^{\frac{\lambda}{2}-k} \Gamma(n - \lambda + 2k - 1) \cdot
$$
$$
\left[q((n - \lambda + 2k - 1)A_\lambda^k + B_\lambda^k) \sin \left((n - \lambda + 2k) \arctan \left(\frac{q}{\zeta} \right) \right) + \right.
$$
$$
\left. \zeta B_\lambda^k \cos \left((n - \lambda + 2k) \arctan \left(\frac{q}{\zeta} \right) \right) \right]. \tag{3.104}
$$

This formula looks much more complicated than it is in actual calculations, in which λ is typically a small number, e.g., $\lambda \leq 2$. Therefore, the sum is reduced to only very few terms. In particular, for dipole-allowed transitions ($\lambda = 1$), the weighted radial wave function overlap is given by[27]

$$
\langle j_1(q) \rangle = \frac{N_I N_F \Gamma(n-1)}{q(\zeta^2 + q^2)^{\frac{n}{2}}} \left[\sqrt{\frac{\zeta^2 + q^2}{q^2}} \sin \left((n-1) \arctan \left(\frac{q}{\zeta} \right) \right) - \right.
$$
$$
\left. (n-1) \cos \left(n \arctan \left(\frac{q}{\zeta} \right) \right) \right]
$$
$$
= \frac{N_I N_F \Gamma(n-1)}{q^2 (\zeta^2 + q^2)^{\frac{n}{2}}} \left[\zeta \sin \left(n \arctan \left(\frac{q}{\zeta} \right) \right) - nq \cos \left(n \arctan \left(\frac{q}{\zeta} \right) \right) \right]. \tag{3.105}
$$

As stated before, this formula only uses elementary functions and simple operations and is therefore easy to implement in a simulation program. Unlike the small-angle approximation, it is valid for all q. One minor disadvantage is that, for $q \to 0$, some terms diverge. In total, the formula still gives the correct, finite results, of course. However, numerically, it is favorable to use the small angle approximation (see sec. 3.7.1) for $q \approx 0$. For STOs, eq. 3.92 gives

$$
\langle j_\lambda(q) \rangle \approx \frac{N_I N_F q^\lambda}{(2\lambda + 1)!!} \int_0^\infty R^{n+\lambda} e^{-\zeta R} \mathrm{d}R = \frac{N_I N_F \Gamma(n + \lambda + 1)}{(2\lambda + 1)!!} \cdot \frac{q^\lambda}{\zeta^{n+\lambda+1}}. \tag{3.106}
$$

3.7.2.2. Hydrogen-like orbitals

In the previous section, the weighted radial wave function overlap was calculated in the STO approximation, which works well for dipole-allowed transitions, but gives wrong results for some non-dipole transitions because of the lack of nodes. A remedy for this can be found in Hydrogen-like orbitals (HLOs). These are defined as [65]

$$
u_{I,F}(R) := N_{I,F} e^{-\zeta_{I,F} R / (n_{I,F} a_\mu)} \left(\frac{2\zeta_{I,F} R}{n_{I,F} a_\mu} \right)^{l_{I,F}} L_{n_{I,F} - l_{I,F} - 1}^{2l_{I,F}+1} \left(\frac{2\zeta_{I,F} R}{n_{I,F} a_\mu} \right), \tag{3.107}
$$

where $\zeta_{I,F}$ is the (possibly screened) nuclear charge, $n_{I,F}$ is the principal quantum number (contrary to the STOs, it has to be an integer for HLOs), $l_{I,F}$ is the orbital

---

[27]More tables for commonly used cases can be found in [78].

angular momentum quantum number, a_μ is the Bohr radius, $L_n^m(x)$ is the generalized Laguerre polynomial, and

$$N_{I,F} = \sqrt{\left(\frac{2\zeta_{I,F}}{n_{I,F}a_\mu}\right)^3 \frac{(n_{I,F} - l_{I,F} - 1)!}{2n_{I,F}(n_{I,F} + l_{I,F})!}} \tag{3.108}$$

is the normalization constant.

The generalized Laguerre polynomials can be written in the form [31]

$$L_n^\alpha(x) = \sum_{k=0}^{n}(-1)^k \binom{n + \alpha}{n - k}\frac{x^k}{k!}. \tag{3.109}$$

Thus, the product of radial wave functions and the Jacobian determinant R^2 takes the form

$$N_I N_F e^{-\zeta R}R^2 \left(\frac{2\zeta_I R}{n_I a_\mu}\right)^{l_I}\left(\frac{2\zeta_F R}{n_F a_\mu}\right)^{l_F} L_{n_I-l_I-1}^{2l_I+1}\left(\frac{2\zeta_I R}{n_I a_\mu}\right) L_{n_F-l_F-1}^{2l_F+1}\left(\frac{2\zeta_F R}{n_F a_\mu}\right)$$

$$= N_I N_F e^{-\zeta R}\left(\frac{2\zeta_I}{n_I a_\mu}\right)^{l_I}\left(\frac{2\zeta_F}{n_F a_\mu}\right)^{l_F} R^{l_I+l_F+2}\sum_{j=0}^{n_I+n_F-l_I-l_F-2}\sum_{k=0}^{j}\frac{(-1)^j}{k!(j-k)!}\cdot$$

$$\binom{n_I + l_I}{n_I - l_I - 1 - k}\left(\frac{2\zeta_I R}{n_I a_\mu}\right)^k\binom{n_F + l_F}{n_F - l_F - 1 - j + k}\left(\frac{2\zeta_F R}{n_F a_\mu}\right)^{j-k}$$

$$= N_I N_F e^{-\zeta R}\sum_{j=0}^{n_I+n_F-l_I-l_F-2} R^{l_I+l_F+j+2}\sum_{k=0}^{j}\left(\frac{2\zeta_I}{n_I a_\mu}\right)^{k+l_I}\left(\frac{2\zeta_F}{n_F a_\mu}\right)^{j-k+l_F}.$$

$$\frac{(-1)^j}{k!(j-k)!}\binom{n_I + l_I}{n_I - l_I - 1 - k}\binom{n_F + l_F}{n_F - l_F - 1 - j + k}$$

$$= N_I N_F e^{-\zeta R}\sum_{b=l_I+l_F+2}^{n_I+n_F} R^b\left[\sum_{k=0}^{b-l_I-l_F-2}\left(\frac{2\zeta_I}{n_I a_\mu}\right)^{k+l_I}\left(\frac{2\zeta_F}{n_F a_\mu}\right)^{b-k-l_I-2}.\right.$$

$$\left.\frac{(-1)^{b+l_I+l_F}}{k!(b-l_I-l_F-k-2)!}\binom{n_I + l_I}{n_I - l_I - 1 - k}\binom{n_F + l_F}{n_F + l_I + 1 - b + k}\right]$$

$$=: N_I N_F e^{-\zeta R}\sum_{b=l_I+l_F+2}^{n_I+n_F} p_b R^b, \tag{3.110}$$

where $\zeta := \zeta_I/(n_I a_\mu) + \zeta_F/(n_F a_\mu)$ was introduced and the product of the two sums was calculated using the Cauchy product formula. Consequently, the weighted radial wave function overlap reads

$$\langle j_\lambda(q)\rangle = N_I N_F \sum_{b=l_I+l_F+2}^{n_I+n_F} p_b \int_0^\infty R^b e^{-\zeta R}j_\lambda(qR)\mathrm{d}R. \tag{3.111}$$

These integrals are all of the same form as those in eq. 3.97. Consequently, the results can be used directly. In addition, the fact that a is an integer for HLOs allows using

the expansion[28]

$$
\begin{aligned}
(\zeta + iq)^{a+1} &= \zeta^{a+1} \left(1 + \frac{iq}{\zeta} \right)^{a+1} \\
&= \zeta^{a+1} \sum_{j=0}^{a+1} \binom{a+1}{j} \left(\frac{iq}{\zeta} \right)^j \\
&= \zeta^{a+1} \left[\sum_{j=0}^{\lfloor \frac{a+1}{2} \rfloor} \binom{a+1}{2j} (-1)^j \left(\frac{q}{\zeta} \right)^{2j} + i \sum_{j=0}^{\lfloor \frac{a+1}{2} \rfloor} \binom{a+1}{2j+1} (-1)^j \left(\frac{q}{\zeta} \right)^{2j+1} \right].
\end{aligned}
\tag{3.112}
$$

Thus, the weighted radial wave function overlap takes the form

$$
\begin{aligned}
\langle j_\lambda(q) \rangle &= N_I N_F \sum_{b=l_I+l_F+2}^{n_I+n_F} p_b \sum_{k=0}^{\lfloor \frac{\lambda+1}{2} \rfloor} \Bigg[A_\lambda^k \cdot \\
&\quad \frac{\Gamma(b-\lambda+2k)\zeta^{b-\lambda+2k} \sum_{j=0}^{\lfloor \frac{b-\lambda+2k}{2} \rfloor} \binom{b-\lambda+2k}{2j+1}(-1)^j \left(\frac{q}{\zeta} \right)^{2j+1}}{q^{\lambda-2k+1}(\zeta^2+q^2)^{b-\lambda+2k}} + B_\lambda^k \cdot \\
&\quad \frac{\Gamma(b-\lambda+2k-1)\zeta^{b-\lambda+2k-1} \sum_{j=0}^{\lfloor \frac{b-\lambda+2k-1}{2} \rfloor} \binom{b-\lambda+2k-1}{2j}(-1)^j \left(\frac{q}{\zeta} \right)^{2j}}{q^{\lambda-2k+2}(\zeta^2+q^2)^{b-\lambda+2k-1}} \Bigg] \\
&= N_I N_F \sum_{b=l_I+l_F+2}^{n_I+n_F} p_b \sum_{k=0}^{\lfloor \frac{\lambda+1}{2} \rfloor} \frac{\zeta^{b-\lambda+2k+1}\Gamma(b-\lambda+2k-1)}{q^{\lambda-2k+2}(\zeta^2+q^2)^{b-\lambda+2k}} \cdot \\
&\quad \Bigg[A_\lambda^k (b-\lambda+2k-1) \sum_{j=0}^{\lfloor \frac{b-\lambda+2k}{2} \rfloor} \binom{b-\lambda+2k}{2j+1}(-1)^j \left(\frac{q}{\zeta} \right)^{2j+2} + \\
&\quad \frac{\zeta^2+q^2}{\zeta^2} B_\lambda^k \sum_{j=0}^{\lfloor \frac{b-\lambda+2k-1}{2} \rfloor} \binom{b-\lambda+2k-1}{2j}(-1)^j \left(\frac{q}{\zeta} \right)^{2j} \Bigg].
\end{aligned}
\tag{3.113}
$$

Again, this formula looks rather complicated. However, it has the simple structure $P(q)/Q(q)$, where P and Q are polynomials. This avoids the (computationally time consuming) trigonometric functions in eq. 3.104 for STOs. In addition, it is more realistic as states with different n but the same L are orthogonal.

3.7.3. DFT radial wave functions

A third alternative is to use radial wave functions that were calculated ab-initio. In this work, the DFT code WIEN2K [49] together with the program TELNES.3 [70, 81]

---

[28]For odd a, this holds because $\binom{a+1}{a+2} = 0$.

was used for that purpose. The obvious advantages of this method are the improved accuracy over the simple models based on isolated atoms, as well as the proper inclusion of the energy dependence of the wave function (which is quite weak, though). The major disadvantage is that the wave functions — and hence the wave function overlap — cannot be expressed in a closed algebraic form as they are only known on a (logarithmic) grid.

To obtain the radial wave functions, I wrote a program that uses the TELNES.3 code to extract the (real) large and small components of the spinor $(\psi^{\text{large}}, \psi^{\text{small}})^{\top}$ and calculates the weighted radial wave function overlap by

$$\langle j_\lambda(q) \rangle = \int_0^{R_{\text{MT}}} (\psi_I^{\text{large}}(R)\psi_F^{\text{large}}(R) + \alpha_f^2 \psi_I^{\text{small}}(R)\psi_F^{\text{small}}(R))j_\lambda(qR)\mathrm{d}R. \qquad (3.114)$$

Here, α_f is the fine structure constant and R_{MT} is the muffin-tin radius defined in the WIEN2K structure file. The integration is performed numerically using a trapezoidal scheme and a linear interpolation of the wave functions between the sampling points.

3.7.4. Comparison of radial wave function models

Probably the most important observation can be made by looking at transitions of the form $(n_I, l_I = n_I - 1) \to (n_F = n_I + 1, l_F = n_F - 1)$. These are of special importance because for dipole-allowed transitions, both K edges ($s \to p$) and the (dominant) white-line contributions to $L_{2,3}$ edges ($p \to d$) are of this form. Under the circumstances mentioned above, the Laguerre polynomials take the form

$$L_{n_I - l_I - 1}^{2l_I + 1}(x) = L_0^{2n_I - 1}(x) = 1 \quad \text{and} \quad L_{n_F - l_F - 1}^{2l_F + 1}(x) = L_0^{2n_I + 1}(x) = 1. \qquad (3.115)$$

Hence, the wave functions contributing to these transitions are nodeless and, consequently, the results of HLOs and STOs coincide. So, for these transitions, the main difference between STOs and HLOs lies in the choice of parametrization (quotient of polynomials with integer n versus trigonometric functions with (possibly) non-integer n). Only for other transition channels (and, particularly, non-dipolar transitions), HLOs give a significant advantage.

Fig. 3.1 shows a comparison of small angle, STO, HLO, and WIEN2K calculations for several contributions to the $L_{2,3}$ edge in Si. Several points are worth mentioning:

- The small angle scattering approximation fails completely for $\lambda = 0$. For $\lambda > 0$, it works acceptably well only up to $q \approx 1.5\,\text{Å}^{-1}$.

- The STO model fails completely for $\lambda = 0$ even for small q. For $\lambda > 0$, it works better, but does not capture the zero-crossings. Both these effects are due to the lack of orthogonality of the initial and final states involved.

- The HLO model works best compared to the WIEN2K calculations as it properly captures the zero crossings. For large q, it also shows deviations from the WIEN2K data due to the absence of crystal field effects in the HLO model.
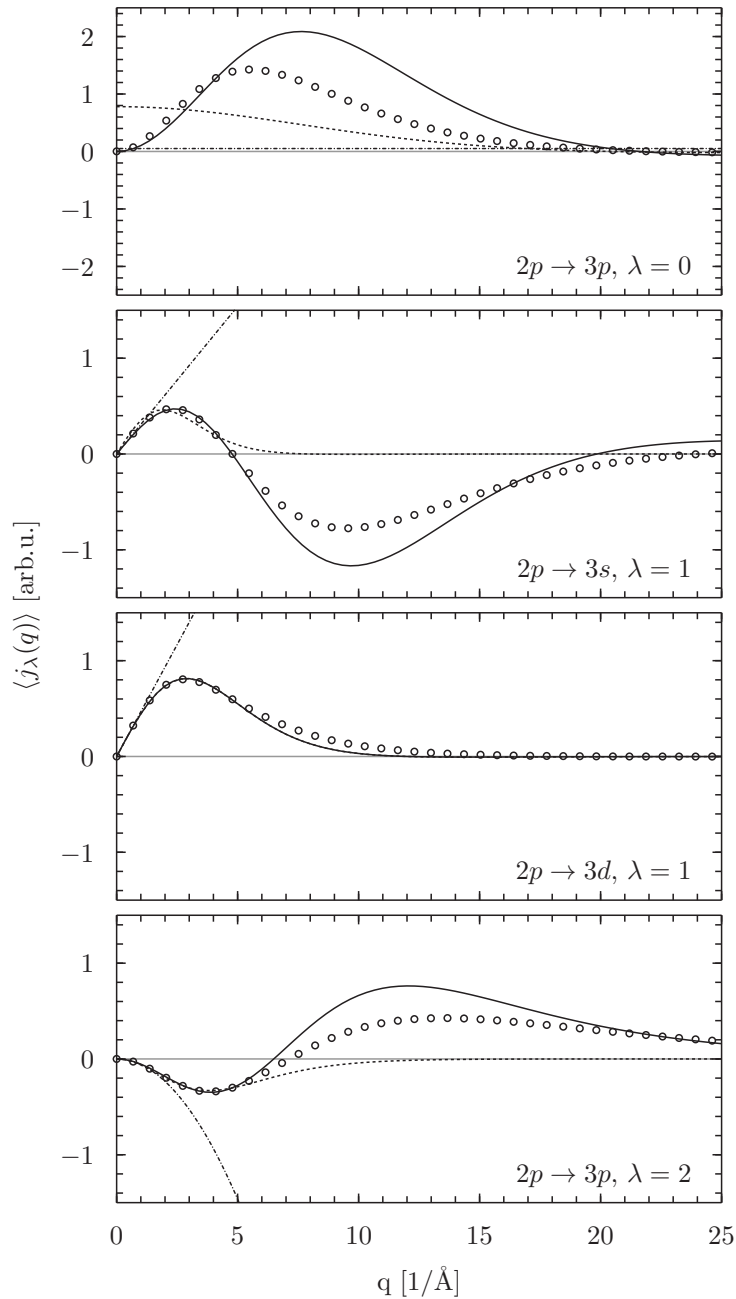
Figure 3.1.: Weighted radial wave function overlap $\langle j_\lambda(q)\rangle$ for the Si L$_{2,3}$ edge calculated using the small angle approximation (dash–dotted line), STOs (dashed line), HLOs (solid line), and WIEN2K (circles). The screening constants of STOs and HLOs were determined by fitting the curves to the WIEN2K data for $0 \leq q \leq 5.3\,\text{Å}^{-1}$. The amplitude of the small-angle scattering approximation was fitted to the WIEN2K data for $0 \leq q \leq 1\,\text{Å}^{-1}$. Note that for $2p \rightarrow 3d, \lambda = 1$, the STO and the HLO model give identical results.

3.8. Combining elastic and inelastic effects

<div align="right">This section is based on [23, 24, 58].</div>

In order to predict and simulate core-loss EELS measurements, both inelastic and elastic effects have to be considered. While the inelastic mean free path for core excitations is very large ($\gtrsim$ μm, owing to the small cross-section [4]), elastic scattering effects can be seen even for monolayered materials [82, 83]. Hence, one only has to deal with single core-excitation events[29], but multiple (in fact: countless) elastic scattering events. In particular, elastic scattering does not only affect the incident beam, but also the outgoing beams. While the combination of inelastic and elastic scattering opens the doors to many exciting methods such as ALCHEMI [17, 18, 84] and ELCE [19], elastic scattering is rather an artifact distorting the scattering profiles when one wants to study the real space wave functions of the target.

3.8.1. Bloch wave formalism

As described in sec. 2.3.1, one possibility for treating elastic scattering effects in a crystal is the Bloch wave formalism. Since the beam is described in a plane wave basis in this approach, it is sensible to use the scattering matrix (or MDFF) in momentum space representation. Owing to eq. 2.55, the possible (initial and final) probe states read

$$|\psi_{j,k_z}\rangle = \sum_{\boldsymbol{g}} C_{\boldsymbol{g}}^j \, |\boldsymbol{\chi}_j + \boldsymbol{g}, k_z + \gamma_j\rangle. \tag{3.116}$$

With the abbreviation $|\boldsymbol{k}_{\boldsymbol{g}}^j\rangle := |\boldsymbol{\chi}_j + \boldsymbol{g}, k_z + \gamma_j\rangle$, the incident density operator thus takes the form

$$\hat{\rho}_i = \sum_{jj'} \sum_{\boldsymbol{g}\boldsymbol{g}'} \varepsilon_j C_{\boldsymbol{g}}^j \left(\varepsilon_{j'} C_{\boldsymbol{g}'}^{j'} \right)^* |\boldsymbol{k}_{\boldsymbol{g}}^j\rangle \langle \boldsymbol{k}_{\boldsymbol{g}'}^{j'}|. \tag{3.117}$$

After the inelastic scattering event, the (reduced) density matrix (eq. 3.23) reads

$$\boldsymbol{\rho}(\boldsymbol{k}, \boldsymbol{k}') = \sum_{jj'} \sum_{\boldsymbol{g}\boldsymbol{g}'} \mathbb{S}(\boldsymbol{k}_{\boldsymbol{g}}^j - \boldsymbol{k}, \boldsymbol{k}_{\boldsymbol{g}'}^{j'} - \boldsymbol{k}') \varepsilon_j C_{\boldsymbol{g}}^j \left(\varepsilon_{j'} C_{\boldsymbol{g}'}^{j'} \right)^*. \tag{3.118}$$

Consequently, the probability that the density matrix collapses into a final state $|f\rangle$ (which is directly proportional to the EELS signal one can expect from such a process when measuring $|f\rangle$) is

$$P = \langle f|\hat{\rho}|f\rangle = \iint \mathrm{d}\boldsymbol{k}\mathrm{d}\boldsymbol{k}' \, \langle f|\boldsymbol{k}\rangle \, \langle \boldsymbol{k}'|f\rangle \, \boldsymbol{\rho}(\boldsymbol{k}, \boldsymbol{k}'). \tag{3.119}$$

---

[29]Not only is the probability for double excitation extremely small, it would also double the energy loss of the probe beam and hence would no longer be in the energy region under investigation.

For a final Bloch state

$$\langle \boldsymbol{k}'|f\rangle = \sum_l \sum_{\boldsymbol{h}} \varepsilon_l C_{\boldsymbol{h}}^l \delta(\boldsymbol{k}'_\perp - \boldsymbol{\chi}_l - \boldsymbol{h})\delta(k'_z - k_z + q_E - \gamma_l) =: \sum_l \sum_{\boldsymbol{h}} \varepsilon_l C_{\boldsymbol{h}}^l \delta(\boldsymbol{k}' - \boldsymbol{k}_{\boldsymbol{h}}^l),$$
(3.120)

this gives rise to

$$P = \sum_{jj'll'} \sum_{\boldsymbol{gg'hh'}} \varepsilon_j C_{\boldsymbol{g}}^j \left(\varepsilon_{j'} C_{\boldsymbol{g'}}^{j'}\right)^* \varepsilon_{l'} C_{\boldsymbol{h'}}^{l'} \left(\varepsilon_l C_{\boldsymbol{h}}^l\right)^* \mathbb{S}(\boldsymbol{k}_{\boldsymbol{g}}^j - \boldsymbol{k}_{\boldsymbol{h}}^l, \boldsymbol{k}_{\boldsymbol{g'}}^{j'} - \boldsymbol{k}_{\boldsymbol{h'}}^{l'}).$$
(3.121)

If one is interested, e.g., in the intensity measured in one particular point in the diffraction plane, the state $|f\rangle$ can be determined by employing the reciprocity theorem [85, 86]. With it, one can obtain the Bloch state corresponding to a plane wave coming from the detector and impinging on the bottom crystal surface (also known as "Kainuma's reciprocal wave" [87]). One complication here is that in practice, Bloch waves are typically calculated in such a way that the plane $z = 0$ is chosen at the crystal surface. In the present case, this means that the incident wave and the outgoing wave are calculated with respect to different points of origin and one of them (typically the outgoing wave) has to be translated accordingly. This gives rise to a phase factor of

$$e^{i(\boldsymbol{k}_{\boldsymbol{h}}^l - \boldsymbol{k}_{\boldsymbol{h'}}^{l'})\cdot\delta\boldsymbol{z}} = e^{i(\gamma_l - \gamma_{l'})\cdot t},$$
(3.122)

where $\delta\boldsymbol{z}$ is the offset between the two points of origin and t is the sample thickness.

In addition, if one wants to use the MDFF as described in sec. 3.4 (or one of the simplifications derived from it in secs. 3.5 and 3.7), one has take into account that the MDFF is defined with respect to a coordinate system centered on the scattering atom. This, too, has to be displaced — e.g., by virtue of the Fourier shift theorem (eq. C.5). For an atom at position $\boldsymbol{x}$, this results in a phase factor of

$$e^{i(\boldsymbol{k}_{\boldsymbol{h}}^l - \boldsymbol{k}_{\boldsymbol{h'}}^{l'})\cdot\boldsymbol{x}}.$$
(3.123)

Finally, if one has several scattering atoms, the contributions from all of them have to be summed over incoherently, ultimately leading to[30]

$$P = \sum_{\boldsymbol{x}} \sum_{jj'll'} \sum_{\boldsymbol{gg'hh'}} \varepsilon_j C_{\boldsymbol{g}}^j \left(\varepsilon_{j'} C_{\boldsymbol{g'}}^{j'}\right)^* \varepsilon_{l'} C_{\boldsymbol{h'}}^{l'} \left(\varepsilon_l C_{\boldsymbol{h}}^l\right)^* \cdot$$

$$e^{i(\gamma_l - \gamma_{l'})\cdot t} e^{i(\boldsymbol{k}_{\boldsymbol{h}}^l - \boldsymbol{k}_{\boldsymbol{h'}}^{l'})\cdot\boldsymbol{x}} \mathbb{S}(\boldsymbol{k}_{\boldsymbol{g}}^j - \boldsymbol{k}_{\boldsymbol{h}}^l, \boldsymbol{k}_{\boldsymbol{g'}}^{j'} - \boldsymbol{k}_{\boldsymbol{h'}}^{l'}).$$
(3.124)

This has numerical complexity $\mathcal{O}(tR_{\text{in}}^2 R_{\text{out}}^2 B_{\text{in}}^2 B_{\text{out}}^2)$, where R denotes the number of reciprocal vectors to include and B denotes the number of Bloch waves.[31] Note that the scattering kernel only needs to be evaluated at a few points in momentum space, which can be exploited to speed up calculations (e.g., by caching).

---

[30]In eq. 3.124, $\gamma_l, \gamma_{l'} \in \mathbb{R}$ was assumed, i.e., absorption effects were neglected.

[31]Note that $B \leq R$ always holds, as each Bloch wave can be written as linear combination of plane waves and both the set of plane waves and the set of Bloch waves are linearly independent. Hence, an upper boundary for the numerical complexity is $\mathcal{O}(tR_{\text{in}}^4 R_{\text{out}}^4)$.

3.8.2. Multislice formalism

Incorporating inelastic scattering in the multislice approach is even more straight forward. First, the initial wave function has to be propagated elastically through the crystal. In each layer, this gives rise to a pure state density matrix (see chap. 2 and sec. 2.1.1) that can easily be expressed in real space. Therefore, the reduced density matrix after inelastic scattering is simply given by multiplying the initial density matrix with the scattering kernel (see eq. 3.23)[32]. This density matrix has to be propagated elastically to the end of the crystal. The easiest way to do this is to exploit the unique properties of the evolution operator (see sec. 2.1.1), to express the density matrix in some basis, propagate the basis states independently, and reassemble the density matrix at the exit surface. Obviously, to keep the computational complexity small, it is beneficial to minimize the number of contributing states, which can be achieved, e.g., by diagonalizing the scattering kernel first as described in sec. 3.6).

Note that — as in the Bloch wave case — the scattering kernel has to be translated from the origin to the position of the scattering center. This can be done either directly or by multiplying the momentum space representation with an appropriate phase factor before applying the Fourier back transform (see eq. C.5). The former method is obviously faster, but the latter has the huge advantage that it can properly handle sub-pixel shifts.

Assuming that the time needed to multiply a density matrix with the scattering kernel is negligible compared to the multislice propagation (this usually is the case as the scattering kernels can be calculated beforehand) and that FFTs are used, the numerical complexity is $\mathcal{O}(t^2 B N \log N)$. Here, B denotes the number of non-negligible basis states needed to describe the scattering kernel and N is the number of pixels used. Compared to the Bloch wave formalism, the multislice method scales much better with respect to the number of "expansion states" (in the multislice case, this number corresponds to the number of pixels and the number of basis states; in the Bloch wave formalism, it corresponds to the number of reciprocal space vectors and the number of Bloch waves). However, the multislice approach scales worse with respect to thickness, rendering it fairly inefficient for thick crystals.

---

[32]In principle, the product in eq. 3.23 has to be performed in three dimensions. In the multislice approach, the state is by definition only expressed in two dimensions. However, as is apparent from eq. 3.24, the only z dependence of the scattering kernel in real space is a plane wave with momentum q_E. This simply describes the characteristic change of momentum in z direction and can most easily be taken into account by choosing a suitable basis for propagation after the inelastic scattering event.

4. Applications

The primary goal of this work is to study the real space wave functions of (thin crystalline) targets with EELS. According to the previous chapter, direct imaging of target states is not possible in the TEM. Instead, only *transitions* between an initial and a final state influence the probe beam. In particular, after triggering such a transition, the outgoing beams will have a characteristic energy and momentum distribution, which can be measured in practice.

Nevertheless, much can be learned about the real space wave functions of the target's final states, because the target's initial state can typically be assumed to be known (because of the tight binding of the initial state, it behaves atom-like in very good approximation). Thus, studying the transitions from a (known) initial state to a final state can actually be used to investigate said final state. In particular, the final states are sensitive to crystal field effects, dopant atoms, defects, etc. Moreover, they are decisive for transport properties such as conductivity, but also for optic properties. So, being able to measure and understand them is the key to understanding the whole system.

In this chapter, EELS measurements are presented from which conclusions about the real space wave functions of the target can be drawn. In addition, predictions are made about future experiments and applications.

In practice, the dominant contribution to an EEL spectrum comes from dipole-allowed transitions. Therefore, this chapter will use $\lambda = \lambda' = 1$ unless explicitly stated otherwise.

4.1. Radial wave functions

This section is based on [88, 89].

From eq. 3.41 as well as eqs. 3.51 and 3.50, it can be deduced that the target's radial wave functions only enter into the computation in the $\langle j_\lambda(q) \rangle$. In particular, for a single $L = L'$ and in the absence of spin-polarization, the MDFF (eq. 3.73) reads

$$S(\boldsymbol{q}, \boldsymbol{q}', E) = \langle j_1(q) \rangle^* \, \langle j_1(q') \rangle \sum_{\mu\mu'} Y_1^\mu(\boldsymbol{q}/q)^* \Xi_{\mu,\mu'} Y_1^{\mu'}(\boldsymbol{q}'/q'). \tag{4.1}$$

69

If elastic scattering can be neglected (i.e., for very thin specimens), an EELS measurement in momentum space corresponds to $\boldsymbol{q} = \boldsymbol{q}'$.[1] For such momentum transfers, the MDFF gives

$$S(\boldsymbol{q}, \boldsymbol{q}, E) = |\langle j_1(q)\rangle|^2 \sum_{\mu\mu'} Y_1^{\mu}(\boldsymbol{q}/q)^* \Xi_{\mu,\mu'} Y_1^{\mu'}(\boldsymbol{q}/q). \tag{4.2}$$

Assuming that the system's symmetry is high enough that $\boldsymbol{\Xi} = \Xi\mathbf{1}$ (see sec. 3.5), this simplifies further to

$$S(\boldsymbol{q}, \boldsymbol{q}, E) = |\langle j_1(q)\rangle|^2 \, \Xi. \tag{4.3}$$

Likewise, under these circumstances, the scattering matrix $\mathbb{S}$ and, with it, the DDSCS are proportional to

$$\frac{\partial^2 \sigma}{\partial E \partial \Omega} \propto \mathbb{S}(\boldsymbol{q}, \boldsymbol{q}, E) \propto \frac{|\langle j_1(q)\rangle|^2}{q^4} \tag{4.4}$$

(see sec. 3.3). Thus, the measurement of the DDSCS (which corresponds directly to the measurement of the intensity distribution in the diffraction pattern) allows drawing conclusions about the weighted radial wave function overlap $\langle j_1(q)\rangle$.

From the latter, in turn, information about the radial wave functions can be determined. In principle, the wave function overlap can be determined exactly by virtue of the closure relation (eq. C.18):

$$\langle j_1(q)\rangle = \int_0^\infty u_I(R) u_F(R) j_1(qR) R^2 \mathrm{d}R$$

$$\int_0^\infty \langle j_1(q)\rangle j_1(qx) q^2 \mathrm{d}q = \int_0^\infty \int_0^\infty u_I(R) u_F(R) j_1(qR) j_1(qx) R^2 \mathrm{d}R \, q^2 \mathrm{d}q$$

$$\int_0^\infty \langle j_1(q)\rangle j_1(qx) q^2 \mathrm{d}q = \frac{\pi}{2} \int_0^\infty u_I(R) u_F(R) \delta(R - x) \mathrm{d}R$$

$$\frac{2}{\pi} \int_0^\infty \langle j_1(q)\rangle j_1(qx) q^2 \mathrm{d}q = u_I(x) u_F(x). \tag{4.5}$$

This would require one to determine $\langle j_1(q)\rangle$ accurately over a large (ideally the whole) q range. This is challenging in practice for two reasons. First, the DDSCS falls off roughly like $1/q^2$, so the intensity falls off rapidly with increasing q. Consequently, the signal to noise ratio (SNR) quickly becomes very low. Secondly, for large q, the assumption that dipole-allowed transitions are dominant breaks down as well [69]. Therefore, $\langle j_1(q)\rangle$ and, e.g., $\langle j_2(q)\rangle$ can no longer be distinguished easily at large q.

Consequently, it is normally more favorable to use the inverse approach, i.e., verifying or disproving a model for the radial wave functions in the target by comparing measurements to simulated intensity profiles. This has the additional benefit that,

---

[1]The intensity in a point $\boldsymbol{k}$ in momentum space is given by the probability of finding the reduced density operator $\hat{\rho}$ in the state $|\boldsymbol{k}\rangle$, i.e., $\langle \boldsymbol{k}|\hat{\rho}|\boldsymbol{k}\rangle = \rho(\boldsymbol{k}, \boldsymbol{k})$. If the incident wave is a plane wave with wave vector $\boldsymbol{k}_i$ and elastic scattering can be neglected, the initial density matrix before the inelastic interaction reads $\rho_i(\boldsymbol{k}, \boldsymbol{k}') = \delta(\boldsymbol{k} - \boldsymbol{k}_i)\delta(\boldsymbol{k}' - \boldsymbol{k}_i)$ (see eq. 3.28). Hence, the reduced density matrix after the inelastic interaction (eq. 3.23) reads $\rho(\boldsymbol{k}, \boldsymbol{k}') = \mathbb{S}(\boldsymbol{k}_i - \boldsymbol{k}, \boldsymbol{k}_i - \boldsymbol{k}', E)$. Therefore, the intensity is given by $\mathbb{S}(\boldsymbol{k}_i - \boldsymbol{k}, \boldsymbol{k}_i - \boldsymbol{k}, E) = \mathbb{S}(\boldsymbol{q}, \boldsymbol{q}, E) \propto S(\boldsymbol{q}, \boldsymbol{q}, E)/(q^2 q'^2)$.

e.g., elastic scattering or non-dipole allowed transitions can be included easily in the simulation and hence the results become much more accurate.

There are two complementary methods to measure $\langle j_1(q) \rangle$ — or, relatedly, the DDSCS. The DDSCS — and with it the measured intensity — depends on the four-dimensional parameter space $(\boldsymbol{q}, E)$. This is reduced by the fact that $q_z = q_E$ is the (energy-dependent) characteristic momentum transfer. Thus, the parameter space is essentially three-dimensional. The common methods to measure the DDSCS are to either fix E and measure the momentum distribution in the diffraction plane, or to fix $\boldsymbol{q}$ and measure the EEL spectrum.[2] The former method is called energy-filtered selected area diffraction (EFSAD) (or energy-filtered diffraction (EFDIF) [93]), the latter angle resolved electron energy loss spectrometry (AREELS).

In angle resolved electron energy loss spectrometry (AREELS), the primary issue is the q resolution, which is limited by the aperture used. Since the aperture is finite, many different $\boldsymbol{q}$ contribute to the spectrum. This significantly hampers the simulation and interpretation of the results. In EFSAD, on the other hand, the energy resolution is low due to the use of a finite energy slit. This introduces complications in the background subtraction, which are manageable, however (see sec. D.2.2). Hence, the EFSAD method was used in this work.

4.1.1. EFSAD

EFSAD combines the two well-known techniques of selected area diffraction (SAD) and energy-filtered transmission electron microscopy (EFTEM). By recording an energy-filtered diffraction pattern, one can obtain very good q resolution (normally at the cost of energy resolution, defined by the spectrometer slit width). For the purpose of measuring $\langle j_1(q) \rangle$, this is ideal. Also, the whole q range is recorded simultaneously, i.e., under identical conditions — although several measurements at different energies are necessary in order to be able to subtract the pre-edge background. The experimental challenge in EFSAD lies mostly in the TEM alignment. In order to get accurate energy-filtered measurements, the spectrometer has to be tuned carefully under the conditions (i.e., magnification/camera length, illumination, etc.) under which it will be used afterwards for the measurements. To this end, a (more or less) even illumination of the spectrometer entrance aperture (SEA) is required. This, however, is very difficult to achieve in diffraction mode where the intensity is naturally peaked at a few very intense diffraction spots. Moreover, for an easy analysis of the measurements, it is necessary to reduce the intensities of all but the central spot as much as possible, as will be outlined below. This can be achieved, e.g., by using very thin samples and/or tilting into a systematic row condition where the $\boldsymbol{G}$ and $-\boldsymbol{G}$ spots are far away from the $\boldsymbol{0}$ spot.

---

[2]A third principal possibility would be to measure in (q_y, E) mode [90–92]. This, however, is limited in q resolution and q range (given by the SEA). Moreover, it requires the precise orientation of the specimen with respect to the dispersive axis of the spectrometer — a task far from trivial in practice — and a slit or wedge aperture which was not available for this work.

After a successful alignment, the measurements can be performed. Note that it is imperative to have diffraction spots that are as narrow as possible (at the energy-loss under investigation)[3] to be able to interpret the data easily. The background subtraction can be performed as usual (see sec. D.2.2).[4]

For the data analysis, one is interested in

$$I_{\text{norm}}(q_\perp) := \frac{I(\boldsymbol{q}_\perp)}{I(\boldsymbol{0})} = \left| \frac{\left\langle j_1 \left(\sqrt{q_\perp^2 + q_E^2} \right) \right\rangle}{\langle j_1 (q_E) \rangle} \right|^2 \cdot \frac{q_E^4}{(q_\perp^2 + q_E^2)^2}. \tag{4.6}$$

After some algebraic manipulation, this can be rearranged to read

$$\langle j_1 (q) \rangle \propto \frac{q^2}{q_E^2} \sqrt{I_{\text{norm}} \left(\sqrt{q^2 - q_E^2} \right)} \quad \forall q \geq q_E, \tag{4.7}$$

where $q^2 = q_\perp^2 + q_E^2$ was used.

In practice, a relevant issue here is the SNR. The signal and, hence, the SNR[5] are large for small q. However, small q are not particularly interesting, because there, the small-angle approximation holds. Hence, $\langle j_1(q) \rangle$ becomes independent of the radial shape of the orbitals. For the interesting case of larger q, on the other hand, the signal and SNR become low. Therefore, long exposure times are desirable. However, they are limited by the necessity of having a point of reference ($q_\perp = 0$) for normalization, which implies that the CCD must not be overexposed at the position of the strong central peak.

To further improve the SNR as well as extend the q range and/or the q resolution, several images (taken at different q ranges with different exposure times) could be spliced together. This procedure would lack a fixed reference point, however, and is therefore not pursued here. Instead, a different approach was used to improve the SNR. If no diffraction spot would exist, the diffraction pattern would ideally be rotationally symmetric (since it was assumed above that $I(\boldsymbol{q}_\perp)$ only depends on the magnitude but not on the direction of $\boldsymbol{q}_\perp$). Then, instead of taking just a single line of pixels, one can average the image over a circle with radius $q_\perp$. Obviously, this gives a dramatic improvement in the SNR. Unfortunately, the diffraction pattern is never truly rotationally symmetric. As a compromise, instead of averaging over a whole circle, the signal was averaged over the circular sector shown in fig. 4.1. This emphasizes the importance of having weak diffraction spots, which are the main cause for a breaking of the rotational symmetry and which get stronger with increasing sample thickness.

Another way of viewing the negative effect (relatively) thick specimens have is the following: as the specimen thickness increases, the $\boldsymbol{G}$ and -$\boldsymbol{G}$ diffraction spots increase

---

[3]This typically involves a parallel incident beam [94] and proper focusing of the energy-filtered diffraction pattern.

[4]Interestingly, the exponent r of the E^{-r} background model [4] was found to be independent of the position in momentum space.

[5]In the simple case that the shot-noise is dominant, the SNR is $\sqrt{N}$, where N is the signal.
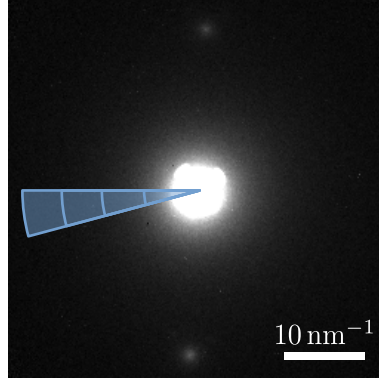
Figure 4.1.: Contrast-enhanced EFSAD pattern taken at $(80.0 \pm 2.5)\,\mathrm{eV}$ energy loss with an exposure of $40\,\mathrm{s}$ and an $\approx 10\,\mathrm{nm}$ thick Si sample in systematic row condition (including the $(1\,1\,1)$ spot). The blue area indicates the area used for the wedge-integration with an opening angle of $15°$. The wedge was not chosen ideally perpendicular to the systematic row due to aperture artifacts visible in the upper part of the rim of the central spot.

in intensity. At the same time, inelastic scattering from these spots increases as well and the signal becomes a sum over contributions from all non-negligible diffraction spots. For small $q_\perp \ll G$ (i.e., close to the $\mathbf{0}$ spot), the $1/(q_\perp^2 + q_E^2)$ term naturally dominates the $1/(q_\perp^2 + G^2 + q_E^2)$ term.[6] However, for larger $q_\perp$ (i.e., in the interesting case), the latter becomes comparable in intensity to the former. In that case, the intensity (normalized to $I(\mathbf{0})$) would be unnaturally high, owing to the additional signal coming from the other diffraction spots. Therefore, thin samples and large $\mathbf{G}$ vectors are of paramount importance for the direct interpretability of EFSAD.

A similar (detrimental) effect can originate from convergent illumination or an unfocused diffraction pattern. Both have the effect of broadening the EFSAD pattern, with the side-effect of redistributing intensity from high signal areas to low signal areas. The resulting profile (erroneously) looks as if q_E were larger than it actually is.[7]

Fig. 4.2 shows some experimental data for Si after wedge-integration (as described above), background subtraction (see sec. D.2.2), and rescaling according to eq. 4.7. It is clearly evident that $\langle j_1(q) \rangle$ starts to deviate from the dipole approximation at $q \approx 10\,\mathrm{nm}^{-1}$. It also shows the inherently low SNR at larger q, owing to the very low signal intensity in that region. Nevertheless, the deviations from the dipole-approximation are rather striking and in good agreement with $\langle j_1(q) \rangle$ as calculated in the STO approach (see sec. 3.7.2.1). This clearly shows that information about the radial wave functions in the target can indeed be obtained by the EFSAD method.

---

[6]In this simple estimation, $\mathbf{G} \perp \mathbf{q}_\perp$ was assumed.

[7]q_E is fixed by the energy loss. Hence, the accuracy of a measurement can easily be tested by comparing it to a Lorentzian with half-width at half-maximum (HWHM) of q_E.
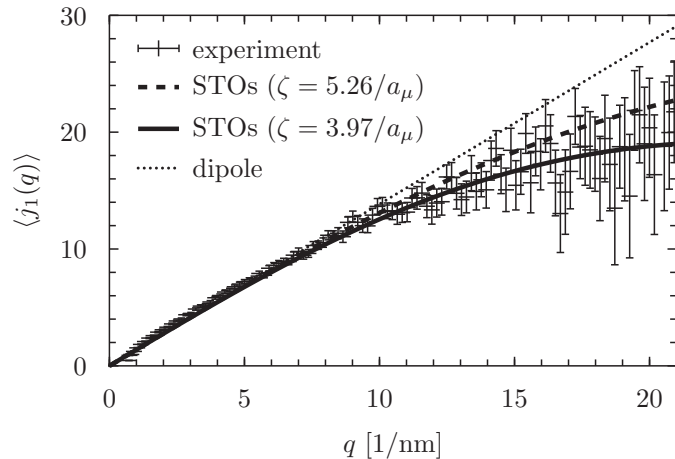
Figure 4.2.: $\langle j_1(q) \rangle$ as determined from eq. 4.7 for the same specimen as in fig. 4.1. The dipole and STO curves were calculated ab-initio for an energy loss of 99.2 eV (consistent with the Si L$_3$ edge). For the STOs, a $2p \to 3d$ transition was used. $\zeta = 5.26/a_\mu$ was taken from [79], $\zeta = 3.97/a_\mu$ was obtained from a least square fit in the range $10\,\mathrm{nm}^{-1} \leq q \leq 20\,\mathrm{nm}^{-1}$. For reference, the $\boldsymbol{G} = (1\,1\,1)$ diffraction spot in Si has $|\boldsymbol{G}| = 20.04\,\mathrm{nm}^{-1}$.

4.2. Azimuthal wave functions

This section is based on [58, 73].

Knowledge about the radial wave functions (see sec. 4.1) sheds light on several important physical properties such as bond lengths, relativistic corrections in close proximity to the nucleus, screening effects, or deviations from the isolated atom case. However, one crucial piece of information is missing: the direction. For example, it would be possible to determine that there are dopant atoms in the vicinity, but the radial wave function does not reveal *where* they are located.

The directional dependence of the MDFF is given by the spherical harmonics $Y_\lambda^\mu(\boldsymbol{q})$ in eq. 3.51, which are scaled by the XDOS. So it is actually the XDOS that determines the directional dependence of the MDFF. Thus, by measuring the angular dependence of the MDFF, one can learn something about the cross density of states and hence the angular states in the crystal.

Experimentally, the interesting aspects typically are the electronic properties in the vicinity of, e.g., boundary layers, defects, etc. Hence, a real space resolving approach such as EFTEM or energy-filtered scanning transmission electron microscopy (EFSTEM) should be employed. Practically, one obtains a background-subtracted atomic resolution image at the EELS edge in question (e.g., using the three window method (sec. D.2.2) in EFTEM, or the power law fit (sec. D.2.1) after acquiring a data cube). In this image, one would directly see the local angular dependence of the scattering kernel as will be shown below. From such an image, one could, for example, deduce bond directions.

For current microscopes, the spatial resolution is sufficient to record such high resolution energy-filtered images. Unfortunately, the intensity at the required energy slit widths is roughly an order of magnitude too low and hence the SNR is too bad to accomplish such measurements today. Nevertheless, it is an exciting application for future microscopes in the years to come.

4.2.1. The influence of XDOS symmetries

In this section, a qualitative motivation will be given how symmetries in the XDOS (which can be derived from symmetries of the crystal [70]) influence high-resolution EFTEM images. This does not replace a thorough group-theoretical study or numerical simulations (which will be given in sec. 4.2.2), but should give a general idea of the image formation in real space and provide some hints under which circumstances more detailed investigations are necessary (or superfluous).

In order to obtain the real space representation of the scattering kernel (eq. 3.24), one can start from its momentum space representation

$$\mathbb{S}(\boldsymbol{q}, \boldsymbol{q}', E) = \sum_{\lambda\mu\lambda'\mu'} C_{\lambda\mu\lambda'\mu'} f_\lambda^\mu(q, \theta_q) \mathrm{e}^{\mathrm{i}\mu\varphi_q} f_{\lambda'}^{\mu'}(q', \theta_q') \mathrm{e}^{-\mathrm{i}\mu'\varphi_q'}, \tag{4.8}$$

where $C_{\lambda\mu\lambda'\mu'}$ collects all terms independent of $\boldsymbol{q}$ and $\boldsymbol{q}'$ and the abbreviation

$$f_\lambda^\mu(q, \theta_q) := P_\lambda^\mu(\cos\theta_q)\frac{\langle j_\lambda(q)\rangle}{q^2} \tag{4.9}$$

was used. To obtain the real space representation, two Fourier transforms (one with respect to $\boldsymbol{q}$ and one with respect to $-\boldsymbol{q}'$) have to be performed. As the two work in the same manner, only the Fourier transform with respect to $\boldsymbol{q}$ will be discussed here.

The Fourier transform of the $\boldsymbol{q}$-dependent part reads

$$\frac{1}{(2\pi)^{3/2}} \int_0^\infty \int_0^\pi \int_0^{2\pi} f_\lambda^\mu(q, \theta_q) \mathrm{e}^{\mathrm{i}\mu\varphi_q} \mathrm{e}^{\mathrm{i}\boldsymbol{q}\cdot\boldsymbol{r}} r^2 \sin\theta_r \mathrm{d}\varphi_r \mathrm{d}\theta_r \mathrm{d}r. \tag{4.10}$$

By virtue of

$$\begin{aligned}
\boldsymbol{q} \cdot \boldsymbol{r} &= \begin{pmatrix} q\sin\theta_q\cos\varphi_q \\ q\sin\theta_q\sin\varphi_q \\ q\cos\theta_q \end{pmatrix} \cdot \begin{pmatrix} r\sin\theta_r\cos\varphi_r \\ r\sin\theta_r\sin\varphi_r \\ r\cos\theta_r \end{pmatrix} \\
&= qr\left[\sin\theta_q\sin\theta_r(\cos\varphi_q\cos\varphi_r + \sin\varphi_q\sin\varphi_r) + \cos\theta_q\cos\theta_r\right] \\
&= qr\left[\sin\theta_q\sin\theta_r\cos(\varphi_q - \varphi_r) + \cos\theta_q\cos\theta_r\right]
\end{aligned} \tag{4.11}$$

and eq. C.14, eq. 4.10 can be rewritten as[8]

$$\frac{1}{(2\pi)^{3/2}} \int_0^\infty \int_0^\pi \int_0^{2\pi} f_\lambda^\mu(q,\theta_q) e^{i\mu\varphi_q} e^{i\boldsymbol{q}\cdot\boldsymbol{r}} r^2 \sin\theta_r \mathrm{d}\varphi_r \mathrm{d}\theta_r \mathrm{d}r$$

$$= \frac{e^{i\mu\varphi_r}}{(2\pi)^{3/2}} \int_0^\infty \int_0^\pi \int_0^{2\pi} f_\lambda^\mu(q,\theta_q) e^{iqr\cos\theta_q\cos\theta_r} e^{i(\mu\varphi + qr\sin\theta_q\sin\theta_r\cos\varphi)} r^2 \sin\theta_r \mathrm{d}\varphi \mathrm{d}\theta_r \mathrm{d}r$$

$$= \frac{e^{i\mu\varphi_r} i^\mu}{\sqrt{2\pi}} \int_0^\infty \int_0^\pi f_\lambda^\mu(q,\theta_q) e^{iqr\cos\theta_q\cos\theta_r} J_\mu(qr\sin\theta_q\sin\theta_r) r^2 \sin\theta_r \mathrm{d}\theta_r \mathrm{d}r. \tag{4.12}$$

Thus, the scattering kernel in real space representation takes the form

$$\mathbb{S}(\boldsymbol{r},\boldsymbol{r}',E) = \frac{1}{2\pi} \sum_{\lambda\mu\lambda'\mu'} i^{\mu-\mu'} e^{i(\mu\varphi_r - \mu'\varphi_r')} C_{\lambda\mu\lambda'\mu'} \tilde{f}_\lambda^\mu(r,\theta_r) \tilde{f}_{\lambda'}^{\mu'}(r',\theta_r'), \tag{4.13}$$

where $\tilde{f}_\lambda^\mu(r,\theta_r)$ stands for the double-integral in eq. 4.12.

For the sake of simplicity, only a single, isolated atom will be considered in this section (in particular, no elastic scattering effects will be considered; a more complex example will be given in sec. 4.2.2). Under these conditions and assuming an incident plane wave, the exit density matrix is given directly by the scattering kernel $\mathbb{S}(\boldsymbol{r},\boldsymbol{r}')$. In this case, EFTEM images are described by the diagonal terms $\mathbb{S}(\boldsymbol{r},\boldsymbol{r},E)$.

If there are no $\mu \neq \mu'$ coupling terms, one has $C_{\lambda\mu\lambda'\mu'} = C_{\lambda\mu\lambda'}\delta_{\mu\mu'}$ and hence

$$\mathbb{S}(\boldsymbol{r},\boldsymbol{r}',E) = \frac{1}{2\pi} \sum_\mu e^{i\mu(\varphi_r - \varphi_r')} \sum_{\lambda\lambda'} C_{\lambda\mu\lambda'} \tilde{f}_\lambda^\mu(r,\theta_r) \tilde{f}_{\lambda'}^\mu(r',\theta_r'). \tag{4.14}$$

Thus, the intensity in an EFTEM image would be described by

$$\mathbb{S}(\boldsymbol{r},\boldsymbol{r},E) = \frac{1}{2\pi} \sum_\mu \sum_{\lambda\lambda'} C_{\lambda\mu\lambda'} \tilde{f}_\lambda^\mu(r,\theta_r) \tilde{f}_{\lambda'}^\mu(r,\theta_r). \tag{4.15}$$

This is independent of φ_r and, therefore, circularly symmetric.

If, on the other hand, there are $\mu \neq \mu'$ cross-terms, there will be contributions of the form

$$2\Re\left(e^{i(\mu-\mu')\varphi_r} \sum_{\lambda\lambda'} C_{\lambda\mu\lambda'\mu'} \tilde{f}_\lambda^\mu(r,\theta_r) \tilde{f}_{\lambda'}^{\mu'}(r,\theta_r) \right) \tag{4.16}$$

which, for $\mu \neq \mu'$, vary with φ_r.

In conclusion, the appearance of correlations between $\mu \neq \mu'$ in $C_{\lambda\mu\lambda'\mu'}$ is a prerequisite for the imaging of the (azimuthal) angular dependence of the inelastic excitation.

In the spin-unpolarized case, for example, $C_{\lambda\mu\lambda'\mu'}$ takes the form

$$C_{\lambda\mu\lambda'\mu'} = \sum_{LL'MM'm} \alpha_{\lambda LM}^{\lambda'L'M'} \begin{pmatrix} L & \lambda & l \\ -M & \mu & m \end{pmatrix} \begin{pmatrix} L' & \lambda' & l \\ -M' & \mu' & m \end{pmatrix}, \tag{4.17}$$

---

[8]Eq. 4.12 shows that an azimuthal phase of $e^{i\mu\varphi_q}$ becomes $e^{i\mu\varphi_r}$ in the Fourier transform (up to some φ_r-independent prefactors). Thus, the azimuthal dependencies in real space (in which HRTEM measurements are performed) and in real space (in which most calculations are performed) are identical.

where $\alpha_{\lambda L M}^{\lambda' L' M'}$ stands for all prefactors independent of μ, μ' (see also eqs. 3.52 and 3.55). In order for the Wigner 3j symbols not to vanish, the two equations

$$m + \mu = M \quad \text{and} \quad m + \mu' = M' \tag{4.18}$$

must hold, which implies

$$\mu - \mu' = M - M'. \tag{4.19}$$

If the scattering atom has, for example, an n-fold rotation symmetry around the z axis, this implies that $M - M'$ must be an integer multiple of n [70]. In the absence of $\lambda \neq \lambda'$ cross-terms (e.g., if only dipole-allowed transitions are considered), $|\mu - \mu'| \leq 2\lambda$ must hold, so the above-mentioned criterion can only be fulfilled for $\mu \neq \mu'$ if[9]

$$2\lambda \geq n. \tag{4.20}$$

This has far-reaching consequences. For the technically relevant case of dipole-allowed transitions with $\lambda = \lambda' = 1$, for example, it implies that 3-fold or higher fold rotational symmetries[10] directly imply that the scattering kernel — and hence the EFTEM image — will be rotationally symmetric. In particular, this holds for many atomic positions in cubic and hexagonal systems, especially when using low-indexed zone axes. For instance, in clean graphene, all atoms have a three-fold rotational symmetry. Consequently, no directional information is expected to be visible in EFTEM images of graphene for dipole-allowed transitions (although, e.g., quadrupole transitions could cause small deviations from the circular form in practice). However, the "ideal" case of a perfect lattice is usually of little interest anyway. In the interesting cases of, e.g., interfaces, defects, dopants, etc., the symmetry is broken by definition, and hence directional information could be determined from a high-resolution EFTEM image.

4.2.2. Case study: Rutile

As an example system, TiO_2 in Rutile position was chosen. It has a tetragonal unit cell (see fig. 4.3; detailed parameters can be found in tab. 4.1) with sufficiently low symmetry, in particular of the O atoms. O was chosen because it has a K-edge at relatively low energy-loss (532 eV [95]) and is also easy to simulate. Note that all O atoms (and also all Ti atoms) are symmetry-equivalent, i.e., they share the same properties, XDOS, etc., except for a rotation (and possibly inversion) of the local coordinate system (see fig. 4.3).

First, ab-initio calculations with WIEN2κ were performed. Fig. 4.4 shows the resulting O pDOS, both for the valence band (below the Fermi energy) and the conduction band (above the Fermi energy). For core-loss EELS, only the states above the Fermi energy, which are unoccupied, are of interest.

Although O has no contributing d orbitals, a splitting of the p orbitals into two "bands" (roughly 2 eV to 4 eV and 5 eV to 7 eV above the Fermi energy, labeled "t_{2g}"

---

[9]For $\mu = \mu'$, the criterion is always fulfilled trivially.

[10]Note that the symmetries in question are local point group symmetries of individual atoms, not symmetries of the unit cell as a whole.
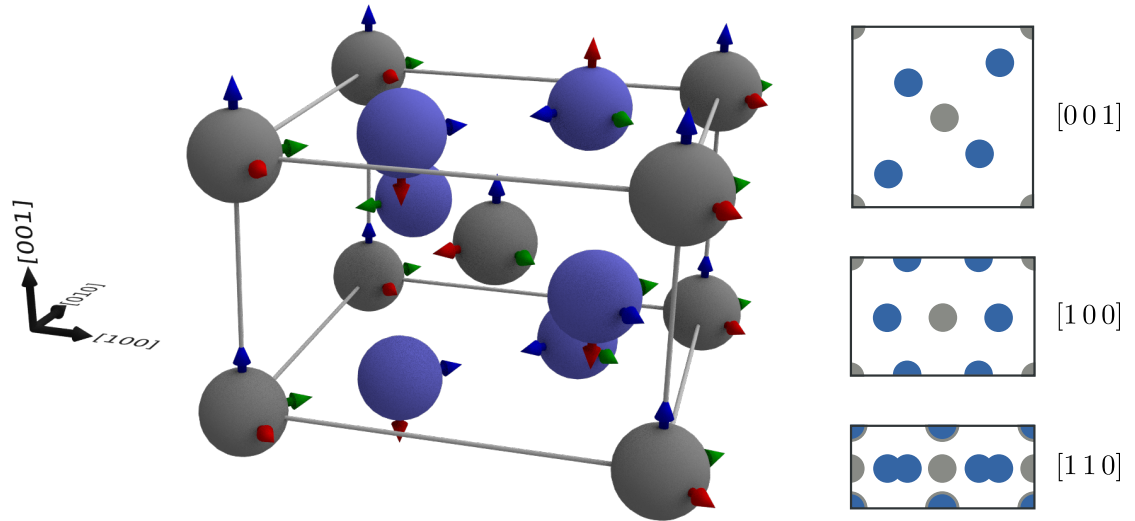
Figure 4.3.: Sketch of the Rutile unit cell (left) and projections along several low-indexed zone axes (right). The detailed parameters are given in tab. 4.1. Ti atoms in gray, O atoms in blue. The colored arrows indicate the local, symmetry adapted coordinate system as used by WIEN2K (red: x, green: y, blue: z).

	space group	a [nm]	c [nm]	Ti positions	O positions
TiO_2	136	0.45929	0.29591	$x = y = z = 0$	$x = y = 0.3056, z = 0$

Table 4.1.: Crystal structure parameters for Rutile [50].
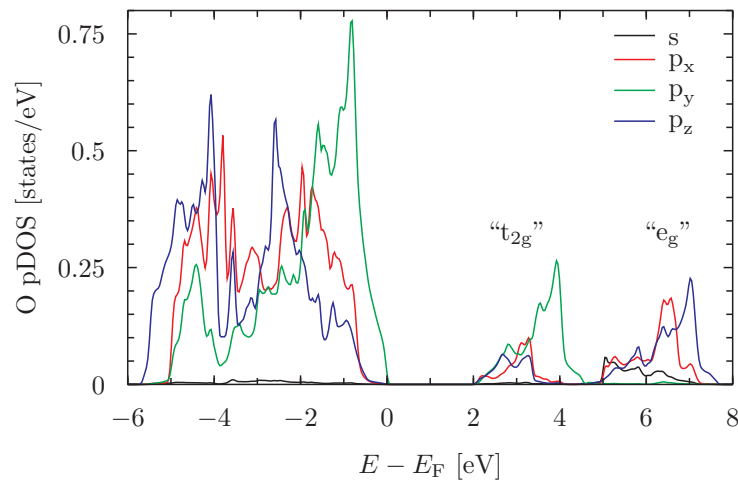

Figure 4.4.: Rutile O pDOS as calculated by WIEN2K. E_F denotes the Fermi energy, the labels "e_g" and "t_{2g}" are referenced in the text.
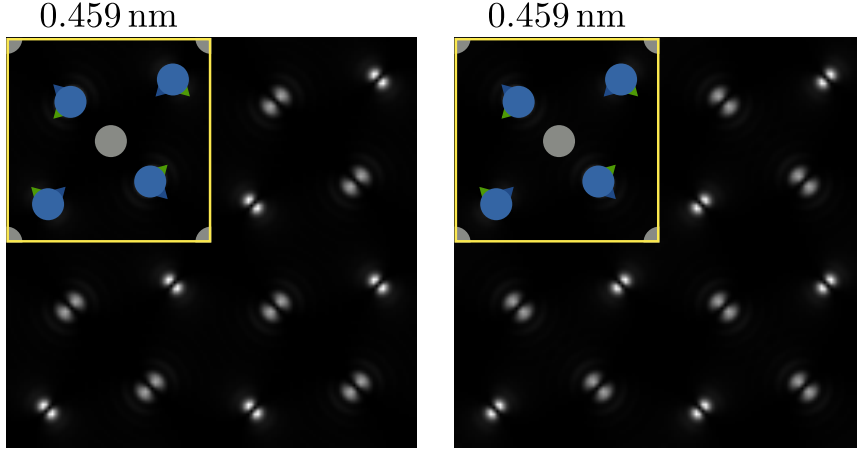
Figure 4.5.: Simulated EFTEM images for $E = E_\mathrm{F} + 4\,\mathrm{eV}$ (left) and $E = E_\mathrm{F} + 7\,\mathrm{eV}$ (right) using a 200 keV incident plane wave, a one unit cell thick crystal, and ideal imaging conditions. Superimposed are sketches of the (projected) unit cell with the colored arrows indicating the local coordinate systems (see fig. 4.3).

and "e_g", respectively) is visible, similar to the e_g / t_2g splitting of d orbitals. This is attributed to the e_g / t_2g splitting of the Ti orbitals due to the tetragonal distortion of the unit cell [96, 97]. Through the overlap (hybridization) between the O and Ti orbitals (which form bonding and anti-bonding states), this effect is carried over to the O states.

From fig. 4.4, it is also obvious that in the "t_2g" band, the p_y orbital is dominant, whereas in the "e_g" band, the p_x and p_z orbitals dominate. Hence, one can expect different directional dependencies in high resolution EFTEM images obtained from the "e_g" and "t_2g" bands, respectively.

Based on the TELNES.3 code [81], the XDOS and the radial wave functions were extracted from the WIEN2K calculations. Subsequently, the XDOS was transformed for each atom from the local coordinate systems (indicated by the arrows in fig. 4.4) to the global coordinate system defined by the imaging conditions [73]. In addition, the $\langle j_\lambda(q) \rangle$ were computed from the radial wave functions.

With all the data in place, the MDFF could be constructed and diagonalized according to the procedure outlined in sec. 3.6. Then, the scattering kernel $\mathbb{S}(\boldsymbol{q}, \boldsymbol{q}', E)$ was derived and from it, the real space scattering kernel $\mathbb{S}(\boldsymbol{r}, \boldsymbol{r}', E)$ was obtained by an FFT.

Once the scattering kernel was calculated, a multislice calculation was performed using the IXCHEL program (see sec. A.3). The setup was chosen to correspond to ideal EFTEM conditions, namely, an incident plane wave with an energy of 200 keV with the optic axis aligned to the [0 0 1] zone axis of the Rutile crystal. After the multislice calculation, the effect of the objective lens was included by a CTF approach [3].

Fig. 4.5 shows the resulting images for the ideal case of a one unit cell thick crystal and ideal imaging conditions ($C_s = 0, \beta = 90\,\mathrm{mrad}$, where C_s is the coefficient of

spherical aberration and β is the collection angle given by the objective aperture). It is clearly visible that at $E = E_{\mathrm{F}} + 4\,\mathrm{eV}$, the lobes are pointing in the direction of the green arrows (corresponding to the direction of the p_y orbitals), whereas at $E = E_{\mathrm{F}} + 7\,\mathrm{eV}$, the lobes are pointing in the direction of the blue arrows (corresponding to the direction of the p_z orbitals), in excellent agreement with the predictions.

It is also visible in fig. 4.5 that some of the lobes appear brighter and sharper than others. This is due to the fact that the scattering kernel is very localized in real space and, therefore, broad in momentum space. Hence, the outgoing density matrix is divergent, which has more effect for atoms located farther from the exit surface. Consequently, atoms located closer to the crystal's exit surface give sharper lobes.

Note that although fig. 4.5 shows lobe-like structures, one cannot, in general, infer the type of orbitals involved in the transition directly and solely from the image. What one can see in the images is in fact the transition probability, which is influenced by both the initial and the final state. Only if one of those is rotationally symmetric (i.e., an s state), information about the other orbital involved can be retrieved directly. This is the case, e.g., for K-edges (as in the present case), which are transitions from the 1s state to a p state.

Fig. 4.6 shows more realistic simulations for a $10\,\mathrm{nm}$ thick crystal including the effects of a non-ideal imaging system (the parameters, which are given in the figure caption, correspond to realistic values of modern C_s corrected microscopes). It is clearly visible that the general lobe-like shape is the same as in the ideal case. The images appear somewhat blurred, which is a result of the damping of higher frequencies by the non-ideal lens system. In addition, all lobes have the same intensity, as they represent an average over atoms in many different depths. On the other hand, new features begin to emerge between the lobes, an effect that is due to both the divergence of the outgoing density matrix and channeling effects on the Ti columns.

The bottom row of fig. 4.6 shows the situation assuming a $2\,\mathrm{eV}$ energy window. This was calculated by summing over different energies with a step size of $0.2\,\mathrm{eV}$. Again, the general shape remains the same, but additional contributions of other orbitals result in a slight wash-out effect.

4.3. Spin components and magnetism

This section is based on [23, 24, 98]

The radial and azimuthal components of a wave function fully determine its real space behavior, but they do not fully determine the electronic state. Therefor, additional information about the electron spin needs to be obtained. Although this is beyond the scope of this work, a short summary will be given below for the sake of completeness.

Since the spin–spin interaction between the probe beam and the target is negligible compared to the Coulomb interaction (owing to the high speed of the probe electron and the thinness of the sample), one cannot measure the spin state of the target directly in the TEM. Instead, one can measure the influence of the spin-splitting on
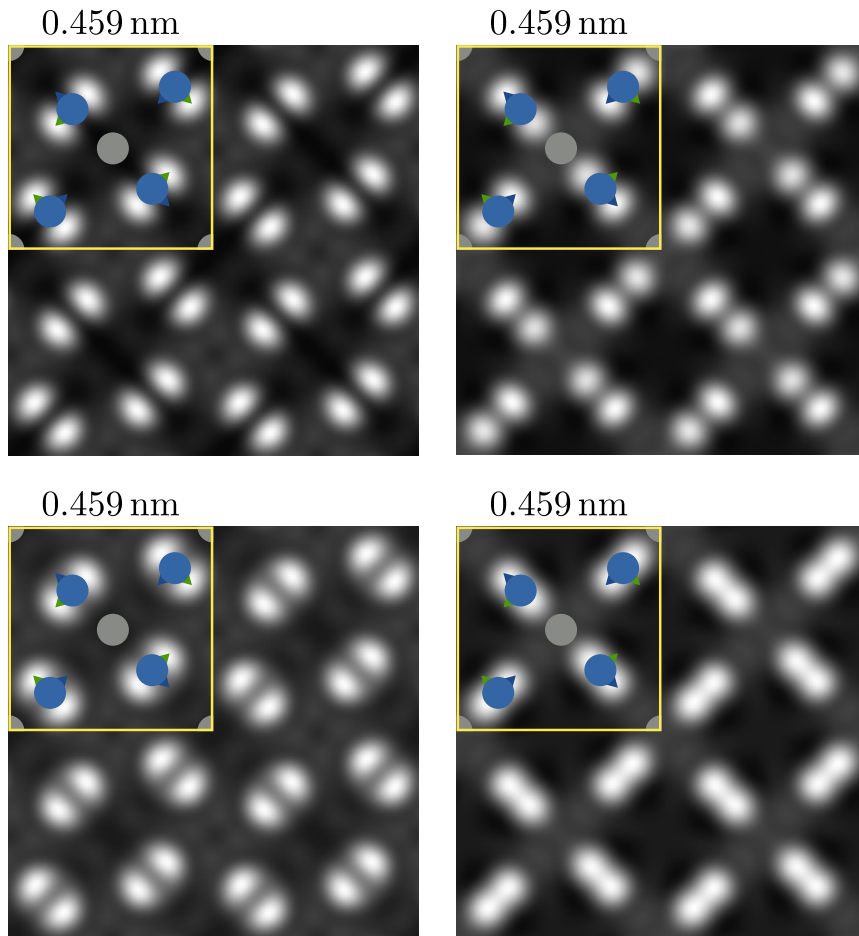
Figure 4.6.: Simulated EFTEM images using a 200 keV incident plane wave, a 10 nm thick crystal, and realistic imaging conditions ($C_s = 0$, $\beta = 20$ mrad). The top row shows images simulated for single energy losses (top left: $E = E_F + 4$ eV, top right: $E = E_F + 7$ eV, corresponding to fig. 4.5). The bottom row shows images integrated over the 2 eV energy windows $E_F + 2.6$ eV $\leq E \leq E_F + 4.6$ eV (bottom left, corresponding to the "t_{2g}" band) and $E_F + 5.6$ eV $\leq E \leq E_F + 7.6$ eV (bottom right, corresponding to the "e_g" band). Superimposed are sketches of the (projected) unit cell with the colored arrows indicating the local coordinate systems (see fig. 4.3).
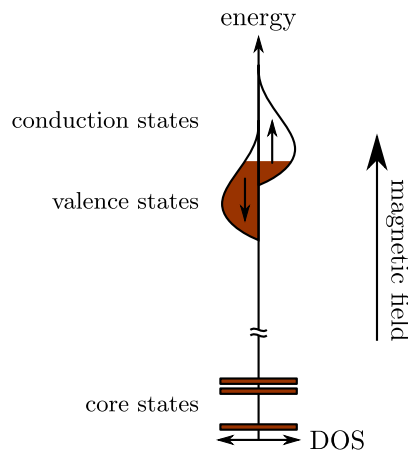
Figure 4.7.: Schematic drawing of a spin-split DOS in a magnetic field (which is assumed to act as quantization axis). The arrows indicate spin directions.

the DOS in inelastic scattering.

Fig. 4.7 shows a schematic diagram of a spin-split DOS.[11] It visualizes the fact that states with one spin are more favorable than states with the opposite spin. As a result, there is an asymmetry of the unoccupied states $|F\rangle$, which are one of the decisive factors in inelastic scattering and hence EELS (see sec. 3.1).

Due to spin-orbit coupling, this asymmetry in spin translates directly to an asymmetry of the OAM [47, 99]. As discussed in sec. 3.6.1.2, the MDFF is diagonal in μ, μ'. Furthermore, sec. 3.5.2 and tab. 3.1 show that different values of μ have different weights. This means that it is more likely to excite, say, a transition with an azimuthal characteristic of $e^{i\varphi}$ than it is to excite one with $e^{-i\varphi}$. Such a disproportional excitation gives rise to vortex waves as described in sec. 2.2.

4.3.1. Traditional EMCD

In order to measure this vorticity, one needs to study the azimuthal phase or — equivalently — the OAM of the outgoing beam. Traditionally, this is achieved by using the EMCD method [68, 100], which is the TEM analogue to X-ray magnetic circular dichroism (XMCD) in the synchrotron. In the original variant of EMCD, an incident plane wave is used and the phase of the outgoing beam is analyzed using an interferometric setup. In particular, the crystalline specimen itself acts as beam splitter due to elastic scattering on the lattice planes. At the same time, different diffracted beams are influenced by different potentials (U_g in eq. 2.53) and thus accumulate a phase difference which is well understood (see sec. 2.3.1) and can be calculated. Finally, one records spectra in the diffraction plane. Around each diffraction spot, there is

---

[11]It is assumed throughout this section that the spin quantization axis coincides with the optical axis and that the sample is fully spin-polarized (which corresponds roughly to a saturated magnetization). This is a reasonable approximation for most common magnetic materials in the $\approx 2\,\mathrm{T}$ magnetic field of the objective lens of a TEM [71].
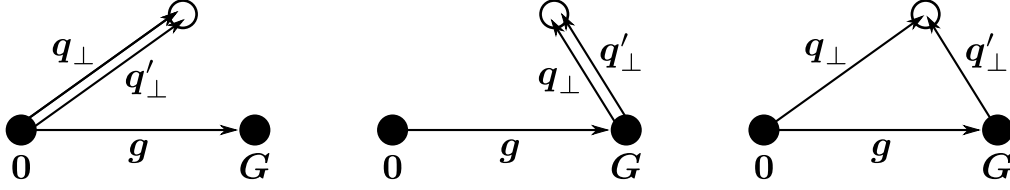
Figure 4.8.: Sketches of the scattering geometry for an EMCD experiment in two-beam condition. Each diagram depicts a single contribution to the total signal. The first two are direct terms, whereas the third is a cross-term. Diffraction spots are depicted as black discs and the detector is depicted as circle.

a (roughly) Lorentzian distribution of the inelastic scattering signal. In between the diffraction spots — where the scattering distributions overlap — interference occurs.

Typically, the crystal is tilted into a systematic row condition (such as a three beam case or a two beam case). Then, the intensity is essentially given by eq. 3.124. Fig. 4.8 shows a sketch of the two beam case situation with the detector positioned arbitrarily in the interference regime and all possible combinations of momentum transfers $\boldsymbol{q}_\perp := (\boldsymbol{k}_{\boldsymbol{g}}^j - \boldsymbol{k}_{\boldsymbol{h}}^l)_\perp$. Two distinct contributions can be seen: the direct terms with $\boldsymbol{q} = \boldsymbol{q}'$ and the cross-term with $\boldsymbol{q} \neq \boldsymbol{q}'$.[12]

Using eq. 3.72 for the MDFF and eq. 3.24 for the scattering kernel, some physical meaning can be assigned to the different contributions. For the direct terms, $\boldsymbol{q} \times \boldsymbol{q}' = 0$, so they manifest themselves as "nonmagnetic background" in the signal. At the same time, one wants to maximize the magnetic contributions coming from the cross-terms, i.e., one wants to maximize $(\boldsymbol{q} \times \boldsymbol{q}')/(q^2 q'^2)$.[13] This is typically done by choosing $\boldsymbol{q}_\perp \perp \boldsymbol{q}'_\perp$ and $q_\perp = q'_\perp$, i.e., the detector is positioned on the Thales circle through the two diffraction spots and on the symmetry axis [68, 98].[14]

In order to separate the magnetic and nonmagnetic contributions, at least two measurements must be conducted. To this end, it is advantageous to choose the second detector position such that the non-magnetic contributions are the same (i.e., the distance between the diffraction spots and the detector remains the same), but the magnetic contributions change sign. This can be modeled as $(\boldsymbol{q}_\perp, \boldsymbol{q}'_\perp) \to (-\boldsymbol{q}'_\perp, -\boldsymbol{q}_\perp)$, which (approximately) gives rise to a sign change in the cross terms as intended. Thus, measuring at the two positions shown in fig. 4.9 and subtracting the two signals removes the non-magnetic contributions and leaves the magnetic ones. This is a direct measure of, e.g., spin-polarization and magnetic moments [98, 102, 103].[15]

---

[12]Additional terms with the same form, but with $\boldsymbol{q}_\perp$ and $\boldsymbol{q}'_\perp$ reversed, have been omitted for the sake of clarity.

[13]This assumes the small angle approximation (sec. 3.7.1) to hold, i.e., $j_1(q) \propto q$, which is adequate for the scattering angles considered.

[14]While this does neither completely maximize the magnetic contributions nor completely minimize the nonmagnetic contributions due to the characteristic momentum transfer q_E and (to a lesser extent) the Anpassungsfehler γ, it is still a viable option for EMCD experiments and very easy to realize in practice. In fact, since the interference effects are present (almost) everywhere in the diffraction plane, many other detector positions are acceptable in practice [101].

[15]Note, though, that this signal is also very sensitive to sample thickness, tilt, etc. [23].
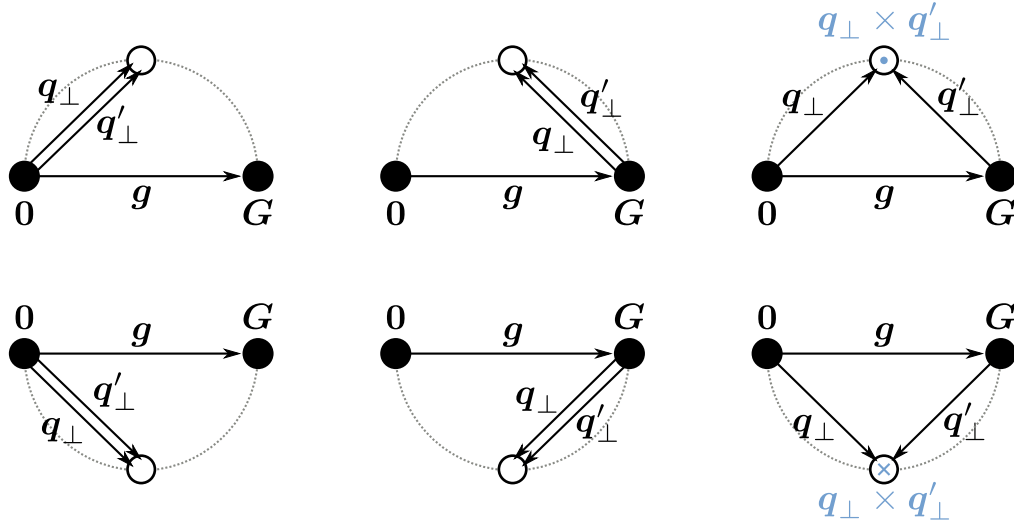
Figure 4.9.: Sketches of the contributions for the two EMCD detector positions for a two-beam condition. Each diagram depicts a single contribution to the total signal. The first two columns are direct terms, whereas the third is a cross-term. The top and the bottom row show the situations for the two EMCD detector positions on the Thales circle (dashed gray). Diffraction spots are depicted as black discs and the detector is depicted as circle.

4.3.2. Future applications of EMCD

With the increasing popularity of electron vortices, other possibilities to measure a magnetic signal were begun to be explored as well. The most direct approach is using a fork mask aperture (see sec. 2.2.4) in the objective plane as an OAM analyzer. This was first reported by Verbeeck et al. [38]. The theoretical description of this approach is numerically challenging due to the large defocus used, however, and not completely understood so far.

Another new concept is looking at the experiment the other way round. If one uses an incident beam carrying OAM (such as a vortex beam, see sec. 2.2), a transfer of OAM to the target would change the vorticity of the beam. This would change its radial profile as well, which — in principle — could be measured easily. In practice, this approach is not without challenges, though. First of all, the detector must be aligned with the beam precisely, which is a technical problem when displacing the beam to measure different parts of the sample. Additionally, elastic scattering effects can significantly change a vortex beam (see sec. 2.3.2) so that the wave incident on the scattering center is far from the ideal vortex shape. This, in turn, gives rise to severe complications. In particular, Schattschneider et al. [104] recently concluded that the EMCD signal will drop below the detection limit for reasonable aperture sizes and an illuminated area larger than $\approx 3\,\mathrm{nm}^2$.

Another approach for high-resolution EMCD is the use of off-axis half-plane objective apertures [72, 77]. In the objective plane, the magnetic contribution to a diffraction

spot has a vortex-like azimuthal phase structure. By blocking one half of it, this is converted to a quasi-linear phase gradient, which gives rise to a small shift of intensity in the (high-resolution) real space image. It must be noted, however, that this puts rather extreme conditions on the sample and the instrument, particularly in terms of stability [105]. Nevertheless, a successful experiment was reported recently by Schattschneider et al. [91].

5. Conclusion

Dass ich erkenne, was die Welt
Im Innersten zusammenhält.
"So that I may perceive whatever holds
The world together in its inmost
folds."

(Johann Wolfgang von Goethe)

For millennia, people have been wondering and speculating about the nature of the matter that surrounds us. Today, it is universally acknowledged that it is made of atoms, which in turn are composed of a nucleus surrounded by electrons. It is these electrons that govern almost all the properties that we can see in every day life, ranging from the hardness of materials over electrical and optical properties to the cohesion between different materials. Thus, electrons are the decisive factor in material science. However, except for calculations, little is known about the electrons' real space wave functions, as they are not accessible in experiments directly.

In this work, the possibility to investigate the real space wave functions of electrons in a target using TEM and EELS was studied. It was discussed that both elastic and inelastic scattering effects of the probe beam are vital for an accurate description of experiments, and a complete theory based on first principles and the density matrix formalism was presented (see chaps. 2 and 3). In addition, several approximations — together with their validity — were discussed, which facilitate computations in many cases. Moreover, in sec. 3.6, it was shown how the central quantity in inelastic electron scattering — the MDFF — can be diagonalized and how this enables the simple and efficient simulation of high resolution energy filtered TEM images with unprecedented accuracy.

In chap. 4, several applications were presented. First, a method for measuring radial wave functions was described and applied to bulk silicon, for which experiments and predictions are in excellent agreement. Subsequently, predictions were made about the possibility to directly measure the azimuthal dependence of wave functions. It was found that this is possible if the symmetry of the system under investigation is low enough, or if sufficiently high multipole orders are used. While the experimental proof of the presented predictions is not quite possible with current instruments, future generations of TEMs should be powerful enough to visualize the azimuthal dependence of wave functions.

It will probably require a few years before such experiments can be performed routinely and interesting systems such as defects, dopants, or interfaces can be tackled efficiently. However, the theoretical foundations are laid and the first experimental steps done, as presented in this thesis, promising a bright future for electron microscopy.

87

A. Programs

Throughout this work, simulations are necessary to predict experiments, compare them to the theory, and gain a better understanding of inelastic scattering, elastic scattering effects, and the interplay between the two. To this end, several simulation software packages were used that are briefly described here.

A.1. WIEN2k

This section is based on [49, 106].

WIEN2K is a state of the art DFT simulation package based on the seminal articles of Hohenberg and Kohn [107] and Kohn and Sham [108]. It works in a reciprocal space representation and describes the electronic states using the augmented plane waves with local orbitals (APW+lo) method [109] and the full (i.e. untruncated) Coulomb potential of the surrounding charges. For the exchange–correlation term in the Hamiltonian (i.e., the term describing all contributions other than the kinetic energy and the single-particle Coulomb energy), several approximations can be used, including the generalized gradient approximation (GGA), local density approximation with (Hubbard) U (LDA+U), or the modified Becke-Johnson (mBJ) potential [110].

In a nutshell, WIEN2K divides the unit cell of a crystal into spherical, non-overlapping regions (the so-called "muffin-tin spheres") surrounding the atoms and an interstitial region. Inside the spheres, the wave functions are expanded into spherical harmonics, whereas in the interstitial region, they are expanded into plane waves. At the boundary of the spheres, those two descriptions must match, of course. Then, an initial electron density is constructed based on isolated atoms. From this density, a Hamiltonian is calculated and the (relativistic) eigenvalue problem is solved. The resulting eigenfunctions give rise to a density, which can again serve as the starting point for constructing a Hamiltonian. This procedure is repeated until self-consistency is reached.

WIEN2K is not the main topic of this work. Guidelines how to apply it to different materials fill hundreds of reports, articles, and text books and will not be repeated here. In this work, WIEN2K is used only as a tool for calculating material properties such as the target's radial wave functions or the XDOS. To this end, a program was written based on the TELNES.3 code [81] to extract those quantities in a manner suitable for inclusion in BW and IXCHEL (see secs. A.2 and A.3).

A.2. bw

The BW program was written as part of this thesis in order to study the interplay between elastic and inelastic scattering (see, e.g., sec. 3.8). It is designed primarily for predicting intensities in the diffraction plane, which is important for applications like measuring the radial wave function (sec. 4.1) or EMCD (sec. 4.3). For the simulation, the Bloch waves for both the incident and the outgoing waves are calculated. For the incident wave, plane wave illumination is assumed (which corresponds to a point-like cross-over in the focal point of the condenser lens). For the outgoing wave, a reciprocal Kainuma wave is assumed [87] that — similar to the incident wave — originates from a single point in the diffraction plane (the position of the detector).[1]

The advantage of using a Bloch wave approach is that, once the secular equation (eq. 2.53) is solved, the probe wave is known immediately everywhere inside the sample, independent of the sample thickness. This is particularly useful when one wants to predict the optimal sample thickness for particular measurements.

BW is written in an object-oriented way in C++. It uses an extensible markup language (XML) file as input which is easy to create and edit, either computationally or by hand. Aside from the Bloch wave functions in the crystal, it can also output inelastic scattering intensities as a function of the position of the scattering center in the crystal or as a function of sample thickness. These intensities can also be calculated as a function of energy loss (corresponding to an EEL spectrum), provided the energy dependence of the wave functions and the XDOS is known.

A.3. ixchel

IXCHEL is based on the multislice code for elastic electron scattering by Kirkland [37]. The inelastic scattering was implemented as outlined in sec. 3.8.2. The initial approach followed the procedure of Verbeeck et al. [51] by implementing XDOS-agnostic scattering kernels [111]. Since this proved insufficient for simulating the directional dependence (see sec. 4.2), it was later adapted to calculate the scattering kernel based on WIEN2k using the diagonalization method described in sec. 3.6 [73].

---

[1] In the density matrix formalism, the probe beam is in a mixed state after an inelastic interaction, of course. It is this mixed state that actually needs to be propagated through the crystal to the detector. However, measuring with a point-like detector in the diffraction plane ultimately projects this mixed state density matrix onto a single plane wave state. This is exactly the Kainuma wave. It's contribution can be followed backwards through all elastic scattering processes to the point of the inelastic scattering. Owing to the hermiticity of the evolution operator (see sec. 2.1), the elastic forward and backward propagation of a single plane wave are equivalent. Thus, the probability of finding the mixed state density matrix in the state measurable by the detector is identical to the probability of the inelastic scattering event transforming the incident wave into the (back-propagated) Kainuma wave.

For the simulation, the projected scattering potential is calculated for each slice from atomic scattering factors in the first step. Then, an (arbitrarily choosable) wave function is sent into and propagated through the crystal. For each layer, the components of the density matrix after inelastic scattering are computed and propagated through the rest of the crystal to the exit surface. Finally, an image can be assembled by employing a CTF approach.

B. Normalization

In quantum mechanics, the absolute value squared of a wave function is conventionally interpreted as a probability density, e.g.,

$$P(\boldsymbol{x}) = |\psi(\boldsymbol{x})|^2 = \langle \psi | \boldsymbol{x} \rangle \langle \boldsymbol{x} | \psi \rangle \tag{B.1}$$

is the probability of finding a particle in an infinitesimal space element surrounding the point $\boldsymbol{x}$. Obviously, the probability of finding a given particle anywhere is

$$\int P(\boldsymbol{x}) \mathrm{d}\boldsymbol{x} = \int |\psi(\boldsymbol{x})|^2 \mathrm{d}\boldsymbol{x} = 1. \tag{B.2}$$

This can also be interpreted using expectation values. The expectation value of an operator $\hat{A}$, given a state $|\psi\rangle$, is defined as

$$\langle \hat{A} \rangle := \langle \psi | \hat{A} | \psi \rangle. \tag{B.3}$$

Using $\hat{1} = \int |\boldsymbol{x}\rangle \langle \boldsymbol{x}| \, \mathrm{d}\boldsymbol{x}$ results in

$$\int P(\boldsymbol{x}) \mathrm{d}\boldsymbol{x} = \int \langle \psi | \boldsymbol{x} \rangle \langle \boldsymbol{x} | \psi \rangle \, \mathrm{d}\boldsymbol{x} = \langle \psi | \hat{1} | \psi \rangle = 1, \tag{B.4}$$

as the unit operator has an expectation value of 1.

This approach to the normalization of wave functions works well as long as the wave function is L²-integrable, i.e., as long as $\int |\psi(\boldsymbol{x})|^2 \mathrm{d}\boldsymbol{x}$ is finite. This is the case, e.g., for all states with finite support. For a large class of states, however, it is not applicable. These states are called continuum states. Most notable representatives are plane waves, for which $|\psi(\boldsymbol{x})|^2 = \mathrm{const.}$ and hence the integral does not converge.

However, it must be emphasized that, by definition, plane waves have infinite spatial extent, zero energy width, and hence can not be created in finite time. They are merely idealizations of wave packets with finite spatial extent and finite energy width which are emitted in a finite time. As such, plane waves do not fall into the L² Hilbert space normally used.

In analogy to the orthonormalization of square integrable states using the Kronecker delta, i.e.,

$$\langle \phi | \psi \rangle = \delta_{\phi\psi}, \tag{B.5}$$

plane waves can be orthonormalized in a distributional sense with the Dirac delta using the continuum orthonormalization, i.e.,

$$\langle \boldsymbol{k}' | \boldsymbol{k} \rangle = \delta(\boldsymbol{k} - \boldsymbol{k}'). \tag{B.6}$$

This ensures that different plane waves are orthogonal. However, single plane waves are not normalizable in the conventional sense, i.e., $\langle \boldsymbol{k} | \boldsymbol{k} \rangle$ is not a real number. For wave packets

$$| \psi \rangle = \int c(\boldsymbol{k}) | \boldsymbol{k} \rangle \, \mathrm{d}\boldsymbol{k} \tag{B.7}$$

(with square integrable amplitude function $c(\boldsymbol{k})$), the squared norm gives

$$\begin{aligned} \langle \psi | \psi \rangle &= \iint c(\boldsymbol{k}')^* c(\boldsymbol{k}) \langle \boldsymbol{k}' | \boldsymbol{k} \rangle \, \mathrm{d}\boldsymbol{k}' \mathrm{d}\boldsymbol{k} \\ &= \iint c(\boldsymbol{k}')^* c(\boldsymbol{k}) \delta(\boldsymbol{k} - \boldsymbol{k}') \mathrm{d}\boldsymbol{k}' \mathrm{d}\boldsymbol{k} \\ &= \int |c(\boldsymbol{k})|^2 \mathrm{d}\boldsymbol{k}, \end{aligned} \tag{B.8}$$

which is finite. Similarly, a pure-state density matrix composed of a wave packet reads

$$\hat{\rho} = | \psi \rangle \langle \psi | = \iint c(\boldsymbol{k}) c(\tilde{\boldsymbol{k}})^* | \boldsymbol{k} \rangle \langle \tilde{\boldsymbol{k}} | \, \mathrm{d}\boldsymbol{k} \mathrm{d}\tilde{\boldsymbol{k}}. \tag{B.9}$$

It's trace (in momentum space) is given by

$$\begin{aligned} \operatorname{tr} \hat{\rho} &= \iiint c(\boldsymbol{k}) c(\tilde{\boldsymbol{k}})^* \langle \boldsymbol{k}' | \boldsymbol{k} \rangle \langle \tilde{\boldsymbol{k}} | \boldsymbol{k}' \rangle \, \mathrm{d}\boldsymbol{k} \mathrm{d}\tilde{\boldsymbol{k}} \mathrm{d}\boldsymbol{k}' \\ &= \iiint c(\boldsymbol{k}) c(\tilde{\boldsymbol{k}})^* \delta(\boldsymbol{k} - \boldsymbol{k}') \delta(\boldsymbol{k}' - \tilde{\boldsymbol{k}}) \mathrm{d}\boldsymbol{k} \mathrm{d}\tilde{\boldsymbol{k}} \mathrm{d}\boldsymbol{k}' \\ &= \int |c(\boldsymbol{k})|^2 \mathrm{d}\boldsymbol{k} \end{aligned} \tag{B.10}$$

as before.

A similar approach works for the expectation value of operators. For instance, it holds that

$$\hat{\boldsymbol{p}} | k \rangle = \hbar \boldsymbol{k} | k \rangle . \tag{B.11}$$

Thus, one would expect $\langle \hat{\boldsymbol{p}} \rangle = \langle \boldsymbol{k} | \hat{\boldsymbol{p}} | \boldsymbol{k} \rangle = \hbar \boldsymbol{k} \langle \boldsymbol{k} | \boldsymbol{k} \rangle$ to yield the same result, which it only does in a distributional sense. For a wave packet, on the other hand, the calculation yields

$$\begin{aligned} \langle \psi | \hat{\boldsymbol{p}} | \psi \rangle &= \iint c(\boldsymbol{k}')^* c(\boldsymbol{k}) \langle \boldsymbol{k}' | \hat{\boldsymbol{p}} | \boldsymbol{k} \rangle \, \mathrm{d}\boldsymbol{k}' \mathrm{d}\boldsymbol{k} \\ &= \iint c(\boldsymbol{k}')^* c(\boldsymbol{k}) \hbar \boldsymbol{k} \delta(\boldsymbol{k} - \boldsymbol{k}') \mathrm{d}\boldsymbol{k}' \mathrm{d}\boldsymbol{k} \\ &= \int \hbar \boldsymbol{k} |c(\boldsymbol{k})|^2 \mathrm{d}\boldsymbol{k}, \end{aligned} \tag{B.12}$$

which is the expected weighted average over contributing $\boldsymbol{k}$ vectors. Analogously, the expectation value in the density matrix formalism can be defined as

$$\langle \hat{\boldsymbol{p}} \rangle := \operatorname{tr}[\hat{\boldsymbol{p}} \hat{\rho}]. \tag{B.13}$$

C. Calculations

C.1. Conventions

Real space representation of plane waves:

$$\langle \boldsymbol{r}|\boldsymbol{k}\rangle = \frac{1}{(2\pi)^{3/2}}\mathrm{e}^{\mathrm{i}\boldsymbol{k}\cdot\boldsymbol{r}}. \tag{C.1}$$

Fourier transform in n dimensions:

$$\hat{\mathcal{F}}_{\boldsymbol{k}}[f] = \frac{1}{(2\pi)^{n/2}}\int \mathrm{e}^{-\mathrm{i}\boldsymbol{k}\cdot\boldsymbol{r}}f(\boldsymbol{r})\mathrm{d}\boldsymbol{r}. \tag{C.2}$$

Fourier back-transform in n dimensions:

$$\hat{\mathcal{F}}_{-\boldsymbol{r}}[\tilde{f}] = \frac{1}{(2\pi)^{n/2}}\int \mathrm{e}^{\mathrm{i}\boldsymbol{k}\cdot\boldsymbol{r}}\tilde{f}(\boldsymbol{k})\mathrm{d}\boldsymbol{k}. \tag{C.3}$$

In this convention, the convolution theorem reads:

$$
\begin{aligned}
\hat{\mathcal{F}}_{\boldsymbol{k}}[f\cdot g] &= \frac{1}{(2\pi)^{n/2}}\int \mathrm{e}^{-\mathrm{i}\boldsymbol{k}\cdot\boldsymbol{r}}f(\boldsymbol{r})g(\boldsymbol{r})\mathrm{d}\boldsymbol{r} \\
&= \frac{1}{(2\pi)^{n}}\int \mathrm{e}^{-\mathrm{i}\boldsymbol{k}\cdot\boldsymbol{r}}\int \mathrm{e}^{\mathrm{i}\boldsymbol{k}'\cdot\boldsymbol{r}}\tilde{f}(\boldsymbol{k}')\mathrm{d}\boldsymbol{k}'g(\boldsymbol{r})\mathrm{d}\boldsymbol{r} \\
&= \frac{1}{(2\pi)^{n}}\int \tilde{f}(\boldsymbol{k}')\int \mathrm{e}^{-\mathrm{i}(\boldsymbol{k}-\boldsymbol{k}')\cdot\boldsymbol{r}}g(\boldsymbol{r})\mathrm{d}\boldsymbol{r}\mathrm{d}\boldsymbol{k}' \\
&= \frac{1}{(2\pi)^{n/2}}\int \tilde{f}(\boldsymbol{k}')\tilde{g}(\boldsymbol{k}-\boldsymbol{k}')\mathrm{d}\boldsymbol{k}' \\
&= \frac{1}{(2\pi)^{n/2}}\hat{\mathcal{F}}_{\boldsymbol{k}}[f]\circledast\hat{\mathcal{F}}_{\boldsymbol{k}}[g].
\end{aligned}
\tag{C.4}
$$

Shift theorem:

$$
\begin{aligned}
\hat{\mathcal{F}}_{\boldsymbol{k}}[f(\boldsymbol{r}+\boldsymbol{\delta})] &= \frac{1}{(2\pi)^{n/2}}\int \mathrm{e}^{-\mathrm{i}\boldsymbol{k}\cdot\boldsymbol{r}}f(\boldsymbol{r}+\boldsymbol{\delta})\mathrm{d}\boldsymbol{r} \\
&= \frac{1}{(2\pi)^{n/2}}\int \mathrm{e}^{-\mathrm{i}\boldsymbol{k}\cdot(\boldsymbol{r}-\boldsymbol{\delta})}f(\boldsymbol{r})\mathrm{d}\boldsymbol{r} \\
&= \mathrm{e}^{\mathrm{i}\boldsymbol{k}\cdot\boldsymbol{\delta}}\hat{\mathcal{F}}_{\boldsymbol{k}}[f(\boldsymbol{r})].
\end{aligned}
\tag{C.5}
$$

Orthonormalization of spherical harmonics:

$$\int Y_l^m(\Omega)^*Y_{l'}^{m'}(\Omega)\mathrm{d}\Omega = \delta_{ll'}\delta_{mm'}. \tag{C.6}$$

C.2. Useful relations

C.2.1. Relations of the Dirac delta distribution

From a Fourier transform, followed by a Fourier back transform, the following representation of the Dirac delta can be derived [112]:

$$\delta(\boldsymbol{x} - \boldsymbol{\chi}) = \frac{1}{(2\pi)^n} \int e^{i(\boldsymbol{x}-\boldsymbol{\chi})\cdot\boldsymbol{k}} d\boldsymbol{k}. \tag{C.7}$$

Representation in cylindrical coordinates [112]:

$$\delta(\boldsymbol{r}_1 - \boldsymbol{r}_2) = \frac{\delta(r_{1\perp} - r_{2\perp})\delta(\theta_1 - \theta_2)\delta(z_1 - z_2)}{r_{1\perp}}. \tag{C.8}$$

C.2.2. Relations of Bessel functions

Series expansion [31, 9.1.10]:

$$J_n(z) = \sum_{k=0}^{\infty} \frac{(-1)^k}{k!\Gamma(n+k+1)} \left(\frac{z}{2}\right)^{n+k}. \tag{C.9}$$

Generating function [31, 9.1.41]:

$$e^{\frac{z}{2}\left(t-\frac{1}{t}\right)} = \sum_{k=-\infty}^{\infty} t^k J_k(z) \quad (t \neq 0). \tag{C.10}$$

Jacobi-Anger expansion (by setting $t = ie^{i\varphi}$ in eq. C.10):

$$e^{iz\cos(\varphi)} = \sum_{k=-\infty}^{\infty} i^k e^{ik\varphi} J_k(z). \tag{C.11}$$

Orthogonality relation [30]:

$$\int_0^1 J_\alpha(\lambda_{\alpha,m}x) J_\alpha(\lambda_{\alpha,n}x) x dx = \frac{\delta_{m,n}}{2} \left[J_{\alpha+1}(\lambda_{\alpha,m})\right]^2. \tag{C.12}$$

Closure relation [30]:

$$\int_0^\infty J_\nu(qR) J_\nu(q'R) R dR = \frac{\delta(q-q')}{q} \quad \nu > \frac{1}{2}. \tag{C.13}$$

Integral representation [30]:

$$J_n(x) = \frac{1}{2\pi i^n} \int_0^{2\pi} e^{i(n\varphi + x\cos\varphi)} d\varphi. \tag{C.14}$$

C.2.3. Relations of modified Bessel functions

Integral representation [30]:

$$I_n(x) = \frac{1}{\pi} \int_0^\pi \mathrm{e}^{x \cos \varphi} \cos(n\varphi) \mathrm{d}\varphi. \tag{C.15}$$

Hankel-Nicholson type integral [31, 11.4.44]:

$$K_\nu(az) = \frac{2^\mu \Gamma(\mu + 1)}{a^\mu z^\nu} \int_0^\infty \frac{t^{\nu+\mu+1} J_{\nu+\mu}(at)}{(t^2 + z^2)^{\mu+1}} \mathrm{d}t \quad a > 0, z > 0, -1 - \mu < \nu < \mu + \frac{3}{2}. \tag{C.16}$$

C.2.4. Relations of spherical Bessel functions

Relation between Bessel functions and spherical Bessel functions [31, 10.1.1]:

$$j_n(z) = \sqrt{\frac{\pi}{2z}} J_{n+\frac{1}{2}}(z). \tag{C.17}$$

Closure relation [30, 113]:

$$\int_0^\infty j_n(qR) j_n(q'R) R^2 \mathrm{d}R = \frac{\pi}{2} \cdot \frac{\delta(q - q')}{q^2} \quad n \geq 0. \tag{C.18}$$

Taylor series [31, 10.1.2]:

$$j_n(z) = \sum_{k=0}^\infty \frac{(-1)^k z^{2k+n}}{2^k k! (2n + 2k + 1)!!}. \tag{C.19}$$

Representation by a finite sum over trigonometric functions [31, 10.1.8]:

$$j_n(z) = \frac{1}{z} \left[\sum_{k=0}^{\lfloor \frac{n}{2} \rfloor} \frac{(-1)^k (n + 2k)! \sin(z - \frac{n\pi}{2})}{(2k)! (n - 2k)! (2z)^{2k}} + \sum_{k=0}^{\lfloor \frac{n-1}{2} \rfloor} \frac{(-1)^k (n + 2k + 1)! \cos(z - \frac{n\pi}{2})}{(2k + 1)! (n - 2k - 1)! (2z)^{2k+1}} \right]. \tag{C.20}$$

For even $n = 2\nu$, note that $\sin(z - \nu\pi) = (-1)^\nu \sin(z)$ as well as $\cos(z - \nu\pi) = (-1)^\nu \cos(z)$. Using these relations, reversing the sum and some algebraic manipulations

yield

$$
\begin{aligned}
j_n(z) &= \sum_{k=0}^{\nu} \frac{(-1)^{k+\nu}(n+2k)!}{2^{2k}(2k)!(n-2k)!} \cdot \frac{\sin(z)}{z^{2k+1}} + \sum_{k=0}^{\nu-1} \frac{(-1)^{k+\nu}(n+2k+1)!}{2^{2k+1}(2k+1)!(n-2k-1)!} \cdot \frac{\cos(z)}{z^{2k+2}} \\
&= \sum_{k=0}^{\nu} \frac{(-1)^{-k}(2n-2k)!}{2^{n-2k}(n-2k)!(2k)!} \cdot \frac{\sin(z)}{z^{n-2k+1}} + \\
&\quad \sum_{k=0}^{\nu-1} \frac{(-1)^{-1-k}(2n-2k-1)!}{2^{n-2k-1}(n-2k-1)!(2k+1)!} \cdot \frac{\cos(z)}{z^{n-2k}} \\
&= \sum_{k=0}^{\nu} \frac{(-1)^{k}(2n-2k)!}{2^{n-2k}(n-2k)!(2k)!} \cdot \frac{\sin(z)}{z^{n-2k+1}} + \\
&\quad \sum_{k=1}^{\nu} \frac{(-1)^{k}(2n-2k+1)!}{2^{n-2k+1}(n-2k+1)!(2k-1)!} \cdot \frac{\cos(z)}{z^{n-2k+2}} \\
&= \sum_{k=0}^{\nu} \frac{(-1)^{k}(2n-2k)!}{2^{n-2k}(n-2k)!(2k)!} \cdot \frac{\sin(z)}{z^{n-2k+1}} + \\
&\quad \sum_{k=1}^{\nu} \frac{k}{n-k+1} \cdot \frac{(-1)^{k}(2n-2k+2)!}{2^{n-2k+1}(n-2k+1)!(2k)!} \cdot \frac{\cos(z)}{z^{n-2k+2}} \\
&= \sum_{k=0}^{\lfloor \frac{n+1}{2} \rfloor} \left[\frac{(-1)^{k}(2n-2k)!}{2^{n-2k}(n-2k)!(2k)!} \cdot \frac{\sin(z)}{z^{n-2k+1}} + \right. \\
&\quad \left. \frac{(-1)^{k}k(2n-2k+2)!}{2^{n-2k+1}(n-k+1)(n-2k+1)!(2k)!} \cdot \frac{\cos(z)}{z^{n-2k+2}} \right].
\end{aligned}
\tag{C.21}
$$

Likewise, for odd $n = 2\nu + 1$, observing that $\sin(z - \nu\pi - \pi/2) = (-1)^{\nu-1}\cos(z)$ as well as $\cos(z - \nu\pi - \pi/2) = (-1)^{\nu}\sin(z)$, setting $1/(-1)! = 0$,[1] reversing the sum and some algebraic manipulations yield

$$
\begin{aligned}
j_n(z) &= \sum_{k=0}^{\nu} \frac{(-1)^{k+\nu-1}(n+2k)!}{2^{2k}(2k)!(n-2k)!} \cdot \frac{\cos(z)}{z^{2k+1}} + \sum_{k=0}^{\nu} \frac{(-1)^{k+\nu}(n+2k+1)!}{2^{2k+1}(2k+1)!(n-2k-1)!} \cdot \frac{\sin(z)}{z^{2k+2}} \\
&= \sum_{k=0}^{\nu} \frac{(-1)^{k}(2n-2k)!}{2^{n-2k}(n-2k)!(2k)!} \cdot \frac{\sin(z)}{z^{n-2k+1}} + \\
&\quad \sum_{k=0}^{\nu} \frac{(-1)^{-k-1}(2n-2k-1)!}{2^{n-2k-1}(n-2k-1)!(2k+1)!} \cdot \frac{\cos(z)}{z^{n-2k}}
\end{aligned}
$$

---

[1] $n!$ is defined as $\Gamma(n+1)$. Therefore, $1/(-1)! = 1/\Gamma(0)$. Since the Γ function has a simple pole at 0, $\lim_{z\to 0} 1/\Gamma(z) = 0$ [31, 6.1.7].

$$= \sum_{k=0}^{\nu+1} \frac{(-1)^k(2n-2k)!}{2^{n-2k}(n-2k)!(2k)!} \cdot \frac{\sin(z)}{z^{n-2k+1}} +$$

$$\sum_{k=1}^{\nu+1} \frac{(-1)^k(2n-2k+1)!}{2^{n-2k+1}(n-2k+1)!(2k-1)!} \cdot \frac{\cos(z)}{z^{n-2k+2}}$$

$$= \sum_{k=0}^{\lfloor \frac{n+1}{2} \rfloor} \left[\frac{(-1)^k(2n-2k)!}{2^{n-2k}(n-2k)!(2k)!} \cdot \frac{\sin(z)}{z^{n-2k+1}} + \right.$$

$$\left. \frac{(-1)^k k(2n-2k+2)!}{2^{n-2k+1}(n-k+1)(n-2k+1)!(2k)!} \cdot \frac{\cos(z)}{z^{n-2k+2}} \right], \tag{C.22}$$

which is exactly the same expression as for even n. Thus, spherical Bessel functions can be written as

$$j_n(z) = \sum_{k=0}^{\lfloor \frac{n+1}{2} \rfloor} \left[A_n^k \frac{\sin(z)}{z^{n-2k+1}} + B_n^k \frac{\cos(z)}{z^{n-2k+2}} \right]$$

$$A_n^k = \frac{(-1)^k 2^{2k-n}(2n-2k)!}{(n-2k)!(2k)!}$$

$$B_n^k = \frac{(-1)^k 2^{2k-n-1} k(2n-2k+2)!}{(n-k+1)(n-2k+1)!(2k)!}. \tag{C.23}$$

In actual computer implementations, it is beneficial to calculate the coefficients A_n^k and B_n^k recursively via

$$A_n^0 = \frac{(2n)!}{2^n n!} = (2n-1)!!$$

$$B_n^0 = 0$$

$$B_n^1 = -\frac{(2n)!}{2^n n!} = -(2n-1)!!$$

$$A_n^{k+1} = -\frac{(n-2k)(n-2k-1)}{(k+1)(2k+1)(n-k)(2n-2k-1)} A_n^k$$

$$B_n^{k+1} = -\frac{(n-2k)(n-2k+1)}{k(2k+1)(n-k)(2n-2k+1)} B_n^k. \tag{C.24}$$

This also avoids the divergence of $(-1)!$.

C.2.5. Relations of the Gamma function

Euler's integral [31, 6.1.1]:

$$\Gamma(z+1) = \int_0^\infty t^z e^{-t} dt = k^{z+1} \int_0^\infty t^z e^{-kt} \quad \Re(z) > -1, \Re(k) > 0. \tag{C.25}$$

Special values [31, 6.1.8]:

$$\Gamma\left(\frac{1}{2}\right) = \sqrt{\pi}. \tag{C.26}$$

Relationship with the factorial [31, 6.1.5]:

$$z! = \Gamma(z+1). \tag{C.27}$$

Relationship with the double factorial [31, 6.1.12]:

$$\Gamma\left(n + \frac{1}{2}\right) = \frac{(2n-1)!!}{2^n}\Gamma\left(\frac{1}{2}\right) = \frac{(2n-1)!!\sqrt{\pi}}{2^n}. \tag{C.28}$$

C.2.6. Relations of Wigner 3j symbols

These identities can be found, e.g., in [34].

Relation to the spherical harmonics:

$$\int_{4\pi} Y_{l_1}^{m_1}(\Omega)Y_{l_2}^{m_2}(\Omega)Y_{l_3}^{m_3}(\Omega)\mathrm{d}\Omega =$$

$$\sqrt{\frac{(2l_1+1)(2l_2+1)(2l_3+1)}{4\pi}} \begin{pmatrix} l_1 & l_2 & l_3 \\ 0 & 0 & 0 \end{pmatrix} \begin{pmatrix} l_1 & l_2 & l_3 \\ m_1 & m_2 & m_3 \end{pmatrix}. \tag{C.29}$$

Relation to the Clebsch-Gordan coefficients:

$$\langle j_1 m_1 j_2 m_2 | j_3 m_3 \rangle = (-1)^{-j_1+j_2-m_3}\sqrt{2j_3+1} \begin{pmatrix} j_1 & j_2 & j_3 \\ m_1 & m_2 & -m_3 \end{pmatrix}. \tag{C.30}$$

Orthogonality relation:

$$\sum_{m_1 m_2} \begin{pmatrix} j_1 & j_2 & j \\ m_1 & m_2 & m \end{pmatrix} \begin{pmatrix} j_1 & j_2 & j' \\ m_1 & m_2 & m' \end{pmatrix} = \frac{\delta_{jj'}\delta_{mm'}}{2j+1}. \tag{C.31}$$

Permutation relations (for odd and even permutations, respectively):

$$(-1)^{j_1+j_2+j_3} \begin{pmatrix} j_1 & j_2 & j_3 \\ m_1 & m_2 & m_3 \end{pmatrix} = \begin{pmatrix} j_2 & j_1 & j_3 \\ m_2 & m_1 & m_3 \end{pmatrix} = \begin{pmatrix} j_1 & j_3 & j_2 \\ m_1 & m_3 & m_2 \end{pmatrix} = \begin{pmatrix} j_3 & j_2 & j_1 \\ m_3 & m_2 & m_1 \end{pmatrix}$$

$$\begin{pmatrix} j_1 & j_2 & j_3 \\ m_1 & m_2 & m_3 \end{pmatrix} = \begin{pmatrix} j_2 & j_3 & j_1 \\ m_2 & m_3 & m_1 \end{pmatrix} = \begin{pmatrix} j_3 & j_1 & j_2 \\ m_3 & m_1 & m_2 \end{pmatrix}. \tag{C.32}$$

C.2.7. Relations of spherical harmonics

These identities can be found, e.g., in [65].

Complex conjugation:

$$Y_l^m(\Omega)^* = (-1)^m Y_l^{-m}(\Omega). \tag{C.33}$$

Addition theorem:

$$\sum_m Y_l^m \left(\frac{\boldsymbol{x}}{x}\right)^* Y_l^m \left(\frac{\boldsymbol{y}}{y}\right) = \frac{2l+1}{4\pi} P_l \left(\frac{\boldsymbol{x}}{x} \cdot \frac{\boldsymbol{y}}{y}\right). \tag{C.34}$$

Rayleigh expansion:

$$\mathrm{e}^{\mathrm{i}\boldsymbol{q}\cdot\boldsymbol{R}} = 4\pi \sum_{\lambda=0}^{\infty} \sum_{\mu=-\lambda}^{\lambda} \mathrm{i}^\lambda Y_\lambda^\mu (\boldsymbol{q}/q)^* Y_\lambda^\mu (\boldsymbol{R}/R) j_\lambda(qR). \tag{C.35}$$

C.3. The Coulomb potential in momentum space

A similar derivation can also be found, e.g., in [114].

The real space representation of the Coulomb potential is given by (compare eq. 3.18)

$$\langle \boldsymbol{r} | \hat{V} | \tilde{\boldsymbol{r}} \rangle = \frac{e^2}{4\pi\epsilon_0} \frac{\delta(\boldsymbol{r}-\tilde{\boldsymbol{r}})}{|\boldsymbol{r}-\boldsymbol{R}|} =: \hat{V}(\boldsymbol{r})\delta(\boldsymbol{r}-\tilde{\boldsymbol{r}}). \tag{C.36}$$

Hence, the momentum space representation can be expressed as

$$\langle \boldsymbol{k} | \hat{V} | \tilde{\boldsymbol{k}} \rangle = \iint \mathrm{d}\boldsymbol{r}\mathrm{d}\tilde{\boldsymbol{r}} \, \langle \boldsymbol{k} | \boldsymbol{r} \rangle \langle \boldsymbol{r} | \hat{V} | \tilde{\boldsymbol{r}} \rangle \langle \tilde{\boldsymbol{r}} | \tilde{\boldsymbol{k}} \rangle. \tag{C.37}$$

Using

$$\langle \boldsymbol{r} | \boldsymbol{k} \rangle = \frac{1}{(2\pi)^{3/2}} \mathrm{e}^{\mathrm{i}\boldsymbol{k}\cdot\boldsymbol{r}}, \tag{C.38}$$

this yields

$$\begin{aligned}
\langle \boldsymbol{k} | \hat{V} | \tilde{\boldsymbol{k}} \rangle &= \frac{1}{8\pi^3} \iint \mathrm{d}\boldsymbol{r}\mathrm{d}\tilde{\boldsymbol{r}} \mathrm{e}^{-\mathrm{i}\boldsymbol{k}\cdot\boldsymbol{r}} \hat{V}(\boldsymbol{r})\delta(\boldsymbol{r}-\tilde{\boldsymbol{r}})\mathrm{e}^{\mathrm{i}\tilde{\boldsymbol{k}}\cdot\tilde{\boldsymbol{r}}} \\
&= \frac{1}{8\pi^3} \int \mathrm{d}\boldsymbol{r}\mathrm{e}^{\mathrm{i}(\tilde{\boldsymbol{k}}-\boldsymbol{k})\cdot\boldsymbol{r}} \hat{V}(\boldsymbol{r}) \\
&=: \frac{1}{8\pi^3} \int \mathrm{d}\boldsymbol{r}\mathrm{e}^{\mathrm{i}\boldsymbol{q}\cdot\boldsymbol{r}} \hat{V}(\boldsymbol{r}).
\end{aligned} \tag{C.39}$$

This describes the Fourier transform of the Coulomb potential, which, unfortunately, does not converge in the conventional sense. One way around this is to calculate the momentum space representation of a screened Coulomb potential (Yukawa potential)

and take the limit of zero screening in the end:

$$
\begin{aligned}
\langle \boldsymbol{k}|\hat{V}|\tilde{\boldsymbol{k}}\rangle &= \frac{e^2}{32\pi^4\epsilon_0}\lim_{\sigma\to 0}\int \mathrm{d}\boldsymbol{r}\,\mathrm{e}^{\mathrm{i}\boldsymbol{q}\cdot\boldsymbol{r}}\frac{\mathrm{e}^{-\sigma|\boldsymbol{r}-\boldsymbol{R}|}}{|\boldsymbol{r}-\boldsymbol{R}|} \\
&= \frac{e^2}{32\pi^4\epsilon_0}\mathrm{e}^{\mathrm{i}\boldsymbol{q}\cdot\boldsymbol{R}}\lim_{\sigma\to 0}\int \mathrm{d}\boldsymbol{r}\frac{\mathrm{e}^{\mathrm{i}\boldsymbol{q}\cdot(\boldsymbol{r}-\boldsymbol{R})-\sigma|\boldsymbol{r}-\boldsymbol{R}|}}{|\boldsymbol{r}-\boldsymbol{R}|} \\
&= \frac{e^2}{4\pi\epsilon_0}\mathrm{e}^{\mathrm{i}\boldsymbol{q}\cdot\boldsymbol{R}}\lim_{\sigma\to 0}\int \mathrm{d}\boldsymbol{r}\frac{\mathrm{e}^{\mathrm{i}\boldsymbol{q}\cdot\boldsymbol{r}-\sigma r}}{r} \\
&= \frac{e^2}{32\pi^4\epsilon_0}\mathrm{e}^{\mathrm{i}\boldsymbol{q}\cdot\boldsymbol{R}}\lim_{\sigma\to 0}\int_0^\infty\int_0^\pi\int_0^{2\pi}\mathrm{e}^{\mathrm{i}qr\cos(\theta)-\sigma r}r\sin(\theta)\mathrm{d}\varphi\mathrm{d}\theta\mathrm{d}r \\
&= \frac{e^2}{16\pi^3\epsilon_0}\mathrm{e}^{\mathrm{i}\boldsymbol{q}\cdot\boldsymbol{R}}\lim_{\sigma\to 0}\int_0^\infty\int_{-1}^1\mathrm{e}^{\mathrm{i}qru-\sigma r}r\mathrm{d}u\mathrm{d}r \\
&= \frac{e^2}{16\pi^3\epsilon_0\mathrm{i}q}\mathrm{e}^{\mathrm{i}\boldsymbol{q}\cdot\boldsymbol{R}}\lim_{\sigma\to 0}\int_0^\infty\left(\mathrm{e}^{(\mathrm{i}q-\sigma)r}-\mathrm{e}^{(-\mathrm{i}q-\sigma)r}\right)\mathrm{d}r \\
&= \frac{e^2}{16\pi^3\epsilon_0\mathrm{i}q}\mathrm{e}^{\mathrm{i}\boldsymbol{q}\cdot\boldsymbol{R}}\lim_{\sigma\to 0}\left(\frac{1}{\sigma-\mathrm{i}q}-\frac{1}{\sigma+\mathrm{i}q}\right) \\
&= \frac{e^2}{16\pi^3\epsilon_0\mathrm{i}q}\mathrm{e}^{\mathrm{i}\boldsymbol{q}\cdot\boldsymbol{R}}\lim_{\sigma\to 0}\frac{2\mathrm{i}q}{\sigma^2+q^2} \\
&= \frac{e^2}{(2\pi)^3\epsilon_0}\frac{\mathrm{e}^{\mathrm{i}\boldsymbol{q}\cdot\boldsymbol{R}}}{q^2}.
\end{aligned}
\tag{C.40}
$$

C.4. The Fourier transform of the scattering kernel

The scattering kernel in momentum space (eq. 3.24) is given by

$$
\mathbb{S}(\boldsymbol{q},\boldsymbol{q}',E) = \left(\frac{e^2}{4\pi^2\epsilon_0}\right)^2\frac{S(\boldsymbol{q},\boldsymbol{q}',E)}{q^2q'^2}.
\tag{C.41}
$$

According to eq. 3.22, the scattering kernel in real space, $\mathbb{S}(\boldsymbol{r},\boldsymbol{r}',E)$, can be calculated as the (double) Fourier transform of $\mathbb{S}(\boldsymbol{q},\boldsymbol{q}',E)$. Enforcing $q_z = q_z' = -q_E$, one therefore arrives at

$$
\begin{aligned}
\mathbb{S}(\boldsymbol{r},\boldsymbol{r}',E) &= \left(\frac{e^2}{4\pi^2\epsilon_0}\right)^2\hat{\mathcal{F}}_{\boldsymbol{q},-\boldsymbol{q}'}\left[\delta(q_z+q_E)\delta(q_z'+q_E)\frac{S(\boldsymbol{q},\boldsymbol{q}',E)}{q^2q'^2}\right] \\
&= \left(\frac{e^2}{4\pi^2\epsilon_0}\right)^2\frac{1}{(2\pi)^3}\hat{\mathcal{F}}_{\boldsymbol{q},-\boldsymbol{q}'}\left[\frac{\delta(q_z+q_E)\delta(q_z'+q_E)}{q^2q'^2}\right]\circledast\hat{\mathcal{F}}_{\boldsymbol{q},-\boldsymbol{q}'}[S(\boldsymbol{q},\boldsymbol{q}',E)] \\
&= \left(\frac{e^2}{4\pi^2\epsilon_0}\right)^2\frac{1}{(2\pi)^3}\hat{\mathcal{F}}_{\boldsymbol{q}_\perp,-\boldsymbol{q}_\perp'}\left[\frac{\mathrm{e}^{\mathrm{i}q_E(z-z')}}{(q_\perp^2+q_E^2)((q_\perp')^2+q_E^2)}\right]\circledast\hat{\mathcal{F}}_{\boldsymbol{q},-\boldsymbol{q}'}[S(\boldsymbol{q},\boldsymbol{q}',E)].
\end{aligned}
\tag{C.42}
$$

The 2D Fourier transform of the Lorentzian terms give

$$\hat{\mathcal{F}}_{\boldsymbol{q}_\perp}\left[\frac{1}{q_\perp^2 + q_E^2}\right] = \frac{1}{2\pi}\int_0^\infty\int_0^{2\pi}\frac{\mathrm{e}^{-\mathrm{i}q_\perp r_\perp\cos\varphi}}{q_\perp^2 + q_E^2}q_\perp\,\mathrm{d}\varphi\,\mathrm{d}q_\perp$$

$$= \int_0^\infty\frac{q_\perp}{q_\perp^2 + q_E^2}J_0(q_\perp r_\perp)\,\mathrm{d}q_\perp$$

$$= K_0(q_E r_\perp). \tag{C.43}$$

With

$$\hat{\mathcal{F}}_{\boldsymbol{q},-\boldsymbol{q}'}[S(\boldsymbol{q},\boldsymbol{q}',E)] = S(\boldsymbol{r},\boldsymbol{r}',E), \tag{C.44}$$

the scattering kernel consequently takes the form

$$\mathbb{S}(\boldsymbol{r},\boldsymbol{r}',E) = \left(\frac{e^2}{4\pi^2\epsilon_0}\right)^2\frac{1}{(2\pi)^3}\left[K_0(q_E r_\perp)K_0(q_E r'_\perp)\mathrm{e}^{\mathrm{i}q_E(z-z')}\right] \circledast S(\boldsymbol{r},\boldsymbol{r}',E). \tag{C.45}$$

Carrying out the convolution in z direction yields

$$\mathbb{S}(\boldsymbol{r},\boldsymbol{r}',E) = \left(\frac{e^2}{4\pi^2\epsilon_0}\right)^2\frac{\mathrm{e}^{\mathrm{i}q_E(z-z')}}{(2\pi)^3}\cdot$$

$$[K_0(q_E r_\perp)K_0(q_E r'_\perp)]\circledast_\perp\iint\mathrm{d}z\,\mathrm{d}z'\mathrm{e}^{-\mathrm{i}q_E(z-z')}S(\boldsymbol{r},\boldsymbol{r}',E). \tag{C.46}$$

It is noteworthy that the z and z' dependency of the scattering kernel is given solely by the $\mathrm{e}^{\mathrm{i}q_E(z-z')}$ term which describes the effect of the characteristic momentum transfer $q_E\boldsymbol{e}_z$. All other terms are independent of z and z' in analogy to the locality approximation [51].

D. Uncertainties and Fitting

Measurements are always uncertain to a degree. If a certain event (e.g., a particular scattering process) occurs with a certain *average* rate, one would (in theory) have to measure for an infinitely long time to determine the *exact* value. For finite measurements, there always remains a finite uncertainty, even in the absence of systematic errors.

Throughout this work, CCDs are used to record data. Images taken with a CCD suffer from the well-known shot noise. This noise actually has a (discrete) Poisson distribution. For a large number of counts (of the order of thousands), this distribution is virtually indistinguishable from a normal distribution with mean μ and standard deviation $\sigma := \sqrt{\mu}$, so the latter will be used for the sake of simplicity.[1]

Generally, the uncertainty of a vector $\boldsymbol{X} = (x_1, \dots, x_n)$ is described by its covariance matrix $\boldsymbol{\Sigma}$. The diagonal elements of $\boldsymbol{\Sigma}$ are the variances (i.e., squared standard deviations) of the individual elements of $\boldsymbol{X}$, whereas the off-diagonal elements give the correlations between the corresponding elements of $\boldsymbol{X}$. For uncorrelated (i.e., statistically independent) variables, $\boldsymbol{\Sigma}$ is a diagonal matrix.

When applying a (possibly vector-valued) function $\boldsymbol{f} : \mathbb{R}^n \to \mathbb{R}^m$ to the vector $\boldsymbol{X}$, the result $\boldsymbol{f}(\boldsymbol{X})$ has the covariance matrix[2]

$$\boldsymbol{\Sigma}_f = \mathrm{d}\boldsymbol{f}(\boldsymbol{X}) \cdot \boldsymbol{\Sigma} \cdot (\mathrm{d}\boldsymbol{f}(\boldsymbol{X}))^T, \tag{D.1}$$

where

$$\mathrm{d}\boldsymbol{f} = \begin{pmatrix} \frac{\partial f_1}{\partial x_1} & \cdots & \frac{\partial f_1}{\partial x_n} \\ \vdots & \ddots & \vdots \\ \frac{\partial f_m}{\partial x_1} & \cdots & \frac{\partial f_m}{\partial x_n} \end{pmatrix} \tag{D.2}$$

is the Jacobian matrix.

In the particular case of statistically independent (i.e., uncorrelated) arguments and a scalar function, eq. D.1 simplifies to the well-known expression

$$\Delta f(\boldsymbol{X}) \approx \sqrt{\sum_{i,j} \left(\frac{\partial f}{\partial x_i}(\boldsymbol{X})\Delta x_i \right)^2}. \tag{D.3}$$

---

[1]In fact, some preprocessing — such as dark reference subtraction and gain correction — is performed before the data is made available to the user. This is not taken into account in this work.

[2]Eq. D.1 uses a linearized model following the standard procedure outlined in [115–117]. For a more rigorous approach, one would have to consider the different distributions of the errors in detail. For example, if x and y are uncorrelated scalars that are normally distributed, then x/y is not. In fact, x/y follows a Cauchy distribution, for which such properties as mean or standard deviation are undefined. Incidentally, however, the confidence interval for the Cauchy-distribution in this case is very similar to the uncertainty predicted by eq. D.1.

D.1. Least squares fitting

Least squares fitting is a common approach to estimate model parameters from an (experimental) dataset. Linear least squares fitting is a text-book example that can be solved analytically. In general, however, any differentiable function that is sufficiently well approximated by a linear function can be used, giving rise to the non-linear least squares method.

Given a dataset $((\boldsymbol{x}_1, y_1), \ldots (\boldsymbol{x}_m, y_m))$ and a model function $f(\boldsymbol{x}, \boldsymbol{p}) \to \mathbb{R}$, where $\boldsymbol{p} = (p_1, \ldots, p_n)$ are the parameters, the residual of a data point (with a given parameter vector) is

$$r_i(\boldsymbol{p}) := y_i - f(\boldsymbol{x}_i, \boldsymbol{p}). \tag{D.4}$$

The least squares method endeavors to find a parameter vector $\boldsymbol{p}_{\mathrm{opt}}$ that minimizes the sum of squared residuals,

$$S(\boldsymbol{p}) = \sum_{i=1}^{m} r_i(\boldsymbol{p})^2. \tag{D.5}$$

A necessary condition for this is

$$\frac{\partial S}{\partial p_j}(\boldsymbol{p}_{\mathrm{opt}}) = \sum_{i=1}^{m} 2 r_i(\boldsymbol{p}_{\mathrm{opt}}) \frac{\partial r_i}{\partial p_j}(\boldsymbol{p}_{\mathrm{opt}}) = 2 \sum_{i=1}^{m} (y_i - f(\boldsymbol{x}_i, \boldsymbol{p}_{\mathrm{opt}})) \frac{\partial f}{\partial p_j}(\boldsymbol{x}_i, \boldsymbol{p}_{\mathrm{opt}}) = 0. \tag{D.6}$$

A linear approximation around some fixed parameter guess $\boldsymbol{p}_0$ (and neglecting second order derivatives) yields

$$\sum_{i=1}^{m} \left(y_i - f(\boldsymbol{x}_i, \boldsymbol{p}_0) - \sum_{k=1}^{n} \frac{\partial f}{\partial p_k}(\boldsymbol{x}_i, \boldsymbol{p}_0) \delta p_k \right) \frac{\partial f}{\partial p_j}(\boldsymbol{x}_i, \boldsymbol{p}_0) = 0. \tag{D.7}$$

With the abbreviation

$$J_{ij} := \frac{\partial f}{\partial p_j}(\boldsymbol{x}_i, \boldsymbol{p}_0), \tag{D.8}$$

this takes the form

$$\sum_{i=1}^{m} J_{ij} (y_i - f(\boldsymbol{x}_i, \boldsymbol{p}_0)) = \sum_{i=1}^{m} \sum_{k=1}^{n} J_{ij} J_{ik} \delta p_k, \tag{D.9}$$

or, as matrix equation,

$$\boldsymbol{J}^T \boldsymbol{r}(\boldsymbol{p}_0) = \boldsymbol{J}^T \boldsymbol{J} \delta \boldsymbol{p}. \tag{D.10}$$

This is a system of linear equations for $\delta \boldsymbol{p}$ that is solved easily[3]:

$$\delta \boldsymbol{p} = (\boldsymbol{J}^T \boldsymbol{J})^{-1} \boldsymbol{J}^T \boldsymbol{r}(\boldsymbol{p}_0). \tag{D.11}$$

---

[3]Provided that the inverse matrix exists. For singular matrices, other procedures such as the singular value decomposition algorithm can be used.

Using eq. D.11, the original guess $\boldsymbol{p}_0$ can be improved by $\boldsymbol{p}_0 \mapsto \boldsymbol{p}_0 + \delta\boldsymbol{p}$. This procedure can subsequently be repeated until self-consistency is reached and $\delta\boldsymbol{p}_{\mathrm{opt}} = \boldsymbol{0}$. The (asymptotic) covariance matrix of the fitted parameters is typically estimated by [115, 116]

$$\boldsymbol{\Sigma} = \frac{S(\boldsymbol{p}_{\mathrm{opt}})}{m - n}(\boldsymbol{J}^T\boldsymbol{J})^{-1}. \tag{D.12}$$

D.2. Background subtraction

One particularly important application of fitting in core-loss EELS is background subtraction. Due to, e.g., multiple scattering effects and the post-edge tails of ionization edges at lower energy-loss, the signal of interest is superimposed on a (possibly quite large) background. Commonly, this is modeled by a power-low [4], i.e.,

$$I_{\mathrm{bg}}(E) = AE^{-r}, \tag{D.13}$$

which is a good approximation over an energy range of some tens of eV.

What is often overlooked, however, is that the original, measured signal I_{m} is noisy, with the uncertainty typically dominated by shot noise ($\sqrt{I_{\mathrm{m}}}$). As a result, the fit parameters used in background subtraction also have certain confidence intervals, as does the extrapolated background I_{bg}. Consequently, the uncertainties of the original signal and of the background estimation accumulate. Ultimately, the noise of the final, background-subtracted data I_{signal}, $\sqrt{I_{\mathrm{m}} + \Delta I_{\mathrm{bg}}^2}$, will be *larger* than that of the *original* dataset. This is contrary to the common assumption that the data processing only acts on the background-subtracted signal $I_{\mathrm{signal}} := I_{\mathrm{m}} - I_{\mathrm{bg}}$ which, in the absence of a better approach, is assumed to be subject to shot-noise (this would result in an uncertainty of $\sqrt{I_{\mathrm{signal}}} = \sqrt{I_{\mathrm{m}} - I_{\mathrm{bg}}}$).

D.2.1. EELS

In EELS, one typically has data for enough energies to fit the background model to the measurement in the pre-edge region. For the purpose of this derivation, the background will be modeled as

$$I_{\mathrm{bg}}(E) = A\left(\frac{E}{\mathscr{E}}\right)^{-r}, \tag{D.14}$$

where $\mathscr{E}$ is a constant. At this point, $\mathscr{E}$ is arbitrary (setting $\mathscr{E} = 1$ gives eq. D.13, for example), but it will be shown below how it can be chosen such that the fit parameters are uncorrelated. The parameter vector in this case is $\boldsymbol{p} = (A, r)^T$, and eq. D.8 takes the form

$$J_{i1} = \frac{\partial I_{\mathrm{bg}}}{\partial A} = \left(\frac{E_i}{\mathscr{E}}\right)^{-r} \qquad J_{i2} = \frac{\partial I_{\mathrm{bg}}}{\partial r} = -A\left(\frac{E_i}{\mathscr{E}}\right)^{-r}\ln\left(\frac{E_i}{\mathscr{E}}\right). \tag{D.15}$$

Consequently, one gets

$$
\begin{aligned}
\boldsymbol{J}^T \boldsymbol{J} &= \begin{pmatrix} \sum_i J_{i1}^2 & \sum_i J_{i1} J_{i2} \\ \sum_i J_{i1} J_{i2} & \sum_i J_{i1}^2 \end{pmatrix} \\
&= \sum_i \left(\frac{E_i}{\mathscr{E}} \right)^{-2r} \begin{pmatrix} 1 & -A \ln \left(\frac{E_i}{\mathscr{E}} \right) \\ -A \ln \left(\frac{E_i}{\mathscr{E}} \right) & \left[A \ln \left(\frac{E_i}{\mathscr{E}} \right) \right]^2 \end{pmatrix}.
\end{aligned}
\tag{D.16}
$$

A and r are uncorrelated if $\boldsymbol{\Sigma}$ is diagonal, which is the case if $(\boldsymbol{J}^T \boldsymbol{J})^{-1}$ is diagonal, which is equivalent to $\boldsymbol{J}^T \boldsymbol{J}$ being diagonal. This, in turn, is the case if

$$
-\sum_i A \left(\frac{E_i}{\mathscr{E}} \right)^{-2r} \ln \left(\frac{E_i}{\mathscr{E}} \right) = 0
$$

$$
\sum_i E_i^{-2r} \ln E_i = \ln \mathscr{E} \sum_i E_i^{-2r}
$$

$$
\ln \mathscr{E} = \frac{\sum_i E_i^{-2r} \ln E_i}{\sum_i E_i^{-2r}}.
\tag{D.17}
$$

Note that this constant does not depend on the data values y_i. However, in order to determine $\mathscr{E}$, it is necessary to know r, which is not the case at the beginning of the procedure. One possibility to remedy this problem is to assume some reasonable value for r (e.g., from literature, previous calculations, first principle considerations, etc.). Another possibility well suited for core-loss EELS is the following: assuming that, for the fit interval $[E_1, E_n]$, $E_n - E_1 \ll E1$ holds, one can use in first order approximation $E_i^{-2r} \approx \bar{E}^{-2r}$, yielding

$$
\ln \mathscr{E} = \frac{\ln E_i}{n} \quad \Rightarrow \quad \mathscr{E} = \left(\prod_i E_i \right)^{\frac{1}{n}}.
\tag{D.18}
$$

D.2.2. EFTEM / EFSAD

In EFTEM, the common background subtraction method is the three-window method, in which one records energy-filtered images for two pre-edge energy ranges and one image in the energy range of interest. From the two pre-edge images, the background is extrapolated and subsequently subtracted from the edge image.

Ideally, all background parameters are determined separately for each pixel (i.e., locally). This is particularly important if the properties of the sample — such as thickness, composition, etc. — change from pixel to pixel, which has a dramatic influence on the shape of the background. This is the typical case when recording EFTEM images in real space. The caveat is that the two parameters of the background model are determined from only two data values. Hence, a good SNR (or, equivalently, a low noise level) is required for this procedure.

If, on the other hand, the SNR is low (or, equivalently, the noise level is high), it is beneficial to determine at least some parameters through fitting to a large data range.

This is possible, e.g., if the power law exponent r does not change from pixel to pixel (which is a good approximation if the sample does not change from pixel to pixel, as is the case, e.g., in EFSAD which works in momentum space and hence always captures the same area of the sample). In such cases, r can be determined from the whole image (i.e., globally), whereas A still has to be determined locally (as it reflects the local intensity variations in the image).

D.2.2.1. Local approach

Because, in EFTEM mode, the spectrometer is set up to integrate over a specific energy range $[E, \tilde{E}]$, the background model has to be modified to read

$$
I_{\text{bg}}(E, \tilde{E}) = A \int_E^{\tilde{E}} \left(\frac{\varepsilon}{\mathscr{E}} \right)^{-r} \mathrm{d}\varepsilon = \frac{A\mathscr{E}}{1-r} \left[\left(\frac{\tilde{E}}{\mathscr{E}} \right)^{1-r} - \left(\frac{E}{\mathscr{E}} \right)^{1-r} \right]
$$

$$
= \frac{A\mathscr{E}^r}{1-r} \left[\tilde{E}^{1-r} - E^{1-r} \right]. \tag{D.19}
$$

Once again, the parameters to determine are $\boldsymbol{p} = (A, r)$, and $\mathscr{E}$ is a constant than can be chosen such that the resulting algorithms (in particular the matrix inversions appearing below) are not ill-conditioned and, hence, numerically stable.

With the measured values $\boldsymbol{y} = (y_1, y_2)$, the background model gives rise to the (nonlinear) system of equations

$$
\boldsymbol{f}(\boldsymbol{p}) = \boldsymbol{y} \qquad \text{with} \qquad f_i(\boldsymbol{p}) := I_{\text{bg}}(E_i, \tilde{E}_i). \tag{D.20}
$$

Dividing the two equations yields

$$
\frac{f_1(\boldsymbol{p})}{f_2(\boldsymbol{p})} = \frac{\tilde{E}_1^{1-r} - E_1^{1-r}}{\tilde{E}_2^{1-r} - E_2^{1-r}} = \frac{y_1}{y_2}, \tag{D.21}
$$

from which r can be determined. Once r is known, it is beneficial to define

$$
\ln \mathscr{E} = \frac{\tilde{E}_1^{1-r} \ln \tilde{E}_1 - E_1^{1-r} \ln E_1}{\tilde{E}_1^{1-r} - E_1^{1-r}} - \frac{1}{1-r}, \tag{D.22}
$$

which fulfills

$$
\tilde{E}_1^{1-r} \left[\frac{1}{1-r} - \ln \left(\frac{\tilde{E}_1}{\mathscr{E}} \right) \right] = E_1^{1-r} \left[\frac{1}{1-r} - \ln \left(\frac{E_1}{\mathscr{E}} \right) \right]. \tag{D.23}
$$

For known r and $\mathscr{E}$, A can be determined easily from either of the two original equations, owing to the fact that they are both linear in A.

Interpreting the solution $\boldsymbol{p}$ as $\boldsymbol{p}(\boldsymbol{y})$ and differentiating eq. D.20 yields

$$
\mathrm{d}\boldsymbol{f}(\boldsymbol{p}(\boldsymbol{y})) \cdot \mathrm{d}\boldsymbol{p}(\boldsymbol{y}) = \boldsymbol{1}, \tag{D.24}
$$

with

$$
\mathrm{d}\boldsymbol{p}(\boldsymbol{y}) = \begin{pmatrix} \frac{\partial f_1}{\partial A} & \frac{\partial f_1}{\partial r} \\ \frac{\partial f_2}{\partial A} & \frac{\partial f_2}{\partial r} \end{pmatrix}
$$

$$
\frac{\partial f_i}{\partial A} = \frac{\mathscr{E}^r}{1-r} \left(\tilde{E}_i^{1-r} - E_i^{1-r} \right)
$$

$$
\frac{\partial f_i}{\partial r} = \frac{A\mathscr{E}^r}{1-r} \left[\tilde{E}_i^{1-r} \left(\frac{1}{1-r} - \ln\left(\frac{\tilde{E}_i}{\mathscr{E}}\right) \right) - E_i^{1-r} \left(\frac{1}{1-r} - \ln\left(\frac{E_i}{\mathscr{E}}\right) \right) \right].
$$

(D.25)

Owing to the definition of $\mathscr{E}$, this simplifies to the lower triangular matrix

$$
\mathrm{d}\boldsymbol{p}(\boldsymbol{y}) = \begin{pmatrix} \frac{\partial f_1}{\partial A} & 0 \\ \frac{\partial f_2}{\partial A} & \frac{\partial f_2}{\partial r} \end{pmatrix},
$$

(D.26)

which, after rearranging, gives

$$
\mathrm{d}\boldsymbol{p}(\boldsymbol{y}) = (\mathrm{d}\boldsymbol{f}(\boldsymbol{p}(\boldsymbol{y})))^{-1} = \frac{1}{\frac{\partial f_1}{\partial A}\frac{\partial f_2}{\partial r}} \begin{pmatrix} \frac{\partial f_2}{\partial r} & 0 \\ -\frac{\partial f_2}{\partial A} & \frac{\partial f_1}{\partial A} \end{pmatrix}.
$$

(D.27)

Thus, the covariance matrix of $\boldsymbol{p}$ reads

$$
\boldsymbol{\Sigma_p} = (\mathrm{d}\boldsymbol{f}(\boldsymbol{p}))^{-1} \cdot \boldsymbol{\Sigma_y} \cdot \left((\mathrm{d}\boldsymbol{f}(\boldsymbol{p}))^{-1} \right)^T.
$$

(D.28)

For the uncertainty of the background prediction in the edge range $[E_3, \tilde{E}_3]$, this gives

$$
\sigma^2 = \boldsymbol{\iota} \cdot (\mathrm{d}\boldsymbol{f}(\boldsymbol{p}))^{-1} \cdot \boldsymbol{\Sigma_y} \cdot \left((\mathrm{d}\boldsymbol{f}(\boldsymbol{p}))^{-1} \right)^T \cdot \boldsymbol{\iota}^T
$$

(D.29)

with

$$
\boldsymbol{\iota}^T = \frac{\mathscr{E}^r}{1-r} \begin{pmatrix} \left(\tilde{E}_3^{1-r} - E_3^{1-r} \right) \\ A\left[\tilde{E}_3^{1-r} \left(\frac{1}{1-r} - \ln\left(\frac{\tilde{E}_3}{\mathscr{E}}\right) \right) - E_3^{1-r} \left(\frac{1}{1-r} - \ln\left(\frac{E_3}{\mathscr{E}}\right) \right) \right] \end{pmatrix}.
$$

(D.30)

D.2.2.2. Global approach

In the global approach, one first uses a weighted sum instead of eq. D.21, i.e., one determines r from

$$
\frac{\tilde{E}_1^{1-r} - E_1^{1-r}}{\tilde{E}_2^{1-r} - E_2^{1-r}} = \frac{1}{\sum_{i=1}^m w_i} \sum_{i=1}^m w_i \frac{y_{1,i}}{y_{2,i}} =: \frac{\sum_{i=1}^m w_i \nu_i}{\sum_{i=1}^m w_i},
$$

(D.31)

where the uncertainties of the ν_i are calculated using the normal propagation of uncertainty formalism. The weights w_i typically reflect the quality of a data point and are usually chosen as

$$
w_i := \frac{1}{\sigma_{\nu_i}},
$$

(D.32)

in which case the right hand side has an uncertainty of

$$\sigma_y := \frac{\sqrt{m}}{\sum_{i=1}^m w_i} = \frac{\sqrt{m}}{\sum_{i=1}^m \frac{1}{\sigma_{\nu_i}}}. \tag{D.33}$$

The uncertainty of r thus takes the form

$$\sigma_r = \frac{(\tilde{E}_2^{1-r} - E_2^{1-r})^2}{\left| \tilde{E}_2^{1-r} \left[\tilde{E}_1^{1-r} \ln\left(\frac{\tilde{E}_1}{\tilde{E}_2}\right) - E_1^{1-r} \ln\left(\frac{E_1}{\tilde{E}_2}\right) \right] - E_2^{1-r} \left[\tilde{E}_1^{1-r} \ln\left(\frac{\tilde{E}_1}{E_2}\right) - E_1^{1-r} \ln\left(\frac{E_1}{E_2}\right) \right] \right|} \sigma_y. \tag{D.34}$$

With the knowledge of r, A can be determined easily on a per-pixel basis by fitting to the two data values (y_1, y_2) (using, e.g., $\mathscr{E} = \sqrt{E_1 \tilde{E}_1})^4$. Since the background model is linear in A, this can be done analytically, yielding

$$A = \frac{y_1 f_1 + y_2 f_2}{f_1^2 + f_2^2} \qquad \text{with} \qquad f_i := \mathscr{E}^r \frac{\tilde{E}_i^{1-r} - E_i^{1-r}}{1-r}. \tag{D.35}$$

The variance of A reads[5]

$$\sigma_A^2 = \frac{\sigma_{y_1}^2}{f_1^2} + \frac{\sigma_{y_2}^2}{f_2^2} + \frac{f_1'^2 \left[y_1 \left(f_2^2 - f_1^2 \right) - 2 y_2 f_1 f_2 \right]^2 + f_2'^2 \left[y_2 \left(f_1^2 - f_2^2 \right) - 2 y_1 f_1 f_2 \right]^2}{\left[f_1^2 + f_2^2 \right]^4} \sigma_r^2 \tag{D.36}$$

with

$$f_i' = \frac{\mathscr{E}^r}{1-r} \left[\tilde{E}_i^{1-r} \left(\frac{1}{1-r} - \ln\left(\frac{\tilde{E}_i}{\mathscr{E}}\right) \right) - E_i^{1-r} \left(\frac{1}{1-r} - \ln\left(\frac{E_i}{\mathscr{E}}\right) \right) \right]. \tag{D.37}$$

Finally, the extrapolated background can be calculated, which has the variance

$$\sigma^2 = \mathscr{E}^{2r} \left(\frac{\tilde{E}_3^{1-r} - E_3^{1-r}}{1-r} \right)^2 \sigma_A^2 + A^2 f_3'^2 \sigma_r^2. \tag{D.38}$$

---

[4]As above, the choice of $\mathscr{E}$ influences the numerical stability and also the statistical error of the fit. Because of the complex dependence of the fit error on $\mathscr{E}$ it is not feasible to look for an analytical expression for $\mathscr{E}$; one has to use an approximation instead.

[5]Note that, due to the approach and the approximations used here, A and r are considered independent.

Bibliography

[1] J. Repp, G. Meyer, S. M. Stojković, A. Gourdon, and C. Joachim. "Molecules on Insulating Films: Scanning-Tunneling Microscopy Imaging of Individual Molecular Orbitals". *Phys. Rev. Lett.*, 94 p. 026803, 2005. doi: 10.1103/PhysRevLett.94.026803.

[2] J. Repp, G. Meyer, S. Paavilainen, F. E. Olsson, and M. Persson. "Imaging Bond Formation Between a Gold Atom and Pentacene on an Insulating Surface". *Science*, 312 (5777) pp. 1196–1199, 2006. doi: 10.1126/science.1126073.

[3] D. B. Williams and C. B. Carter. *Transmission electron microscopy* (Plenum Press, New York, 1996). ISBN 0-306-45247-2.

[4] R. F. Egerton. *Electron Energy-Loss Spectroscopy in the Electron Microscope* (Plenum, 1996), 2nd ed. ISBN 0-306-45223-5.

[5] M. Knoll and E. Ruska. "Das Elektronenmikroskop". *Zeitschrift für Physik*, 78 (5–6) pp. 318–339, 1932. doi: 10.1007/BF01342199.

[6] M. Haider, H. Rose, S. Uhlemann, E. Schwan, B. Kabius, and K. Urban. "A spherical-aberration-corrected 200 kV transmission electron microscope". *Ultramicroscopy*, 75 (1) pp. 53–60, 1998. doi: 10.1016/S0304-3991(98)00048-5.

[7] N. F. Mott and H. S. W. Massey. *The Theory of Atomic Collisions* (Oxford University Press, 1965), 3rd ed. ISBN 978-0198512424.

[8] W. Glaser. *Grundlagen der Elektronenoptik* (Springer-Verlag, 1952).

[9] B. Jouffrey, P. Schattschneider, and C. Hébert. "The magic angle: a solved mystery". *Ultramicroscopy*, 102 (1) pp. 61–66, 2004. doi: 10.1016/j.ultramic.2004.08.006.

[10] R. Egerton. "Quantitative analysis of electron-energy-loss spectra". *Ultramicroscopy*, 28 (1–4) pp. 215–225, 1989. doi: 10.1016/0304-3991(89)90299-4.

[11] A. Berger and H. Kohl. "Optimum imaging parameters for elemental mapping in an energy filtering transmission electron microscope". *Optik*, 92 (4) pp. 175–193, 1993.

[12] P. E. Batson and J. Silcox. "Experimental energy-loss function, Im$[-\frac{1}{\epsilon}(q,\omega)]$, for aluminum". *Phys. Rev. B*, 27 (9) pp. 5224–5239, 1983. doi: 10.1103/PhysRevB.27.5224.

[13] K. Blum. *Density Matrix Theory and Applications.* Physics of Atoms and Molecules (Springer, 1996), 2nd ed. ISBN 0-306-45341-X.

[14] E. Merzenbacher. *Quantum Mechanics* (John Wiley & Sons, Inc., 1998), 3rd ed. ISBN 0-471-88702-1.

[15] U. Fano. "Description of States in Quantum Mechanics by Density Matrix and Operator Techniques". *Rev. Mod. Phys.*, 29 pp. 74–93, 1957. doi: 10.1103/RevModPhys.29.74.

[16] P. Schattschneider, M. Nelhiebel, H. Souchay, and B. Jouffrey. "The physical significance of the mixed dynamic form factor". *Micron*, 31 (4) pp. 333–345, 2000. doi: 10.1016/S0968-4328(99)00112-2.

[17] J. Taftø and J. C. H. Spence. "Crystal Site Location of Iron and Trace Elements in a Magnesium-Iron Olivine by a New Crystallographic Technique". *Science*, 218 (4567) pp. 49–51, 1982. doi: 10.1126/science.218.4567.49.

[18] J. C. H. Spence and J. Taftø. "ALCHEMI: a new technique for locating atoms in small crystals". *Journal of Microscopy-Oxford*, 130 (2) pp. 147–154, 1983. doi: 10.1111/j.1365-2818.1983.tb04213.x.

[19] O. L. Krivanek, M. M. Disko, J. Taftø, and J. C. H. Spence. "Electron energy loss spectroscopy as a probe of the local atomic environment". *Ultramicroscopy*, 9 (3) pp. 249–254, 1982. doi: 10.1016/0304-3991(82)90208-X.

[20] W. Hetaba. *Fine structure and site specific energy loss spectra of NiO.* Master's thesis, Vienna University of Technology, 2011.

[21] C. Dwyer and J. Etheridge. "Scattering of Å-scale electron probes in silicon". *Ultramicroscopy*, 96 (3–4) pp. 343–360, 2003. doi: 10.1016/S0304-3991(03)00100-1.

[22] J. Rusz, S. Rubino, and P. Schattschneider. "First-principles theory of chiral dichroism in electron microscopy applied to 3d ferromagnets". *Phys. Rev. B*, 75 (21) 214425, 2007. doi: 10.1103/PhysRevB.75.214425.

[23] S. Löffler and P. Schattschneider. "A software package for the simulation of energy-loss magnetic chiral dichroism". *Ultramicroscopy*, 110 (7) pp. 831–835, 2010. doi: 10.1016/j.ultramic.2010.02.044.

[24] M. Nelhiebel. *Effects of crystal orientation and interferometry in electron energy loss spectroscopy.* Ph.D. thesis, École Centrale Paris, Châtenay-Malabry, 1999.

[25] J. J. Sakurai and J. Napolitano. *Modern quantum mechanics* (Addison-Wesley, 2011), 2nd ed. ISBN 978-0-8053-8291-4.

[26] P. Stadelmann. "Dynamical theory of elastic electron diffraction at small angles". Tech. rep., École polytechnique fédérale de Lausanne, 2003. Distributed with JEMS [118].

[27] C. Cohen-Tannoudji, B. Diu, and Laloë. *Quantenmechanik.* 1 (Walter de Gruyter, 1999), 2$^{\text{nd}}$ ed. ISBN 3-11-016458-2.

[28] P. Schattschneider and J. Verbeeck. "Theory of free electron vortices". *Ultramicroscopy*, 111 (9–10) pp. 1461–1468, 2011. doi: 10.1016/j.ultramic.2011.07.004.

[29] L. C. Green, S. Matsushima, and E. K. Kolchin. "Tables of the Continuum Wave Functions for Hydrogen." *Astrophysical Journal Supplement*, 3 p. 459, 1958. doi: 10.1086/190041.

[30] G. B. Arfken and H. J. Weber. *Mathematical Methods for Physicists* (Academic Press, 1995), 4$^{\text{th}}$ ed. ISBN 0-12-059816-7.

[31] M. Abramowitz and I. A. Stegun (eds.). *Handbook of mathematical functions* (Dover, 1965). ISBN 0-486-61272-4. Also avavilable online at `http://people.math.sfu.ca/~cbm/aands/`.

[32] K.-J. Hanßen and L. Trepte. "Die Kontrastübertragung im Elektronenmikroskop bei partiell kohärenter Beleuchtung, Teil A: Ringkondensor". *Optik*, 33 (2) pp. 166–181, 1971.

[33] B. J. McMorran, A. Agrawal, I. M. Anderson, A. A. Herzing, H. J. Lezec, J. J. McClelland, and J. Unguris. "Electron Vortex Beams with High Quanta of Orbital Angular Momentum". *Science*, 331 (6014) pp. 192–195, 2011. doi: 10.1126/science.1198804.

[34] A. R. Edmonds. *Angular momentum in quantum mechanics* (Princeton University Press, 1957). ISBN 0-691-07912-9.

[35] C. Huygens. *Traité de la lumière* (Leyden, 1690).

[36] W. Raith, L. Bergmann, and C. Schaefer (eds.). *Lehrbuch der Experimentalphysik. 2. Elektromagnetismus* (de Gruyter, 1999). ISBN 3-11-016097-8.

[37] E. J. Kirkland. *Advanced computing in electron microscopy* (Plenum Press, 1998). ISBN 0-306-45936-1.

[38] J. Verbeeck, H. Tian, and P. Schattschneider. "Production and application of electron vortex beams". *Nat.*, 467 (7313) pp. 301–304, 2010. doi: 10.1038/nature09366.

[39] M. Uchida and A. Tonomura. "Generation of electron beams carrying orbital angular momentum". *Nat.*, 464 pp. 737–739, 2010. doi: 10.1038/nature08904.

[40] J. Verbeeck, P. Schattschneider, S. Lazar, M. Stöger-Pollach, S. Löffler, A. Steiger-Thirsfeld, and G. Van Tendeloo. "Atomic scale electron vortices for nanoresearch". *Appl. Phys. Lett.*, 99 (20) 203109, 2011. doi: 10.1063/1.3662012.

[41] P. Schattschneider, M. Stöger-Pollach, S. Löffler, A. Steiger-Thirsfeld, J. Hell, and J. Verbeeck. "Sub-nanometer free electrons with topological charge". *Ultramicroscopy*, 115 (0) pp. 21 – 25, 2012. doi: 10.1016/j.ultramic.2012.01.010.

[42] G. K. Ackermann and J. Eichler. *Holography* (WILEY-VCH, 2007). ISBN 3-527-40663-8.

[43] A. Tonomura. *Electron holography* (Springer, 1999). ISBN 3-540-64555-1.

[44] A. I. Kirkland and R. R. Meyer. ""Indirect" High-Resolution Transmission Electron Microscopy: Aberration Measurement and Wavefunction Reconstruction". *Microsc. Microanal.*, 10 pp. 401–413, 2004. doi: 10.1017/S1431927604040437.

[45] E. J. Kirkland. "Nonlinear high resolution image processing of conventional transmission electron micrographs: I. Theory". *Ultramicroscopy*, 9 (1–2) pp. 45–64, 1982. doi: 10.1016/0304-3991(82)90228-5.

[46] E. J. Kirkland, B. Siegel, N. Uyeda, and Y. Fujiyoshi. "Nonlinear high resolution image processing of conventional transmission electron micrographs: II. Experiment". *Ultramicroscopy*, 9 (1–2) pp. 65–74, 1982. doi: 10.1016/0304-3991(82)90229-7.

[47] S. Rubino. *Magnetic circular dichroism in the transmission electron microscope.* Ph.D. thesis, Vienna University of Technology, 2008.

[48] L.-M. Peng, G. Ren, S. L. Dudarev, and M. J. Whelan. "Robust Parameterization of Elastic and Absorptive Electron Atomic Scattering Factors". *Acta Cryst. A*, 52 (2) pp. 257–276, 1996. doi: 10.1107/S0108767395014371.

[49] P. Blaha, K. Schwarz, G. Madsen, D. Kvasnicka, and J. Luitz. "WIEN2k, An Augmented Plane Wave + Local Orbitals Program for Calculating Crystal Properties". 2001. URL `http://www.wien2k.at/`. (Karlheinz Schwarz, Techn. Universität Wien, Austria).

[50] P. Villars and L. D. Calvert. *Pearson's handbook of crystallographic data for intermetallic phases*, vol. 4 (ASM International, 1991), 2nd ed. ISBN 0-87170-420-X.

[51] J. Verbeeck, P. Schattschneider, and A. Rosenauer. "Image simulation of high resolution energy filtered TEM images". *Ultramicroscopy*, 109 (4) pp. 350–360, 2009. doi: 10.1016/j.ultramic.2009.01.003.

[52] J. M. Cowley and A. F. Moodie. "The scattering of electrons by atoms and crystals. I. A new theoretical approach". *Acta Crystallogr.*, 10 (10) pp. 609–619, 1957. doi: 10.1107/S0365110X57002194.

[53] S. Löffler and P. Schattschneider. "Elastic propagation of fast electron vortices through crystals". *Acta Cryst. A*, 68 pp. 443 – 447, 2012. doi: 10.1107/S0108767312013189.

[54] D. van Dyck. "Improved methods for the high speed calculation of electron microscopic structure images". *Physica Status Solidi (a)*, 52 (1) pp. 283–292, 1979. doi: 10.1002/pssa.2210520131.

[55] C. Y. Cai, S. J. Zeng, H. R. Liu, and Q. B. Yang. "Computational comparison of the conventional multislice method and the real space multislice method for simulating exit wavefunctions". *Micron*, 40 (3) pp. 313–319, 2009. doi: 10.1016/j.micron.2008.11.003.

[56] A. Lubk, L. Clark, G. Guzzinati, and J. Verbeeck. "Topological analysis of paraxially scattered electron vortex beams". *Phys. Rev. A*, 87 p. 033834, 2013. doi: 10.1103/PhysRevA.87.033834.

[57] H. L. Xin and H. Zheng. "On-Column 2p Bound State with Topological Charge 1 Excited by an Atomic-Size Vortex Beam in an Aberration-Corrected Scanning Transmission Electron Microscope". *Microsc. Microanal.*, 18 pp. 711–719, 2012. doi: 10.1017/S1431927612000499.

[58] S. Löffler, V. Motsch, and P. Schattschneider. "A pure state decomposition approach of the mixed dynamic form factor for mapping atomic orbitals". *Ultramicroscopy*, 131 pp. 39 – 45, 2013. doi: 10.1016/j.ultramic.2013.03.021.

[59] H. Rose. "Image formation by inelasticallty scattered electrons in electron microscopy". *Optik*, 45 pp. 139–158, 1976.

[60] H. Rose. "Image formation by inelastically scattered electrons in electron microscopy. II." *Optik*, 45 pp. 187–208, 1976.

[61] H. Kohl and H. Rose. "Theory of Image Formation by Inelastically Scattered Electrons in the Electron Microscope". *Advances in Electronics and Electron Physics*, 65 pp. 173–227, 1985. doi: 10.1016/S0065-2539(08)60878-1.

[62] P. Schattschneider, M. Nelhiebel, and B. Jouffrey. "Density matrix of inelastically scattered fast electrons". *Phys. Rev. B*, 59 (16) pp. 10959–10969, 1999. doi: 10.1103/PhysRevB.59.10959.

[63] P. Schattschneider and H. Lichte. "Correlation and the density-matrix approach to inelastic electron holography in solid state plasmas". *Phys. Rev. B*, 71 (4) p. 045130, 2005. doi: 10.1103/PhysRevB.71.045130.

[64] P. Schattschneider. *Fundamentals of inelastic electron scattering* (Springer, 1986). ISBN 3-211-81937-1.

[65] A. Messiah. *Quantenmechanik*, vol. 1 (de Gruyter, 1991), 2nd ed. ISBN 3-11-011452-6.

[66] G. M. Wysin. "Probability Current and Current Operators in Quantum Mechanics". Tech. rep., Kansas State University, 2011. URL `http://www.phys.ksu.edu/personal/wysin/notes/qmcurrent.pdf`. Accessed online 8. Feb. 2013.

[67] C. Cohen-Tannoudji, B. Diu, and Laloë. *Quantenmechanik.* 2 (Walter de Gruyter, 1999), 2nd ed. ISBN 3-11-016459-0.

[68] P. Schattschneider, S. Rubino, C. Hebert, J. Rusz, J. Kunes, P. Novák, E. Carlino, M. Fabrizioli, G. Panaccione, and G. Rossi. "Detection of magnetic circular dichroism using a transmission electron microscope". *Nat.*, 441 pp. 486–488, 2006. doi: 10.1038/nature04778.

[69] J. M. Auerhammer and P. Rez. "Dipole-forbidden excitations in electron-energy-loss spectroscopy". *Phys. Rev. B*, 40 (4) pp. 2024–2030, 1989. doi: 10.1103/PhysRevB.40.2024.

[70] K. Jorissen. *The ab initio calculation of relativistic electron energy loss spectra.* Ph.D. thesis, Universiteit Antwerpen, 2007.

[71] C. Hurm. *Towards an unambiguous Electron Magnetic Chiral Dichroism (EMCD) measurement in a Transmission Electron Microscope (TEM).* Ph.D. thesis, Universität Regensburg, 2008.

[72] P. Schattschneider, I. Ennen, S. Löffler, M. Stöger-Pollach, and J. Verbeeck. "Circular dichroism in the electron microscope: Progress and applications (invited)". *J. Appl. Phys.*, 107 (9) 09D311, 2010. doi: 10.1063/1.3365517.

[73] V. Motsch. *Diagonalization of the Mixed Dynamic Form Factor for mapping orbital information.* Master's thesis, Vienna University of Technology, 2012.

[74] A. D'Alfonso, S. Findlay, M. Oxley, and L. Allen. "Volcano structure in atomic resolution core-loss images". *Ultramicroscopy*, 108 (7) pp. 677–687, 2008. doi: 10.1016/j.ultramic.2007.10.011.

[75] K. Tatsumi and S. Muto. "Local electronic structure analysis by site-selective ELNES using electron channeling and first-principles calculations". *J. Phys.: Condens. Matter*, 21 (10) p. 104213, 2009. doi: 10.1088/0953-8984/21/10/104213.

[76] P. Schattschneider, J. Verbeeck, and A. Hamon. "Real space maps of atomic transitions". *Ultramicroscopy*, 109 (7) pp. 781–787, 2009. doi: 10.1016/j.ultramic.2009.01.016.

[77] P. Schattschneider, J. Verbeeck, V. Mauchamp, M. Jaouen, and A.-L. Hamon. "Real-space simulations of spin-polarized electronic transitions in iron". *Phys. Rev. B*, 82 p. 144418, 2010. doi: 10.1103/PhysRevB.82.144418.

[78] S. Löffler and P. Schattschneider. "Transition probability functions for applications of inelastic electron scattering". *Micron*, 43 (9) pp. 971 – 977, 2012. doi: 10.1016/j.micron.2012.03.020.

[79] J. C. Slater. "Atomic Shielding Constants". *Phys. Rev.*, 36 (1) pp. 57–64, 1930. doi: 10.1103/PhysRev.36.57.

[80] E. Clementi and D. L. Raimondi. "Atomic Screening Constants from SCF Functions". *The Journal of Chemical Physics*, 38 (11) pp. 2686–2689, 1963. doi: 10.1063/1.1733573.

[81] K. Jorissen, J. Luitz, and C. Hébert. in preparation.

[82] J. C. Meyer, C. Kisielowski, R. Erni, M. D. Rossell, M. F. Crommie, and A. Zettl. "Direct Imaging of Lattice Atoms and Topological Defects in Graphene Membranes". *Nano Lett.*, 8 (11) pp. 3582–3586, 2008. doi: 10.1021/nl801386m.

[83] J. C. Meyer, A. Chuvilin, G. Algara-Siller, J. Biskupek, and U. Kaiser. "Selective Sputtering and Atomic Resolution Imaging of Atomically Thin Boron Nitride Membranes". *Nano Lett.*, 9 (7) pp. 2683–2689, 2009. doi: 10.1021/nl9011497.

[84] J. Taftø and Z. Liliental. "Studies of the cation atom distribution in $ZnCr_xFe_{2-x}O_4$ spinels using the channeling effect in electron-induced X-ray emission". *J. Appl. Crystallogr.*, 15 (3) pp. 260–265, 1982. doi: 10.1107/S0021889882011960.

[85] A. P. Pogany and P. S. Turner. "Reciprocity in electron diffraction and microscopy". *Acta Cryst. A*, 24 (1) pp. 103–109, 1968. doi: 10.1107/S0567739468000136.

[86] J. M. Cowley. "Image Contrast in a Transmission Scanning Electron Microscope". *Appl. Phys. Lett.*, 15 (2) pp. 58–59, 1969. doi: 10.1063/1.1652901.

[87] Y. Kainuma. "The Theory of Kikuchi patterns". *Acta Crystallogr.*, 8 (5) pp. 247–257, 1955. doi: 10.1107/S0365110X55000832.

[88] S. Löffler, I. Ennen, F. Tian, P. Schattschneider, and N. Jaouen. "Breakdown of the Dipole Approximation in Core Losses". *Ultramicroscopy*, 111 pp. 1163 – 1167, 2011. doi: 10.1016/j.ultramic.2011.03.006.

[89] C. Hébert, A. Alkauskas, S. Löffler, B. Jouffrey, and P. Schattschneider. "Capturing EELS in the reciprocal space". *European Physical Journal - Applied Physics*, 54 p. 33510, 2011. doi: 10.1051/epjap/2011100469.

[90] I. Ennen, S. Löffler, C. Kübel, D. Wang, A. Auge, A. Hütten, and P. Schattschneider. "Site-specific chirality in magnetic transitions". *J. Magn. Magn. Mater.*, 324 (18) pp. 2723 – 2726, 2012. doi: 10.1016/j.jmmm.2012.03.050.

[91] P. Schattschneider, B. Schaffer, I. Ennen, and J. Verbeeck. "Mapping spin-polarized transitions with atomic resolution". *Phys. Rev. B*, 85 p. 134422, 2012. doi: 10.1103/PhysRevB.85.134422.

[92] M. Stöger-Pollach, H. Franco, P. Schattschneider, S. Lazar, B. Schaffer, W. Grogger, and H. Zandbergen. "Čerenkov losses: A limit for bandgap determination and Kramers-Kronig analysis". *Micron*, 37 (5) pp. 396–402, 2006. doi: 10.1016/j.micron.2006.01.001.

[93] H. Lidbaum, J. Rusz, S. Rubino, A. Liebig, B. Hjörvarsson, P. M. Oppeneer, O. Eriksson, and K. Leifer. "Reciprocal and real space maps for EMCD experiments". *Ultramicroscopy*, 110 (11) pp. 1380–1389, 2010. doi: 10.1016/j.ultramic.2010.07.004.

[94] D. Eyidi, C. Hébert, and P. Schattschneider. "Short note on parallel illumination in the TEM". *Ultramicroscopy*, 106 (11–12) pp. 1144–1149, 2006. doi: 10.1016/j.ultramic.2006.04.029.

[95] O. L. Krivanek, C. C. Ahn, R. P. Burgner, M. M. Disko, and P. R. Swann. *EELS Atlas* (ASU HREM facility and Gatan Inc., 1983).

[96] L. A. Grunes, R. D. Leapman, C. N. Wilker, R. Hoffmann, and A. B. Kunz. "Oxygen K near-edge fine structure: An electron-energy-loss investigation with comparisons to new theory for selected 3d Transition-metal oxides". *Phys. Rev. B*, 25 pp. 7157–7173, 1982. doi: 10.1103/PhysRevB.25.7157.

[97] B. Jiang, J. M. Zuo, N. Jiang, M. O'Keeffe, and J. C. H. Spence. "Charge density and chemical bonding in rutile, TiO_2". *Acta Cryst. A*, 59 (4) pp. 341–350, 2003. doi: 10.1107/S010876730301122X.

[98] P. Schattschneider (ed.). *Linear and Chiral Dichroism in the Electron Microscope* (Pan Stanford Publishing Pte Ltd., 2011). ISBN 9789814267489.

[99] P. Schattschneider. "Exchange of angular momentum in EMCD experiments". *Ultramicroscopy*, 109 (1) pp. 91–95, 2008. doi: 10.1016/j.ultramic.2008.08.004.

[100] C. Hébert and P. Schattschneider. "A proposal for dichroic experiments in the electron microscope". *Ultramicroscopy*, 96 (3–4) pp. 463–468, 2003. doi: 10.1016/S0304-3991(03)00108-6.

[101] J. Verbeeck, C. Hébert, S. Rubino, P. Novák, J. Rusz, F. Houdellier, C. Gatel, and P. Schattschneider. "Optimal aperture sizes and positions for EMCD experiments". *Ultramicroscopy*, 108 (9) pp. 865–872, 2008. doi: 10.1016/j.ultramic.2008.02.007.

[102] J. Rusz, O. Eriksson, P. Novák, and P. M. Oppeneer. "Sum rules for electron energy loss near edge spectra". *Phys. Rev. B*, 76 (6) 060408, 2007. doi: 10.1103/PhysRevB.76.060408.

[103] L. Calmels, F. Houdellier, B. Warot-Fonrose, C. Gatel, M. J. Hÿtch, V. Serin, E. Snoeck, and P. Schattschneider. "Experimental application of sum rules for electron energy loss magnetic chiral dichroism". *Phys. Rev. B*, 76 (6) 060409, 2007. doi: 10.1103/PhysRevB.76.060409.

[104] P. Schattschneider, S. Löffler, M. Stöger-Pollach, and J. Verbeeck. "Is magnetic chiral dichroism feasible with electron vortices?" *Ultramicroscopy*, 136 pp. 81–85, 2014. doi: 10.1016/j.ultramic.2013.07.012.

[105] P. Schattschneider, I. Ennen, M. Stöger-Pollach, J. Verbeeck, V. Mauchamp, and M. Jaouen. "Real space maps of magnetic moments on the atomic scale: Theory and feasibility". *Ultramicroscopy*, 110 (8) pp. 1038–1041, 2010. doi: 10.1016/j.ultramic.2009.11.020.

[106] S. Cottenier. *Density Functional Theory and the family of (L)APW-methods: a step-by-step introduction* (2013), 2nd ed. ISBN 978-90-807215-1-7. Freely available at `http://www.wien2k.at/`.

[107] P. Hohenberg and W. Kohn. "Inhomogeneous Electron Gas". *Phys. Rev.*, 136 (3B) pp. B864–B871, 1964. doi: 10.1103/PhysRev.136.B864.

[108] W. Kohn and L. J. Sham. "Self-Consistent Equations Including Exchange and Correlation Effects". *Phys. Rev.*, 140 pp. A1133–A1138, 1965. doi: 10.1103/PhysRev.140.A1133.

[109] K. Schwarz, P. Blaha, and G. Madsen. "Electronic structure calculations of solids using the WIEN2k package for material sciences". *Computer Physics Communications*, 147 (1–2) pp. 71–76, 2002. doi: 10.1016/S0010-4655(02)00206-0.

[110] W. Hetaba, P. Blaha, F. Tran, and P. Schattschneider. "Calculating energy loss spectra of NiO: Advantages of the modified Becke-Johnson potential". *Phys. Rev. B*, 85 p. 205108, 2012. doi: 10.1103/PhysRevB.85.205108.

[111] M. Zauner. *Multislice Approach for High Resolution Energy Filtered Inelastic Image Simulation*. Master's thesis, Vienna University of Technology, 2010.

[112] S. Mauch. "Introduction to Methods of Applied Mathematics or: Advanced Mathematical Methods for Scientists and Engineers". Tech. rep., California Institute of Technology, 2004. URL `http://www.its.caltech.edu/~sean/book.html`. (accessed Oct. 2, 2013).

[113] P. Uginčius. "An Integral Representation for the Dirac Delta Function". *American Journal of Physics*, 40 (11) pp. 1690–1691, 1972. doi: 10.1119/1.1987016.

[114] M. Reiher and A. Wolf. *Relativistic Quantum Chemistry: The Fundamental Theory of Molecular Science* (Wiley-VCH, 2009). ISBN 9783527312924. doi: 10.1002/9783527627486.

[115] G. A. F. Seber and C. J. Wild. *Nonlinear Regression* (John Wiley & Sons, Inc., 2003). ISBN 0-471-47135-6.

[116] P. T. Boggs and J. E. Rogers. "The Computation and Use of the Asymptotic Covariance Matrix for Measurement Error Models". Tech. rep., National Institute of Standards and Technology, 1990. NISTIR 89—4102.

[117] H. H. Ku. "Notes on the Use of Propagation of Error Formulas". *Journal of Research of the National Bureau of Standards*, 70C pp. 263–273, 1966.

[118] P. Stadelmann. "EMS - a software package for electron diffraction analysis and HREM image simulation in materials science". *Ultramicroscopy*, 21 (2) pp. 131–145, 1987. doi: 10.1016/0304-3991(87)90080-5.

Index

Stefan Löffler
Curriculum vitae

✉ *stefan.loeffler@tuwien.ac.at*

26. 04. 1984	**Born in Vienna**.

Education

1990–1994	**Volksschule Kreindlgasse 24**, *Vienna, Austria*.
1994–2002	**AHS BG 19 Gymnasiumstraße 83**, *Vienna, Austria*.
2003	**Military service**, *Austria*.
2003–2009	**Study of technical physics at the Vienna University of Technology**, *Vienna, Austria*.
2005	**BEST summer course: Sim Robots**, *Lund, Sweden*.
2007	**Exchange semester**, *Uppsala, Sweden*.
2009–2013	**PhD at Vienna University of Technology**, *Vienna, Austria*.

Teaching

2006–2009	**Tutor**, *Vienna University of Technology*. Analysis 2, Electrodynamics and Special Relativity, Fundamentals of Physics
2009–2011	**Lecturer**, *Vienna University of Technology*. Fundamentals of Physics (exercises)

Prizes and Awards

1998	**1st place in the internet competition cyber-school**.
2001	**3rd place in the BCG contest business@school**.
2002	**2nd place in the Austrian Mathematical Olympiad**.
2004	**Achievement scholarship**, *Vienna University of Technology*.
2005	**1st place in BEST summer course: Sim Robots**.
2007	**Participation in the High excellency program TUtheTop**, *Vienna University of Technology*.
2011	**Fritz Grasenick Award**, *Austrian Society of Electron Microscopy*.

Publications

Oct. 2013	h index = 6 (source: Scopus)
since 2012	Reviewer for Ultramicroscopy

Papers in peer-reviewed journals

E. Auer, A. Lugstein, S. Löffler, Y.-J. Hyun, W. Brezna, E. Bertagnolli, P. Pongratz. "Ultrafast VLS growth of epitaxial β-Ga_2O_3 nanowires". *Nanotechnology*, 20 (43), 434017, 2009. doi: 10.1088/0957-4484/20/43/434017.

S. Löffler, P. Schattschneider. "A software package for the simulation of energy-loss magnetic chiral dichroism". *Ultramicroscopy*, 110 (7), 831, 2010. doi: 10.1016/j.ultramic.2010.02.044.

P. Schattschneider, I. Ennen, S. Löffler, M. Stöger-Pollach, J. Verbeeck. "Circular dichroism in the electron microscope: Progress and applications (invited)". *J. Appl. Phys.*, 107 (9), 09D311, 2010. doi: 10.1063/1.3365517.

S. Löffler, E. Auer, M. Weil, A. Lugstein, E. Bertagnolli. "Impact of growth temperature on the crystal habits, forms and structures of VO_2 nanocrystals". *Applied Physics A: Materials Science & Processing*, 102, 201, 2011. doi: 10.1007/s00339-010-5940-5.

C. Hébert, A. Alkauskas, S. Löffler, B. Jouffrey, P. Schattschneider. "Capturing EELS in the reciprocal space". *European Physical Journal - Applied Physics*, 54, 33510, 2011. doi: 10.1051/epjap/2011100469.

S. Löffler, I. Ennen, F. Tian, P. Schattschneider, N. Jaouen. "Breakdown of the Dipole Approximation in Core Losses". *Ultramicroscopy*, 111, 1163 , 2011. doi: 10.1016/j.ultramic.2011.03.006.

S. Löffler. "TeXworks — As you like it". *TUGboat*, 32 (2), 133, 2011.

J. Verbeeck, P. Schattschneider, S. Lazar, M. Stöger-Pollach, S. Löffler, A. Steiger-Thirsfeld, G. Van Tendeloo. "Atomic scale electron vortices for nanoresearch". *Appl. Phys. Lett.*, 99 (20), 203109, 2011. doi: 10.1063/1.3662012.

P. Schattschneider, M. Stöger-Pollach, S. Löffler, A. Steiger-Thirsfeld, J. Hell, J. Verbeeck. "Sub-nanometer free electrons with topological charge". *Ultramicroscopy*, 115 (0), 21 , 2012. doi: 10.1016/j.ultramic.2012.01.010.

I. Ennen, S. Löffler, C. Kübel, D. Wang, A. Auge, A. Hütten, P. Schattschneider. "Site-specific chirality in magnetic transitions". *J. Magn. Magn. Mater.*, 324 (18), 2723 , 2012. doi: 10.1016/j.jmmm.2012.03.050.

S. Löffler, P. Schattschneider. "Elastic propagation of fast electron vortices through crystals". *Acta Cryst. A*, 68, 443 , 2012. doi: 10.1107/S0108767312013189.

S. Löffler, P. Schattschneider. "Transition probability functions for applications of inelastic electron scattering". *Micron*, 43 (9), 971 , 2012. doi: 10.1016/j.micron.2012.03.020.

A. Wolff, K. Frese, M. Wißbrock, K. Eckstädt, I. Ennen, W. Hetaba, S. Löffler, A. Regtmeier, P. Thomas, N. Sewald, P. Schattschneider, A. Hütten. "Influence of the synthetic polypeptide c25-mms6 on cobalt ferrite nanoparticle formation". *Journal of Nanoparticle Research*, 14 (10), 1161, 2012. doi: 10.1007/s11051-012-1161-5.

P. Schattschneider, S. Löffler, J. Verbeeck. "Comment on "Quantized orbital angular momentum transfer and magnetic dichroism in the interaction of electron vortices with matter"". *Phys. Rev. Lett.*, 110, 189501, 2013. doi: 10.1103/PhysRevLett.110.189501.

S. Löffler, V. Motsch, P. Schattschneider. "A pure state decomposition approach of the mixed dynamic form factor for mapping atomic orbitals". *Ultramicroscopy*, 131, 39 , 2013. doi: 10.1016/j.ultramic.2013.03.021.

P. Schattschneider, S. Löffler, M. Stöger-Pollach, J. Verbeeck. "Is magnetic chiral dichroism feasible with electron vortices?" *Ultramicroscopy*, 136, 81, 2014. doi: 10.1016/j.ultramic.2013.07.012.

(Co-supervised) Master Theses

S. Löffler. *Synthesis, Analysis and Device Integration of Vanadium-Dioxide Nanowires.* Master's thesis, Vienna University of Technology, 2009.

M. Zauner. *Multislice Approach for High Resolution Energy Filtered Inelastic Image Simulation.* Master's thesis, Vienna University of Technology, 2010.

W. Hetaba. *Fine structure and site specific energy loss spectra of NiO.* Master's thesis, Vienna University of Technology, 2011.

V. Motsch. *Diagonalization of the Mixed Dynamic Form Factor for mapping orbital information.* Master's thesis, Vienna University of Technology, 2012.

Talks

E. Auer, S. Löffler, A. Lugstein, E. Bertagnolli. "Influence of Oxygen and Temperature on β-Ga_2O_3 Nanowire Synthesis". 2nd International Symposium on Transparent Conductive Oxides in Kreta, Greece, 2008.

S. Löffler, A. Lugstein, E. Auer, E. Bertagnolli. "Epitaxial Catalyst-free Growth and Characterization of Nanowires of Strongly Correlated VO_2 Exhibiting a MIT Transition". MRS Fall Meeting 2008 in Boston, USA, 2008.

S. Löffler, I. Ennen, M. Stöger-Pollach, P. Schattschneider. "Energy-Loss Magnetic Chiral Dichroism — Investigating Magnetism on the Nanometer Scale". Junior Scientist Conference in Wien, Austria, 2010.

W. Hetaba, S. Löffler, P. Schattschneider. "Site Selective Analysis Using Electron Channeling". 7. Workshop on EELS & EFTEM in Zürich, Switzerland, 2010.

I. Ennen, S. Löffler, M. Stöger-Pollach, P. Schattschneider, A. Hütten. "Highlights and Applications of Energy Loss Magnetic Chiral Dichroism". 7. Workshop on EELS & EFTEM in Zürich, Switzerland, 2010.

S. Löffler, I. Ennen, M. Stöger-Pollach, P. Schattschneider. "Non-Lorentzian Scattering Behavior in Core-Losses — a Glimpse of Wave Functions". 7. Workshop on EELS & EFTEM in Zürich, Switzerland, 2010.

W. Hetaba, S. Löffler, M. Stöger-Pollach, P. Schattschneider. "Site selective analysis under electron channelling conditions". 1st ASEM Workshop on Advanced Electron Microscopy in Graz, Austria, 2011.

S. Löffler, I. Ennen, M. Stöger-Pollach, P. Schattschneider. "Non-Lorentzian Scattering Behavior in CoreLosses — A Glimpse of Wave Functions". 1st ASEM Workshop on Advanced Electron Microscopy in Graz, Austria, 2011.

S. Löffler, P. Schattschneider, M. Stöger-Pollach, J. Verbeeck. "Propagation of electrons carrying topological charge". Microscopy Conference in Kiel, Germany, 2011.

I. Ennen, S. Löffler, M. Stöger-Pollach, A. Hütten, *P. Schattschneider*. "Magnetic dichroism in the TEM: a tool for the investigation of magnetism on the nanoscale". 10th Multinational Congress on Microscopy in Urbino, Italy, 2011.

P. Schattschneider, J. Verbeeck, S. Löffler, M. Stöger-Pollach. "Electrons with a twist: Chiral electronic transitions and vortex beams (invited)". 10th Multinational Congress on Microscopy in Urbino, Italy, 2011.

S. Löffler. "Magnetic dichroism on the nanoscale (invited)". 3rd ANKA/KNMF Joint Users' Meeting in Karlsruhe, Germany, 2011.

S. Löffler. "Breakdown of the dipole approximation in core losses (invited)". Fritz Grasenick Award Lecture, Wien, Austria, 2012.

P. Schattschneider, S. Löffler, M. Stöger-Pollach, K. Bliokh, J. Verbeeck. "Electron Vortices: A Novel Probe for Electron Microscopy (invited)". 10th Asia-Pacific Microscopy Conference in Perth, Australia, 2012.

A. Wolff, K. Frese, M. Wißbrock, K. Eckstädt, I. Ennen, W. Hetaba, S. Löffler, A. Regtmeier, P. Thomas, N. Sewald, P. Schattschneider, A. Hütten. "Influence of the synthetic polypeptide c25-mms6 on nanoparticle growth". DPG Spring Meeting in Berlin, Germany, 2012.

V. Motsch, S. Löffler, W. Hetaba, P. Schattschneider. "Simulating HR-EFTEM images". 2nd ASEM Workshop on Advanced Electron Microscopy in Salzburg, Austria, 2012.

W. Hetaba, S. Löffler, P. Schattschneider. "Simulations of energy loss spectra: Advances and future prospects". 2nd ASEM Workshop on Advanced Electron Microscopy in Salzburg, Austria, 2012.

T. Schachinger, S. Löffler, P. Schattschneider. "Numerical simulations of classical 200 keV electrons passing atomic magnetostatic dipoles". 2nd ASEM Workshop on Advanced Electron Microscopy in Salzburg, Austria, 2012.

S. Löffler, M. Stöger-Pollach, A. Steiger-Thirsfeld, J. Hell, J. Verbeeck, P. Schattschneider. "Electron vortex beams: a novel probe for nano-analysis". 2nd ASEM Workshop on Advanced Electron Microscopy in Salzburg, Austria, 2012.

S. Löffler, V. Motsch. "Towards Orbital Mapping". Project meeting at the Vienna University of Technology, Wien, Austria, 2012.

W. Hetaba, S. Löffler, P. Schattschneider. "Site-specific elemental analysis under electron channelling conditions". 15th European Microscopy Congress in Manchester, UK, 2012.

J. Verbeeck, H. Tian, A. Béché, S. Lazar, S. Löffler, M. Stöger-Pollach, P. Schattschneider, G. Van Tendeloo. "Vortex electrons as a probe for novel spectroscopic information at the atomic scale (invited)". 15th European Microscopy Congress in Manchester, UK, 2012.

S. Löffler, P. Schattschneider. "Elastic propagation of fast electron vortices through crystals". 15th European Microscopy Congress in Manchester, UK, 2012.

A. Wolff, K. Eckstädt, W. Hetaba, M. Wißbrock, N. Mill, S. Löffler, N. Sewald, P. Schattschneider, A. Hütten. "Synthetic Polypeptide c25-mms6 alters Cobalt Ferrite Nanoparticle Growth". 16. Deutschen Physikerinnentagung der DPG in Freiburg, Germany, 2012.

S. Löffler, V. Motsch, P. Schattschneider. "Optical concepts for mapping atomic orbitals". Meeting on Optical Response in Extended Systems in Wien, Austria, 2012.

T. Schachinger, S. Löffler, M. Stöger-Pollach, A. Steiger-Thirsfeld, P. Schattschneider. "Influences of the objective lens on electron vortices". 3rd ASEM Workshop on Advanced Electron Microscopy in Wien, Austria, 2013.

W. Hetaba, M. Willinger, M. Schuster, S. Löffler, R. Schlögl, P. Schattschneider. "Site-specific ionisation edge fine-structure in the electron microscope". 3rd ASEM Workshop on Advanced Electron Microscopy in Wien, Austria, 2013.

S. Löffler, I. Ennen, C. Kübel, D. Wang, A. Auge, A. Hütten, P. Schattschneider. "Site-specific measurements of magnetic transitions using energy-loss magnetic chiral dichroism". 3rd ASEM Workshop on Advanced Electron Microscopy in Wien, Austria, 2013.

T. Schachinger, S. Löffler, M. Stöger-Pollach, A. Steiger-Thirsfeld, P. Schattschneider. "Electron vortex propagation in the magnetic lens field". Microscopy Conference in Regensburg, Germany, 2013.

P. Schattschneider, M. Stöger-Pollach, S. Löffler, A. Steiger-Thirsfeld, K. Bliokh. "Mode conversion, peculiar rotations, and the Landau-Zeeman-Berry phase in electron vortex beams (invited)". Microscopy Conference in Regensburg, Germany, 2013.

P. Schattschneider, M. Stöger-Pollach, S. Löffler, T. Schachinger, K. Bliokh. "Electron Vortices and Energy Loss Spectrometry (invited)". MSC-SMC 40th Annual Meeting in Victoria, Canada, 2013.

P. Schattschneider, M. Stöger-Pollach, S. Löffler, T. Schachinger, K. Bliokh. "Vortices and EELS: EMCD and other tricky issues". Enhanced Data Generated by Electrons in Sainte-Maxime, France, 2013.

P. Schattschneider, M. Stöger-Pollach, S. Löffler, T. Schachinger, K. Bliokh. "Peculiar rotation of electron vortices in magnetic fields (invited)". 2nd International Conference on Optical Angular Momentum in Glasgow, UK, 2013.

Posters

I. Letofsky-Papst, S. Löffler, A. Lugstein, M. Albu, W. Grogger. "In situ TEM measurements to study structural changes of VO_2 nanowires". Microscopy Conference in Graz, Austria, 2009.

S. Löffler, I. Ennen, M. Stöger-Pollach, P. Schattschneider. "Energy-Loss Magnetic Chiral Dichroism — Investigating Magnetism on the Nanometer Scale". Junior Scientist Conference in Wien, Austria, 2010.

I. Ennen, S. Löffler, M. Stöger-Pollach, P. Schattschneider. "Energy Loss Magnetic Chiral Dichroism: A Tool for the Investigation of Magnetism on the Nanoscale". Materials Science and Engineering MSE in Frankfurt, Germany, 2010.

M. Stöger-Pollach, S. Löffler, W. Hetaba, *J. Bernardi*. "Low voltage low loss EELS for determination of optical properties of semiconductors". 16. Tagung Festkörperanalytik in Wien, Austria, 2011.

S. Löffler, I. Ennen, M. Stöger-Pollach, P. Schattschneider. "Energy-Loss Magnetic Chiral Dichroism — Investigating Magnetism on the Nanometer Scale". 16. Tagung Festkörperanalytik in Wien, Austria, 2011.

W. Sigle, S. Löffler, P. Schattschneider, R. Höschen, P. A. Koch, Christoph T.and van Aken. "Sub-5 meV precision in plasmon mapping". Microscopy Conference in Kiel, Germany, 2011.

M. Stöger-Pollach, S. Löffler, *W. Hetaba*, I. Ennen. "Low voltage low loss EELS for accurate determination of dielectric properties of semiconductors". Microscopy Conference in Kiel, Germany, 2011.

W. Hetaba, S. Löffler, P. Schattschneider. "Site selective elemental analysis under electron channelling conditions". Microscopy Conference in Kiel, Germany, 2011.

W. Hetaba, M. Stöger-Pollach, S. Löffler, P. Schattschneider. "Advantages of the modified Becke-Johnson Potential in WIEN2k for NiO demonstrated by EELS". Microscopy Conference in Kiel, Germany, 2011.

I. Ennen, *S. Löffler*, W. Hetaba, M. Stöger-Pollach, P. Schattschneider, A. Auge, A. Hütten. "Magnetic dichroism on the nanoscale". Microscopy Conference in Kiel, Germany, 2011.

S. Löffler, I. Ennen, M. Stöger-Pollach, P. Schattschneider. "Towards orbital mapping in the TEM — Non-Lorentzian angular dependence in core losses". Microscopy Conference in Kiel, Germany, 2011.

M. Stöger-Pollach, S. Löffler, W. Hetaba, *P. Schattschneider*. "Investigating the optical properties of $Al_xGa_{1-x}As$ by low voltage VEELS". 10th Multinational Congress on Microscopy in Urbino, Italy, 2011.

W. Hetaba, S. Löffler, *P. Schattschneider*. "Site specific elemental analysis using electron channelling". 10th Multinational Congress on Microscopy in Urbino, Italy, 2011.

W. Hetaba, M. Stöger-Pollach, S. Löffler, *P. Schattschneider*. "Advantages of the modified Becke-Johnson exchange potential for calculating EELS in WIEN2k". 10th Multinational Congress on Microscopy in Urbino, Italy, 2011.

S. Löffler, I. Ennen, M. Stöger-Pollach, *P. Schattschneider*. "Non-Lorentzian scattering behavior in core losses". 10th Multinational Congress on Microscopy in Urbino, Italy, 2011.

V. Motsch, S. Löffler, W. Hetaba, P. Schattschneider. "Simulating HR-EFTEM images for orbital mapping". 15th European Microscopy Congress in Manchester, UK, 2012.

M. Stöger-Pollach, W. Hetaba, S. Löffler. "Is there a chance for mapping optical properties of buried quantum structures by means of Low Voltage Valence EELS in a STEM?" 15th European Microscopy Congress in Manchester, UK, 2012.

W. Hetaba, S. Löffler, P. Blaha, F. Tran, M. Stöger-Pollach. "EELS of NiO: Advantages of core-hole calculations using the modified Becke-Johnson potential". 15th European Microscopy Congress in Manchester, UK, 2012.

W. Hetaba, A. Wolff, S. Löffler, K. Frese, K. Eckstädt, N. Sewald, A. Hütten. "Influence of the polypeptide c25-mms6 on the Cobalt Ferrite nanoparticle formation analysed by TEM and EELS". 15th European Microscopy Congress in Manchester, UK, 2012.

S. Löffler, P. Schattschneider. "Transition probability functions for applications of inelastic core-loss scattering of fast electrons". 15th European Microscopy Congress in Manchester, UK, 2012.

S. Löffler, W. Hetaba, P. Schattschneider. "Simulating the energy-loss near edge structure for interferometric EELS in reciprocal space". 15th European Microscopy Congress in Manchester, UK, 2012.

S. Löffler, V. Motsch, P. Schattschneider. "A factorization approach to the density matrix in energy loss spectrometry". 15th European Microscopy Congress in Manchester, UK, 2012.

S. Löffler, I. Ennen, C. Kübel, A. Auge, A. Hütten, P. Schattschneider. "Site-specific chirality in magnetic transitions". 15th European Microscopy Congress in Manchester, UK, 2012.

A. Wolff, I. Yahiatene, W. Hetaba, N. Mill, M. Wißbrock, S. Löffler, K. Eckstädt, N. Sewald, P. Schattschneider, A. Hütten. "Understanding the protein-inorganic crystal interaction in bioinspired syntheses". DPG Frühjahrstagung in Regensburg, Germany, 2013.

W. Hetaba, M. Willinger, M. Schuster, S. Löffler, R. Schlögl, P. Schattschneider. "Site-specific ionisation edge fine-structure in the electron microscope". Microscopy Conference in Regensburg, Germany, 2013.

R. Hambach, J. Biskupek, S. Löffler, V. Motsch, P. Schattschneider, U. Kaiser. "Towards real-space mapping of valence states using core-loss EFTEM imaging". Microscopy Conference in Regensburg, Germany, 2013.

S. Löffler, V. Motsch, W. Hetaba, R. Hambach, G. Biddau, L. Pardini, C. Draxl, U. Kaiser, P. Schattschneider. "Towards mapping atomic orbitals in the TEM". Microscopy Conference in Regensburg, Germany, 2013.

M. Ikeda, J. Eilertsen, A. Prokofiev, H. Sassik, R. Svagera, M. Waas, S. Löffler, A. Weidenkaff, S. Paschen. "Melt spinning of $CoSb_3$: effect of microstructure on phonon thermal conductivity". Joint Annual Meeting of the Austrian Physical Society and the Swiss Physical Society in Linz, Austria, 2013.

A. Wolff, W. Hetaba, N. Mill, M. Wissbrock, S. Löffler, P. Schattschneider, N. Sewald, A. Hütten. "Biomimetics: A promising route to obtain magnetically anisotropic nanoparticles". Fifth Seeheim Conference on Magnetism in Frankfurt, Germany, 2013.